Electric Field Maps
and
Boundary Element Simulations
of
Electrolocation in Weakly Electric Fish

Thesis by

Christopher Assad

In Partial Fulfillment of the Requirements

for the Degree of

Doctor of Philosophy

California Institute of Technology

Pasadena, California

1997

(Submitted April 24, 1997)

Acknowledgements

I am grateful to many people for their support during my stay at Caltech. It has been a pleasure to work with everyone in the Bower lab over the years. Brian Rasnow has been a great collaborator and sounding board. I thank my advisor, Jim Bower, for his patience, and for allowing me the freedom to pursue my ideas to the end. Discussions with lab colleagues were invaluable and always interesting (special thanks to John Thompson, Mitra Hartmann, Alex Protopapas, Dave Bilitch, Dave Kewley, Mike Vanier, Josee Morissette, and everyone...) Thanks in particular to those who read my preliminary thesis chapters with a critical eye: Jim, Brian, Mitra, and my brother John. Your comments were greatly appreciated. I also had early help in getting started from Mark Nelson and Joe Bastian. Philip Stoddard brought his fish, etomidate, and great enthusiasm to the field mappings of Chapter 3. Jason "Spiff" Leigh lent his virtual reality expertise to demo my fish simulations at conferences. Roy Williams first introduced me to boundary element methods, and Al Barr helped me to analyze the results. I received excellent technical support from Dave Bilitch, Venkat Jagadish, Judy Macias, and John "Millionaire" Uhley. Thanks also to Aaron Petty, Rachel Hunter, and Maritza Alvarado for assistance with the behavioral experiments and fish maintenance.

I dedicate this thesis to my family, my foundation. Thank you Mom and Pops for the love of science you gave me, and for your wisdom and support. I didn't always follow your advice, but in hindsight, you were always right. Frieda, Lily, John and Andy, you will always be my best friends. Lindalee, thanks for your love and support, and for giving me a real life.

Abstract

Weakly electric fish use electroreception – the generation and detection of electric currents – to explore the world around them. Neurophysiological studies of these fish have greatly increased our understanding of central electrosensory processing, and have significant implications for sensory processing in the cerebellum and cerebellar-like neural structures.

This thesis addresses a particular deficiency in our understanding of electrosensory systems: the input pattern of currents stimulating the fish's electroreceptors has not yet been well defined. My goals were to quantitatively reconstruct the electric organ discharge (EOD) and electrosensory images detected by weakly electric fish. These were accomplished by mapping the EODs of six gymnotiform species, simulating the EODs in two (*Eigenmannia* and *Apteronotus*), and predicting the electrosensory input during exploratory behaviors.

The EOD maps display a wide diversity of species-specific patterns, implying significant differences in field generation, sensory input patterns, possible behavioral strategies, and processing algorithms. Each fish must interpret electrosensory images which are highly dependent upon its own particular EOD pattern.

To study electrolocation noninvasively during natural behaviors, I developed a 3-d electric fish simulator based on the boundary element method. The simulator solves Poisson's equation for the electric potential in and around the fish, modeled as an electrostatic boundary value problem. Models of two species were built and optimized to match the measured maps. By varying only a few parameters, I explored how the electric organ structure and activation generate a particular EOD pattern: *Eigenmannia* has a synchronous electric organ and dipolar EOD, while *Apteronotus* is better described as a propagating multipole.

The simulator was used to reconstruct the EOD during a previously published tail-probing behavior of *Eigenmannia*, and from my own videotapes of *Apteronotus* exploring objects under infrared light. Simulations of selected exploratory behaviors revealed the EOD fields, modulations from body orientation and objects, and the resulting electrosensory patterns. The results (1) imply the fish control their body positions to regulate particular features of the electrosensory image, (2) predict features of the electrosensory input reaching the brain, and (3) suggest algorithms needed to extract useful signals from the electrosensory stream.

Table of Contents

"We may hope one day to ... express, at least in physical terms, what it is like to live in an electric world."
Hans W. Lissmann, 1963

1 Introduction and Motivation

A general task shared by most biological sensory systems is to efficiently extract relevant stimuli from a sensory stream filled with noise, redundancies, and other irrelevant information. In particular, an animal's motor activity can cause significant changes in its sensory input, consequences termed "reafference" (von Holst and Mittelstaedt 1950). Reafferent signals must be identified and processed appropriately to correctly interpret external stimuli. Sensory reafference is especially important to animals with active sensory systems, such as echolocating bats and cetaceans, and electrolocating electric fish. These animals control both the signal generation and reception, and so "rely heavily on the analysis of reafferent input to gain information about the environment" (Heiligenberg and Bastian 1984). The study of active sensory systems is helping to answer a more general question in neuroethology: how might the behavior of an animal be directed to optimize its sensory acquisition?

Weakly electric fish constitute an important model system for the study of active control of peripheral sensing. They generate and detect electric currents to explore and communicate with the world around them (see Background), and are known to exhibit a rich repertoire of exploratory and social behaviors. These behaviors presumably include strategies to enhance the information available in the peripheral electrosensory image. The sensory information gathered during such behaviors is relayed to multiple somatotopically organized maps in a single hindbrain structure, and then on to higher centers. These neural structures have been extensively studied, and great progress has been made in understanding central electrosensory processing and control. Results from electrosensory

systems may have significant implications for sensory processing in general, and in particular, for sensory processing in the cerebellum and cerebellar-like neural structures in mammals.

In contrast to the progress made in central neurophysiology, the input to active electrosensory systems has not yet been well defined. To fully understand and model the neural networks underlying electroreception, it is first necessary to quantify the pattern of electrosensory stimuli exciting the receptors, and therefore we need to clearly visualize and quantify the electric fields about the fish. How is the electric image of the fish's environment formed? What do the fields look like? Can we predict changes in the electric field (and thus the patterns of electrosensory stimulation) during natural behaviors? Do the behaviors have significant sensory consequences and thus reflect the animal's particular strategies or computational requirements? To answer these questions requires examining the entire pattern of currents resulting from the fish's discharge and environment.

The primary goals of this thesis were to quantitatively reconstruct first the electric organ discharge (EOD) and then the electrosensory images detected by weakly electric fish. These were accomplished by mapping the EODs of several species, simulating the EODs in two species, and finally recreating the electrosensory input during exploratory behaviors. In this introductory chapter, I first briefly review the major components of active electrosensory systems. The subsequent sections describe the organization of chapters in this thesis, along with a brief synopsis of my contributions to mapping EODs and electrosensory input images. The final section relates some of the interesting history behind electric fish investigations, and explains the motivation for an electrical engineer to study this biological, electric imaging system.

1.1 Background

1.1.1 Electroreception

Two different orders of teleost fish, gymnotiforms in South America and mormyriforms in Africa, have separately evolved the novel sensory modality termed electroreception (for review see Bullock and Heiligenberg 1986; Lissmann 1963; Carr 1990). These "weakly electric"[1] fish have a specialized active electrosensory system for detecting nearby objects in their environment and for social interactions with conspecifics. An electric organ in the animal's body, controlled by a pacemaker nucleus in the brain stem, discharges weak currents through the water surrounding the fish. The currents are detected and measured by an array of electroreceptors throughout the fish's skin, which are sensitive to small changes in amplitude or phase of the local transdermal potential. Active electrolocation, the sensing of environment through this self-generated current, is possible because objects that differ in conductivity and dielectric properties from the surrounding water cause small distortions in the electric field detected at the fish's skin. The distribution of currents across the skin is modulated by body orientation, relative position with respect to nearby objects, and the discharges of other electric fish, the sum of which result in a composite electrosensory "image" which the fish must interpret. Behavioral and physiological studies have demonstrated the fish are extremely sensitive to small modulations superimposed on the self-generated field, which acts as a carrier signal.

Electroreception is the primary sensory modality of weakly electric fish (Hagedorn 1986; Hopkins 1986a). Many are nocturnal and often live in turbid waters, where the advantages conferred by "seeing in the dark" have allowed these species to proliferate. More accurately, electrolocation might be better described as an extended sense of touch - the peripheral image is distributed across the entire body surface, there is no focusing

[1]"Strongly" electric species, such as the electric eel (*Electrophorus*), can also produce fields large enough to stun or kill, for use in predation or defense.

Figure 1.1 Examples of weakly electric fish, and head-to-tail EOD waveforms

A. *Apteronotus albifrons*, South American gymnotiform, "wave" type EOD

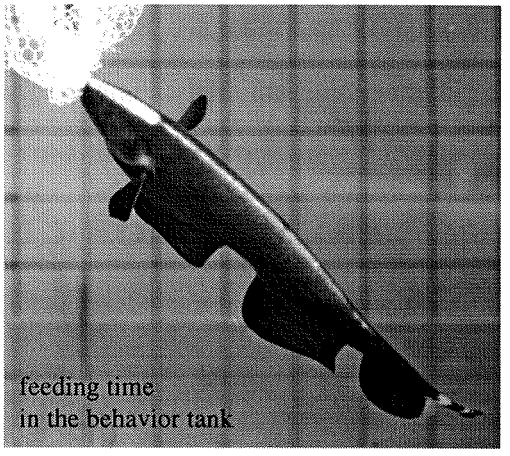

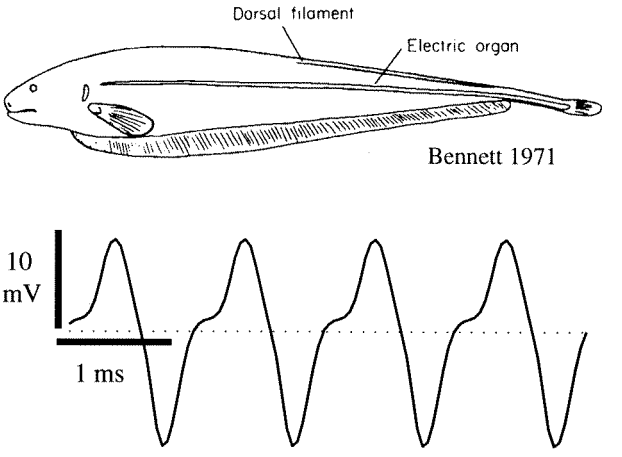

B. *Gnathonemus petersii*, African mormyrid, "pulse" type EOD

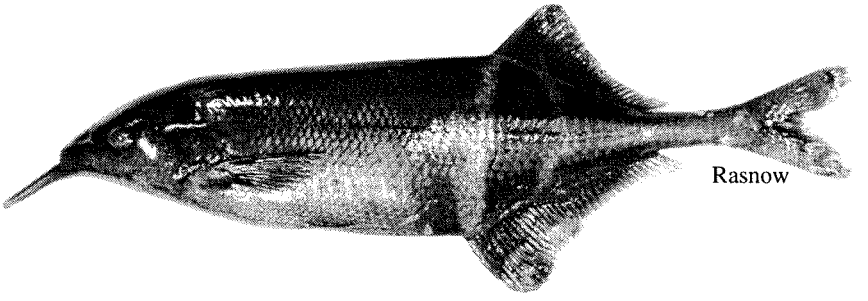

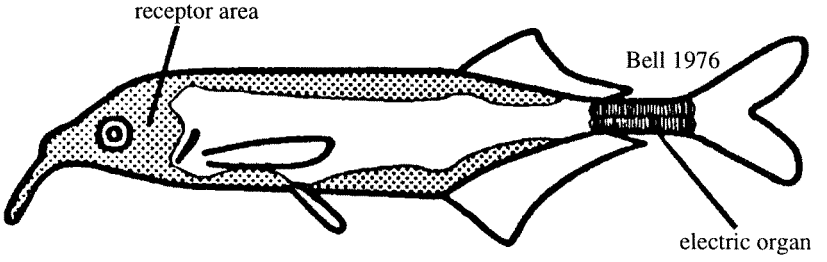

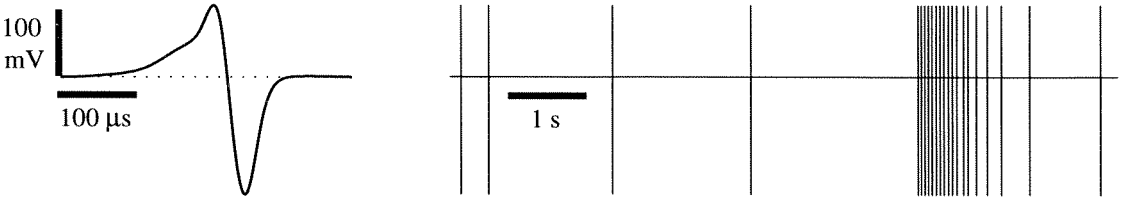

mechanism, and stimulus intensity falls off rapidly with distance to an object. In electrocommunciation, where the EOD plays a significant role in social ordering and mating behaviors, a comparison with acoustic signaling is considered more appropriate (Hopkins 1986b, 1988; Hagedorn and Heiligenberg 1985; Carr 1986). In the far field of a fish's output range, where the field is mainly dipolar, only temporal variations of the EOD signal are unambiguously transmitted to other electric fish.

1.1.2 EOD generation

EODs are traditionally classified by the voltage waveform measured between head and tail: "wave type" fish have continuous, periodic discharges, while "pulse type" fish have silent intervals between brief discharges (Fig. 1; Bennett 1971a; Bass 1986). Wave fish typically have very narrowly tuned frequency spectra, with power in a fundamental frequency and higher harmonics. The different species are segregated by EOD frequency bands, so that each has its own range, and the particular frequency of an individual within its band often depends on gender or status in the social hierarchy (Hagedorn 1986). Pulse fish, with much broader spectra, sample in time rather than frequency, and can interdigitate their EODs in time to avoid contamination from neighbors (Bell et al. 1974; Hopkins and Westby 1986). Most species are recognizable by temporal features of the EOD waveform, such as the number of phases, with individual differences depending on gender and maturity (Hopkins 1986a; Hagedorn 1986). There is evidence that the fish can recognize individual conspecifics based on small differences in EOD waveform (MacGregor and Westby 1992; Crawford 1992).

The EOD is generated by an electric organ usually composed of modified muscle cells, called electrocytes, stacked in series and in parallel to effectively add their outputs (Grundfest 1960; Bennett 1971a). A typical electrocyte is cylindrical and has two large faces along its longitudinal axis, with a high impedance connective tissue tube enclosing the

sides. Either one or both electrocyte faces are composed of active membrane[2], able to generate current across the membrane into the cell. Only one face is active at a time, so there is a net current logitudinally through the cell. When the current from many electrocytes are added together in phase, a large external current results. Electrocytes are innervated and activated by electromotor neuron axons that descend from the spinal cord. The exception to this scheme is the gymnotiform family Apteronotidae, in which the motor neuron axons themselves act as the electrocytes in the adult animal (Waxman et al. 1972; Kirschbaum 1983). This unique family includes the highest frequency wave fish, with EOD frequencies as high as 1800 Hz.

Short term stability of the self-generated EOD is presumably important for the detection of small field perturbations induced by objects. Bullock (1970) proposed that the electric organ of the wave fish *Apteronotus* is the most stable biological oscillator known, with a frequency coefficient of variation of 0.00012 over several seconds. Frequency stability has been mainly attributed to the regularity of the pacemaker nucleus in the brainstem (Dye and Meyer 1986). The cells in the pacemaker are tightly coupled to fire synchronously, and each command volley is relayed down the spinal cord to elicit a single electric organ discharge. Wave fish can modify their firing frequency to avoid electrical interference from neighboring fish at the same frequency (the jamming avoidance response, Heiligenberg 1989), or instead phase lock with the jamming signal (active phase coupling, Langner and Scheich 1978). Pulse fish vary their pulse timing to avoid overlapping EODs, by phase locked alternation or an echo response (Bell et al. 1974). They also can modulate their discharge frequency to assist in electrolocation (Toerring and Belbenoit 1979), but at the same time keep the pulse waveform extremely constant. For electrocommunication, both pulse and wave fish produce transient rises in frequency and interruptions of the EOD, commonly labeled by the sounds that these modulations produce

[2]Active cell membranes contain chemically-gated or voltage-gated channels, specific for particular ions. Differences in ionic concentrations across the membrane provide the driving forces (see Hille 1984).

when played on an audio monitor: chirps, pings, spikes, buzzes, rasps, and even yodels (Bullock 1969; Hagedorn and Heiligenberg 1985; Hopkins 1986a).

The useful range of electrolocation and communication is dependent on water conductivity, the receiver's behavioral threshold, and the sender's EOD amplitude and body size or dipole moment. For communication, the limits of detection are approximately 1-2m (Knudsen 1975). In contrast, active electrolocation only appears useable within one body length from the fish, or 5-10 cm for 1 cm objects (Heiligenberg 1977). Object distortions are induced in proportion to the magnitude of the electric field at the location of the object, and so depend strongly on the rate of decay of the field with distance. The field strength is related to dipole moment, the length between the poles multiplied by the magnitude. A bigger dipole moment leads to better range for electrolocation (Heiligenberg 1975; Knudsen 1975), and often indicates social dominance (Hagedorn 1986). Many species, particularly gymnotiforms, have therefore developed long electric organs and tails. However, this also confers some disadvantages: a longer electric organ is more difficult to synchronize (Bullock 1986), and a stronger signal increases vulnerability to electrically sensitive predators or belligerent conspecifics (Hagedorn 1986). For example, Westby (1988) recorded the signals of an electric eel, which has both strongly and weakly electric systems, as it seemingly quartered a stream and homed in on the signal of a smaller weakly electric pulse fish before capturing it.

1.1.3 Electroreceptors

Weakly electric fish detect their own discharges with an array of several thousand tuberous electroreceptor organs[3] in the skin (Scheich et al. 1973; Bennett 1971b; Zakon 1986). There typically is found a higher spatial density in rostral regions, especially around the head, compared to caudal regions (15/mm^2 vs. about 3/mm^2 in *A. albifrons*; Carr et al.,

[3] There is another class of receptors, the ampullary electroreceptors, which respond to low frequency, weak external voltage sources, such as those produced by muscle and nerve tissue tissue in other organisms. Ampullary receptors are also found in many different fish and other animals, including sharks, many catfish, some amphibians, and even on the bill of the platypus. Since they are mainly thought to be used in passive electrolocation, I do not discuss them further.

1982), as well as more dorsal and ventral, away from the midline. Derived from lateral line mechanoreceptors, the receptor cells share many of the same biophysical characteristics as hair cells in the mammalian inner ear, except that the hair bundle is absent. Instead of responding to mechanical stimuli, the electroreceptor cell directly transduces the voltage drop or current across the skin.

Most electroreceptor types fall into one of two broad functional categories: rapid timing units or amplitude-modulated units. Rapid timing units have very small absolute thresholds[4] (as low as 10 μV/cm, depending on species) and fire one-for-one with the EOD, encoding phase information. Amplitude-modulated units have higher absolute thresholds (0.5-10 mV/cm) and a wider dynamic range to encode stimulus intensity, but still maintain high sensitivity to small modulations (differential thresholds below 1 μV/cm). While these general classifications have been applied to most electric fish, the particular coding schemes used for realistic stimuli are still poorly understood for many species. For example, timing units are rarely recorded in high frequency *Apteronotus* (Scheich and Bullock 1974); instead, two subtypes of amplitude coders have been found (Bastian 1981). In addition, there is recent anatomical evidence for a spatially segregated population of timing units in the dorsal filament of apteronotids (Franchina and Hopkins 1996).

Electroreceptors are generally tuned to respond to each fish's own EOD frequencies. Most electroreceptor types have V-shaped threshold vs. frequency tuning curves, which are very sharp in wave species and often broader in pulse species, and are centered close to the peak frequency in the fish's EOD spectrum. The tuning properties arise from electrical filtering in the active membrane of the receptor cell, which can include nonlinearities such as rapid adaptation (Xu et al. 1996). Since the tuning curves are measured using sine wave stimuli, the responses of receptor cells to complicated EOD waveforms are not yet well understood. For example, tuning curves for receptors in

[4]Receptor reponses are typically measured in both *absolute* threshold, the smallest field strength at the skin that evokes activity in the receptor afferent, and *incremental* threshold or sensitivity, which is the smallest change in input for which changes are perceptible in the receptor's output.

Apteronotus have two sensitivity peaks, one near the EOD fundamental and the other at the second harmonic (Hopkins 1976). More complicated spatial variations in receptor tuning have been found in *G. carapo*, a pulse gymnotiform with a long electric organ and a complex EOD (Watson and Bastian 1979; Bastian 1977). The results of our study of *A. leptorhynchus* (Rasnow et al. 1993) also suggest spatial variations in receptor properties, dependent upon the local EOD waveform at each receptor's location on the body surface. Furthermore, although the best stimulus configuration is usually assumed to be with electric field directed perpendicular to the skin surface, directional tuning to tangential field angles was recently reported in *Hypopomus* (Yager and Hopkins 1993; McKibben et al. 1993). The spatial and temporal pattern of electroreceptor responses to the fish's own EOD alone can therefore already be quite complex, and probably requires normalization in central processing structures.

1.1.4 Electrosensory Image Processing

Considerable regions of the electric fish brain are devoted to electrosensory processing and integration of electrosensory information with other sensory modalities and motor control. Sensory information coded by the receptor afferents first projects to multiple somatotopically organized maps in a bilateral hindbrain structure, the electrosensory lateral line lobe (ELL), where it terminates on the basal dendrites of principal cells (Fig. 2a; Heiligenberg 1988). The ELL also receives extensive descending inputs from granule cells in the caudal cerebellar lobe and praeeminential nucleus, inputs that arrive on parallel fibers through the large principal cell apical dendrites. These pathways incorporate proprioceptive information (e.g, tail angle, Bastian 1974, 1995, 1996ab), electroreceptive feedback (e.g., gain control from cerebellar parallel fiber inputs to ELL, Bastian 1986a), and motor command information (e.g., corollary discharge in mormyrid pulse fish, Bell 1986, 1993). In addition to afferent and descending inputs, a commissural pathway projects between the two bilateral ELL lobes, so each map in the ipsilateral lobe receives inputs from its corresponding map in the contralateral lobe (Bastian et al. 1993).

The ELL circuitry has been well characterized in both gymnotids (Maler et al. 1981; Carr and Maler 1986; Bastian 1993) and mormyrids (Bell and Szabo 1986; Bell 1986; Meek 1993). Principal cells in each ELL map make lateral connections and have inputs from local interneurons, resulting in center-surround receptive fields for spatial filtering. Response properties of the pyramidal output cells indicate that the multiple ELL maps filter the incoming data at different spatial and temporal resolutions (Shumway 1989a,b). The laminar circuitry falls well within the class of networks usually considered cerebellar (Paulin 1993). The ELL principal cells send their axons to the praeeminential nucleus and the torus semicircularis (Fig. 2b; Carr and Maler 1986). Somatotopic mappings are preserved in many of the ascending projections of the electrosensory system, including areas that integrate information from other sensory modalities, such as the optic tectum.

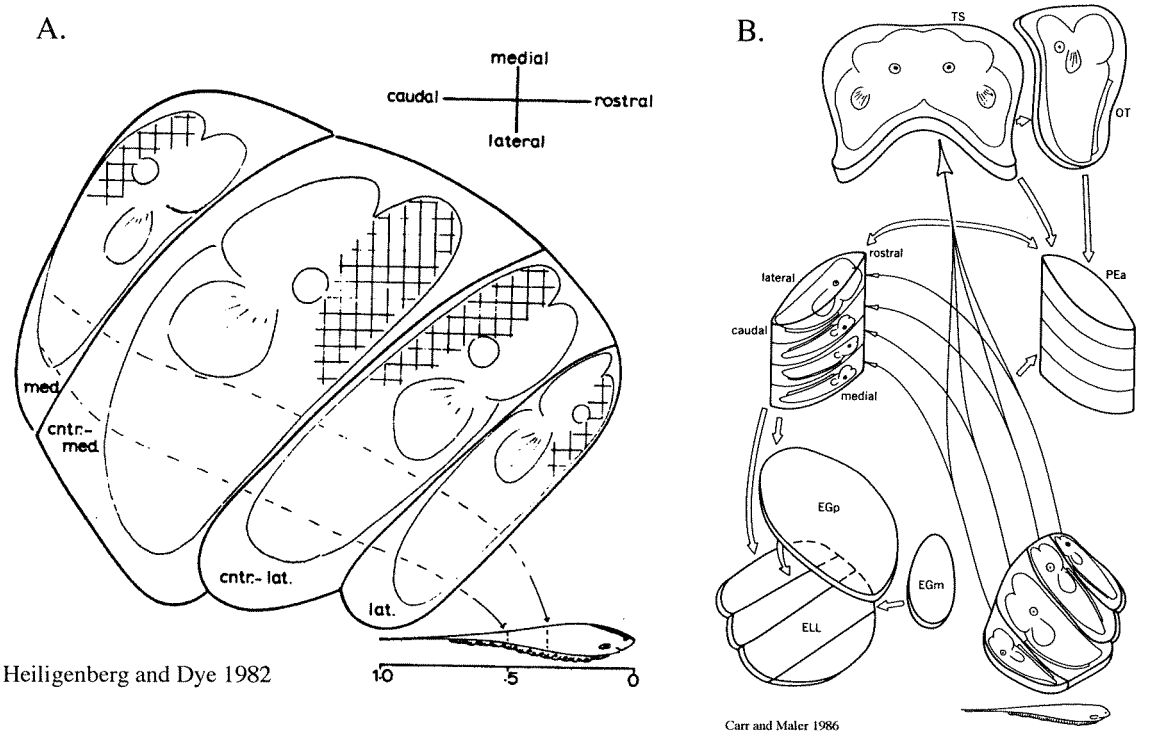

Figure 1.2 Somatotopic organization of *Eigenmannia* ELL (A) and map of electrosensory projections (B). ELL - electrosensory lateral line lobe, EGp - eminentia granularis posterior, EGm - eminentia granularis medialis, Npd - nucleus praeeminentialis, TS - torus semicircularis, OT - optic tectum. EGp and EGm are in the caudal lobe of the cerebellum.

The existence of efficient electrosensory processing algorithms is indicated by the extremely fine behavioral sensitivity of electric fish to a variety of electrosensory stimuli: in object detection (Lissmann 1963; Bastian 1976, 1986b), direct electrical stimuli (Knudsen 1974), or extreme phase sensitivity (Kawasaki *et al.* 1988; von der Emde and Bleckmann 1992; Langner and Scheich 1978). For example, Knudsen (1974) measured behavioral thresholds to applied electric fields as low as 0.2 $\mu V_{p\text{-}p}$/cm in *Apteronotus*, well below the 30 $\mu V_{p\text{-}p}$/cm minimum perceptible differential threshold of receptors reported by Hopkins (1976). Bastian (1981a,b) similarly found that the sensitivity of ELL cells was already 16 times that of individual receptors.[5] In higher central processing structures, convergence of sensory information from progressively larger areas of the body surface is used to achieve the fine behavioral responses for detection of external stimuli.

1.1.5 Behavior and electrosensory input

Weakly electric fish exhibit a rich repertoire of exploratory and social behaviors, presumably utilizing strategies to enhance the information available in the peripheral electrosensory image. They perform characteristic body movements and modulations of EOD pulse intervals while exploring their environment (Fig. 3, from Toerring and Belbenoit 1979; Behrend 1984; Bastian 1986b). Movements of the fish result in significant changes in the sensory input, both in the object image and from the movement itself, a consequence termed sensory reafference (von Holst and Mittelstaedt 1950). Distinguishing sensory exafference from reafference is critical to the success of active electrolocation. Many species, especially those with long electric organs, swim by undulating only a single elongated ventral or dorsal fin, while at the same time holding their bodies rigid (Lissmann 1963; Behrend 1984). This allows the fish to swim equally well forward or backward, and to hold the body in an arc while scanning objects (Bastian 1986b), while maintaining rigid control over the orientation of their electroreceptive surfaces. Presumably this reduces the

[5]The use of different methods made measurement of receptor reponses difficult to compare between investigators - this is discussed further in Chapter 6.

number of variables that must be taken into account while interpreting electrosensory information, by keeping the detector array in fixed orientation with respect to the field generation. Therefore these behaviors should help distinguish electrosensory reafference from effects of external objects.

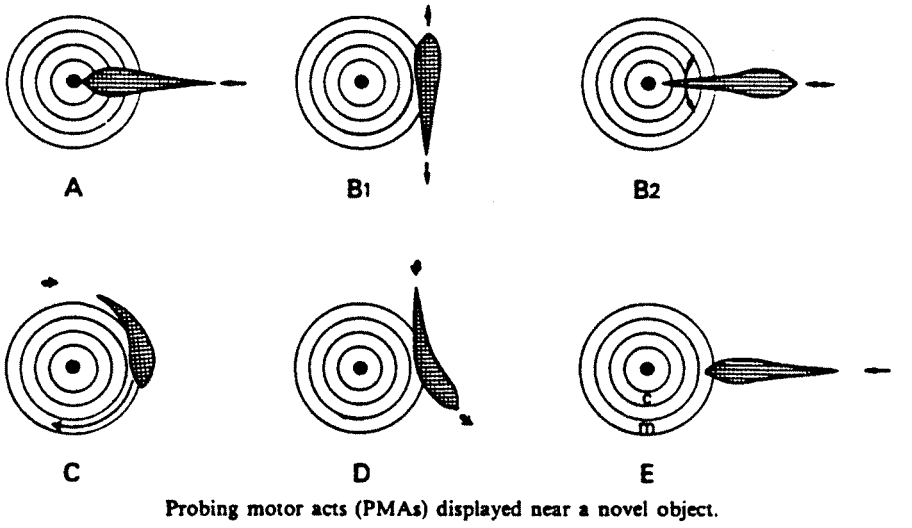

Figure 1.3 Examples of probing behaviors (Fig. 2 in Toerring and Belbenoit 1979)

Besides its obvious use in exploration, electrosensory input plays an important role in maintaining body position and orientation with respect to external objects such as plants, both during swimming and at rest. Heiligenberg (1973) showed that *Eigenmannia* maintained hovering distances from objects in the surrounding water on the basis of electrical cues. Behrend's lesion studies in *Eigenmannia* (1984) showed that disruption of normal cerebellar function led to an inability of the fish to maintain its specialized swimming and probing postures. Cells in the cerebellum have also been found to respond bimodally to electrosensory and proprioceptive stimuli (Bastian 1974, 1995). Although the cerebellum has been implicated in integrating electrosensory information with motor functions, the details of the circuitry involved are not yet well understood.

The neural substrates underlying extreme amplitude and temporal sensitivities have been well documented in the jamming avoidance response (JAR) exhibited by wave fish

such as *Eigenmannia* (Watanabe and Takeda 1963; Heiligenberg 1973, 1989, 1991). If neighboring conspecifics have EOD frequencies too close together, the signals interfere with a beat cycle that "jams" the electrosensory pathway, degrading the ability to electrolocate (Heiligenberg 1973). The fish's JAR shifts the EOD frequency away from that of the conflicting jamming signal. Correct performance of the JAR requires detailed comparisons of spatio-temporal information across different regions of the body surface; empirically, the overall system performance is proportional to functional surface area (Heiligenberg 1989). Heiligenberg and his colleagues have elucidated the principal neural circuits involved, spanning over a dozen synaptic levels from electroreceptive periphery to electric organ pacemaker. This electrosensory-electromotor loop establishes sub-microsecond temporal acuity in *Eigenmannia* - among the highest found in the animal kingdom (Kawasaki et al. 1988). A similar JAR is found in other gymnotiform wave fish, and has also evolved in the only known mormyriform wave species, *Gymnarchus niloticus* (Bullock et al. 1975; Kawasaki 1996). The JAR may be the only non-reflexive vertebrate behavior in which the entire neural circuit has been described from peripheral receptor to motor effector (Heiligenberg 1991).

In most sensory systems it is very difficult to investigate responses to realistic stimuli during normal motor behaviors. Weakly electric fish have several advantages in this regard. Modulations of the electric organ output, such as the JAR and chirping behaviors, are easy to evoke and manipulate in well controlled experimental preparations. In addition, when allowed to swim freely, the fish naturally explore novel objects in our laboratory fish tanks, and can be trained in tasks based upon discrimination of electrical cues (e.g., Lissmann 1963; Knudsen 1974). The electric fields in the water about the fish can be both measured directly and numerically simulated, allowing the prediction of sensory input. There is no neural feedback to the peripheral sensory receptors, and the receptor afferents project directly to somatotopic maps in the hindbrain ELL. Therefore, the readily predicted

sensory input is only two synapses away from central sensory processing in a cerebellar-like laminar circuit.

In all animals, motor behaviors produce correlations between motor commands, proprioceptive input, and sensory reafference, correlations that can be learned and then predicted. Patterns of input that can be predicted contain no new information, and so can be ignored. Therefore, central brain structures commonly use descending feedback and other signals to filter ascending sensory information. For example, motor command signals used to modulate incoming sensory information are termed corollary discharges (Sperry 1950), or efference copy when they produce a negative image of the expected sensory reafference (von Holst and Mittelstaedt 1950). These signals are found in the ELL of mormyrid pulse fish in conjunction with the electromotor command driving the electric organ (Bell 1981, 1986), but not in gymnotiforms. However, all electric fish make similar use of proprioceptive and electrosensory feedback to exploit correlations in time and space to enhance the electrosensory image. To be robust to changes, sensory systems must also be adaptive- they must learn and continuously update an internal representation of the external world, to generate accurate expectations of the impending sensory signals.

Current research in electroreception is focused on the role of descending feedback to the ELL and adaptive filtering of electrosensory information (Bell 1981, 1993; Maler 1993; Bastian 1995, 1996ab; Nelson and Paulin 1995; Bell et al. in press). The descending control functions as a slowly adapting negative image template to subtract from the immediate sensory input, effectively masking steady-state signals and enhancing novel features (termed expectation generation, Bell 1993). This "predictive" function of cerebellar input to ELL appears due to anti-Hebbian synaptic plasticity at the parallel fiber-principal cell synapse. Other more direct electrosensory feedback arrives on parallel fibers in the ventral molecular layer, more proximal to the pyramidal cell bodies. This input, modulated by higher brain areas, has been proposed to provide a searchlight or attentional mechanism to enhance regions of noteworthy activity (Maler and Mugnaini 1993). The

proposed functions stem from a common theme: in order to maximize information content of the ascending data, the brain must enhance novel stimuli while ignoring or suppressing predictable inputs. These functions, clearly observed in electrosensory and mechanosensory lateral line systems (Bell et al. in press), would prove very useful in other sensory modalities and systems, and may be common to cerebellar-like circuits.

1.2 Thesis Overview

1.2.1 Mapping the EODs of weakly electric fish

In order to study active electroreception in weakly electric fish, we began by investigating the electrosensory input pattern generated by the EOD. In the course of this work, we constructed an EOD mapping apparatus that allowed full waveform electric potential and field measurements. It includes a recording tank equipped with a water recirculation system to respirate the fish while paralyzed, a computer controlled 3-d robot (a modified XY plotter) for rapid and precise positioning of electrode arrays, low noise electronics to amplify and digitally sample up to 6 channels simultaneously at high resolution, and a Macintosh IIfx to control the experiments. We also developed a large set of software tools to manage both data collection and processing. The software includes an application for viewing animated EOD maps, which is available to the research community along with our EOD map database (http: www.bbb.caltech.edu/ElectricFish).

Chapters 2 and 3 describe the mapping procedures in detail, and present EOD maps of six different gymnotiform species commonly used in studies of electroreception. From these maps we conclude there is a wide diversity of species-specific EOD patterns, each correlated with the idiosyncrasies of its owner's electric organ. Furthermore, the great variety implies significant differences in possible behavioral strategies and processing algorithms between species. Each fish must interpret peripheral electrosensory images which are highly dependent upon its particular EOD pattern. Analyses of the spatial and

temporal organization of the EODs suggested mechanisms by which they are generated and their sensory significance.

1.2.2 Simulating the EOD

In order to better study electrolocation noninvasively during natural behaviors, I developed a computer simulator of the fish and EOD. The physics of the electric field in the water about an electric fish are well understood and are amenable to modern numerical techniques. Furthermore, the low frequencies and ohmic domains involved allow modeling as a quasistatic boundary value problem, the goal of which is to solve Poisson's equation for the electric potential in and around the fish.

Chapter 4 describes the construction and use of a 3-d electric fish simulator based on a boundary element method. In **Chapter 5**, I apply the simulator to build and calibrate models of two wave fish species: *Eigenmannia virescens* and *Apteronotus leptorhynchus*. With a few parameters it was possible to explore the models and optimize them to match the measured maps. The optimization process provided new insights into how the electric organ structure and activation generate a particular EOD pattern.

1.2.3 Reconstructing electrosensory images during active exploration

The EOD simulator can accurately reconstruct the fields around the fish. It therefore allows a quantitative investigation of the electrosensory consequences of fish movements during exploratory behavior. **Chapter 6** describes the quantification of electrosensory stimuli over the receptor array, and predicted images reaching the ELL during active exploration. I first used the simulator to recreate the electric fields during a probing behavior of *Eigenmannia*, as reported by Behrend (1984). I next built a large behavioral tank, and videotaped specimens of *Apteronotus* freely swimming, foraging, and exploring objects, under infrared light only (to prevent visual cues). The videotape records were studied to identify exploratory behaviors, reconstruct them in the model, and then to simulate the EOD during sequences of the behaviors. The simulations reveal the EOD

fields, modulations from body orientation and objects, and the resulting electrosensory stimulus patterns. The results suggest that the fish are actively controlling their body position in order to regulate particular features of the electrosensory reafferent stimuli. The results also allow us to predict both the information available to the ELL, and some of the difficulties inherent in extracting useful signals from the electrosensory stream.

Part of this work was done in collaboration with Brian Rasnow (Chapters 2, 3) and Philip Stoddard (Chapter 3). Credit is also due Roy Williams, who first outlined the boundary element method for me (Chapter 4), and to Rachel Hunter for assistance with the behavioral experiments (Chapter 6).

1.3 Significance

1.3.1 Contributions of this thesis

The work presented in this thesis provides a new level of insight into the sensory and neural mechanisms underlying electrolocation. My main contribution has been to precisely define the electrosensory input. For the electroreceptors, I provide a detailed description of the peripheral electrosensory input from the entire skin surface, with measurements of the local field waveform relevant to receptors in each region of the fish. In order to analyze electroreceptor organ responses and model their transfer functions, we need to know input-output relations using realistic stimuli. For sensory processing in central structures, maps of the entire input will facilitate both electrophysiological studies and network modeling. Finally, the study of electrolocation would not be complete without analyzing exploratory behaviors. Reproducing the EOD fields in these situations illuminates the sensory consequences of such behaviors. In a sense, I hope to convey a feeling for what an electric fish might "feel" as it goes about its nightly excursions.

The measurements and simulations are the first quantitatively accurate 3-d views of the EOD, and of its modulations from natural behaviors and nearby objects. These improved methods were a logical step in a progression made clear from previous electric

fish mappings and simulations: EOD measurements were limited to waveforms from several spatial positions, or to contour maps of RMS potential (e.g., Bennett 1971a; Heiligenberg 1973; Knudsen 1975; Hoshimiya et al. 1980; Bastian 1981a), and modeling efforts produced insightful but qualitative results from 2-d finite difference and finite element simulations (Heiliginberg 1975; Hoshimiya et al. 1980), and from a 3-d analytical model (Bacher 1983). I have added resolution to the spatial and temporal dimensions, both of which are essential to understanding how this sensory modality works.

While the electrophysiology of the ELL has proven very fruitful for studies of central sensory processing, the electrosensory input has only been examined one receptor or cell at a time. Given a complicated circuit to analyze, such as the ELL, an electrical engineer will first try to ascertain the entire input-output relation, i.e., the system transfer function. The EOD maps and simulations detailed here provide the entire input – and hopefully also provide a detailed terrain in which to study the EO, electroreceptors, electrolocation, and even electric fish phylogeny, all contributing to the neuroethology of active electrosensory systems.

1.3.2 Electric fish and cerebellar sensory processing

The ultimate objective of this research is to help in understanding the role of the cerebellum in sensory-motor processing. Traditionally, the cerebellum has been considered a motor control center, coordinating fine motor timing to produce smooth, well-balanced movements. But from control theory, we know that fine and fast motor control requires fast and accurate sensory and proprioceptive feedback, especially for system dynamics where forces must be considered. High quality sensory acquisition also requires fine motor control to appropriately position the sensory receptive surfaces (e.g., in the vestibular-ocular reflex). Different areas of the cerebellum have clearly been shown to receive fast sensory input pathways from a variety of sensory modalities and to participate in sensory processing and integration. Paulin (1993a) pointed out that other cerebellar-like structures, such as the ELL of electric fish or the dorsal cochlear nucleus in mammals, are

not considered cerebellar precisely because of their obvious sensory functions. It has even been proposed that optimal aquisition of sensory information (e.g., as a tracking system, Paulin 1993b) may be the primary contribution of the cerebellum's influence on motor control (Bower and Kassel 1991; Bower 1992). However, the idea that processing sensory information is as important to cerebellar function as motor control is still not widely accepted. Quantitatively understanding this system in mammals is very difficult: despite its famous crystalline structure, the cerebellar inputs and outputs are complex, often ill defined, and are not known across large areas of the cortex.

Weakly electric fish constitute an excellent system to study the role of the cerebellum in the active control of sensory aquisition and in sensory-motor integration. We can simulate the EOD during natural behaviors, and then predict the sensory image and the information being passed on to the ELL. The ELL is cerebellar-like in structure, and receives most of its parallel fibers from an overlying granule cell mass considered part of the caudal cerebellar lobe. The cerebellum itself is greatly enlarged in many of these fish, especially in the mormyrids (Fig. 4), and plays an important role in processing of electrosensory information, integrating it with other sensory modalities, and contributing to the control of swimming and body posture. The ELL is therefore a good place to explore the role of cerebellar-like circuits and central feedback in adaptive filtering of sensory information.

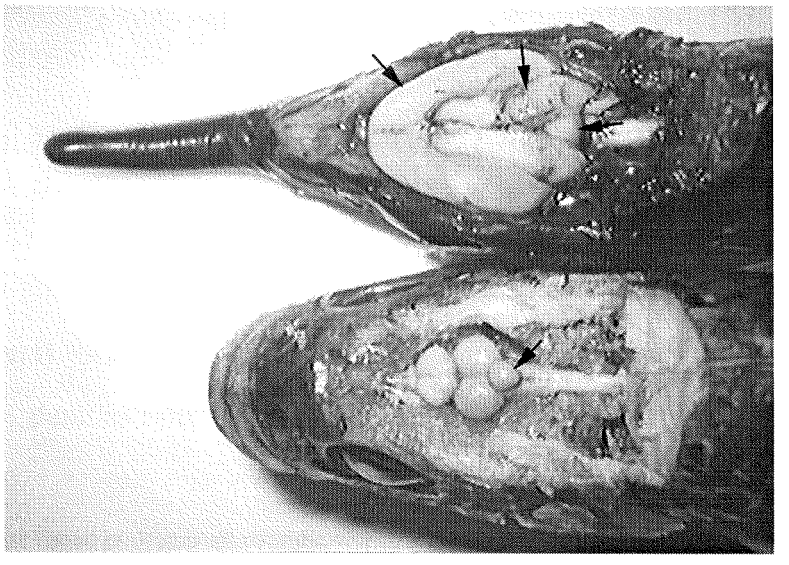

Figure 1.4 Brain comparison between an electric mormyrid (top) and a non-electric fish (bottom). Arrows indicate lobes of the cerebellum.

1.4 Why would an EE study electric fish?

1.4.1 Strongly electric fish and the discovery of electricity

The fact that certain fish emitted strange energies has been known for centuries (Wu 1984; Moller and Fritzsch 1993). Ancient Egyptians, Greeks, and Chinese all recorded the use of strongly electric species for various therapeutic purposes. By the 1700's, strongly electric fish were helping to shape early discoveries in electricity: Cavendish (1776) built artificial torpedos[6] out of leather, wood and pewter, complete with Leyden jars to supply the shock, to prove the fish's power was from an equivalent source; Volta (1800) patterned his voltaic pile, the first battery, after the stacked disks of the electric organ; Faraday (1839) studied the electric eel, and wrote a treatise entitled "Notice of the character and direction of the electric force of the Gymnotus"; and even Maxwell (1879) recognized the influences of electric fish. The existence of strongly electric fish also forced the acceptance of animal electricity near the end of the 18th century, inspiring biologists to the new field of electrophysiology (Wu 1984), and electric organs were later used to study chemical synapses and active membranes in nerve and muscle tissue (Grundfest 1960). However, strongly electric organs posed a problem for Darwin (1859), for they should not have evolved from muscle tissue with no intermediate purpose. "Pseudoelectric" organs had been described in what we now know are weakly electric fish, but they were considered useless at the time.

1.4.2 Weakly electric fish: biological, electric imaging systems

In 1773, John Walsh (a British colleague of Ben Franklin) conducted the first laboratory experiments that suggested an electric eel could somehow detect unseen changes in its environment. However, it wasn't until the 1950's that the use of electrical imaging by weakly electric fish was demonstrated definitively (Lissmann and Machin 1958;

[6]Electric rays such as the torpedo are found in oceans all over the world, and in the Mediterranean Sea.

Lissmann 1963). Since then, electrosensory systems have been extensively investigated by electrophysiologists and neuroethologists studying central processing of sensory pathways (Bullock and Heiligenberg 1986; Carr 1990; Heiligenberg 1991). By now the anatomy and circuitry are well known, and the focus has turned to function: specifically, issues in adaptive filtering, synaptic plasticity and learning in the ELL and other cerebellar-like structures (as described above).

The electric fish "field" has thus moved from "power electronics" to signal processing, the other domain of electrical engineers.[7] Coincidentally, sensory prediction and predictive control are becoming hot topics in robotics, neural networks and adaptive control, and the search for biological inspiration is just beginning to target the cerebellum (for review see Miall and Wolpert 1996; Miall et al. 1993). Make way for the ELL - it is high time for electrical engineers to return to their origins!

> *"He, who predicted and shewed that electricity wings the formidable bolt of the atmosphere, will hear with attention, that in the deep it speeds an humbler bolt, silent and invisible: He, who analyzed the electrified Phial, will hear with pleasure that its laws prevail in animate Phials: He, who by Reason became an electrician, will hear with reverence of an instinctive electrician, gifted in his birth with a wonderful apparatus, and with the skill to use it."*
>
> John Walsh, 1773, in a letter to Ben Franklin

---

[7]From an electrical engineer's point of view, an electric fish consists of the following components:

[1] Source transmitter. These fish are very stable waveform generators, and the EOD acts as a carrier with zero information content (except to other electric fish).

[2] Information channel. During electrolocation, the carrier field is distorted by the medium around the fish. During electrocommunication, the EODs of other fish interfere with and modulate the carrier.

[3] Receiving array. The electroreceptors are field transducers and encoders, and are distributed in an array across the fish's skin.

[4] Information processing. The fish's central nervous system must extract signals contained in the field distortions and perform pattern recognition.

[5] Sensory acquisition control strategies. Through its movements the animal controls the orientation of both transmitter and detector array relative to external objects and to each other.

"It is evident from all the experiments, as well as from simple considerations, that all the water and all the conducting matter around the fish through which a discharge circuit can in any way be completed, is filled at the moment with circulating electric power; and this state might easily be represented generally in a diagram by drawing the lines of inductive action upon it...."

Michael Faraday, 1839

2 Phase and amplitude maps of the electric organ discharge of the weakly electric fish, *Apteronotus leptorhynchus*[1]

2.0 Summary

The electric organ discharge (EOD) potential was mapped on the skin and midplane of several *Apteronotus leptorhynchus*. The frequency components of the EOD on the surface of the fish have extremely stable amplitude and phase. However the waveform varies considerably with different positions on the body surface. Peaks and zero crossings of the potential propagate along the fish's body, and there is no point where the potential is always zero. The EOD differs significantly from a sinusoid over at least one third of the body and tail. A qualitative comparison between fish showed that each individual had a unique spatiotemporal pattern of the EOD potential on its body.

The potential waveforms have been assembled into high temporal and spatial resolution maps which show the dynamics of the EOD. Animation sequences and Macintosh software are available from our web site (www.bbb.caltech.edu/ElectricFish).

We interpret the EOD maps in terms of ramifications on electric organ control and electroreception. The electrocytes comprising the electric organ do not all fire in unison, indicating that the command pathway is not synchronized overall. The maps suggest that electroreceptors in different regions fulfill different computational roles in electroreception.

---

[1]Published as: Rasnow B, Assad C, Bower J (1993) Phase and Amplitude Maps of the Electric Organ Discharge of the Weakly Electric Fish, *Apteronotus leptorhynchus*. *J Comp Physiol* **172**:481-491

Receptor mechanisms may exist to make use of the phase information or harmonic content of the EOD, so that both spatial and temporal patterns could contribute information useful for electrolocation and communication.

2.1 Introduction

Two orders of freshwater fish possess a specialized electrosensory system that allows them to detect nearby objects in their environment (Carr 1990; Bullock and Heiligenberg 1986; Lissmann 1963). These animals, referred to as weakly electric fish, generate high frequency electric fields (< 100 mV/cm, 0.1-10 kHz) which they sense with a few thousand electroreceptor organs distributed across their body surface. Some species emit short pulses with broad spectra, and other species generate a continuous wave-like discharge. The fish's electric organ (EO) which generates the field consists of hundreds or thousands of specialized current-generating cells stacked in series and parallel. The firing of these electrocytes is synchronized so that their currents add to produce a macroscopic electric field, referred to as the electric organ discharge (EOD). The electroreceptors are sensitive to local transepidermal potential and current. Electrolocation, the sensing of the environment via this electric field, is possible because objects such as other fish, food, and plants differ in their conductivity and dielectric properties from the surrounding water, and therefore can be detected as perturbations in the sensed field.

In this paper we describe the three-dimensional structure of the EOD potential generated by the South American gymnotiform fish *Apteronotus leptorhynchus* (brown ghost). The results reveal that the EOD creates a complex temporal and spatial potential surrounding the fish. The particular structure of this potential suggests several hypotheses concerning the neural control and regulation of the electric organ (EO), and provides information concerning the neural processing and behavioral relevance of the EOD. Whereas previous studies (e.g., Hoshimiya et al. 1980; Heiligenberg 1973; Knudsen 1975) have measured elements of the EOD in the midplane of electric fish (such as the

RMS amplitude), we have focused on the complicated waveforms on the fish's skin, and have combined these waveforms into maps that show the EOD dynamics.

2.2 Materials and Methods

2.2.1 Subjects

These experiments were conducted on six *A. leptorhynchus* 18 to 30 cm long. We identified two of these as males, based on the shape of their heads (Hagedorn 1986). Before recording, each fish was paralyzed with 30 to 50 μg Flaxedil (gallamine triethiodide) given intramuscularly. Since the electric organ of Apteronotids is neurogenic, this paralysis has no effect on the EOD (Bennett 1971a). Once paralyzed, the fish could be oriented for mapping in any desired body configuration.

2.2.2 Recording arrangements

Each fish was placed in the center of a 60x60x18 cm tank upon three 'Y' shaped supports made from 3 millimeter diameter Plexiglass posts and #24 insulated wire that held the fish firmly above the post. A glass tube connected to a water recirculation system was placed in the fish's mouth to respire the fish while paralyzed. All structures near the fish were kept small to minimize field distortions. Though the tank was not large enough to eliminate edge effects, we observed little effect on potentials when moving the fish closer and farther from the walls. Water was maintained at 23° C, pH 6.8, and resistivity of 2 kΩ-cm.

2.2.3 Electrode construction

The electrodes used in these experiments were kept relatively small to minimize their perturbations of the fish's electric field. Two different construction techniques were used depending on whether recording was on or away from the fish's skin. For recordings directly on the skin surface, we constructed flexible electrodes from insulated 25 μm diameter silver wire, the tip of which we melted into a 150-250 μm diameter ball. These

wires were held in glass pipettes for rigidity, with the electrode tip extended approximately 2 cm from the pipette after a 90 degree bend.

For recordings away from the fish's skin, we constructed rigid electrodes by pulling 1 mm O.D. glass pipettes to slender and slowly tapering tips. Each electrode tip was broken at 25 μm I.D. A silver wire was pushed through the pipette and its end was melted to a 150-250 μm sphere that was then pulled flush with the glass. These pipettes were glued together far from the electrode tips so the support structure would minimally alter the electric field at the recording sites (Fig. 1B). The electrodes had impedances of approximately 15 kΩ, dominated by spreading resistance of the water (Robinson 1968): $R_S = \rho/4\pi r_e$, where ρ = water resistivity = 2 kΩ-cm, and r_e = electrode radius ≈ 100 μm).

2.2.4 Electrode positioning

The electrodes were mounted on a stepper-motor controlled microdrive that moved vertically over an 8 cm range. This structure was attached to a shaft extending from an H-P 7035B X-Y plotter, giving 16 inches x 13 inches of travel in the X-Y plane. The electrodes could thus be moved in three dimensions electronically (Fig. 1A) and gently brought in contact with the fish's skin. The exact recording location of the electrodes for each sampling position was determined optically using a video camera (Sony TR-5) and a video overlay board (Computer Friends TV Producer). First, a real-time view of the fish and electrode array were put in the background of a window on a Macintosh II computer. The fish's body was then visually traced, and sequential electrode positions were marked on the computer screen. Resolution was one pixel, which corresponded to less than 500 μm.

2.2.5 Electrical instrumentation

Each electrode was connected to a high impedance (100 MΩ) follower amplifier mounted nearby on the stepper motor platform. The follower outputs were differentially amplified with respect to a fixed electrode located on the tank wall at the zero-potential plane of the fish (as in Knudsen 1975). The system bandwidth was extremely wide, 10 Hz

to 50 kHz (-3 dB), to maintain constant gain and phase responses to the EOD fundamental and all harmonics with measurable amplitude.

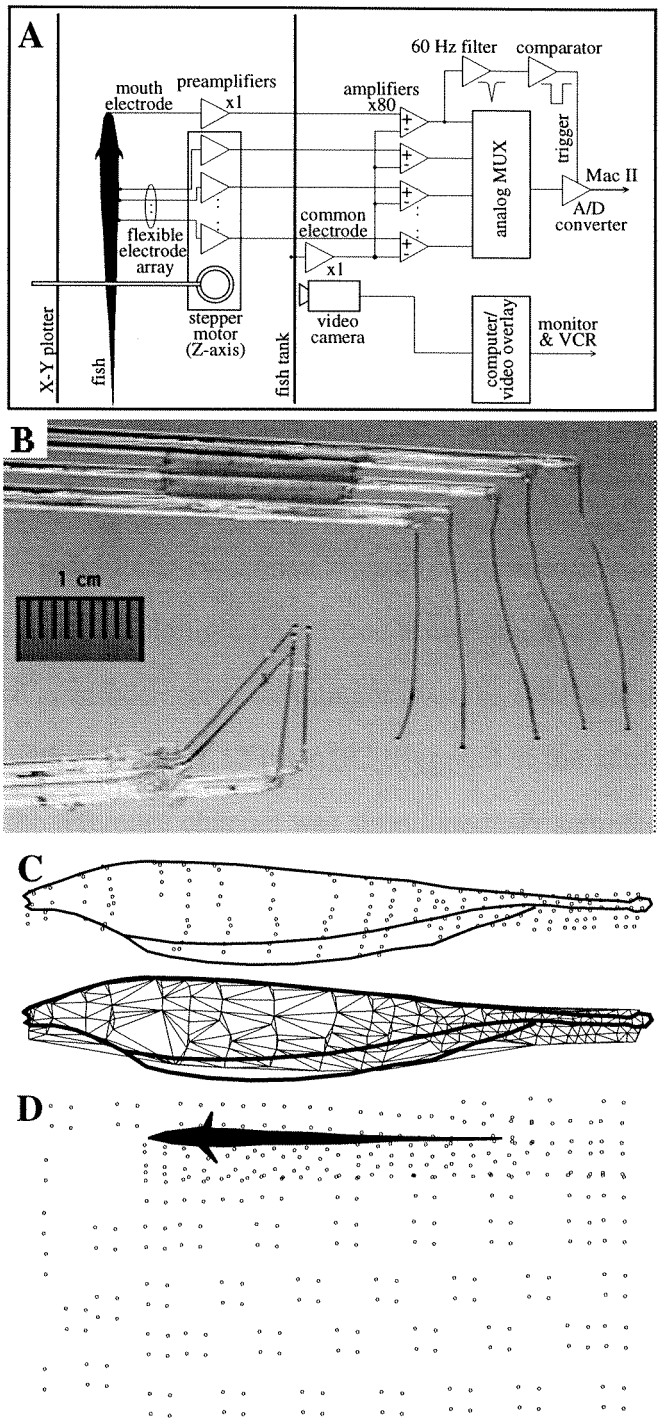

Figure 2.1 A. Diagram of the apparatus used to map electric potentials. B. Flexible (top) and rigid (bottom) electrode arrays used for mapping the EOD. Holes within the glue and gaps between the glass tubes reduce the field distortions from the support structures. C. Side view projection of a fish's surface with typical sampling positions from a five electrode flexible array. Interpolation elements corresponding to the sample points for creating the grayscale potential maps. D. Sample positions for a midplane map using a 4 electrode square array.

Since an experimental objective was to measure the EOD waveform rather than a time average, such as peak-to-peak or RMS amplitude, it was necessary to generate a phase reference signal to align waveforms recorded at different times and locations. This was accomplished using a second fixed electrode located in the respiration tube in the fish's mouth. The potential from this electrode was amplified and heavily filtered to generate a periodic digital pulse at the same phase of each EOD cycle (measured jitter was approximately 6 μsec). This pulse triggered the analog-to-digital conversions of the EOD waveforms. Three to five successive periods were recorded on each channel at 50,000 samples/sec with 16 bit resolution. Noise was approximately 5 μV RMS over a 15 kHz bandwidth, on the order of the Johnson noise of the electrodes (Horowitz and Hill 1989).

2.2.6 Stability measurements

The mapping procedure depends upon EOD constancy at each position from one cycle to the next. This criterion was tested by holding an electrode array stationary and sampling 5 to 15 EOD periods from each electrode every few minutes over the time course of an hour. Each record was sampled with a 125 kHz 12 bit ADC triggered at the same phase of the EOD. In all experiments, the reference channel was simultaneously sampled with every measurement to ensure stability. Average EOD frequency (over a 400 msec gating period) was also constantly monitored with a Fluke 87 multimeter (±0.2 Hz accuracy) and a loudspeaker.

2.2.7 Calibration

Gains were measured and normalized for all channels by placing the electrode array in a metal can connected to a function generator. The potential was constant within the can. We performed many other system calibrations, including mapping dipole fields from a function generator connected to a pair of stainless steel ball bearings, with dipole moment similar to *Apteronotus*. The geometry permits an exact analytical solution (in the form of a rapidly converging series based on the method of images). The analytic and measured potentials nowhere differed by more than 5%. The majority of the difference was

systematic, attributable to an uncertainty in the relative position of the electrodes and the dipole of < 500 μm. The random error was an order of magnitude smaller.

2.2.8 Sampling procedure

The spatiotemporal EOD pattern was measured by moving the electrode array to a series of recording positions and sampling the waveforms from each electrode. For mapping the potential on the fish's body, the array was moved towards the fish until all electrodes were touching the skin. The position of each electrode was then recorded using the video overlay system while the waveforms were recorded. Measurements were taken at variable spatial densities (as in Fig. 1C) because the EOD waveform changes substantially over millimeter distances near the tail and is similar over centimeter distances on parts of the trunk.

The video camera was located above the fish tank for the potential measurements in horizontal planes. The sampling density varied inversely with distance from the fish (Fig. 1D). A typical map of potential on the fish's side, consisting of approximately 40 positions of a flexible 5 electrode array, or 90 points in a plane with a rigid array, required 30 minutes.

2.2.9 Data analysis

The raw data from these experiments consisted of digitized time series containing several periods of the EOD waveform at many positions, and with each time series beginning at the same phase of the EOD recorded in the mouth. These records were trimmed to an integral number of periods of the EOD fundamental and FFT-bandpass filtered with cutoff frequencies of 180 Hz and 5 to 20 kHz (depending on the spectra of the signal). The digital filtering further reduced noise without phase distortions inherent in analog filters.

Though single electrode recordings reveal the temporal structure of the EOD, the overall spatiotemporal structure is more difficult to discern. To visualize the potential on the fish's surface and midplane as it changes in time, we have represented the potential in

grayscale at several consecutive phases of the EOD. For consistency, all waveforms and sequences in this paper begin in phase with the negative-to-positive zero crossing of the EOD recorded in the fish's mouth.

Because the EOD measurements were not at regular spatial intervals, smooth maps were constructed by interpolation. We used a Delaunay triangulation which groups triplets of adjacent points to form a set of triangles that completely cover the measured domain (Fig. 1C; Rasnow et al. 1989; Watson 1981). Within each triangle, the potential is interpolated to lie on the plane defined by the potentials at the vertices. In this manner, the five-dimensional data is visualized by rendering surfaces (typically the fish's skin or the midplane) with potential represented in gray levels at each particular time or phase of the EOD. A nonlinear grayscale was used (intensity proportional to the hyperbolic tangent of potential) because of the large dynamic range of potential around the fish. We have also animated the image sequences presented here in pseudocolor, and made available the data and programs for a color Macintosh on the World Wide Web (www.bbb.caltech.edu/ElectricFish).

2.3 Results

2.3.1 EOD potential

In this study, six A. leptorhynchus were mapped a total of nine times. Their fundamental frequencies varied from 549 Hz to 813 Hz, with males having the highest frequencies. The peak-to-peak potential was 3-5 mV on the anterior body surface, measured relative to the lateral tank wall (near electrical infinity). The potential was slightly larger at the operculum and remained relatively uniform over much of the trunk, then rose to a peak-to-peak value of 30-50 mV near the tip of the tail. The trunk potential also decreased slightly with dorsal and ventral distance from the midline. In the water around the fish, the potential fell steeply with distance from the body. The higher order multipole moments seen in the caudal half of the fish decay most steeply with distance leaving a

dipolar far field oscillating at the fundamental frequency of the EOD (see Discussion). The dominant asymmetry from a dipole extends on the order of the size of each pole, of order 1 cm on the tail and 10 cm on the trunk.

2.3.2 Temporal stability of the EOD waveform

Figure 2 shows the stability of the EOD waveform at two different locations on a fish's skin. The coefficient of variation (CV = standard deviation/mean) of the peak amplitude was 0.01 in each case, while the CV of the frequency was 0.001 over the 50 minute sample period. Over shorter time scales (16 msec, or 11 periods), the amplitude CV was 0.003. Generally, amplitude CV was least at the peaks and increased in proportion to the slope. As discussed below, this is probably a consequence of small frequency shifts in the EOD.

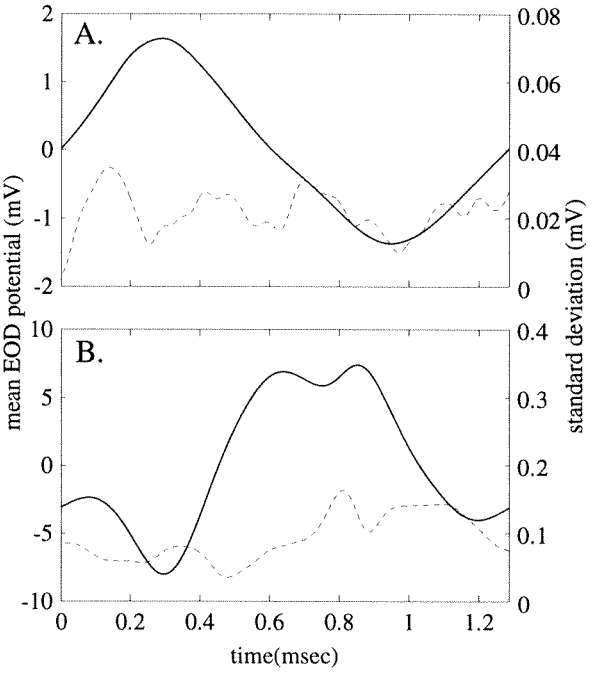

Figure 2.2 Mean and standard deviation (dashed) of 19 EOD periods sampled at approximately 2 minute intervals for 50 minutes. The scale for the standard deviation is 1/50th the scale of the mean. A. The EOD at the reference electrode in the fish's mouth, and B., at an electrode on the skin of the caudal trunk. Coefficient of variation at the peaks is approximately 0.01 in both cases.

The EOD stability was similar at all positions, except near the operculum at the end of the experiments. As the fish eventually recovered from the curare and began to respire, the EOD potential amplitude at the operculum was modulated by as much as 8 percent,

correlated with the opercular opening, at the respiration rate of a few Hz (Montgomery 1984).

2.3.3 Spatial variation of the EOD waveforms

In contrast to the temporal stability of the EOD at any specific location, the potential waveform varied considerably with position, both on and near the fish. Each fish appeared to have a unique potential pattern, and we were able to recognize individuals based on their EOD maps, although our sample size was too small for rigorous statistical analysis. Here we present in detail the EOD of a 19 cm female. Fig. 3A shows the RMS amplitude of the EOD and its first five spectral harmonics along the fish's midline. Over much of the trunk, the second harmonic (twice the fundamental) was roughly one eighth the amplitude of the fundamental. However near the middle of the fish the second harmonic increased and surpassed by nearly a factor of two the amplitude of the fundamental, before falling to half the fundamental amplitude along the tail.

The higher harmonics also contribute significantly to the relative timing of peaks and zeros along the body. The phase of the fundamental alone is compared to the timing of the zero crossing of the EOD in Fig. 3B. In this fish, harmonics shifted the timing of the positive slope zero crossing with respect to the fundamental, so that this zero crossing remained nearly synchronous over 80% of the body. The negative slope zero crossing of the EOD (corresponding to the beginning of inward current flow) is much less synchronous, but varies more smoothly along the body. Behind the midpoint, the "triphasic" region had two zero crossings of each slope per period, up to the last 15% of the body, where the positive slope zero crossing is delayed by approximately 220 degrees relative to the mouth. In other fish examined, the zero crossings were not as well synchronized along the trunk, and could be more appropriately described as sweeping along the entire body (see below).

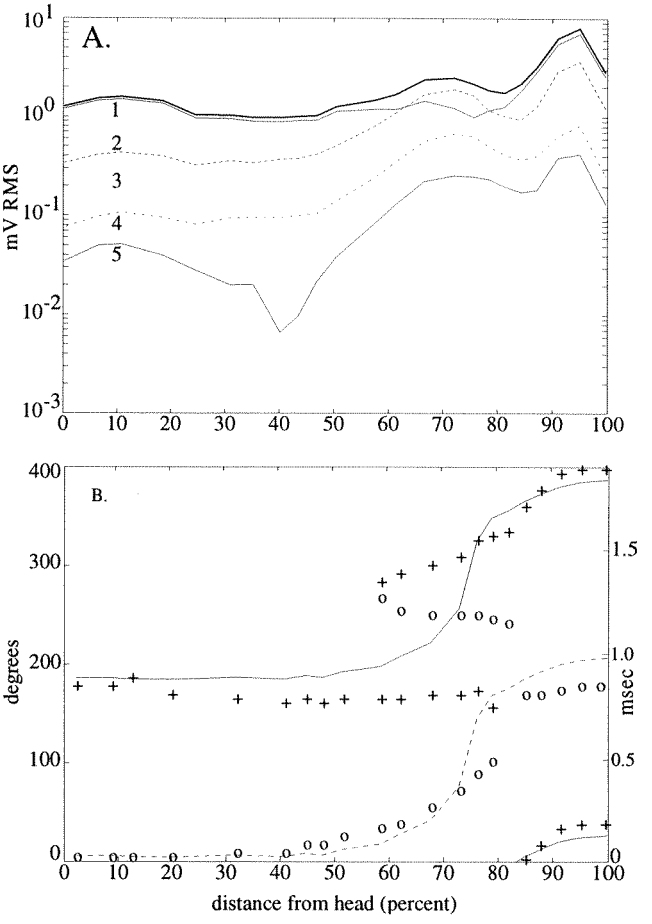

Figure 2.3 A. RMS potential of the EOD along the midline of a 19 cm female *A. leptorhynchus*. Bold curve is the RMS amplitude of the full-spectrum EOD and the traces labeled 1-5 are amplitudes of the fundamental and successive harmonics extracted from the EOD by Fourier analysis. Note there is no point at which the potential is always zero. B. Phase and latencies of the zero crossings of the EOD fundamental and the full spectrum EOD, relative to the negative slope zero crossing in the mouth. The negative and positive slope zero crossings of the fundamental are shown with dashed and solid lines respectively, and those of the full spectrum EOD are shown with 'o' and '+' respectively. Horizontal dotted lines are at 180 and 360 degrees. The EOD is multiphasic between approximately 55%-85% from the head, where both zero crossings are plotted.

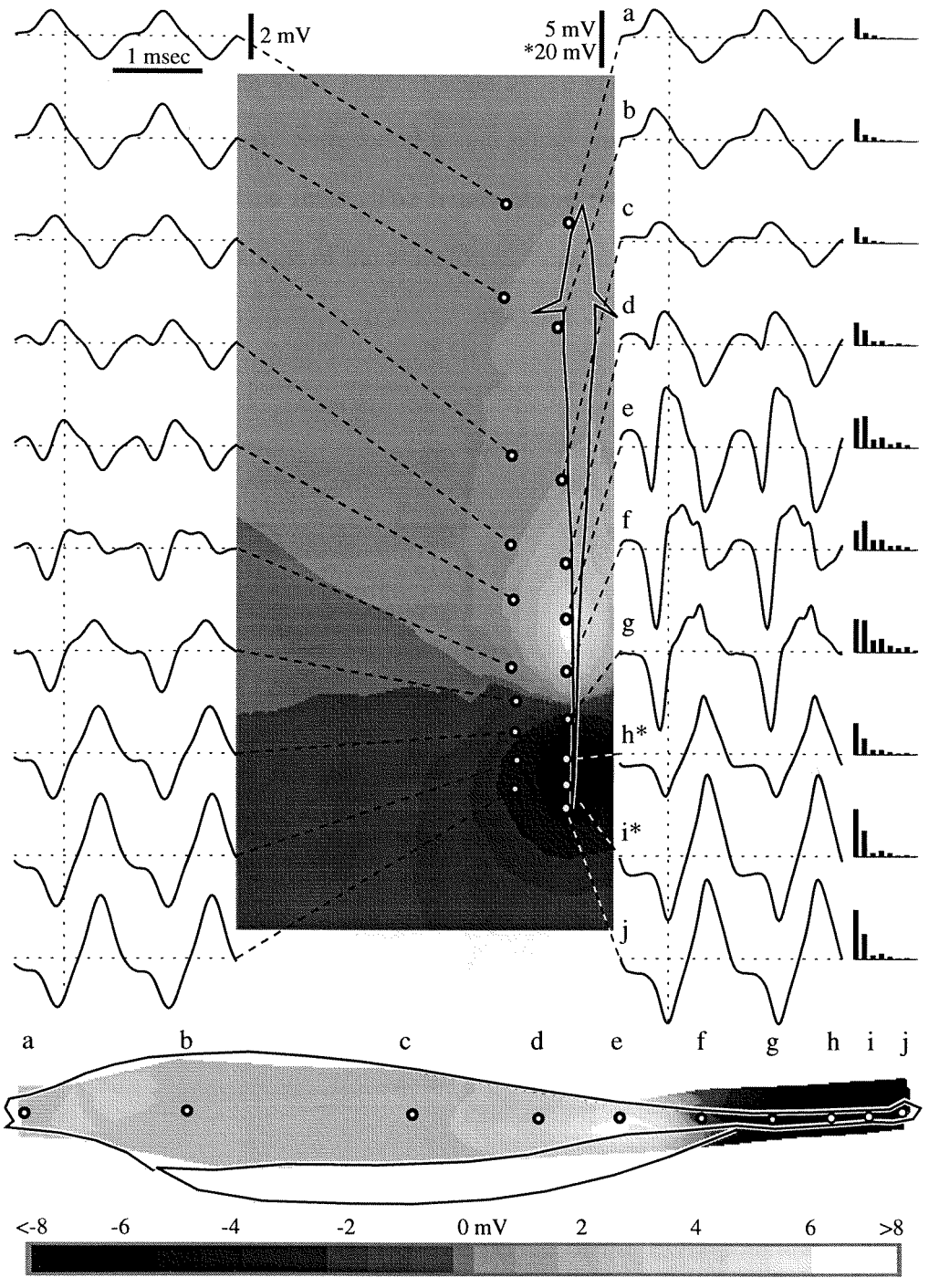

Figure 2.4 An illustration of how the EOD waveforms measured at different locations were used to construct the grayscale images. The waveforms shown (two EOD periods) were measured at points indicated by the black circles. The beginning of each waveform is in phase with the positive slope zero crossing of the EOD recorded in the fish's mouth. On

the right side are amplitude spectra of the fundamental and the next seven harmonics, with the same vertical scale as the corresponding waveforms. The grayscale frames correspond to the phase marked on the waveforms by the vertical dotted lines. The letters above the skin view indicate the corresponding locations of the waveforms measured on the fish's midline.

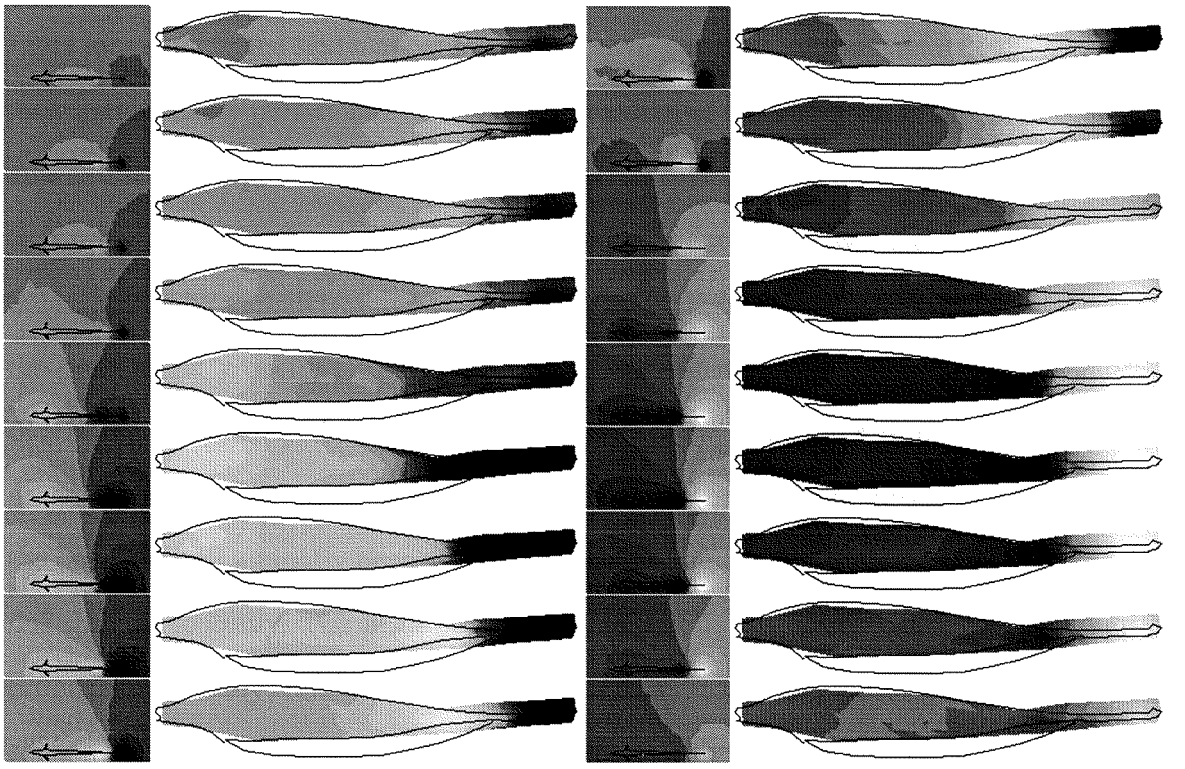

Figure 2.5 Grayscale images of one period of the EOD potential in the midplane and on the skin of the same fish as Fig. 4. Successive frames are 90 μsec apart with the first frame corresponding to the positive slope zero-crossing of the EOD in the mouth. Grayscale is the same as in Fig. 4.

The relative motion of the peaks and zero crossings is evident in the time domain. Fig. 4 shows a set of phase-locked waveforms along the midline of the same fish as in Fig. 3. The EOD differs significantly from a sinusoid over at least one third of the body and tail, and there is no point where the potential is always zero. Although single electrode recordings illustrate these complex waveforms, the overall spatiotemporal structure of the EOD potential across a fish's entire body is more readily apparent in the grayscale representation.

The grayscale maps reveal that the potential peaks (positive and negative) of the EOD move along the body, spontaneously growing and shrinking, and exactly repeating their pattern every period. For example, the potential of the same fish is shown in Fig. 5 at approximately 90 μsec intervals, covering one full period of 1.6 msec. Beginning with the first frame, the EOD is weak over most of the body, except for two negative peaks on the tail separated by a small positive region. The head is slightly negative and the caudal end of the body slightly positive. In the next frame, the tail potential becomes more negative, overriding the small positive peak. The potential at the caudal end of the trunk and head gradually increases over the subsequent two frames. From the fifth through seventh frame, the head and trunk rapidly become positive while simultaneously the negative peak at the tail spreads rostrally. The head potential subsequently decreases and a positive region propagates caudally, finally wiping out the negative peak at the tail in frame 13. Over the second half of the EOD cycle the head and most of the trunk are negative. The positive region of the tail shrinks monotonically until the beginning of the next EOD period.

In several fish the peaks and zeros of the EOD appeared to propagate from head to tail. For example, column A of Fig. 6 shows a pronounced propagation of EOD peaks, especially along the tail. Phase velocities in the tail region were calculated between 5 and 10 cm/msec. The peaks at the head and tail are also approximately 90° out of phase with each other, with an additional 90° phase shift occurring over several centimeters behind the tail.

The EOD's of the other two fish (Fig. 6 C and D) show a less pronounced propagation, with some peaks appearing to grow and decay without substantial movement.

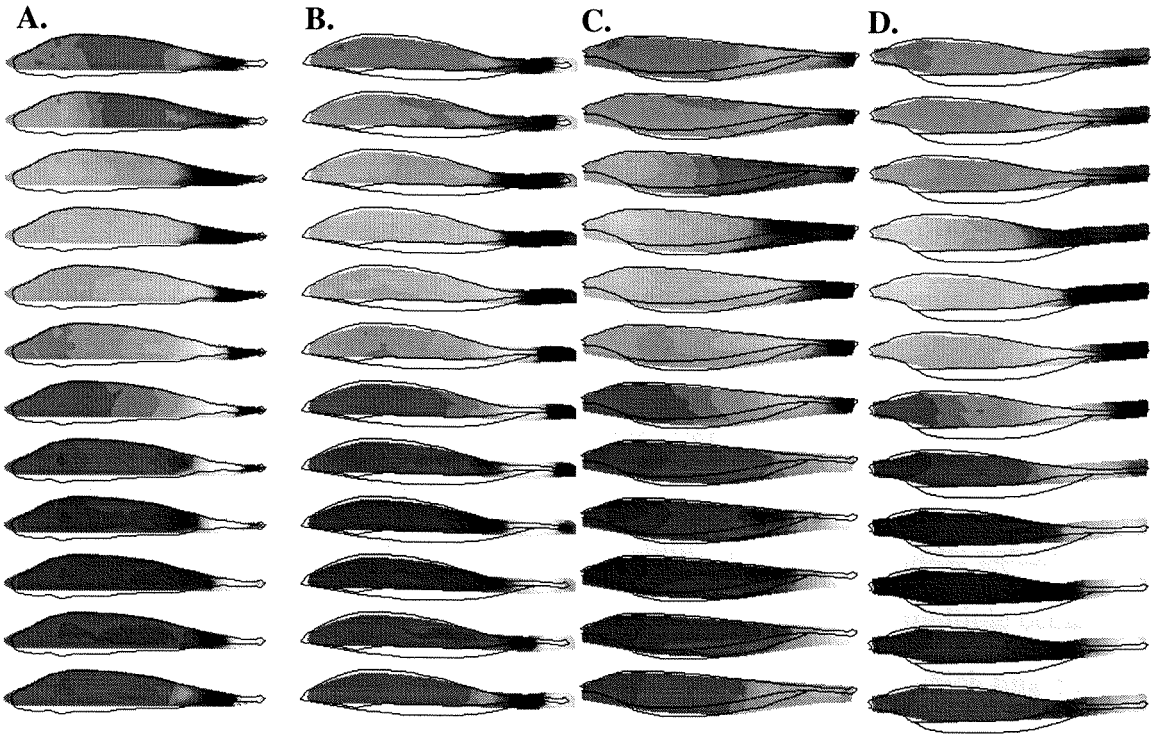

Figure 2.6 Twelve equally spaced phases corresponding to one EOD period on the skin of three *A. leptorhynchus*. Body lengths are normalized to aid compariosn. A, B. A 21.2 cm male (A), and the same fish 9 months later (B), now 26 cm in length. C, D. Two other fish for comparison. Grayscale is the same as in Fig. 4.

2.4 Discussion

2.4.1 Stability

The detection of small field perturbations induced by objects presumably requires electric fish to maintain a stable EOD over short periods of time. Bullock (1970) proposed the electric organ of *Apteronotus* is the most stable biological oscillator known, after reporting a frequency coefficient of variation of 0.00012 over several seconds (similar to an electronic function generator). Our results show that over 50 minutes the variation in

frequency is of order 0.001, and furthermore the EOD amplitude and waveform are stable and conserved at all locations in space and over time scales up to at least an hour in curarized fish.

The measurements of EOD amplitude variance likely represent upper limits. We measured frequency drifts of up to 5 Hz per hour (which could be a consequence of small temperature changes; Enger and Szabo 1968) and occasional frequency steps. These could constitute a major component of the amplitude variance, since waveforms of different frequencies cannot be averaged by time-shifting alone. The variance in amplitude measurement due to frequency shifts is proportional to the slope of the waveform and the distance in samples (time) from the phase-locking trigger (positive slope zero-crossing). Both these trends are visible in Fig. 2.

In addition to amplitude and frequency stability, the spatiotemporal pattern of the EOD waveform also appeared stable for the fish that were mapped on multiple occasions. We measured one large male 8 months after its initial mapping, during which time the fish grew from 21.2 cm to 26 cm in length. The EOD pattern remained similar over this extended time scale when normalized for frequency and the change in body length (Fig. 6, columns A and B). This long term stability seems particularly surprising when one considers the changes in physical and electrical properties that must accompany aging and growth. For example, changes in axon diameter and length almost certainly affect the EOD. In this fish, body length increased 20% in the eight months between recordings, yet the high spatial and temporal frequency components of the EOD were conserved.

The variation between the EOD patterns for the same fish on different days (Fig. 6 A and B) was qualitatively less than between different fish. In fact, the shape of the EOD potential appeared to be unique to each individual (in the few cases that we have studied). If the EOD waveform were to serve as a "fingerprint" that conspecifics use to identify each other at short range, such stability would be advantageous, as would the ability to modulate the EOD pattern as an individual's role in its community changes. The EOD frequency and

waveform is modulated over long time scales by steroids (Bass and Volman 1987; Zakon 1987). Of course, for individual recognition to occur, the fish must have means of interpreting the complicated interference patterns resulting from interacting fields (see below).

2.4.2 Command pathway and electric organ

The potential maps may also provide clues about the composition and timing of the electric organ activity and its command pathway, which has been the subject of numerous studies (e.g., Bennett 1971a; Dye and Meyer 1986). EOD stability has been mainly attributed to the medullary pacemaker nucleus in the brainstem which controls the activity of the electric organ. The pacemaker in *Apteronotus* is much larger and contains many more neurons than other gymnotiforms (Ellis and Szabo 1980). Because these cells are tightly coupled electrotonically, the temporal jitter in the command signals could be reduced in proportion to the square root of the number of cells (by the law of large numbers). However, the extreme stability of the EOD waveform, with stable harmonics exceeding 5 kHz, implies all components of the electromotor system must be functioning at high fidelity. Even with a stable signal from the pacemaker nucleus, this signal must still propagate through several other components.

The EO in *Apteronotus* extends along the entire trunk to the tip of the tail, lying ventral to the spinal cord (Bennett 1971). Axons from the relay cells in the pacemaker project down the spinal cord to innervate electromotor neurons. At regular intervals along the spinal cord, the electromotor neuron axons descend in nerve branches into the EO, where the specialized axon terminals function as electrocytes (Waxman et al. 1972). Neurotransmission is electrotonic at every stage of this command pathway.

Our data suggest that a distinction must be drawn between local synchronized discharge to generate large stable fields, and overall synchronization of the entire electric organ, particularly in wave fish like *Apteronotus*, with long electric organs. Bennett, in his 1971 review, showed that synchronization plays an important role in generating large stable

output because the currents of individual electrocytes are channeled and summed to produce the overall EOD. He also proposed mechanisms for achieving simultaneous activation along the electric organ, using conduction delays to equalize effective command path lengths. But synchrony of electrocyte discharge has been hypothesized to be more crucial for pulse species, while regularity of discharge frequency is paramount for wave fish (Dye and Meyer 1986). Our phase-locked recordings from *A. leptorhynchus* show that, while local groups of electrocytes might be tightly synchronized, the discharge of the EO as a whole is not in unison.

Most of the potential maps of *A. leptorhynchus* displayed a rostro-caudal propagation of the EOD peaks and zeros. This was especially apparent in the tail, where the EO is nearer to the skin and not surrounded by high conductivity body tissue. These potential peaks could be caused by part of the locally generated current exiting the electric organ along its length instead of being channeled to its endpoints. While the peaks of the potential are not necessarily centered over the most active segments of the EO, the observed propagation does suggest sequential activation of electrocytes along the electric organ. Consistent with this interpretation, it has been demonstrated in the related species, *A. albifrons*, that axons from the pacemaker relay cells run the length of the spinal cord and contact electromotor neurons at all spinal levels (Ellis and Szabo 1980). The apparent propagation of EOD peaks could therefore result from uncompensated propagation delays down the spinal cord of the pacemaker command signal. The particularly long electric organs of these fish, coupled with their high firing frequencies, may make it more difficult or even impractical to achieve global synchronization.

For comparison, the pulse gymnotid *Gymnotus carapo* also has a long EO extending over most of its body length, and a complex discharge that indicates "leaky insulation" around the organ (Caputi et al. 1989). However in order to generate effective pulses, this species possesses a mechanism to compensate for different conduction path lengths. Pacemaker relay axons terminate in specific segments of the spinal cord (Ellis and

Szabo 1980), and fibers in the electromotor bulbospinal tract have a wide range of conduction velocities distributed according to path length, from 1 to 9.1 cm/msec (Lorenzo et al. 1990). Therefore command signals simultaneously traveling to widely separated EO segments can remain synchronized upon reaching their respective destinations. If command signal conduction velocities in *A. leptorhynchus* are of the same order of magnitude, but there is no compensatory mechanism, then one might expect the EO segments to be activated sequentially. The phase velocities of potential peaks we measured along the tail of *A. leptorhynchus*, from 5 to 10 cm/msec, are consistent with these hypotheses.

The steep decay of the higher temporal frequency components with distance from the EO is another indication that electrocyte activation is farther out of phase over more distantly separated sections of the EO. On the skin near the thin part of the tail, stable frequency components of up to several kHz are observed, whereas far from the fish the fundamental frequency dominates the EOD. This can be explained as follows. The potential at any point outside the fish is due to the superposition of the discharges from the entire electric organ; however, at locations near the EO, for example on the tail, the potential is dominated by only the few nearest segments. Temporal shifts in waveforms of individual electrocytes or EO segments cause phase shifts proportional to the frequency, so a given time shift will cause greater interference of the higher harmonics compared to the fundamental. Thus, far from the fish where many segments contribute to the EOD, the high frequency components of the segments will destructively superpose if their phases differ, but the lower frequency components can still constructively add to produce a large amplitude. This mechanism could also explain why EOD propagation is much less apparent on the trunk. The high conductivity of the internal body tissue increases the effective electrical distance between the EO and the skin. This tends to average the EOD from distant EO segments within the trunk.

Finally, the fact that the far field of all electric fish is dipolar (Knudsen 1975) is the consequence of an analogous phenomenon. Just as the waveform at a particular point can

be described as a superposition of sine waves of different frequencies and phases (its Fourier series), the electric potential and field in the space surrounding a distribution of sources can be decomposed as a superposition of multipole moments (e.g., Jackson 1975). Each successive multipole moment contains higher spatial frequency information about the field, but decays more steeply with distance from the sources than the lower order multipole. Thus, far from the fish the lowest multipole moment, the dipole, will dominate the field.

2.4.3 Electroreceptors and electrolocation

It is still an open question how much of the phase and harmonic components of the EOD we have described here are transduced by the electroreceptors. Whereas certain EOD components may be just artifacts of controlling a large fast EO, others might have evolved to facilitate electrolocation and communication. Although electric sense inherently has relatively low spatial resolution (e.g., compared to vision), since there is no mechanism for focusing electric fields, time domain cues in electric fields are not corrupted by dispersion, as are most other sensory signals. This fact led Hopkins (1988) to propose that temporal characteristics of electric fish fields might be even more important for electrolocation than temporal characteristics are in the acoustic modality where, for example, they are the basis for object location in bats and owls. Thus we would expect electroreceptors to respond to the stable phase and harmonic components of the transepidermal EOD waveforms.

Weakly electric fish detect their EOD with an array of several thousand tuberous electroreceptor organs in their skin. In the well-studied case of *Eigenmannia* (EOD fundamental around 300 Hz), tuberous electroreceptors have been classified into two general groups: T units which respond phase-locked to the zero crossing of the EOD, and P units whose response is less dependent on phase and whose probability of firing encodes EOD amplitude (Heiligenberg 1988; Scheich et al. 1973). However, different species of fish appear to differ in the types and proportions of these electroreceptors. There has even

been a proposal that there may be a continuum of receptor responses between P and T units in *Eigenmannia* (Viancour 1979).

In the case of *A. albifrons,* which is more closely related to the fish studied here, most tuberous receptors on the body have been reported to correspond to P-type probability encoders rather than the T-type phase detectors (Hopkins 1976; Zakon 1987b). Scheich and Bullock (1974) pointed out an inverse correlation between the number of phase encoders and the fundamental EOD frequency in different species. They concluded that the higher frequency EOD discharge of *Apteronotus* (600-1000 Hz) limits the dynamic range of phase coders, therefore making T units less useful than in lower frequency fish like *Eigenmannia.* A number of studies suggest that P units convey some phase information into the CNS (e.g., Bastian 1981a, Fig. 4; Hopkins 1976; Scheich et al. 1973).

However, Franchina et al. (1990) have recently found evidence that the dorsal filament of Apteronotids contains a population of tuberous receptors resembling phase encoders. The dorsal filament is a thin structure lying in a groove along the center of the back, originating near the middle of the body and extending posteriorly over the EOD triphasic region (see Fig. 42 in Bennett 1971a). It appears to be contiguous with the body only at the anterior end, where upwards of 200 afferent axons join the lateral line nerves bilaterally (in *A. albifrons*; C. Franchina, personal communication). Much of the filament is situated in the large caudal field, which led Franchina et al. to conclude it could serve as a phase reference for the endogenous EOD. This would make it useful for phase comparisons such as needed in the jamming avoidance response. However, the large caudal field is also quite complicated, especially in the triphasic region where there are high frequency components and multiple zero crossings per period. If the dorsal filament is covered with phase encoders, then the response of the population as a whole will reflect the complex phase relationships seen in the maps, such as the propagation of zero crossings down the filament. It is also possible that these receptors are sensitive to phase deviations

caused by strong external sources. In particular, it would be interesting to determine if the dorsal filament is involved in the identification of nearby conspecifics based on their EOD.

In addition to raising questions about the information encoded by the receptors, the details of these potential maps also highlight likely spatial differences in receptor properties. For example, the substantial rostro-caudal differences we have found in EOD amplitude suggest that electroreceptor thresholds and/or spontaneous activity levels should vary with location on the body surface. The large second harmonic in the caudal trunk could also provide significant stimulus to receptors in that region. Hopkins (1976) showed tuning curves for receptors in *A. albifrons* that have two sensitivity peaks, near the EOD fundamental and its second harmonic. More complicated spatial variations in receptor tuning have been found in *G. carapo* (Watson and Bastian 1979; Bastian 1977).

We emphasize that the potentials presented here are recorded with respect to electrical infinity, and are not the potentials across the active membranes of the electroreceptors. We have also measured the EOD potential with respect to an electrode inside a fish's gut. While this more closely approximates the transepidermal potential near the gut electrode, the fish interior was not equipotential. In a 30 cm male, the potential waveform in the gut of the trunk was nearly identical to the potential in the mouth except for amplitude differences; however, towards the tail the waveforms differed as well. The gut potential was 2.7 times larger than in the mouth at a point 3 cm caudal of the operculum, but was only 2.0 times larger 3 cm further caudal.

Another method of estimating the electroreceptor stimulus is from the potential gradient on the skin using differential electrode pairs. This requires consideration of the fish's curvature, and a model of how non-perpendicular current might be channeled to the sensory cells by the high resistance receptor pore walls (Scheich and Bullock 1974). Unfortunately, electroreceptor responses to complicated current perturbations are not well understood, even though electroreceptors have played an important role in the elucidation of different neural codes (Bullock 1986). We are currently modifying our apparatus to map

the electric field vector surrounding the fish, and our preliminary data suggest a strong likeness between the instantaneous potential pattern and the perpendicular electric field when both are measured directly on the fish's skin.

2.4.4 Behavioral significance

If receptor mechanisms do exist to make use of phase information or harmonic content, the spatial pattern of these differences could contribute to the acquisition of information about local objects and influence the fish's exploratory behavior. Electrolocation is based on the principle that the fish's electric field polarizes an object, inducing a perturbation proportional to the field strength at the object. For example, a small sphere (small compared to the spatial variation in the field) will create a dipolar perturbation. The fish subsequently detects this perturbation field superimposed with the unperturbed EOD on its skin. Near the tail, the potential changes significantly in amplitude and spectral composition over millimeter distances. Therefore the perturbation due to a nearby object is not a linear function of the normally detected EOD field. For this reason, an object near the tail will not simply multiply the field on nearby receptors by some constant amount, but will superimpose a field with waveform like that at the object. Having different regions of the electric organ active at different times, the fish could accumulate spatial information about objects from the relative timing of the field perturbations.

Regional variations in the potential and its spatial derivatives may allow electroreceptors in different regions of the body to fulfill different computational roles in electroreception. In particular, because the caudal electric field decreases with distance more steeply than at the head, we speculate that caudal receptors might preferentially encode object distance, and the rostral receptors that are in a weaker, more uniform field might convey higher resolution information about object structure. The electric "image" of a small object decreases with distance like the field. Thus as the body-to-object distance is modulated (e.g., by tail wagging, a common exploratory behavior), the change in the

perturbation field will be larger for an object near the tail versus near the trunk. Furthermore, the spatial nonuniformities of the caudal field could confound an object's spatial structure. In contrast, the more uniform trunk field, with its lower sensitivity to changes in object-body distance and location, would be more suited to extracting object structure. The spatial distribution of tuberous electroreceptors is compatible with this idea, with a higher density in rostral regions, especially around the head, compared to caudal regions (15/mm^2 vs. about 3/mm^2 in *A. albifrons*; (Carr et al. 1982).

We have sought to quantify the temporal and spatial structure of the EOD potential as an initial step in our efforts to understand electroreception from a computational point of view. The results of these experiments have suggested a number of new conjectures regarding the interaction of the fish, its fields, and objects in its environment. We are currently pursuing these ideas by mapping the electric field vector on and around the fish, as well as quantifying perturbations due to nearby objects. This work is intended to facilitate the quantification of electrosensory input as it enters the central nervous system, as well as to provide a more solid basis for interpreting the sensory consequences of the behavioral strategies used by electric fish to locate and identify objects in their environment.

Acknowledgements

We thank Mark Nelson and Caroly Shumway for their ideas and technical assistance, Mike Walsh for advice on electronics, and Dave Bilitch for advice on C programming. We are grateful to the electric fish research community in general, and especially to Lenny Maler, Walter Heiligenberg, and Joe Bastian for their encouragement and advice in getting started. This work was funded in part by NRSA Fellowship Grant #GMO7737, an ONR Graduate Fellowship, and NIH BRSG #RR007003.

Note added in proof

McGregor and Westby (1992) have reported the EOD of *G.carapo* is used for identification of individual conspecifics.

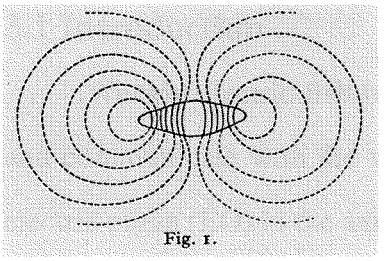

First EOD map, made by hand.

"...if the torpedo is immersed in water, the fluid will pass through the water in all directions, and that even to great distances from its body, as is represented in Fig. 1, where the full lines represent the section of its body, and the dotted lines the direction of the electric fluid; but it must be observed, that the nearer any part of the water is to the fishes body, the greater quantity of fluid will pass through it."

Henry Cavendish, 1776

3 Maps of the Electric Organ Discharges of Weakly Electric Gymnotiform Fish

3.0 Summary

In this chapter I present detailed measurements of the electric organ discharge (EOD) of six species of weakly electric fish, including three gymnotiform wave fish (*Eigenmannia virescens*, *Apteronotus leptorhynchus*, *Apteronotus albifrons*) and three gymnotiform pulse fish (*Gymnotus carapo*, *Brachyhypopomus pinnicaudatus*, *Brachyhypopomus* n. sp.). EODs from individuals of each species were mapped with high resolution in both space and time. These maps complement and extend previous mapping efforts, by clearly illuminating the EOD potential patterns both in the water about the fish and on the skin surface itself. Five of the six species displayed complicated EOD waveforms that varied with location near the fish; only in *Eigenmannia* does the near field approximate a dipole. The specific waveform patterns from each species appear to be correlated with known anatomical and physiological features of their electric organs. The spatial variation of EOD waveforms also implies that there are differences in electroreceptor responses in different body regions of each fish. Furthermore, the diversity of EODs suggests that there may be species specific differences in receptor properties and electrolocation strategies. EOD maps and animations resulting from this study are available via the Internet (anonymous ftp: ftp.bbb.caltech.edu, cd /pub/ElectricFish; Web pages: www.bbb.caltech.edu/ElectricFish).

3.1 Introduction

Weakly electric fish have evolved specialized electrosensory systems to explore and communicate with the world around them (Bullock and Heiligenberg 1986). An electric organ (EO) in the animal's body, controlled by a pacemaker nucleus in the brain stem, generates electric organ discharges (EODs) which produce currents flowing throughout the surrounding water. An array of detectors in the skin, called electroreceptors, measures the distributed transdermal current patterns. Electroreceptors are very sensitive to small changes in amplitude or phase, such as those caused by nearby objects or other electric fish. The fish must then interpret the resulting peripheral electrosensory images, which are highly dependent upon the particular EOD waveform characteristics. Therefore, to fully understand the functions of electrolocation and communication, we first need to clearly visualize and quantify the EODs.

Previous investigations have demonstrated that the EODs of weakly electric fish are highly stereotypical for each species (Bennett 1971a; Bass 1986). Interspecific variations are found in both EOD frequency and waveform. These features of the EOD are commonly used to unambiguously identify species in the wild (Hopkins 1986a; Westby 1988), using classifications primarily based upon head-to-tail potential difference measurements. Comparisons between individuals of the same species have also demonstrated that EOD frequency or waveform can vary to a lesser extent intraspecifically, depending upon gender and status in the social hierarchy (Hagedorn and Heiligenberg 1985; Hagedorn 1986; Hopkins 1986a). The fish themselves use the EOD pattern or frequency to identify conspecifics, and can even recognize individual neighbors based upon slight variations in the individual EOD pattern (demonstrated in *G. carapo*, McGregor and Westby 1992).

The fields recorded near the surface of many of these fish vary significantly from the head-to-tail or far field waveform, especially in species with long electric organs and high frequency components. Previous descriptions of the more complicated EOD

waveforms have addressed issues of spatial variations in shape, frequency, phase and stability; however, the complexity of the full EOD patterns, consisting of time-varying signals in three spatial dimensions, made them difficult to measure and represent in a straightforward manner (e.g., *G. carapo*: see Fig. 7 in Watson and Bastian 1979; *Hypopomus*: Fig. 23 in Bennett 1971a; *A. albifrons*: Fig. 4 in Hoshimiya et al. 1980). We have developed methods to clearly visualize the EOD pattern with high spatial and temporal resolution (see Chapter 2). Using these techniques, waveforms measured at many locations around the fish are combined and interpolated in space to create snapshots of the EOD potential at each point in time. The maps are relevant to both electrolocation, since the fish must interpret the field at the skin, and communication, since many species interact at close range (e.g., see the near-field interactions of *G. carapo* illustrated in Black-Cleworth 1970).

In Chapter 2 we began a systematic mapping of species with detailed EOD maps of *Apteronotus leptorhynchus*. In this chapter, I present the results of extending our mapping procedures to five additional species of gymnotiform weakly electric fish, all possessing relatively long tails with long electric organs running most of the body length (Figure 1). The results demonstrate that the EODs of gymnotiform fish can be quite complex, especially for the higher frequency species. The near field waveforms, recorded directly on the skin of the fish, help illuminate the underlying EO morphology and activation. Comparisons between species show that differences in the EOD maps may directly reflect differences in the respective fishes' electrocyte physiology and electric organ innervation. The data also allow quantification of electrosensory input, and can be used to explore particular electroreceptor transfer responses in each species.

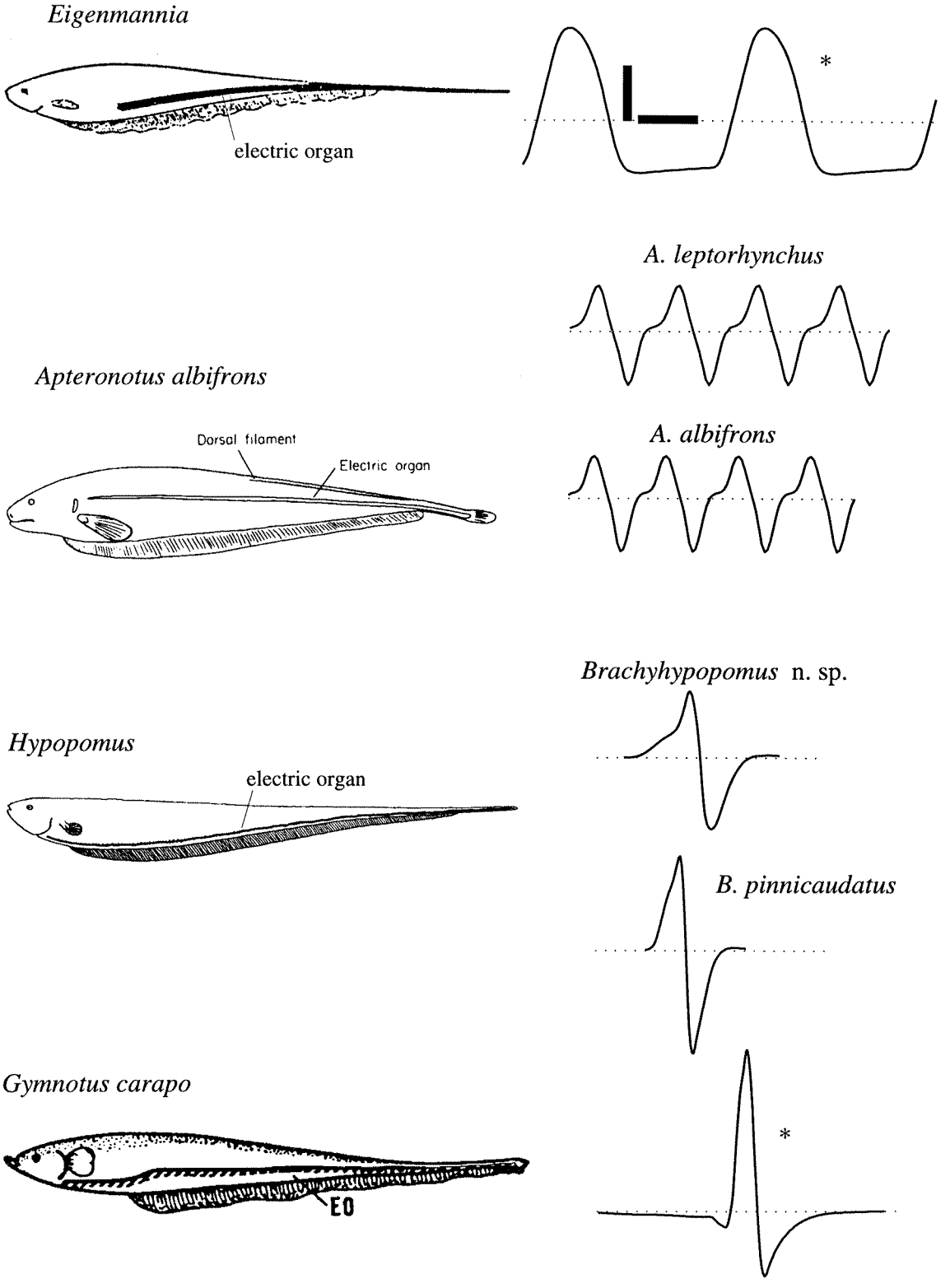

Figure 3.1 Left: body outlines with electric organs. Right: head-to-tail waveforms. Fish bodies adapted from: *Eig* - Heiligenberg 1975; *Apt, Hyp* - Bennett 1971; *Gym* - Trullio-Cenoz et al. 1984. Scale bars: 1 msec, 10 and *20 mV

3.2 Methods

3.2.1 Subjects

In these experiments several fish were mapped in each of six species of South American gymnotiforms, with sample sizes indicated in Table 1; however, full map data is only presented here for one individual from each species. Table 1 also contains the known overall characteristics of each species, as well as the characteristics of the particular fish mapped in each case. Specimens were obtained from local fish suppliers. The pulse species, which were obtained and identified by Dr. Philip K. Stoddard, included a novel species of *Brachyhypopomus* that is currently being formally described by John P. Sullivan at Duke University.

TABLE 1. Subject characteristics

Species	EOD	Comments and References	N	Subject
Eigenmannia virescens	wave type 250-500 Hz	aka "glass knife fish" widely used for physiology and behavior experiments; JAR: Heiligenberg 1989	2	19.5 cm female freq 320 Hz temp 26 C
Apteronotus leptorhynchus	wave type 600-850 Hz	aka "brown ghost knife fish" pacemaker: Dye & Meyer 1986; EOD: Rasnow et al. 1993	7	21 cm female freq 810 Hz temp 27 C
Apteronotus albifrons	wave type 800-1200 Hz	aka "black ghost knife fish" EO: Waxman et al. 1972, Ellis and Szabo 1980; behavior: Knudsen 1974; electrolocation: Bastian 1974	2	9.8 cm freq 911 Hz temp 24 C
Brachyhypopomus pinnicaudatus	pulse type biphasic	formerly *Hypopomus* long thin tail filament EO and EOD: Hopkins 1990	1	14.5 cm temp 28 C
Brachyhypopomus novel species	pulse type biphasic	formerly *Hypopomus* newly described species long, thin tail general EO: Bennett 1971	2	14.4 cm temp 28.5 C
Gymnotus carapo	pulse type triphasic	cylindrical body, complex EO EO: Caputi et al. 1989; EOD: Caputi et al. 1989, Watson and Bastian 1979	3	15.8 cm temp 28 C

3.2.2 Mapping procedures

EOD maps of electric potential were collected using the methods described in Chapter 2 (Rasnow, Assad and Bower 1993), summarized here with changes explained in detail:

Immobilization of test subjects

To carefully map the spatial and temporal properties of the EOD next to the fish, it was first necessary to immobilize the animal and suspend it in the recording tank. The fish were immobilized using one of two methods, depending on the species. Since the neurogenic electric organs of the family Apteronotidae rely on modified motor neuron axons acting as electrocytes (Waxman et al. 1972), drugs acting at the neuromuscular junction, like curare, can be used to paralyze these fish with little effect on the EOD. Therefore for the two *Apteronotus* species, 30 to 50 μg Flaxedil (gallamine triethiodide) was injected intramuscularly prior to recording, and supplemental doses of 10 to 20 μg were applied every few hours over the course of the experiment. However, in the other four species studied here the EOD is generated by a myogenic electric organ, composed of modified muscle cells which are activated by electromotor neurons. As a result, drugs blocking the neuromuscular juction also shut down the EOD. For this reason, immobilization in these four species was accomplished using the drug etomidate.

Etomidate (metomidate hydrochloride) is classified as a human anesthetic, and is also used by commercial fish handlers to sedate fish. The drug (1% Maranil, 0.3 ml/l) was administered continuously through a respiration tube with a gravity feed, following direct application in a small waiting tank. Because this drug is not specifically a paralytic, on occasion a fish did move while being mapped. The few times this did occur, we used video records to accurately reposition the fish in its original position, and took control measurements from previously mapped locations to ensure that the fish had been properly repositioned.

Once immobilized, each fish was then placed in the center of a 70x70x20 cm tank, suspended using thin 'Y' shaped supports, and respired with the aid of a water recirculation system connected to a glass tube in the fish's mouth (Fig. 2). All structures near the fish were kept small to minimize field distortions. The tank water was maintained at nearly constant temperature, resistivity and pH (with typical values 26° C, 5 kΩ-cm, and pH 6.8, respectively).

Measurements of EOD potential

The spatiotemporal EOD pattern was measured by moving an electrode array to a series of recording positions and sampling the waveforms from each electrode. Electrode arrays were built in rigid or flexible configurations for mapping away from the fish or directly on its surface, respectively (as in Chapter 2). The electric potential at each electrode was first buffered by a high impedance follower amplifier, and then differentially amplified with respect to a fixed electrode located on the tank wall near the "zero-potential plane" of the fish (as in Knudsen 1975, for monopolar recording). The analog bandwidth was extremely wide, 1 Hz to 50 kHz, to maintain constant gain and phase responses to all frequency components of the EOD with measurable amplitude. Waveforms were filtered and sampled simultaneously by six sigma-delta A/D converters, resulting in effective sample rates of 48,000 samples/sec/channel with 16 bit resolution.

Since an experimental objective was to measure the EOD waveform rather than a time average, such as peak-to-peak or RMS amplitude, it was necessary to generate a phase reference signal to align waveforms recorded at different times and locations. This was accomplished using either a second fixed electrode located near the fish's head, or two fixed electrodes mounted on the walls in front of the head and behind the tail, respectively. This reference potential was heavily filtered and used to generate a periodic digital pulse at the same phase of each EOD cycle or pulse, triggering the analog-to-digital conversions of the EOD waveforms.

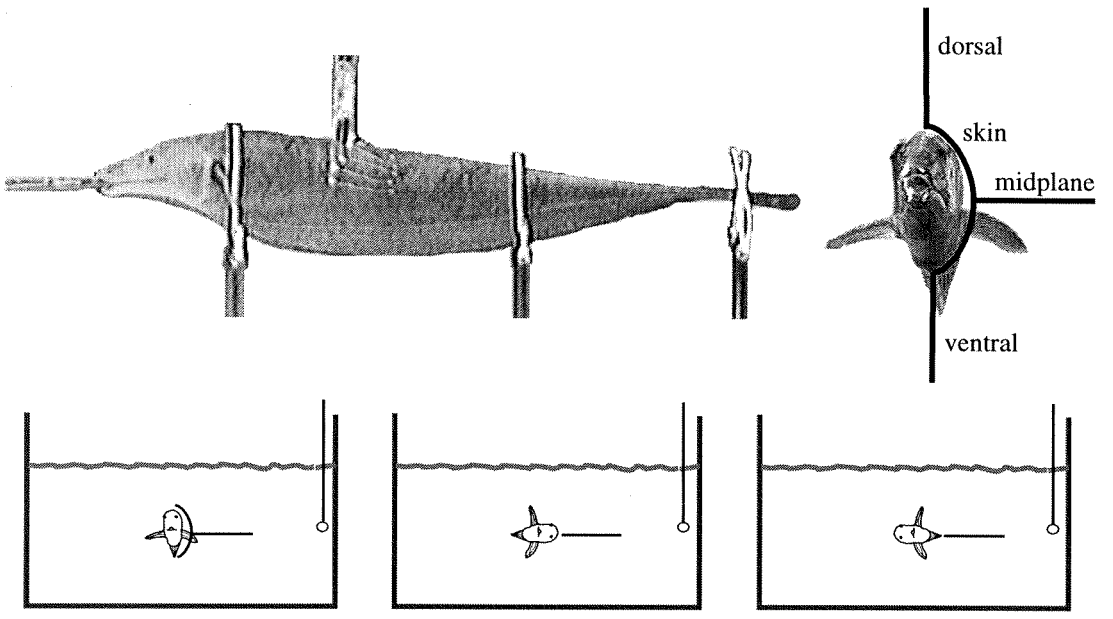

Figure 3.2 Mapping methods (see text)

Map orientation and data analysis

Planar maps were collected with rigid electrode arrays in the midplane, dorsal and ventral planes of each fish, as shown in Figure 2. Skin maps were taken with flexible electrode arrays placed directly on the body surface. Sideview mosaics were composed of three separate maps, the skin map combined with dorsal and ventral planar maps. The three maps were aligned in space using relative body coordinates taken from video records. Figures 5 to 10, c, show the spatial sampling densities for all maps presented. The *Apteronotus* maps presented here do not include full skin maps; however, the data shown in Chapter 2 included full skin maps from several specimens of *A. leptorhynchus*, and the skin map of *A. albifrons* is similar (unpublished data).

For the pulse fish, waveforms were digitally lowpass filtered with the cutoff frequency depending on the EOD spectrum, and temporally aligned by cross-correlation of the reference channel data. For the wave species, a frequency space comb filter was used to save the Fourier coefficients of the fundamental frequency and the next 9 higher

harmonics, allowing the waveforms to be reconstructed and aligned by the phase of the reference channel fundamental frequency.

To visualize the potential on the fish's surface and midplane as it changes in time, the data sets were interpolated in space to create smooth maps, and the potential was then represented in grayscale at regular intervals of time during the EOD waveform cycle (Figs. 5 to 10, d). Animated sequences of such images, when displayed with our custom Macintosh software, reveal the full spatial and temporal patterns of the EOD (full pseudocolor animations are available on our Web site: www.bbb.caltech.edu/ElectricFish, or by anonymous ftp: ftp.bbb.caltech.edu; cd /pub/ElectricFish).

Stability

These mapping procedures depend upon EOD stability at each position from one cycle or pulse to the next. Any variability in the EOD waveform over time may cause errors in temporal alignment or alter the spatial pattern, since different locations in space are recorded at different times. Stability was examined for all species by sampling from the fixed reference electrodes simultaneously with every measurement. The EOD was also constantly monitored with a loudspeaker to detect chirps and other short term modulations, and for the wave species a multimeter was used to detect slow shifts in frequency over the course of the experiment. To test the effects of the administered drugs, time series were also recorded from a fixed electrode at the end of several experiments as the fish were allowed to recover.

3.3 Results

3.3.1 Temporal stability of the EOD waveform

The mapping procedure required several hours for each fish, over which time we usually recorded small changes in the reference waveform. Figure 3 displays the mean and standard deviation of the reference channel from the separate maps of each fish. The standard deviation ranged from 1 to 2 percent of the peak amplitude, and was largest for

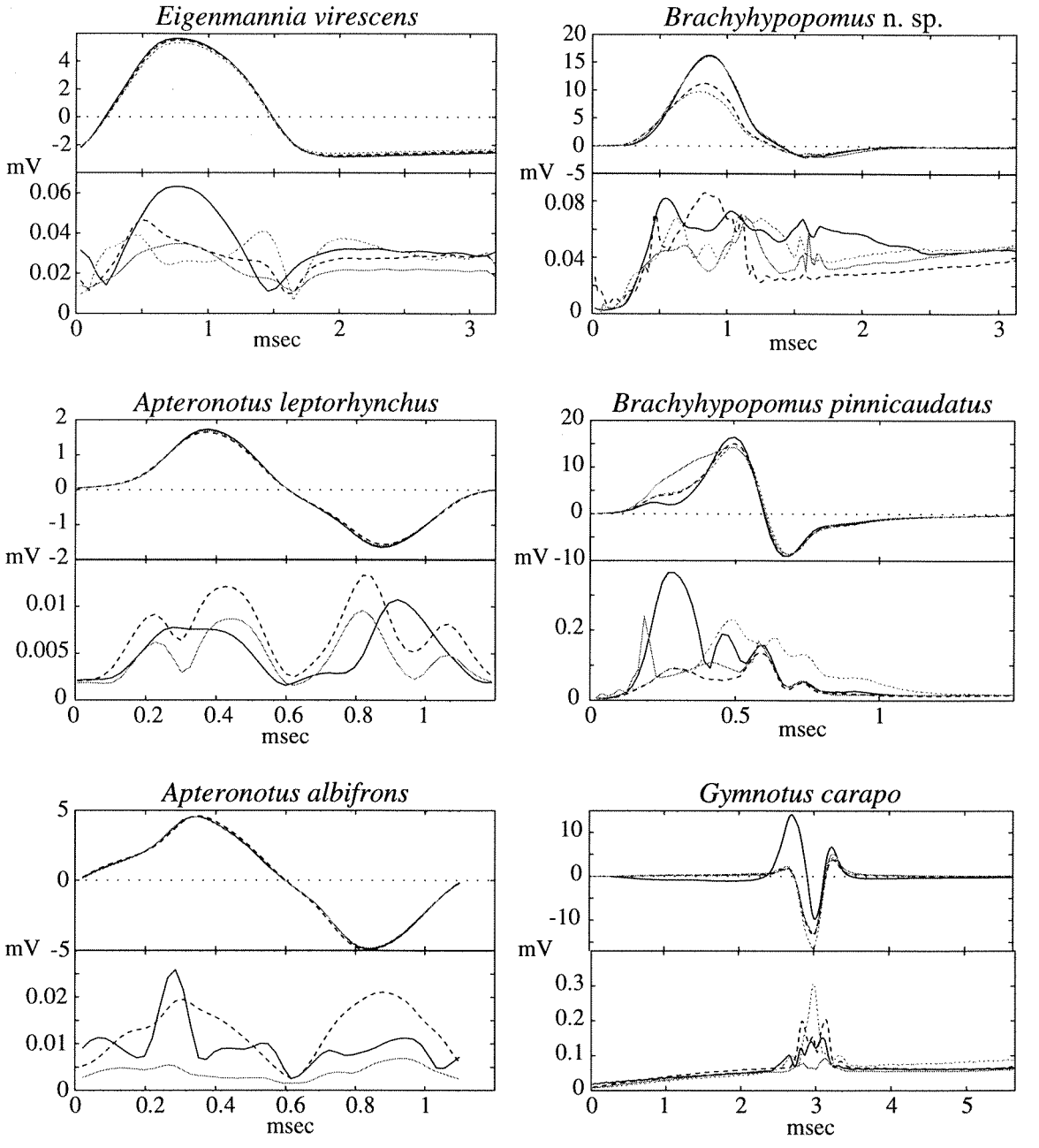

Figure 3.3 EOD reference stability. Left column: wave fish. Right column: pulse fish For each species, the top plot displays the mean reference waveforms for each map orientation, and the bottom shows the standard deviation for the same data. For the wave fish, the reference was measured between electrodes mounted on the walls in front and behind of the fish (*Eig*), or between the mouth and the side wall (*Apts)*; therefore, the waveform did not change much from the rotations between maps. In the pulse fish, the reference waveform changed appreciably between maps, because the reference electrode was fixed near the head, off the center line, and the pulse fish EODs were not radially symmetric; therefore, rotations of the fish placed the electrode in a different field.

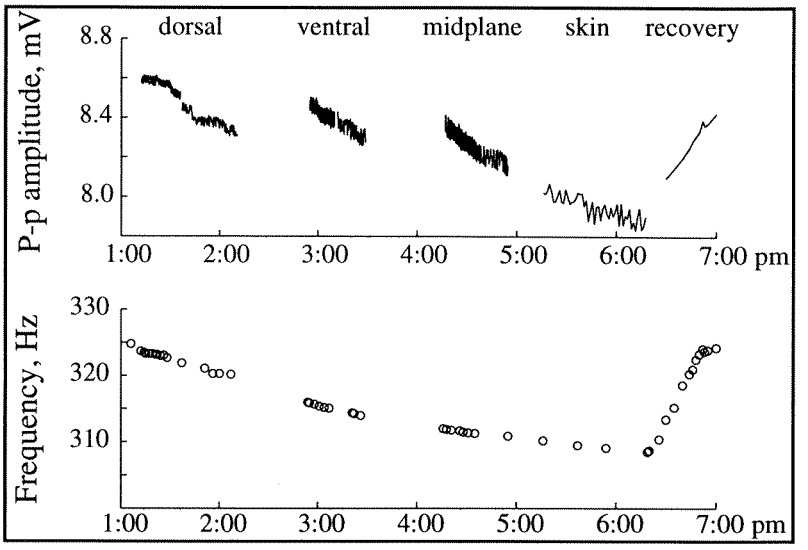

Figure 3.4

Eigenmannia reference stability vs. time

the skin maps. Reference frequency and peak-to-peak amplitude are also plotted vs time (Fig. 4), during all four maps over the course of the *Eigenmannia* experiment. Slow drifts in amplitude did occur, but the peak-to-peak amplitude changed by less than 10% in all species.

It is likely that some of the recorded variation was due to experimental inaccuracy, from small movement artifacts or difficulty in temporal alignment. For example, the zero level of the pulse fish waveforms was set by subtracting the mean of the first 10 or 20 samples, but low frequency power line noise then led to higher variability near the end of the pulse (Fig. 3, d-f). However, as in our study of *A. leptorhynchus* (Chapter 2), some of the recorded variations were due to slow monotonic drifts in frequency or in amplitude over the course of the experiment. The drifts may be attributed to small changes in temperature (Enger and Szabo 1968) or to effects of the drug administration and respiration (see below). Some weakly electric species are also known to have circadian fluctuations in the EOD, strongly influenced by the light cycle (e.g., in *Hypopomus*; Hagedorn 1986). In any event, these changes did not significantly affect the reference waveform shape; i.e., the relative harmonic ratios remained constant throughout each experiment. In particular, features of the EOD from each individual were seen in all four of its maps, which were taken sequentially. Furthermore, general EOD features were

conserved in those species in which multiple individual fish were mapped (unpublished data), indicating that the small variations in time did not affect the maps qualitatively.

As described in the methods section, we also examined the possible effects of the sedative etomidate. Administration of etomidate through the respiration tube sometimes lowered the EOD frequency and may have affected peak amplitude. In *Eigenmannia*, recovery from the etomidate administration took approximately 40 minutes (Fig. 4), during which time both the frequency and amplitude increased steadily, until the fish was too light to maintain in the holder. Not all of the variation was due to the drugs – both frequency and amplitude were also noticeably affected by the respiration flow rate, in all six species, although this was not quantified. Slow drifts also occurred in the case of the *Apteronotus* species, where curare was injected at long intervals, and so may be due to the respiration rate again. However, slow drifts and rare frequency steps are also seen in normal resting black and brown ghosts (unpublished data).

Even if the etomidate did have some effect, it did not substantially alter the EOD pattern when compared to previously reported EOD waveforms. The *Eigenmannia* waveforms are easily identifiable from the literature. The *Hypopomus* waveforms shown in Fig. 7 match the biphasic EOD description by Bennett (see Fig. 23 in Bennett 1971a), except for the initial low amplitude stationary dipole. Though the species were probably different, the discrepancy may also result from his measurements being taken farther from the head of the fish. Weak initial prepulses in the chin region were also seen in *H. pinnicaudatus* and *G. carapo* where they are known to occur naturally (see below). Our *G. carapo* waveforms also are very similar to the current waveforms reported by Caputi et al. (see figure 8 in Caputi et al. 1989).

3.3.2 EOD maps

The remainder of this Results section contains descriptions of the EOD of each species. Waveforms sampled from the midplane and skin are shown for each fish in Figures 5 to 10, a, with representative head-to-tail waveforms in Figures 5 to10, b.

Figures 5 to 10, d, show the EOD midplane and sideview maps for the same individual of each species, interpolated in space from the sample points shown in Figures 5 to 10, c. Successive frames of the wave fish maps depict 16 phases at constant intervals of time over one period of the EOD. The pulse fish maps contain 16 successive frames at the phases indicated on the head-to-tail waveforms. The potential grayscale used for each fish is shown above the maps, spanning -Vs to Vs millivolts, where Vs is scaled for each fish separately. In order to see details of interest, the wide dynamic range of each fish's EOD was limited by clipping the color scale at its extremes; for example, the EOD usually has a very intense peak near the tail tip, which is shown all in one color. Relative distances are cited in percent of body length from the head (i.e. the tail tip is at 100% body length.)

Summary of Figures 5-10:

A. Subset of waveforms sampled in the midplane at the locations indicated by dots.

B. Head-tail waveform, with dotted lines indicating time of samples for the frames in D.

C. Sample points used in the maps in D: left- midplane, right- sideview composite.

D. Linearly interpolated grayscale maps, sequential in time from top to bottom of left column, and then top to bottom of right column. In each column: left- midplane map, right- sideview composite map. The time of each frame is indicated by a dotted line in B. Grayscale (inset in first frame of D): black $\leq$ -Vs, middle gray = 0 mV, and white $\geq$ Vs, where Vs is indicated in part A.

Eigenmannia virescens

The EOD of *Eigenmannia* (Fig. 5) strongly resembles an oscillating dipole, with a long shallow pole spread along the rostral body balanced by a much sharper peak localized at the tail tip. The waveforms appear very uniform in shape over the body, differing from the head-to-tail mainly in magnitude (Fig. 5a). There is a well defined stationary "zero plane" approximately 70% of the body length from the head, near the longitudinal midpoint of the EO. Waveforms recorded rostral to the zero plane are in phase with the head-to-tail waveform; more caudal they are inverted 180 degrees. The phase reversals in time are very rapid (Fig. 5d, frames 1 and 8) and show three or four small but distinct peaks spaced along the length of the fish, with the middle peaks of opposite sign than the two extremes.

Figure 3.5
Eigenmannia virescens

19.5 cm female
310 Hz
Vs = 25 mV

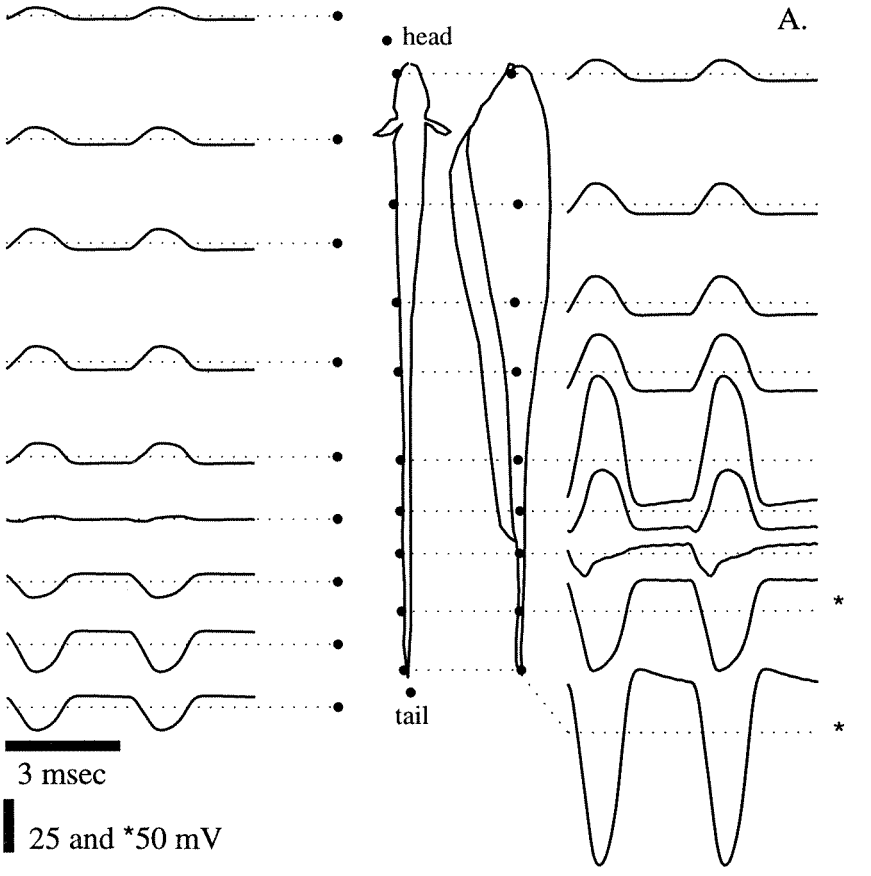

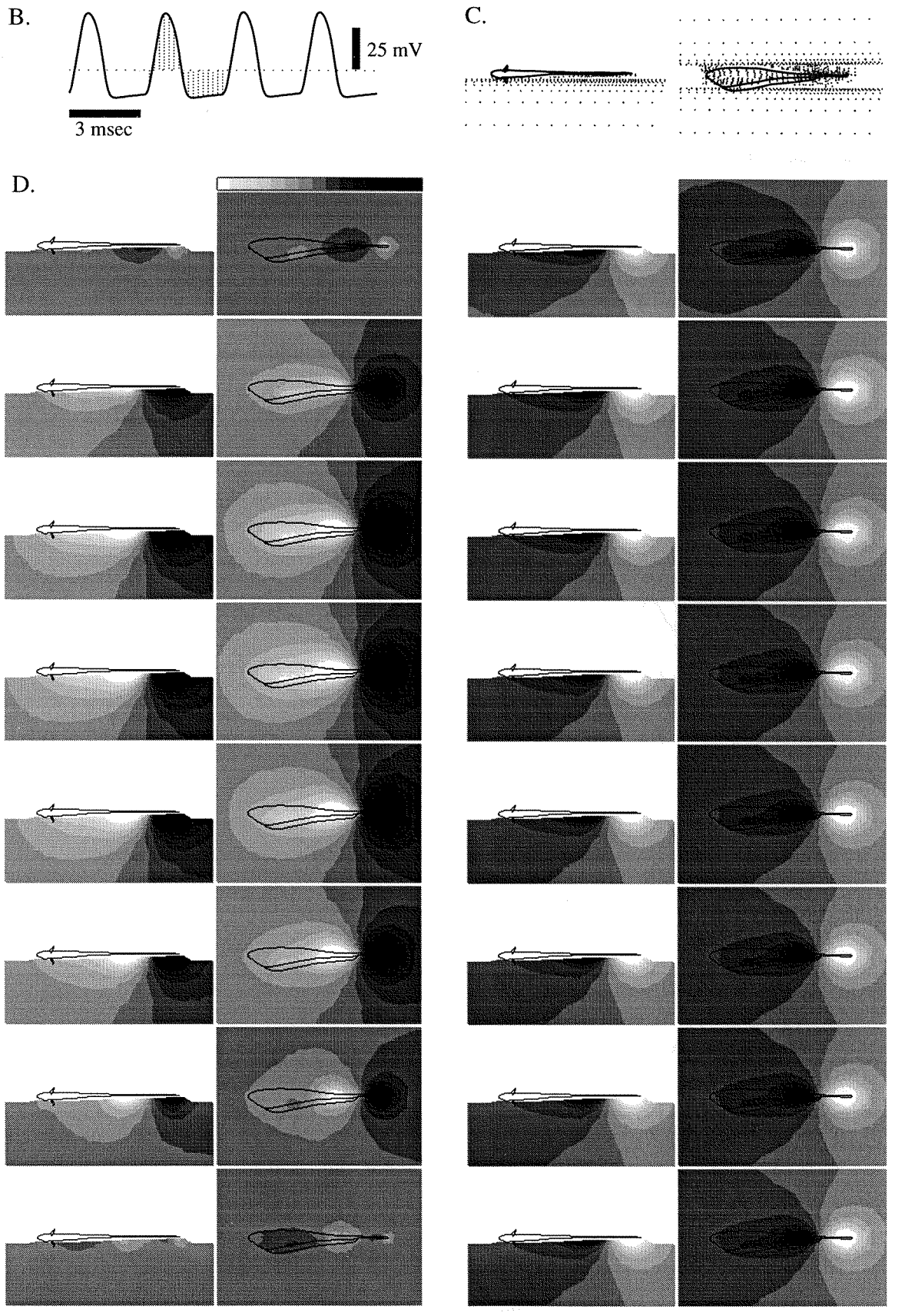
B.
25 mV
3 msec
C.
D.

Apteronotus leptorhynchus

The EOD of the brown ghost cannot be adequately described as a simple oscillating dipole (Figure 6). The waveforms vary considerably from the head-to-tail at different positions on the body. The traces sampled between the middle of the body and end of the tail contain triphasic waveforms in which the second harmonic is comparable in amplitude to the fundamental frequency component. Peaks and zero crossings of the potential propagate along the fish's body, particularly at the tail, where the EO is close to the skin surface and not shunted by high conductivity body tissue. This is especially evident when mapping longer fish and at lower temperatures (see maps in Chapter 2). The velocity of the peaks along the tail appears between 5 and 10 cm/msec. The magnitude of the peaks is also much higher at the tail tip than at the head.

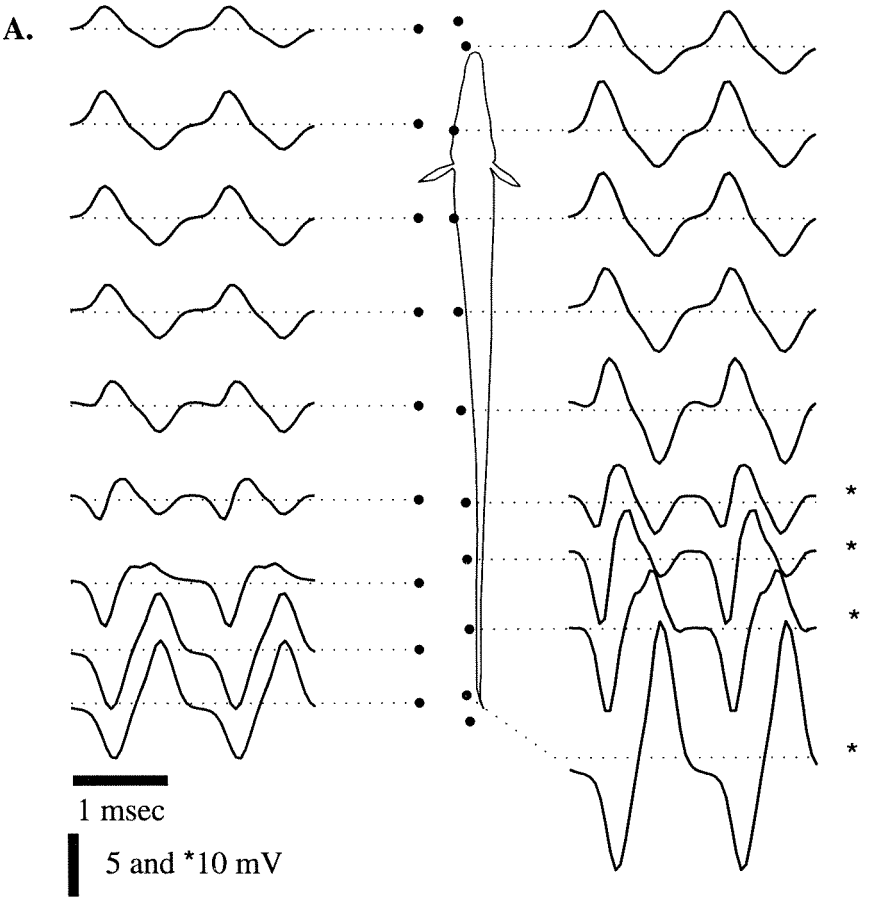

Figure 3.6
Apteronotus leptorhynchus

21 cm female
810 Hz
Vs = 5 mV

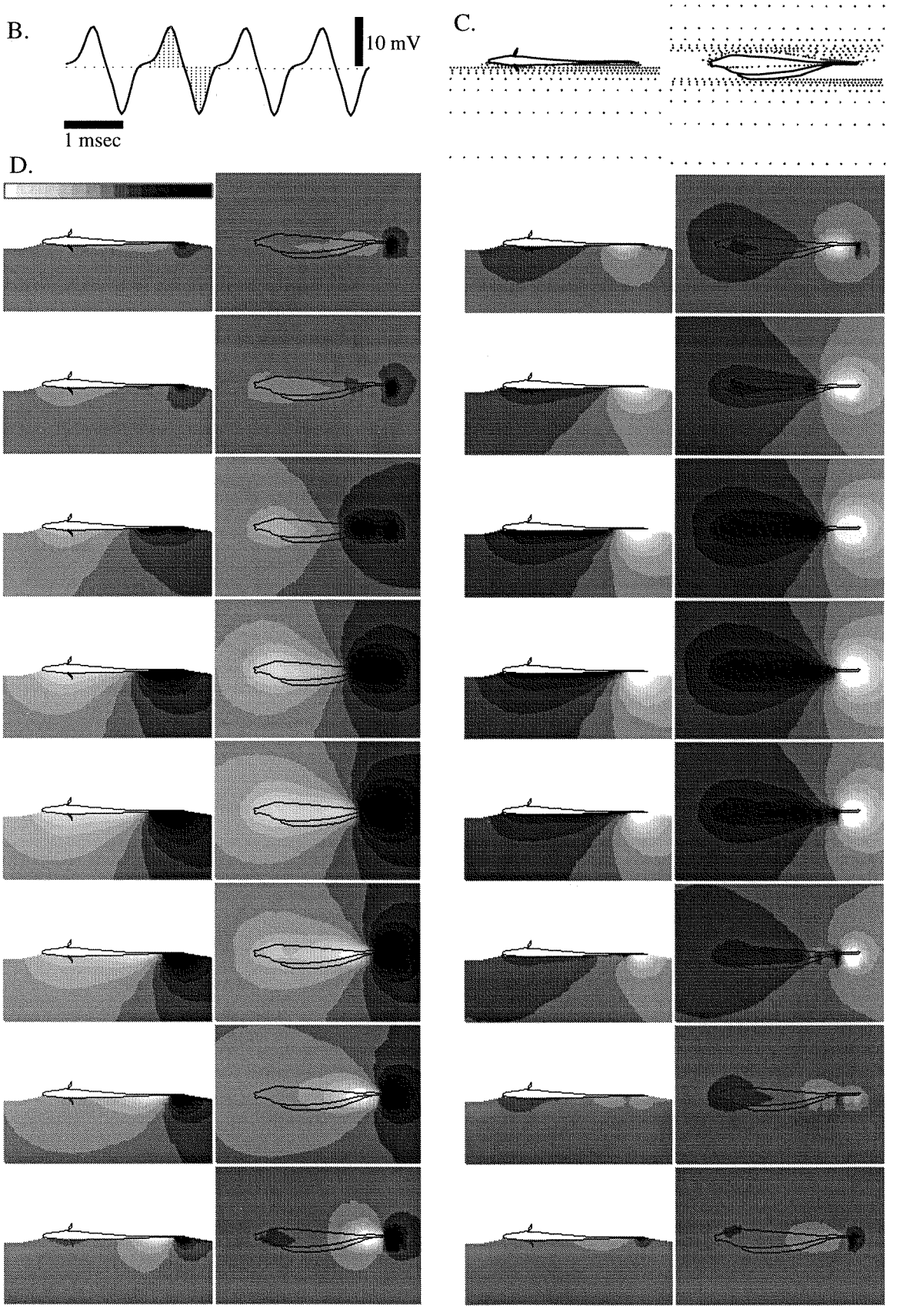
B.
10 mV
1 msec
C.
D.

Apteronotus albifrons

The black ghost knife fish, *A. albifrons*, is very closely related to its brown ghost cousin in EO anatomy and activation, but has a taller, flatter body and a higher frequency EOD. When normalized for frequency differences, as realized in Figures 6 and 7, the EOD pattern appears extremely similar to that of *A. leptorhynchus*. Again, waveforms over the rostral half of the body appear very uniform, while propagation of peaks and zero crossings is evident along the tail. Since this particular specimen was relatively short (< 10 cm), the propagation of peaks is not as obvious as in the other ghost maps.

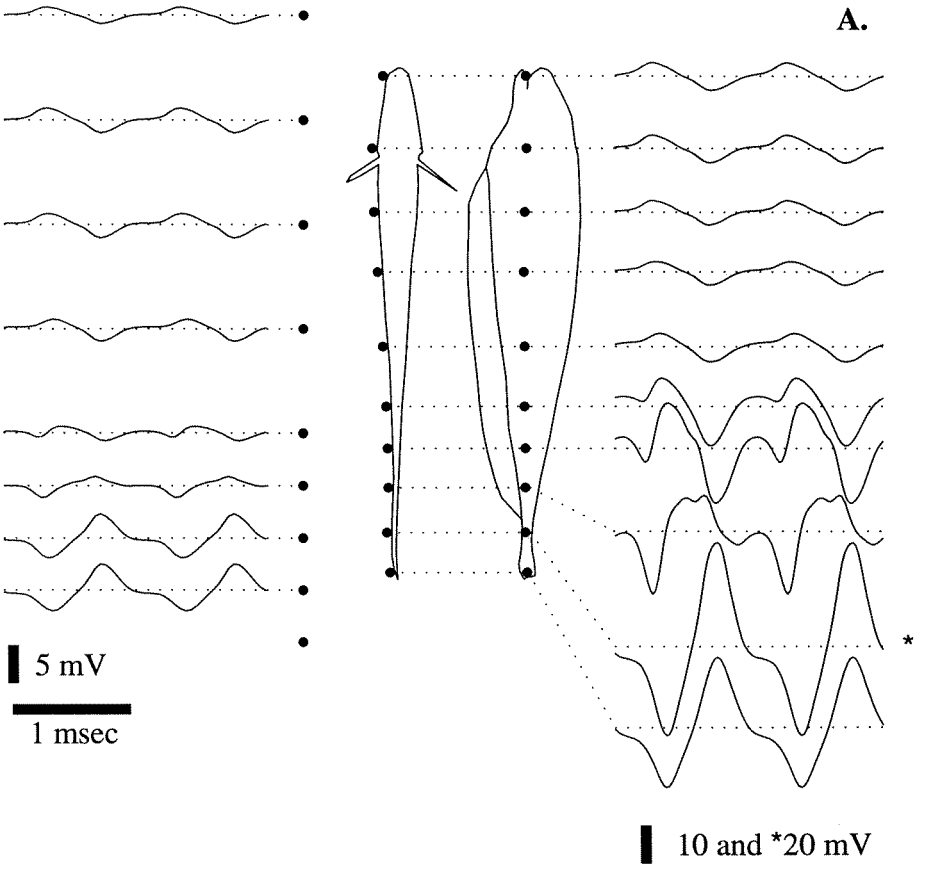

Figure 3.7
Apteronotus albifrons

9.8 cm
910 Hz
Vs = 5 mV

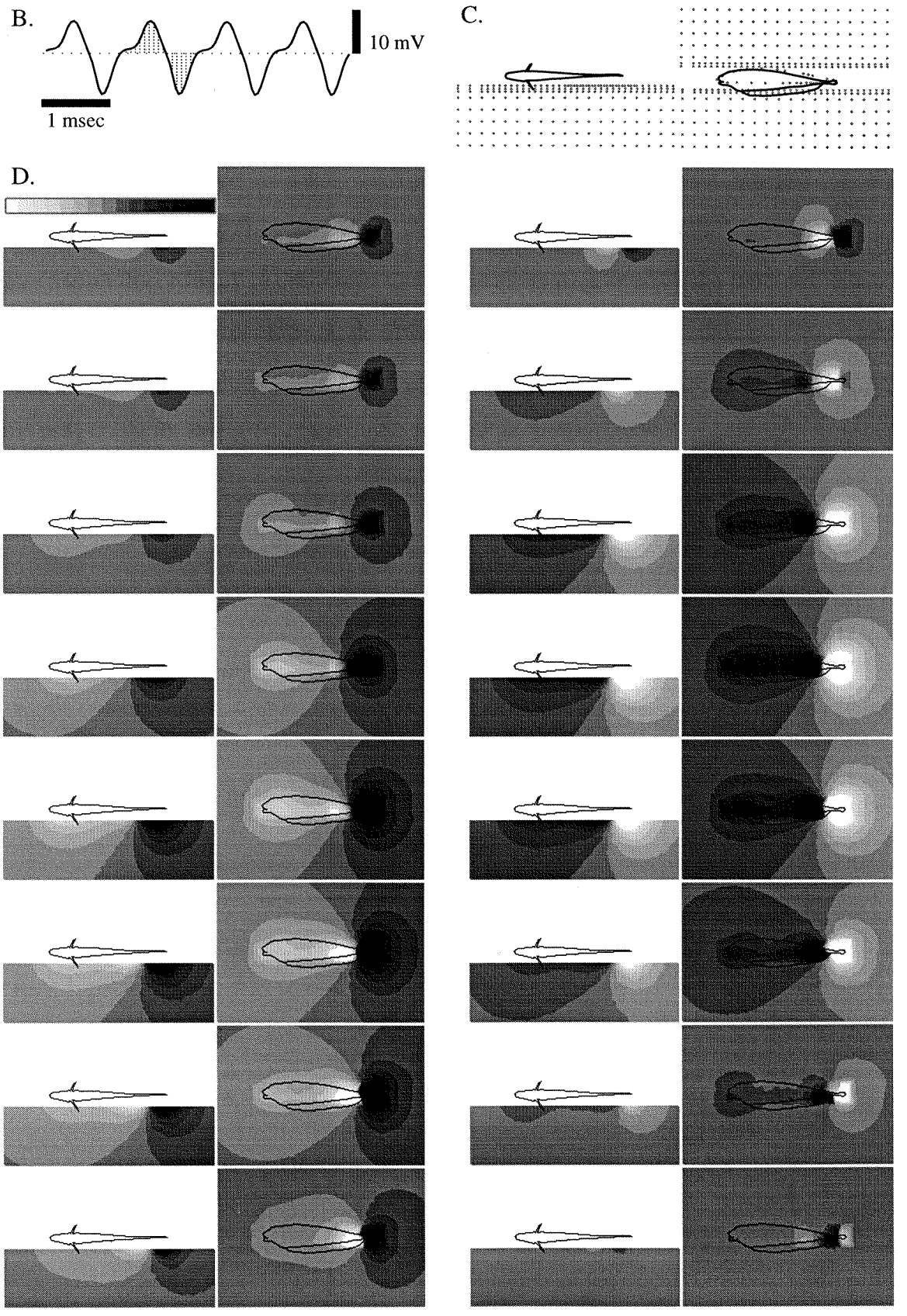
B.
10 mV
1 msec
C.
D.

***Brachyhypopomus* novel species**

In the novel *Brachyhypopomus* species, the EOD pulse begins with a long-lasting dipole field in the rostral body half, positive just behind the head and negative at the midpoint of the body (Fig. 8). This dipole slowly grows in strength for 0.5 msec without changing position, and then begins to move caudally while maintaining the spacing between the poles. "Propagating dipole" describes this phase well, with both peaks moving on the order of 10 cm/msec. Once the caudal peak reaches the tail tip, the head of the fish begins to become negative (frame 7), resulting in three small logitudinal peaks reminiscent of the alternating peaks seen during the polarity switch in *Eigenmannia*. By the next frame the direction of the dipole moment is reversed.

Figure 3.8
***Brachyhypopomus* n. sp.**

14.4 cm
Vs = 15 mV

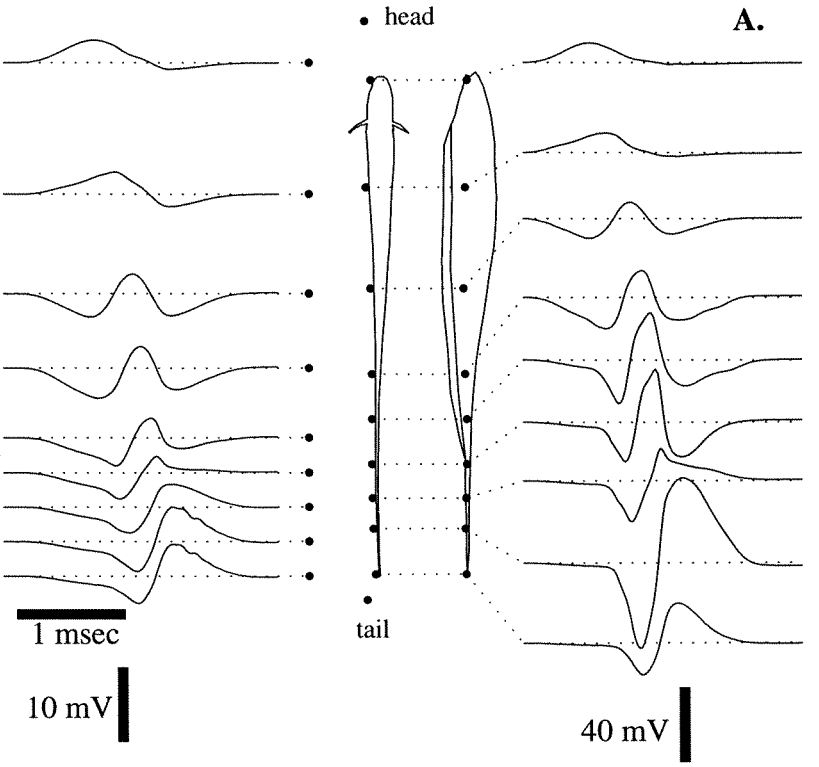

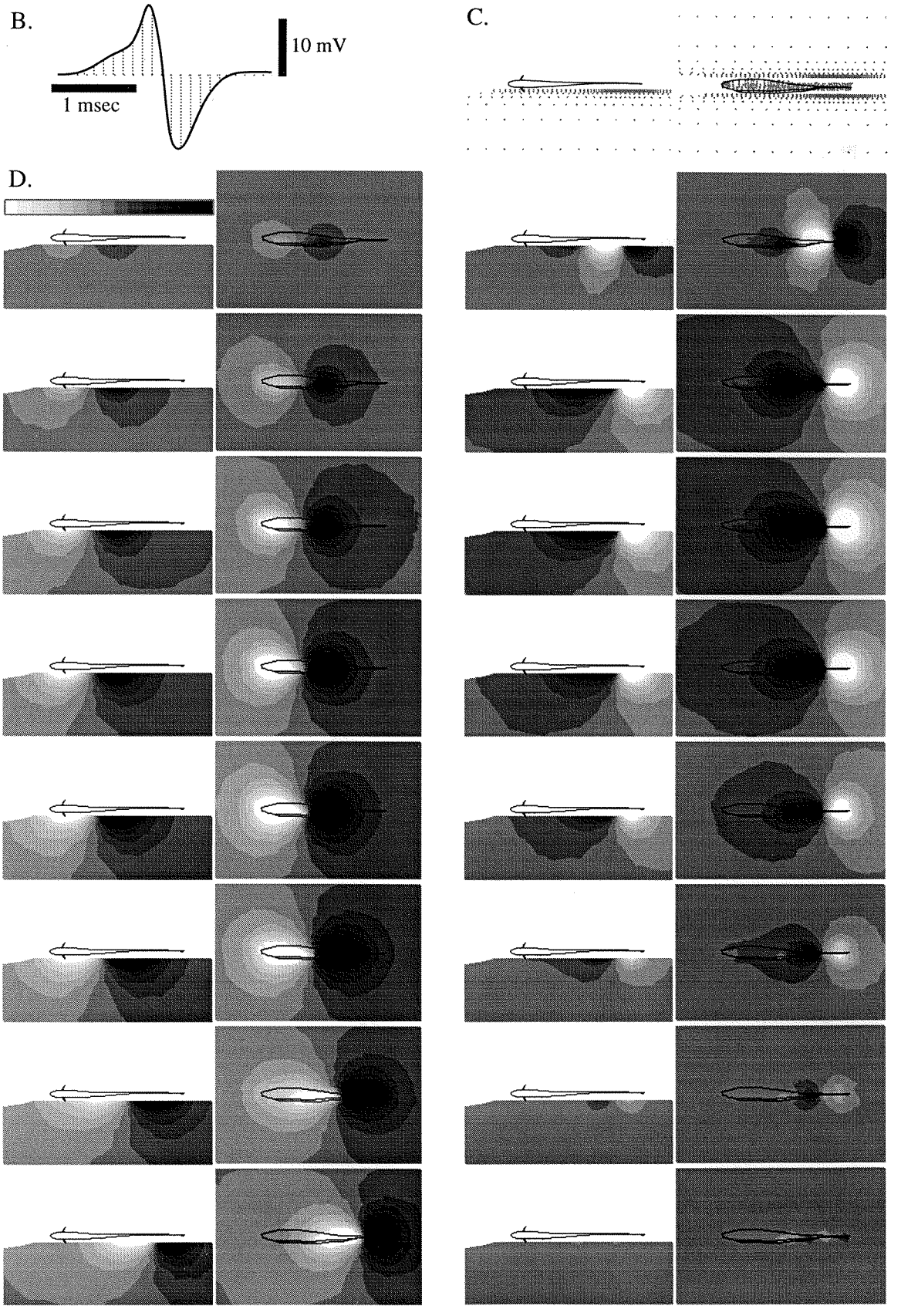
B.
10 mV
1 msec
C.
D.

Brachyhypopomus pinnicaudatus

The faster biphasic pulse EOD of *Brachyhypopomus pinnicaudatus* is not as well synchronized as that of *Brachyhypopomus* n. sp., due to its much shorter pulse width (or equivalently, its higher frequency components; Fig. 9). Frames 6 and 9, containing up to 6 very localized, logitudinally spaced peaks, indicate difficulty in coordinating fast phase changes. The EOD maps also reveal an initial low amplitude dipole under the chin, rotated slightly from horizontal so that there are dorsal-ventral potential differences. In both *Brachyhypopomus* species, the initial EOD phase is too weak to be recorded in typical head-to-tail measurements taken a few centimeters from each end of the fish, and has not been previously reported.

Figure 3.9
Brachyhypopomus pinnicaudatus

14.5 cm
Vs = 15 mV

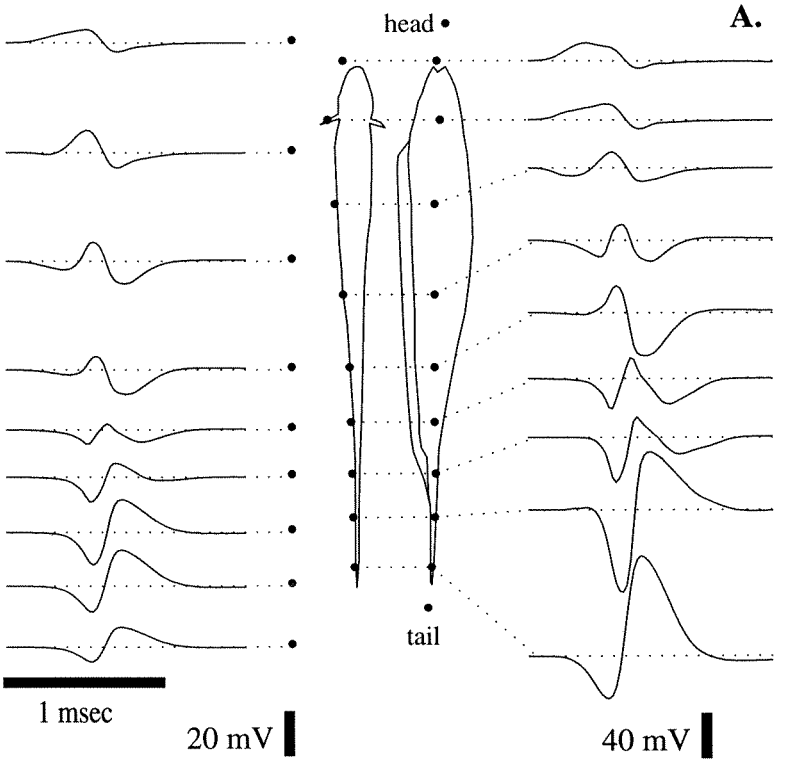

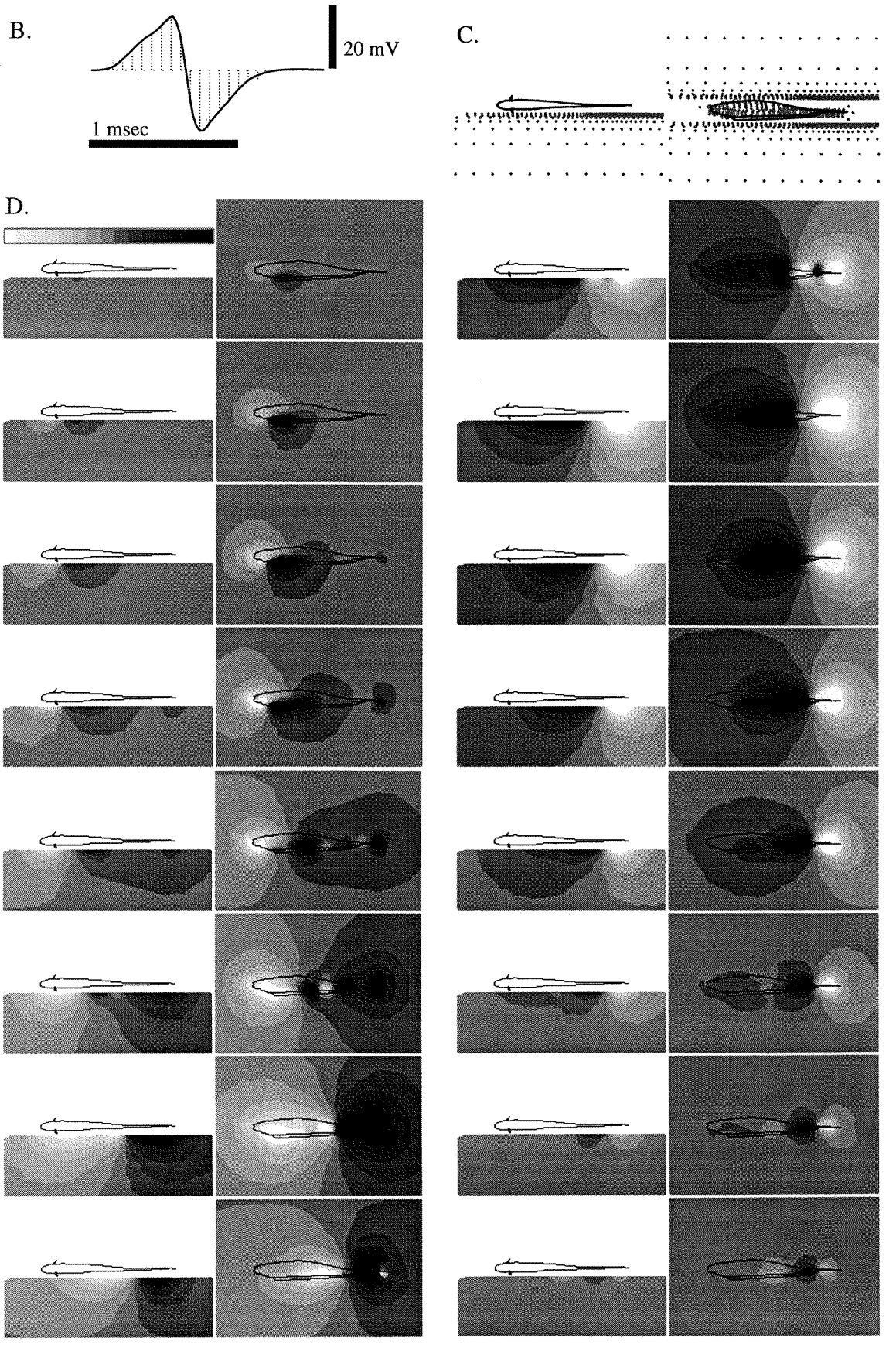
B.
20 mV
1 msec
C.
D.

Gymnotus carapo

The triphasic head-to-tail waveform in *Gymnotus carapo* is a mere shadow of its complex EOD spatio-temporal pattern (Fig 10). The EOD pulse begins with a long weak dipolar phase in the ventral portion of the head, with the dipole axis tilted approximately 30 degrees dorso-ventral. Previously this had been described as a "negative monophasic pulse" (Bennett 1971a) or a "slow head negative deflection" (Trujillo-Cenoz and Macadar 1984), consistent with measurements made only along the midline, or head-to-tail. From the full side view maps it is clear that the chin region of the EO is active first and creates a weak electric dipole field with a significant dorso-ventral component (frame 1 and 2 in Fig. 10d). In the succeeding phases the middle of the fish gets very active and complicated, displaying substantial dorso-ventral gradients, and the tail helps generate some very large peaks. Several phases show a strong dipole separated by the full length of the body, with large peaks at the head and tail tips (frames 7-10).

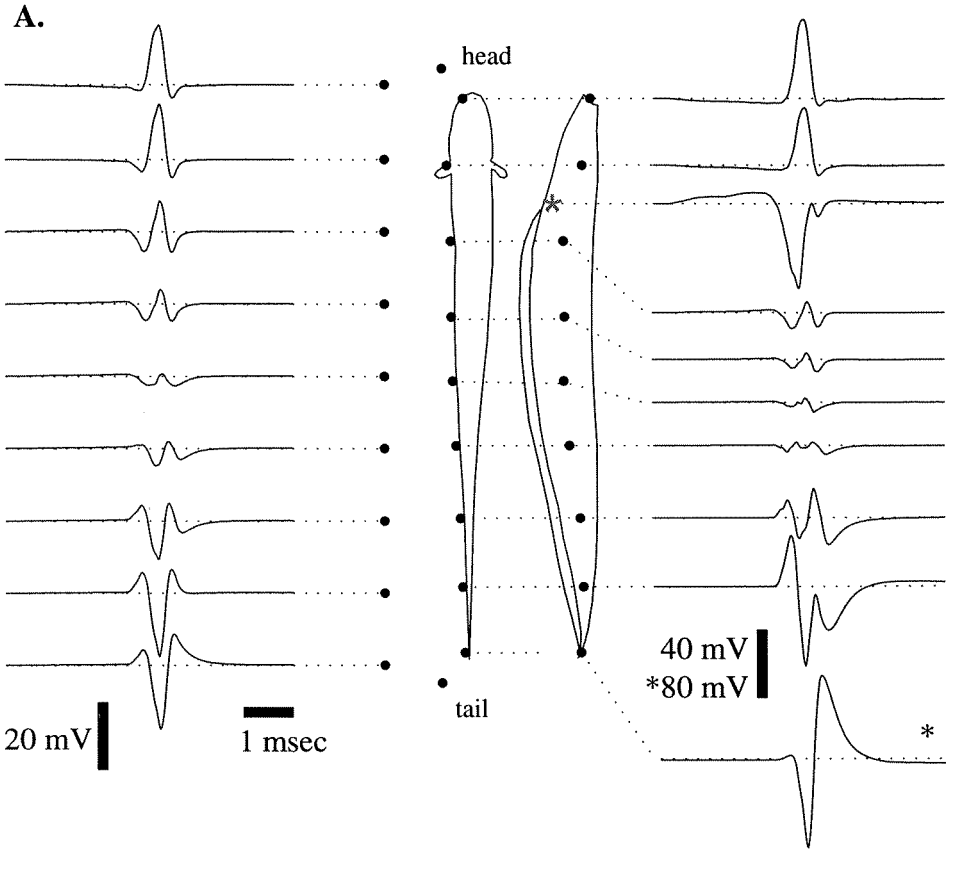

Figure 3-10 ***Gymnotus carapo***

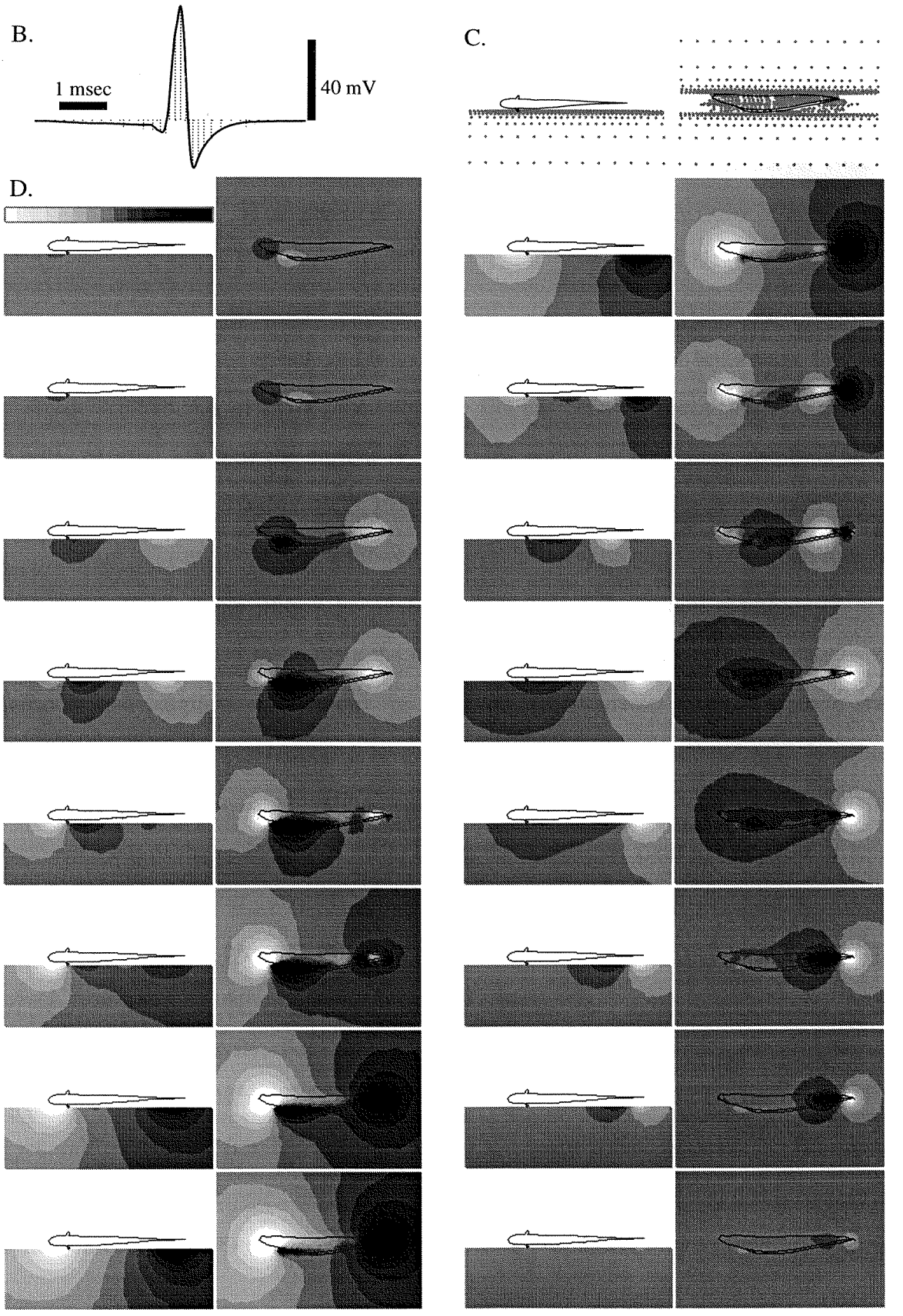
B.
1 msec
40 mV
C.
D.

3.4 Discussion

3.4.1 EOD pattern relation to electric organ morphology and activation

Electrogenesis in electric fish has been the subject of numerous studies and is now well understood at the cellular level (see reviews in Bennett 1971, Dye and Meyer 1986). The electric organ (EO) is composed of electrocytes (modified muscle cells, or in the case of *Apteronotus*, electromotor neuron axons) stacked in parallel columns (see Chapter 1). The electrocytes are innervated by electromotor neurons, and activated by command signals relayed down the spinal cord from a pacemaker nucleus in the brain stem. In most theoretical treatments of EOD generation, the EO has been approximated as a simple dipole, because much of the current is channeled out of its endpoints, resulting in a dipolar far field (e.g., Knudsen 1975; Heiligenberg 1973; Hoshimiya et al. 1980).

In his 1971 review, Bennett showed that synchronization plays an important role in generating large stable output because the currents of individual electrocytes are channeled and summed to produce the overall EOD. He also described mechanisms (termed path length compensation) for achieving simultaneous activation along the electric organ, using conduction delays to equalize effective command path lengths. However, if electrocyte activation was perfectly synchronous and currents were channeled out of the endpoints of the EO, then the dipolar far field would more or less directly reflect the near field. Our data shows this is clearly not the case for many gymnotiform weakly electric species, especially higher frequency fish with long EOs, which would require extraordinary measures to remain synchronous in their firing. This has been noted previously. For example, Bullock (1986, page 667) contrasted the short, well synchronized EOs of most mormyrid pulse fish to the "elongated electric organs" of gymnotiforms that "fire the electrocytes as a rapidly traveling wave." Hopkins, commenting on the complex EOD of *Gymnotus carapo,* also suggested that incomplete synchronization of EO activation could "lead to a propagated dipole field" (Hopkins

1986b, page 50). He further stated "There has been no systematic study.... of these effects which will undoubtedly vary between species".

Our EOD maps now provide the foundations for a systematic, comparative study of the effects of EO coordination on the resulting electric fields. What do the EOD patterns tell us about the EO? In the following sections I highlight likely correlations of each specific EOD pattern with known anatomical and physiological features of each fish's electric organ.

Eigenmannia virescens

The EOD maps of *Eigenmannia* appear to arise from a simple oscillating dipole, with one pole the tip of the tail and the other, elongated pole the rostral body. Potential contours on the fish's skin outline the extent of the EO, from ventral and caudal of the pectoral fins to the tail tip (compare Fig. 5d to Fig. 1). The smaller amplitudes of the rostral waveforms are likely due both to averaging by current spread in the high conductivity tissues in the rostral half of the body, and to a decline in EO volume by 50% from the tail (Ellis and Szabo 1980). The similarity of potential waveforms along most of the body length with the head-to-tail waveform is in part due to averaging in the body, but also indicates that timing of electrocyte activation is well synchronized. In order to sum electrocyte output to generate large stable discharges, separate pacemaker relay axons project to electromotor neurons in specific segments of the spinal cord (Ellis and Szabo 1980), and terminal branches from the spinal cord to the EO are thinner and longer, hence slower, in the paths leading to the anterior EO segments (as in Fig. 77 in Bennett 1971a).

Antidromic collision experiments in the spinal relay axons of *Eigenmannia* have demonstrated the EOD is composed of head positive pulses superimposed on a head negative baseline (Bennett 1971a). The head positive phase of the waveform (Fig. 5d, frames 2 through 6) corresponds to spiking at the innervated posterior face of the electrocytes. Under normal steady state conditions, accumulated charge near the anterior

end of each electrocyte causes a passive return current, resulting in the external head negative baseline (frames 9 through 16). The phase reversals in our maps indicate the switch in polarity begins at the rostral end of the EO, while the caudal half is still finishing the previous phase (frames 1 and 8). However, the speed of the polarity switch again suggests that the command path length compensation works well for this relatively low frequency fish.

Apteronotus

In contrast to *Eigenmannia*, the EODs of the *Apteronotus* species cannot be adequately described as simple oscilating dipoles (Figs. 6, 7). The variation in waveform from the head-to-tail at different positions on the body implies a lack of synchronous activation for the EO. Instead, the observed caudal propagation of peaks and zeros suggests sequential activation of electrocytes along the electric organ as the command volley propagates down the spinal cord. This is consistent with a circuit model of the EO of *A. albifrons*, constructed by Hoshimiya et al. (1980) to replicate the waveforms in the triphasic region of the tail, which required both a phase delay and a local current path between EO segments. It is also consistent with the known anatomy of the command pathway in *Apteronotus*.

As a member of the phylogenetically modern Apteronotidae family (Alves-Gomes et al. 1995), *Apteronotus* has a unique neurogenic EO composed of modified motor neuron axons (Bennett 1971a). The EO extends just ventral to the spinal cord from caudal of the pectoral fins to the tip of the tail. At regular intervals along the spinal cord, electromotor neuron axons descend in nerve branches into the EO, where the specialized axon terminals themselves function as electrocytes (Waxman et al. 1972). Axons from the relay cells in the pacemaker project down the entire spinal cord to innervate electromotor neurons at all levels (Ellis and Szabo 1980), and so preclude most mechanisms for command path length compensation. These fishes' long electric organs and high firing frequency may make electrocyte synchronization impractical.

Brachyhypopomus

As in *Eigenmannia*, the location of potential peaks and contours on the body of the *Brachyhypopomus* species again reveals the EO position, lying inside the ventral body surface from just behind the pectorals to the tail tip (corresponding to the EO outlined along the belly in an unidentified *Hypopomus* species in Figure 1). However, the clear propagation of peaks again suggests sequential activation of electrocytes along the length of the organ. Bennett (1971a) described in detail how the electrocytes in *Hypopomus* contribute to produce the overall EOD: the innervated caudal face fires first, producing a net tail to head current through the electric organ, and resulting in the initial head positive phase in the head-to-tail waveform. Current through each electrocyte then depolarizes the rostral face, causing it to fire and creating the second phase of a typical biphasic *Hypopomus* waveform. Bennett also found species of *Hypopomus* with only monophasic output and with what appeared to be mixes of monophasic and biphasic output (Bennett 1971a, pg 402). Our EOD maps for *Brachyhypopomus* appear to support his suggestion that only the posterior cells generate the second phase in some species, since the peaks of the head negative phase appear stationary in the tail. However, this could also be caused by the second phase becoming synchronized by the large currents flowing through the entire EO during the first phase.

Gymnotus carapo

The complex EOD of *G. carapo*, at the opposite extreme from the simple map of *Eigenmannia*, reflects its complicated EO and command pathway. The EO again extends over most of the body length, running inside the ventral surface of the fish (see Fig. 1). It is composed of multiple electrocyte columns distinctly innervated in three separate segments. The innervation results in complex timing that generates four distinct phases of the head-to-tail waveform (see figure 1 in Trujillo-Cenoz and Echague1989). This species does possess mechanisms to compensate for different conduction path lengths: pacemaker relay axons terminate in specific segments of the spinal cord (Ellis and Szabo

1980), and have a wide range of conduction velocities distributed according to path length, from 1 to 9.1 cm/msec (Lorenzo et al., 1990). The anterior electromotor nerves also branch back to the rostral segments from the midpoint of the spinal cord (Trujillo-Cenoz and Echague 1989). Therefore command signals simultaneously traveling to widely separated EO segments can remain synchronized upon reaching their respective destinations. However, even with path length compensation, the complex innervation and timing of the EO segments still results in the complex discharge evident in the EOD maps.

Individual electrocytes can have one or both faces innervated by multiple nerve branches depending on location in the EO (Macadar et al. 1989), which contributes to explicit features in the EOD map. For instance, the leading seven electrocytes in the lateral abdominal tubes have their rostral surface activated first, causing current to flow caudally under the head. The sideview map elegantly clarifies this initial, long-lasting weak dipole under the chin (Fig. 9, frame 1), corrseponding to wave 1 in Trujillo-Cenoz et al. (1984). The substantial dorso-ventral radial asymmetries in the trunk may be in part caused by a difference in activation times of electrocyte columns composing the EO: the dorsal most column fires prior to the 3 columns below it (see Figure 17 in Bennett 1971a, or Figure 2 in Trujillo-Cenoz et al. 1984). This specialization of EO activation may be an adaptation to maximize the dipole moment in this species (see below).

Similarities and differences between species

The EOD maps are distinctive for each species, but similarities can be seen when they are normalized in scale, body length, and time over a single EOD cycle or pulse, as presented here. All of the species presented here, including *Eigenmannia*, display substantial rostro-caudal differences in EOD amplitude, with the largest amplitudes at the tail. The peaks in potential also appear to clearly indicate the location of the active EO segments in many of these fish. These potential peaks are in part caused by current exiting the electric organ along its length instead of being channeled to its endpoints. EO

insulation is indeed usually quite "leaky," as termed by Caputi et al. (1989). This is more apparent at the tail than at the head: local current paths in the tail are not shunted by high conductivity body tissue, and so must cross the high resistance skin, manifested in the maps as large local peaks in the monopolar potential. The peaks are also stronger on the ventral surface of the body in the pulse fish and in *Eigenmannia*, where the EO again lies close to the surface. Another common feature is that most of the fish (with the exception of *G. carapo*) have an EOD phase during each cycle in which the rostral body appears uniformly negative. This has implications for the receptor stimuli (see below).

The phases with largest near field peaks are mainly dipolar, and the far field is dipolar. Larger dipole moments (magnitude x separation length) offer greater range of communication (Knudsen 1975), and generally indicate a larger fish to the receiver. Wider spacing between the poles is also advantageous in increasing the range of electrolocation (Heiligenberg 1975). In most of the mapped species the rostral peak is located proximal of the tail where the body begins to widen appreciably. *G carapo* is again the exception: while showing this pattern near the end of its pulse, it has evolved a complex EO and timing to produce as wide a spacing as possible during the main peaks (Figure 10d, frames 6-10). The normalized maps also show that the EOD pattern and body shape of *B. pinnicaudatus* appear midway between that of *B.* n. sp. and *G. carapo* (prepulse under chin, slight dorsal-ventral differences, etc.). The detailed EOD maps may prove useful in helping delineate phylogenetic relationships among gymnotiforms (see Alves-Gomes et al. 1995).

Of the six fish mapped, only *Eigenmannia* has a relatively simple, dipolar near field. In contrast to the other more complex EODs, *Eigenmannia* 's waveforms appear to be more uniform and highly synchronous. A comparison between species suggests it is more difficult to synchronize the EO as the frequency increases. At higher frequencies, any fixed time delay will be a larger fraction of the period (or of the pulse width), causing a greater phase shift. While the peaks of the potential are not necessarily centered over

the most active segments of the EO, the observed propagation in the EODs of both *Apteronotus* and *Hypopomus* does suggest sequential activation of electrocytes along the electric organ. The phase velocities of potential peaks we measured, around 10 cm/msec, are comparable to conduction velocities found in *G. carapo* (Lorenzo et al. 1990). The near fields of the EODs in these fish may be more accurately described as "propagating dipole fields" (Hopkins 1986b).

3.4.2 Electrosensory significance of complicated EOD maps

Implications for electroreceptor stimuli

In each of these species, the structure of the EOD has significant implications for the peripheral electrosensory input. Before discussing the implications, I must first note that the potential measurements reported here were monopolar electrode recordings made with respect to a distant electrode on the fish tank wall, and are not the voltages across the active membranes of the electroreceptors. How well do these measurements reflect the actual electrosensory stimuli? To address this issue, Watson and Bastian (1979) compared three indirect measures of the electroreceptor stimulus: monopolar, bipolar perpendicular to the skin, and transdermal. They concluded that the monopolar technique gives the least suitable measure of the effective sensory stimulus. While this may be true when examining the output of a single electroreceptor, there are definite advantages to the monopolar technique for recording entire maps. For example, we have also measured the transdermal EOD potential with respect to an intramuscular electrode (unpublished data). While this more closely approximates the transdermal potential at locations near the reference electrode, the fish interior was not equipotential, and so the recorded voltage is highly dependent on the position of the internal electrode. In contrast, the potential at the side wall far from the fish is a very small percentage of the near field amplitude, and varies only slightly with small changes in position. Therefore measuring with respect to a wall electrode results in maps consistent with an absolute view from

electrical ground at infinity. It also has the advantage of being noninvasive (you know a brown ghost is angry when it chirps repeatedly after being jabbed with a sharp electrode!)

The second method of estimating the electroreceptor stimulus is by measuring the potential gradient perpendicular to the surface of the skin, using differential electrode pairs. This requires consideration of the fish's curvature, and a model of how non-perpendicular current might be channeled to the sensory cells by the high resistance receptor pore walls (e.g., see Scheich and Bullock 1974; Yager and Hopkins 1993). We have built differential electrode arrays and collected electric field data for each of these species (Rasnow thesis on brown ghost; unpublished data on others). However, preliminary analyses of the electric field data suggest a strong likeness between the instantaneous potential pattern and the perpendicular electric field component when both are measured directly on the fish's skin, particularly for fish oriented with straight body and tail, symmetric about the long axis of the body. Besides giving an approximation of the normal component, the surface maps also allow estimates of tangential field strength from the potential gradient along the skin. The surface maps also have another advantage - they are much faster to collect, using a flexible multi-electrode array, and so minimize stability problems related to slow drifts over time.

This issue can be explored with yet another method (for a review, see Plonsey 1969): since there are no current sources outside the fish's body, the electric field at the skin surface can be computed by solving Laplace's equation given the potential on the skin (the Dirichlet boundary condition) and the fish body contour (the shape of the boundary). In Chapters 4 and 5 I describe boundary element method simulations that can be easily adapted to permit computational estimates of current normal to the skin, based upon monopolar, flexible array recordings over the entire fish surface. Therefore, these potential maps not only suffice to describe the EOD, they also contain enough information to allow prediction of electrosensory stimuli over the entire body surface.

Our field mappings include the entire skin surface on one side of the body, providing measurements of the local field waveform relevant to receptors in each region of the fish, and therefore allowing estimation of the entire transepidermal stimuli. The variability of the EOD waveforms with location on the body surface suggests that electroreceptors in different regions may fulfill different computational roles in electroreception. There typically is found a higher spatial density of receptors in rostral regions, especially around the head, compared to caudal regions ($15/mm^2$ vs. about $3/mm^2$ in *A. albifrons*; Carr et al., 1982), as well as more dorsal and ventral, away from the midline. Gross features common to many of the EODs correlate with the receptor densities: the more uniform rostral fields, due to current spread in the low resistance body fluids, may help optimize resolution of objects near the head; large fields at the tail will maximize object perturbations, and may better indicate distance (Knudsen 1975).

Implications for electroreceptor transfer functions

Amplitude and phase information in the electrosensory image is first encoded by two general functional categories of tuberous electroreceptors (Chapter 1; for details see Zakon 1986). Rapid timing units have a very low threshold to inward current and fire one-to-one with the EOD, while amplitude modulated units are sensitive in the range of EOD amplitudes and encode stimulus intensity. These two receptor types have been well characterized in *Eigenmannia*, with T-units encoding the phase of the stimulus zero-crossing, and P-units that fire with a probability dependent on the stimulus amplitude (Scheich et al. 1973; Carr and Maler 1986). Since most of *Eigenmannia*'s receptors are found in the rostral half of the body, their pattern of response should be very uniform in reflection of the uniform field. However, in the other gymnotiforms things are not so simple. For example, the propagation seen in *Apteronotus* may cause waves of receptor stimulation to sweep down its body. Most receptors found on this fish are thought to be subtypes of amplitude coders which respond to the envelope of the EOD waveform, although some phase information is still present (Bastian 1981). The two receptor classes

in the pulse gymnotiforms are called pulse markers and burst duration coders (see Yager and Hopkins 1993), but again their reported responses vary in different studies. It appears from the literature to be difficult to characterize receptor transfer responses to realistic stimuli. The full waveforms collected in our experiments should facilitate the analysis and modeling of electroreceptor transfer responses for all of these fish.

Receptors are generally tuned to the dominant frequencies of the fish's own EOD (Hopkins 1976), but spatial variations in frequency responses have been found in tandem with the local EOD waveforms (Watson and Bastian 1979; Bastian 1977). Receptor thresholds and spontaneous activity levels are obliged to vary with location on the body surface (as proposed by Bastian in 1976), to maximize their sensitivity or computational utility while biased from the local transdermal wavefrom. To further complicate matters, electroreceptors in *Hypopomus* have recently been found with strong directional selectivity (Yager and Hopkins 1993; McKibben et al. 1993), consistent with a model of current channeling through the skin pores. Many receptors in the caudal half of the body were associated with longitudinal 1 to 2 mm canals, parallel to the lateral line; coincidentally, many receptors were found to be most sensitive to fields along the logitudinal axis (see figures 1b and 7 in Yager and Hopkins 1993), and so may be affected by the tangential field components apparent in our maps. Although long tuberous canals have not been reported in the other gymnotiforms, directional tuning would be interesting to examine in *G. carapo*, since our data indicates there are substantial dorsal-ventral currents at its surface as well as longitudinal and radial currents.

Implications for central processing

Behavioral and physiological studies have demonstrated electric fish are extremely sensitive to small distortions in the electrosensory image introduced by a variety of stimuli: in object detection (Bastian 1976, 1986b), direct electrical stimuli (Knudsen 1974), extreme phase sensitivity (Kawasaki et al. 1988; von der Emde and Bleckmann 1992), and in the jamming avoidance response (Heiligenberg 1986). These

prove the existence of effective electrosensory processing algorithms. Ultimately, the fish must extract useful signals contained in small field peturbations superimposed upon its intrinsic EOD pattern. In the context of the maps presented here, spatial variations in local EOD waveforms are likely to be reflected in the patterns of afferent input transmitted to the brain. Central electrosensory processing must then somehow remove the complex carrier bias to better resolve modulations caused by external objects and other fish. This may have driven the evolution of initial processing stages, which probably coevolved from (or with) lateral line mechanosensory areas in parallel with electrogenesis (Fritzsch 1993).

How is the large EOD bias waveform accounted for? Once encoded by the electroreceptors, electrosensory information from the periphery is projected directly to multiple somatotopic maps in the electrosensory lateral line lobe (ELL), a cerebellar-like, bilateral hindbrain structure (Maler et al. 1981; Bullock and Heiligenberg 1986). Amplitude information from the electroreceptors first terminates in the deep layers of ELL, on the basal dendrites of principal cells that exhibit center-surround receptive fields (Bastian 1981b). The different ELL maps are thought to filter the sensory image at a different spatial and temporal resolution (Shumway 1989ab). Each ELL map also receives a commissural projection from the corresponding map in the opposite lobe, presumably for common mode rejection (Bastian et al. 1993). At the same time cerebellar feedback descends on parallel fibers through the large apical dendrites of the principal cells, carrying both sensory and proprioceptive information (Batian 1993; Bell 1993; also efference copy in African mormyrids, Bell 1982).

The descending cerebellar input normalizes ELL output by controlling principal cell gain, such as during tail bending or other postural changes that affect the transdermal fields (Bastian 1986a, 1995). It also has been shown capable of adaptively suppressing predictable sensory inputs and enhancing novel stimuli (Bell 1993; Bastian 1995; Bell et al. in press). For example, in mormyrid pulse fish the effect of the EOD command

corollary discharge on the principal cells of ELL is plastic and depends on the electrosensory input that followed the motor command in the recent past (Bell 1982, 1986). Pairing an electrosensory stimulus in the receptive field of the cell with the EOD motor command for just a few minutes leads to a cancelling of the original stimulus response. When the stimulus is then turned off, a negative image of the original response remains. This adaptation, termed "expectation generation" (Bell 1993), appears due to anti-Hebbian plasiticity at the parallel fiber to pyramidal cell synapses in the molecular layer. Persistent spatial variations in the peripheral electrosensory image would then be inversely reflected in the distribution of synaptic strengths across the ELL molecular layer. Bell proposed the functional role of the plasticity in ELL is to subtract predictable features of the sensory input.

The complexity of the EOD maps presented here implies one specific function for the common mode rejection and adaptive filtering mechanisms in ELL: to subtract (or suppress) a spatio-temporal template of the EOD carrier bias from the incoming sensory stream. This would allow better resolution of small amplitude modulations caused by external objects and other fish. A related function would be to cancel electrosensory reafference due to the fish's own movements, such as tail bending or ventilation (i.e., self-generated modulations of the carrier). Similarly, the fish often hovers or rests near structures or surfaces that greatly affect the EOD fields. Readjusting the output levels of ELL principal cells in all of these situations would be needed to return them to their sensitive ranges. By predicting the ELL input from our EOD maps, we can determine what information is available and what kind of processing is required to extract the information needed by the fish.

Higher levels of electrosensory processing are also likely to be influenced by the EOD patterns reported here. Amidst its uniform field, *Eigenmannia* exhibits an exceptional social behavior called the Jamming Avoidance Response (JAR), which shifts the fish's frequency away from that of a superimposed jamming signal (Watanabe and

Takeda 1963; Heiligenberg 1989). The JAR requires detailed comparisons of spatio-temporal information across different regions of the body surface, with performance proportional to functional surface area. The principal neural circuitry involved, spanning about a dozen synaptic levels from electroreceptive periphery to electric organ pacemaker, establishes sub-microsecond temporal acquity in *Eigenmannia* - among the highest found in the animal kingdom (Kawasaki et al. 1988). However, in other wave fish with strong spatial variations in their local field waveforms, the effects of a jamming signal will vary with location on the body surface, making direct comparisons across regions more difficult. Perhaps for this reason *Apteronotus* has a relatively poor JAR, tending to only increase in frequency, or instead phaselock with the jamming signal (Langner and Scheich 1978). The single known mormyriform wave species, *Gymnarchus niloticus*, also has a relatively low frequency EOD and exhibits an efficient JAR (Bullock et al. 1975; Kawasaki 1993). It would be interesting to map this species to see if its EOD near-field pattern is mainly dipolar, like that of *Eigenmannia*.

Implications for studies of electroreception

Of the six species mapped, only *Eigenmannia* has a simple dipolar EOD, the stereotypical electric fish. Through this fortuitous circumstance the fish has become an elegant model system for studies of electroreceptor responses, central processing, and behavior. Generalizing its results to the other species may prove more problematic because of the spatial variations in their local field waveforms. For example, a commonly used experimental method is to substitute for the EOD a prerecorded or sinusoidal signal played from a pair of electrodes. While this may be a good approximation of the EOD in well synchronized fish such as *Eigenmannia*, it could not emulate the complex spatial patterns of the other fish. Replication of experiments successful with this protocol in *Eigenmannia* may yield anomalous results in other species because of inappropriate stimulus geometry. Instead, it may be necessary to deal with the full waveform pattern when studying electrolocation and natural behaviors.

"The practical electricians, however, were by no means satisfied that the effects of these fishes were really produced by electricity."
"Cavendish admitted them into his laboratory on this memorable occasion ...simply to obtain the testimony of these eminent men to the fact, that the shocks of the artificial torpedo agreed in a sufficient manner with Walsh's description of the effects of the live fish, to warrant the hypothesis that the shock of the real torpedo may also be an electrical phenomenon."
"They got shocks from the torpedo to their complete satisfaction, and probably learnt a great deal about electricity..."
"...the electrical fishes still possess the power of exciting the imagination as well as the nerves of those who have felt their power..."

J. Clerk Maxwell, 1879

4 Electric Field Simulations: Numerical Techniques

4.0 Summary

I describe here the methods used to develop a three-dimensional boundary element method simulator to solve Poisson's equation for a particular class of boundary value problems: reconstructing the electric organ discharge of electric fish. A derivation of the boundary element method is presented first, and its features are compared to those of the finite element method. Details of the full simulator are then described, along with justifications for the approximations used in this application. A 3-d graphical interface was also built for manipulating the model mesh and viewing the resulting solutions. Results from simple test cases were used to verify the accuracy of the simulator.

4.1 Introduction

The results of Chapters 2 and 3 establish our ability to measure the electric organ discharges (EOD) of weakly electric fish. However, several constraints on the field mapping procedure limit its utility for investigations of electrolocation. Most importantly, the fish must be held stationary. Even then it is difficult to measure the small distortions caused by nearby objects, which are typically a very small percentage of the intrinsic EOD magnitude. The fish themselves are much better at it, using central

convergence from their distributed array of receptors to detect signals too weak for us to measure.

In order to better study electrolocation noninvasively during natural behaviors, I developed a computer simulator of the fish and EOD. The first step was to choose an appropriate mathematical model and solution method. The process of simulating real physical systems always creates tradeoffs between the computational complexity of the model and the quality of the results in representing the system. So first I had to define my goals, based upon specific objectives of the modeling:

1. Electric fish use their EODs to electrolocate, or probe, nearby objects in the water. Therefore the simulations should make it possible to quantify the electric fields throughout the fish's body and water, and in particular to extract the entire electrosensory input to the receptors in the skin (the transdermal voltage). Resolution and precision should be high enough to get accurate representation of sensory images: the fish can detect very small modulations of the EOD fields across their skin, including amplitude changes on the order of 1 part in 10000 (or less than 1 μV difference in transdermal potential). In the end, however, the model's sufficiency will be gauged by what new insights the results can provide about electrosensory systems.

2. The fish move and explore in three dimensions, in various orientations with respect to external objects. Also, the fish's electroreceptors are found on all surfaces of the body, usually with higher density away from the midline. Therefore the model must be fully three dimensional. Two-dimensional equations inherently assume no variation in the third dimension (zero divergence), with solutions affected accordingly (decay with distance slower, etc.) Near a large flat body surface, such as the side of the black ghost knife fish, this may be a good approximation, but farther away or near the thin tail this becomes inadequate.

3. The fish body has complex geometry, and is often bent into different configurations. Therefore the model mesh must be flexible, to bend the tail and body

accordingly. This naturally leads to numerical techniques and discretization to break up the domain into smaller pieces. Discretization is also necessary in adding external objects to the model.

4. To make the problem tractable, I need to use several simplifying assumptions. First and foremost, this may be treated as an electrostatics boundary value problem. The quasistatic approximation is appropriate since the dielectric relaxation time (permitivity/conductivity) in water is very small, the frequencies of the selected species are low (< 10 kHz), and the fish body and skin are predominately ohmic. Typical numbers in fresh water would be:

$$\varepsilon = 81 \times 8.85 \times 10^{-12} \text{ F/m}, \sigma = 5 \times 10^{-4} (\Omega\text{cm})^{-1}, \omega = 2\pi \text{ freq} = 2\pi (1000 \text{ Hz})$$

$$\therefore \omega\varepsilon/\sigma = \text{about } 10^{-4}$$

Therefore, displacement current will be negligible compared to conduction current. This could be violated in special circumstances (if, say, a large thin leaf of high dielectric constant floated across the current paths close to the fish), but should hold true for most of the situations in the lab and in the field.

5. To recreate sequences of electric fish behaviors, I will need to run many simulations under different configurations. Therefore the simulator should be optimized for both speed and ease of use. These require an efficient means of configuring the model mesh, and fast methods of solution.

4.2 Simulations of the EOD

The most general starting point for handling a problem in electromagnetics is to pick the appropriate relationship from Maxwell's equations. The differential form of Gauss' Law[1] provides a suitable choice for the unknowns to be solved here. After applying the electrostatics assumption and substituting potential for the electric field

[1] Gauss's Law: the net electric flux flowing out of a closed surface equals the charge enclosed by that surface. Ramo et al. 1984, pg 7.

vector[2], the electric potential generated by an electric fish becomes, appropriately enough, a solution of Poisson's equation (Ramo et al. 1984, pg 36):

$$-\nabla^2\Phi = \frac{\rho}{\varepsilon} \qquad \Phi(\mathbf{x}) = \text{potential at point } \mathbf{x}, \ \rho(\mathbf{x}) = \text{charge density at } \mathbf{x}$$

In good conductors, where displacement current is negligible compared to conduction current, including the conductivity $\sigma(\mathbf{x})$ results in an equation for current source densities:

$$-\nabla\cdot\sigma\nabla\Phi = \sigma\frac{\rho}{\varepsilon} = f \qquad \sigma(\mathbf{x}) = \text{conductivity}, \ f(\mathbf{x}) = \text{current source density}$$

This holds for any point **x**. Our goal can now be stated as a boundary value problem: solve for the potential and electric field, given the geometry of the boundaries (e.g., the fish skin), the conductivities corresponding to the fish, water and external objects, and the current source density generated by the electric organ (see Figure 1). Note that in the following derivation the domain is broken up into regions of homogeneous, isotropic conductivity, so that σ is always constant under integration.

Figure 4.1 Domains of the electric fish BVP

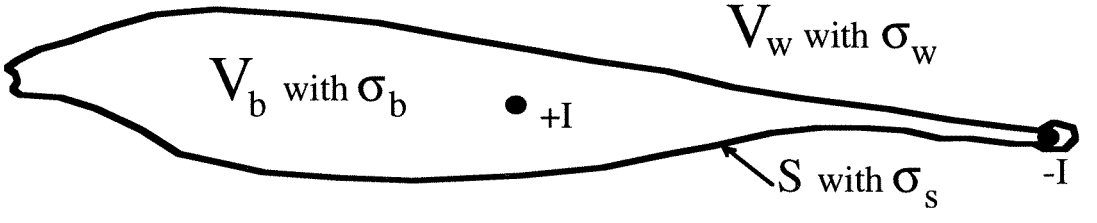

$\mathbf{V_b}$ = volume inside fish, conductivity σ_b

$\mathbf{V_w}$ = volume outside fish, conductivity σ_w

S = boundary layer (fish skin), conductivity $\sigma_s(\mathbf{x})$

I = point current sources representing electric organ

[2]The electric field vector equals the negative gradient of the scalar electric potential: $\mathbf{E} = -\nabla\Phi$.

The electric fish boundary value problem is very difficult to solve with analytical techniques, due to the irregular boundary shape of the fish's body. Instead, the advent of modern computers has made possible numerical methods that divide the problem into smaller pieces, removing geometrical limitations. One such approach, utilizing the calculus of variations, is followed in the sections below. From the variational approach, I derive and contrast two candidate methods, the finite element and boundary element methods, before choosing the latter for my purposes.[3]

4.2.1 Variational method

In variational methods of solution, the problem is recast by multiplying both sides with a test function $\psi(\mathbf{x})$ and integrating over each homogeneous volume in space V with boundary S (for more details, see Strang and Fix 1973; Weinstock 1974):

$$-\sigma\nabla^2\Phi = f \qquad \longrightarrow \qquad \int_V \psi\left[-\sigma\nabla^2\Phi - f\right]dV = 0$$

Next , after noting that:

$$\nabla\cdot(\psi\nabla\Phi) = \nabla\psi\cdot\nabla\Phi + \psi\nabla^2\Phi \longrightarrow -\psi\nabla^2\Phi = \nabla\psi\cdot\nabla\Phi - \nabla\cdot(\psi\nabla\Phi)$$

and applying the Divergence Theorem[4] to the rightmost term:

$$\int_V \nabla\cdot(\psi\nabla\Phi)\,dV = \oint_S \psi\nabla\Phi\cdot\mathbf{n}\,dS = \oint_S \psi\frac{\partial\Phi}{\partial n}dS$$

we arrive at the variational form ($\mathbf{n}$ is the outward normal to S):

$$\int_V \left[\sigma\nabla\psi\cdot\nabla\Phi - \psi f\right]dV - \oint_S \psi\sigma\frac{\partial\Phi}{\partial n}dS = 0 \qquad (1)$$

Equation 1 is also called the "weak" form because differentiation has been transferred from Φ to ψ, weakening the continuity requirements on Φ. The motivation for this approach follows in the next section.

---

[3]Before applying these tools to electric fish, I had to first understand their appropriate use and limitations.
[4]Divergence theorem: the volume integral of the divergence of any vector function throughout a volume is equal to the surface integral of that vector flowing out of the surrounding surface. See Ramo et al., page 33.

4.2.2 Physical interpretation of variational method

Since electrostastic systems are conservative, the solution to the given boundary value problem is both unique and possesses a minimum of potential energy consistent with its constraints. The potential energy U_E in an electric field can be represented as the work needed to set up the charge distribution creating the field (neglecting boundaries; Jackson 1975, pg. 46):

$$U_E = \frac{1}{2}\int_V \varepsilon(\nabla\Phi)^2\, dV = \frac{1}{2}\int_V \rho\Phi\, dV \qquad (2)$$

If U is now treated as a function of Φ, and Φ is allowed to vary independently, then the actual solution can be stated as that which minimizes the potential energy with respect to variations in the potential. However, rather than minimize U directly (which contains self energy terms; Jackson, pg. 47), it is simpler to instead consider the related quadratic functional $I(\Phi)$, constructed to have a minimum when Poisson's equation is satisfied (Strang and Fix 1973):

$$I(\Phi) = \frac{1}{2}\int_V \varepsilon(\nabla\Phi)^2\, dV - \int_V \rho\Phi\, dV$$

To solve for Φ, minimize $I(\Phi)$ with respect to variation $\delta\Phi$ in Φ by setting $\delta I = 0$:

$$\delta I(\Phi) = \frac{\partial I}{\partial \Phi}\,\delta\Phi = \int_V \varepsilon\nabla(\delta\Phi)\cdot\nabla\Phi\, dV - \int_V \rho\,\delta\Phi\, dV = 0$$

Now let the test function ψ = the variation in $\Phi = \delta\Phi$, and multiply both sides by σ/ε:

$$\int_V \sigma\nabla\psi\cdot\nabla\Phi\, dV - \int_V \psi f\, dV = 0$$

This is equivalent to Equation 1, the variational form (except for boundary terms, deleted here for simplicity). In physical terms, this process corresponds to varying Φ until the power loss in the conducting medium (left term) equals the power being input to the domain (right term and boundary terms).

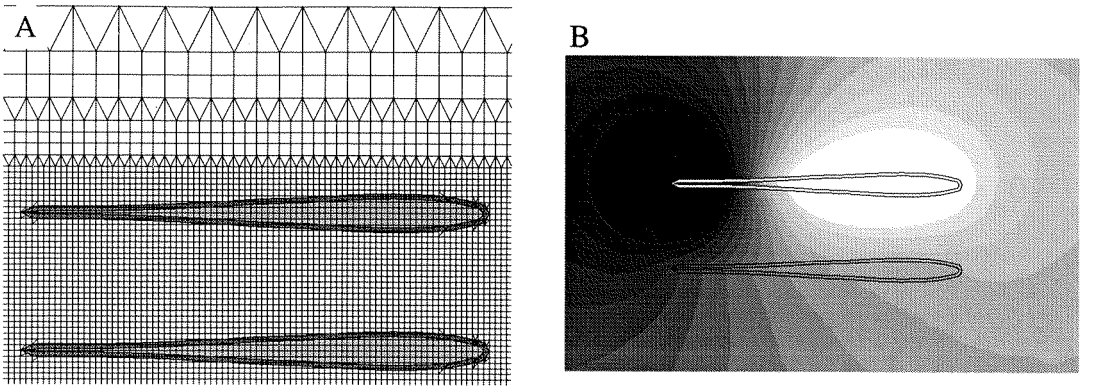

Figure 4.2 Finite element model mesh (A), and results for dipole in top fish (B).

4.2.3 Finite Element Method

In engineering fields today, the most widely used application of the variational form is through the Finite Element Method (FEM; for mathematical details see Reddy 1984). This powerful method breaks the problem domain into many smaller, different sized elements with homogeneous conductivities, which facilitates treatment of irregular shapes, such as the fish boundary in Figure 2a. Nodes defining the element vertices can be efficiently spaced to give higher spatial resolution in the areas of interest, close to the fish's body, where the potential gradient is largest and where errors due to discretization would be most severe. $\Phi(\mathbf{x})$ over each element can be approximated as a linear combination of nodal values Φ_i, using linear interpolation functions:

$$\Phi(\mathbf{x}) = \sum_i N_i(\mathbf{x})\, \Phi_i$$

The linear interpolation functions are local to a node and its neighbors along edges (N_i in Fig 6a), and zero elsewhere. The variational form of Poisson's equation is then applied to each element separately. If we vary Φ on a single node at a time, the resulting test functions ψ become simply the interpolation functions:

$$\frac{\partial I}{\partial \Phi_i} = \frac{\partial I}{\partial \Phi}\frac{\partial \Phi}{\partial \Phi_i} = \frac{\partial I}{\partial \Phi} N_i \qquad \longrightarrow \quad \psi(\mathbf{x}) = N_i(\mathbf{x})$$

For each node (i) of the element (e), we can substitute for Φ and ψ and write one equation:

$$\int_{Ve} [\sigma \nabla N_i \cdot \nabla \sum_j N_j \Phi_j - N_i f] dVe \; - \; \oint_{Se} N_i \sigma \sum_j \Phi_j \frac{\partial N_j}{\partial n} \; dSe \; = \; 0$$

Rearranging the integrations with summations:

$$\sum_j \Phi_j \, \sigma \int_{Ve} \nabla N_i \cdot \nabla N_j \; dVe \; - \; \sum_j \Phi_j \oint_{Se} N_i \, \sigma \frac{\partial N_j}{\partial n} \; dSe \; = \; \int_{Ve} N_i f \; dVe$$

Note the surface integral terms can be ignored: when combined with neighboring elements, they will cancel out for interior elements, and be zero on the domain boundary (e.g., the tank walls block all current). The remaining volume integrands are only dependent on given values, so can be integrated easily to calculate coefficients:

$$\sum_j \Phi_j \, \sigma \, A_{eij} \; = \; F_{ei}$$

The summation has only a few nonzero terms - one for each node defining the element. The resulting equations are combined for all elements to form a linear system, with scalar coefficients defining local interactions between adjacent nodes. The coefficients are functions of the geometry and interpolation functions alone. Each node potential value Φ_i is an unknown representing one independent degree of freedom, so there are as many equations as there are nodes. The resulting system matrix is usually very large and sparse, symmetric and banded, and can be solved using a variety of standard iterative techniques.

The FEM simulator produces high resolution solutions in 2-dimensional domains, such as the midplane of the fish, and we have used it to simulate the effects of body bending and nearby objects, as well as the effect of one fish upon another (Fig. 2b). However, 2-d solutions assume no variation in the third dimension, and hence are inherently skewed from the actual 3-d fields. Realistic 3-d FEM models of irregular fish shapes with very thin skin layers are very difficult to construct: to achieve the desired resolution, the elements, now solid polyhedra, have to be very small and dense around the body, especially in the skin layer. Since the nodes and elements must completely fill the

problem domain, their numbers increase drastically, so the efficiency of this method scales very poorly for 3-dimensional problems. To avoid these difficulties, we must revisit the variational form to look for a different approach.

4.2.4 Boundary Element Method (3 dimensional)

A second integral approach, currently gaining acceptance and popularity in 3-d problems, is to further manipulate the variational form to allow the use of boundary elements. In the Boundary Element Method[5] (BEM), the Divergence Theorem is applied again to the to the first term in Equation 1:

$$-\int_V \Phi \nabla^2 \psi \; dV + \oint_S \left[\Phi \frac{\partial \psi}{\partial n} - \psi \frac{\partial \Phi}{\partial n}\right] dS - \int_V \frac{1}{\sigma} \psi f \, dV = 0 \qquad (3)$$

Equation (3) can also be directly derived from Poisson's equation by applying Green's Theorem (see Jackson 1975, pages 40-45).

Now pick a fixed point **p** in the domain, and define the variation $\psi(\mathbf{x})$ to be the potential of a unit point charge in 3-d[6]:

$$\psi(\mathbf{p},\mathbf{x}) = \frac{1}{|\mathbf{p} - \mathbf{x}|} \quad \therefore \quad \nabla^2 \psi = -4\pi \delta(\mathbf{p} - \mathbf{x})$$

where δ is the Dirac delta function. This is analogous to varying $\Phi(\mathbf{p})$ by adding a unit test charge at point **x**. Substituting for $\psi(\mathbf{x})$ in equation (3), the left most term becomes:

$$-\int_V \Phi \nabla^2 \psi \; dV = \int_V \Phi \, 4\pi \, \delta(\mathbf{p} - \mathbf{x}) \; dV = \begin{cases} 4\pi\Phi(\mathbf{p}) & \mathbf{p} \text{ inside V} \\ 0 & \mathbf{p} \text{ outside V} \end{cases}$$

However, we want to pick points on the surface S, in order to create a system of coupled equations. What happens when **p** is on the boundary itself? We must consider both the volume integral and the surface integrals because the integrand becomes singular when $\mathbf{p} \rightarrow \mathbf{x}$ for **x** on S.

---

[5]Here I follow the method outlined in Williams et al. 1990. For mathematical details, see Brebbia et al. 1984 or Tang 1988.

[6]Also called a Green's function: the fundamental solution of Poisson's equation from a unit charge (Jackson 1975, page 43).

The surface integrands can be shown to be only weakly singular, so they can be integrated over, in the following limit process (as in Brebbia et al. 1984 or Hayami 1992). S is modified by adding a small sphere to V, centered at **p** with radius α (Fig. 3). Point **p** is then within V, so the volume integral evaluates to 4π. The surface integral is broken up into 2 parts, over S_1 and S_2, so the singularity must only be considered on S_2 in the limit as $\alpha \rightarrow 0$. If we let $r = |\mathbf{p} - \mathbf{x}|$, then using local spherical coordinates on S_2 yields:

$$\int_{S_2} \left[\Phi \frac{\partial}{\partial n} \frac{1}{r} - \frac{1}{r} \frac{\partial \Phi}{\partial n} \right] dS_2 = \int_{S_2} \left[\Phi \left(-\frac{1}{r^2}\right) - \frac{1}{r} \frac{\partial \Phi}{\partial r} \right] r^2 \cos\phi \, d\phi \, d\theta$$

$$= \int_{S_2} \left[-\Phi - \alpha \frac{\partial \Phi}{\partial r} \right] \cos\phi \, d\phi \, d\theta \underset{\text{as } \alpha \rightarrow 0}{\longrightarrow} -\Phi(\mathbf{p}) \int_{S_2} \cos\phi \, d\phi \, d\theta$$

The remaining integral equals the solid angle external to the surface at **p**, ranging from 0 to 4π sterradians, and it gets subtracted from the 4π of the volume integral (for smooth surfaces this evaluates to 2π). Therefore, in the limit as $\alpha \rightarrow 0$ and $S_1 \rightarrow S$, the full equation can now be written as:

$$\Phi(\mathbf{p}) A(\mathbf{p}) + \oint_S \left[\Phi \frac{\partial}{\partial n} \frac{1}{|\mathbf{p} - \mathbf{x}|} - \frac{1}{|\mathbf{p} - \mathbf{x}|} \frac{\partial \Phi}{\partial n} \right] dS = \int_V \frac{f}{\sigma |\mathbf{p} - \mathbf{x}|} dV \qquad (\star)$$

where $A(\mathbf{p})$ is a scalar coefficient equal to the interior solid angle (i.e., depending only on the geometry of the surface at **p**). The remaining volume integral contains known values and so is moved to the right-hand side. The unknowns Φ and Φ_n are then only needed for the surface integrals on S. This means that nodes need only be placed on boundary surfaces, drastically cutting down on the number of nodes needed compared to finite element methods, and resulting in a much smaller but fully connected matrix.

Equation $\star$ holds for each domain with homogeneous conductivity. In the case of the electric fish, we can apply it to two regions: inside the body and out in the water. In the water the right-hand side is zero since there are no current sources.

Figure 4.3 Limit process to handle singular integrals

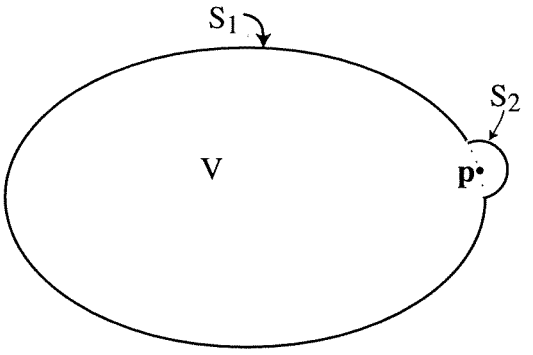

A. Augmented surface boundary

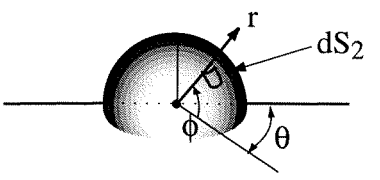

$dS_2 = r^2 \cos\phi \, d\phi \, d\theta$

radius $r = \alpha$

$$S = \lim_{\alpha \to 0} (S_1 + S_2)$$

B. Local spherical coordinates over S_2

Figure 4.4 Boundary conditions across skin layer

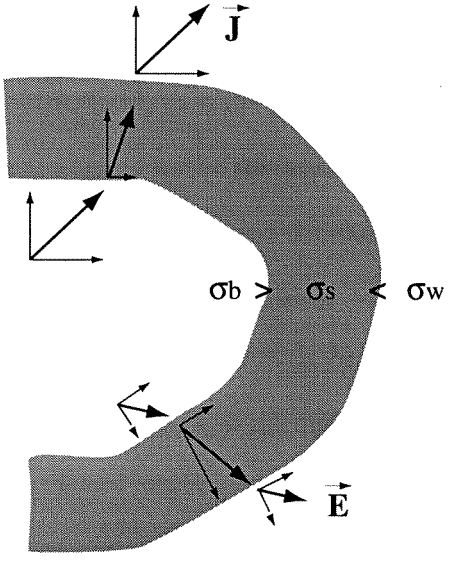

A. Since the lower conductivity of the fish skin (gray) bends the field vectors more perpendicular to the surface, and the skin is very thin (not drawn to scale), the normal current density can be assumed constant.

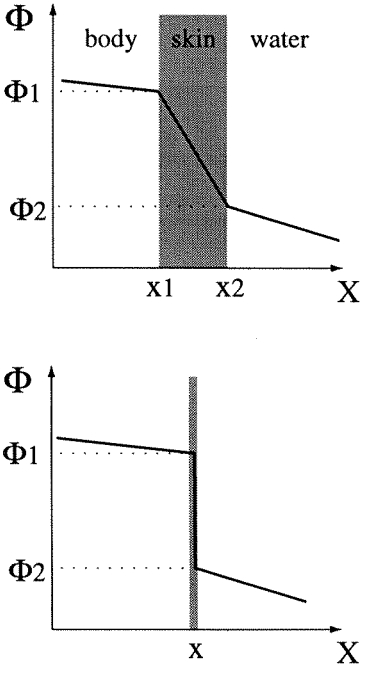

B. One dimensional cross section (top), and monolayer approximation (bottom).

Defining and discretizing the boundary layer

Discretizing the surface of the fish requires a tradeoff: resolution vs complexity of the surface elements. Linear elements are easiest to deal with, since analytic solutions exist for the complex integrals, but they result in a faceted surface and discontinuities in the electric field. The normal surface vector, needed for accurate results in general, is ill-defined at the node points and along edges. For this reason most general BEM applications use higher order elements, e.g., quadratic or isoparametric (see Hayami 1992). I wanted to keep the integrations and surface descriptions as straightforward and computationally efficient as possible while still getting good results; fortunately, we can take advantage of some properties of electric fish. Previous electric fish studies have shown that the skin is specialized with flattened cells to be very thin (see Fig. 2 in Szabo 1974, or Fig. 4 in Zakon 1986) and has very low conductivity. If the skin conductivity, which can vary with location on the body, is much lower than both the internal body and the external water conductivities, and the thickness is small compared to spatial variations in the electric field, then the current through the skin can be approximated to only have a component normal to the surface. Therefore, in order to simplify the BEM application to electric fish fields, I modeled the skin as a single boundary surface separating the internal body from the surrounding water. Mathematically this is effected by using the appropriate boundary conditions between the two domains (n denotes the component normal to the surface, J_n = normal current density; see Fig. 4):

$$\sigma_b E_{bn} = \sigma_w E_{wn} \qquad \text{or equivalently} \quad J_{bn} = J_{wn} = J_n$$

Furthermore, the voltage drop across the ohmic skin layer equals the current density times the resistivity:

$$\Phi_b - \Phi_w = J_n \, t \, / \, \sigma_{skin} = J_n \, / \, \sigma_{eff}$$

where t = skin thickness, σ_{skin} = bulk conductivity of skin, and σ_{eff} = effective membrane conductivity of the skin (i.e., in units of 1/[ohm cm^2]). Treating the skin in this fashion, the normal current density J_n remains constant across the skin boundary,

while the potential Φ has a discontinuous jump corresponding to the transdermal potential (the equivalent of an ideal dipole layer, Jackson 1975, pg. 41). With these approximations, inaccuracies due to the use of linear elements should be alleviated.

The boundary conditions are next substituted into equation ★ for the two volume domains, inside the fish and outside the fish (domains "b" and "w" respectively, assuming no external objects for now), and both equations are cast in terms of the external variables ($\mathbf{n}$ = outward normal from fish, A = internal solid angle, $\mathbf{p}$ = point on the boundary, J = magnitude of the outward normal current density, dropping the "n" subscript, and $r = |\mathbf{p} - \mathbf{x}|$):

Inside fish:

$$[4\pi - A(\mathbf{p})]\,[\Phi(\mathbf{p}) + \frac{J(\mathbf{p})}{\sigma_{eff}}] \;-\; \oint_S [\Phi + \frac{J}{\sigma_{eff}}] \frac{\partial}{\partial n}\frac{1}{r}\,dS \;+\; \oint_S \frac{1}{r}\frac{J}{\sigma_b}\,dS = \int_V \frac{f}{\sigma_b r}\,dV$$

Outside fish:

$$\Phi(\mathbf{p})\,A(\mathbf{p}) \;+\; \oint_S \Phi \frac{\partial}{\partial n}\frac{1}{r}\,dS \;-\; \oint_S \frac{1}{r}\frac{J}{\sigma_w}\,dS \;=\; 0$$

We next discretize the fish surface: pick N node points on S, and cover S with triangular planar elements connecting the nodes. Then again use linear interpolation of nodal values Φ_i with 2-d interpolation functions on each surface element:

$$\Phi(\mathbf{x}) = \sum \Phi_i N_i(\mathbf{x}), \quad \text{where } \Phi_i = \Phi(\mathbf{x}_i)$$

To do the same for the normal current density, J, presents a problem. Since the faceted surface has ill-defined normals at the vertices and along edges, J will also be ill-defined and discontinuous at the nodes. But we would still like a representation for J that can be interpolated from the nodal values. To resolve this I chose to define the normal at each node, $\mathbf{n}_i$, as a weighted average of all the normals of the elements having that node as a vertex[7]. Then J can be defined over each element 'e' with a correction factor:

$$J(\mathbf{x}) = \sum J_i N_i(\mathbf{x})\,(\mathbf{n}_i \bullet \mathbf{n}_e)$$

[7]Another solution to sidestep the difficulty in representation may be to express the variables in terms of Φ_b (inside the boundary) and Φ_w (outside).

where $\mathbf{n}_e$ is the normal to the element, and the summation is over all nodes in the element. (For simplicity the correction factor has been left out of the following steps.)

Substituting for Φ and J, and breaking the surface integrations into summations of element integrals, we can remove the unknown variables from the integrands:

$$[4\pi - A(\mathbf{p})][\Phi(\mathbf{p}) + \frac{J(\mathbf{p})}{\sigma_{eff}}] - \sum_{e}\sum_{j} [\Phi_j + \frac{J_j}{\sigma_{eff}}] \int_{Se} N_j \frac{\partial}{\partial n}\frac{1}{r}\, dS + \sum_{e}\sum_{j} \frac{J_j}{\sigma_b} \int_{Se} \frac{N_j}{r}\, dS = \int_V \frac{f}{\sigma_b r}\, dV$$

$$\Phi(\mathbf{p})\, A(\mathbf{p}) + \sum_{e}\sum_{j} \Phi_j \int_{Se} N_j \frac{\partial}{\partial n}\frac{1}{r}\, dS - \sum_{e}\sum_{j} \frac{J_j}{\sigma_w} \int_{Se} \frac{N_j}{r}\, dS = 0$$

Setting $\mathbf{p} = \mathbf{x}_i$ for each node i=1...N, and computing all the integrals (see Methods),

$$B_j(\mathbf{p}) = \int_{Se} N_j \frac{\partial}{\partial n} \frac{1}{|\mathbf{p} - \mathbf{x}_j|}\, dS \quad \rightarrow \quad B_{ij}$$

$$C_j(\mathbf{p}) = \int_{Se} \frac{N_j}{|\mathbf{p} - \mathbf{x}_j|}\, dS \quad \rightarrow \quad C_{ij}$$

yields a system of 2N equations with two unknowns to solve for at each node, Φ_i and J_i:

$$[4\pi - A_i][\Phi_i + \frac{J_i}{\sigma_{eff}}] - \sum_j B_{ij} [\Phi_j + \frac{J_j}{\sigma_{eff}}] + \sum_j C_{ij} \frac{J_j}{\sigma_b} = F_i$$

$$A_i \Phi_i + \sum_j B_{ij} \Phi_j - \sum_j C_{ij} \frac{J_j}{\sigma_w} = 0$$

Computing potential in the water

Once the potential, Φ_j, and the normal current density, J_j, are solved on the fish surface, the fields in the water about the fish can easily be calculated. For any point $\mathbf{p}$ external to the fish:

$$4\pi\, \Phi(\mathbf{p}) = -\sum_j B_j(\mathbf{p})\, \Phi_j + \sum_j C_j(\mathbf{p})\, \frac{J_j}{\sigma_w}$$

Adding external objects

Adding an object to the water simply requires adding nodes and elements to cover the object's surface, and results in two extra equations for each node, similar to those shown above (see Fig. 6). Note that the first boundary condition becomes $\Phi_w = \Phi_o$, and the object's conductivity (σ_o) must be used in its domain.

There are two special cases to consider: ideal insulators (σ_o=0) and highly conductive objects ($\sigma_o \rightarrow \infty$). In the case of an insulator, we know J=0 on the object surface, and so for convenience we can eliminate half the equations required for the object. Conductors, on the other hand, must be treated explicitly. Analytically, since $\sigma_o \rightarrow \infty$, $\nabla\Phi$ must vanish inside the object so that $\mathbf{J} = \sigma_o \nabla\Phi$ remains finite, and therefore Φ is a constant in the object and on its surface. However, with the approximations used in our discretized variational system, there will be small numerical errors in the coefficients after the integration. These residual errors are in effect multiplied by the conductivity, so for large σ_o the errors dominate the solution results. (Another way to say this is that Laplace's equation has practical limits for computing currents inside a highly conductive object.) The difficulty is avoided by explicitly setting all Φ_m equal for each node on the object's surface (nodes given index "m"). If there are M nodes on the object, then this gives M-1 equations and we are still missing one. The last equation is supplied by the missing current density relations - the sum of all current into the object must equal zero by Kerchoff's law. In terms of the variables used here:

$$\oint_{obj} J \, dS = 0 \quad \rightarrow \quad \sum_e \sum_m J_m \int_{Se} N_m \, dS = 0$$

4.3 Methods

From the considerations discussed above, BEM appeared more suitable than FEM to achieve my goals for 3-d electric fish simulations. Therefore I chose to develop a BEM electric fish simulator, with the particular implementation described below.

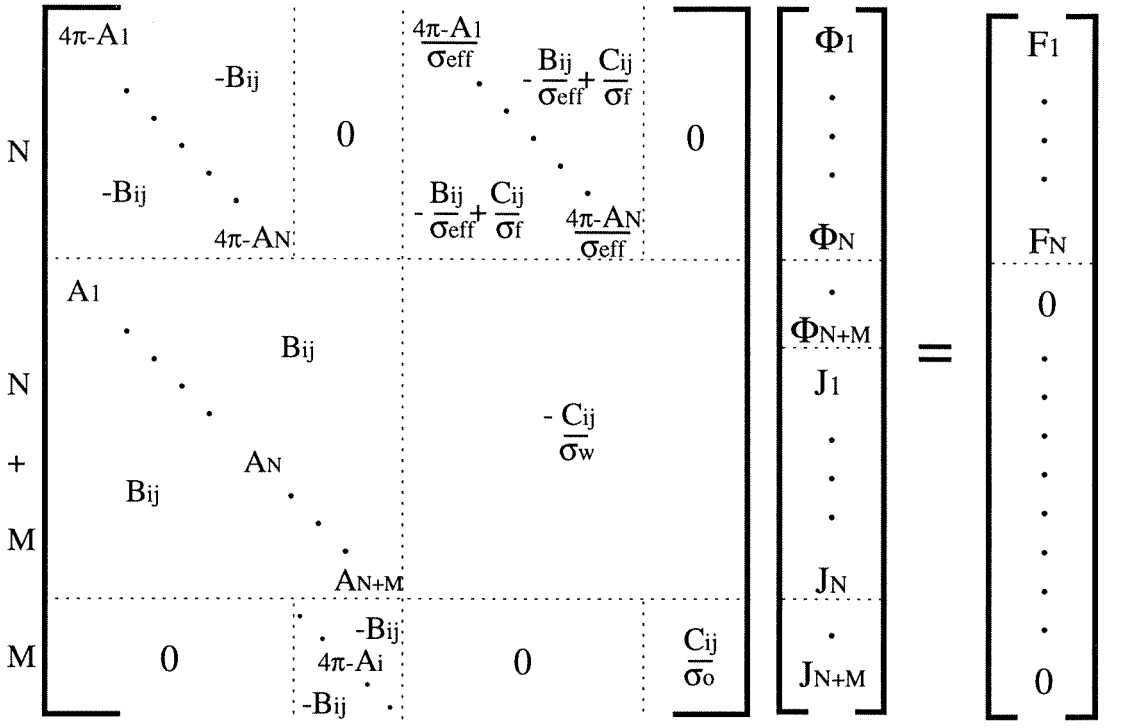

Figure 4.5 Overall system matrix with external object equations included. N = number of nodes on fish surface, M = number of object nodes

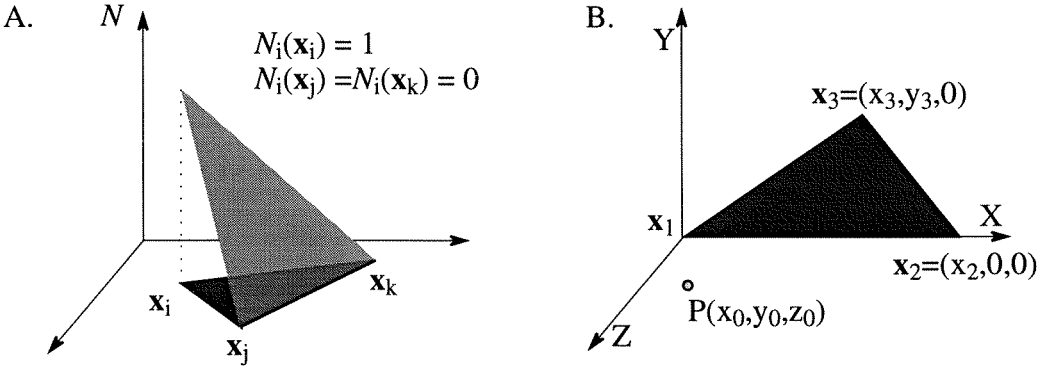

Figure 4.6 A. Linear interpolation function (light gray) for one node of a triangular element (dark gray). B. To simplify the integration, each element is first translated and rotated onto a standard template in the x-y plane.

4.3.1 Implementation of the Boundary Element Method

The implementation can be broken down into three steps: (1) computing the surface integrals to get the coefficients A_i, B_{ij} and C_{ij}; (2) composing the system matrix, adding conductivities σ_b, σ_w, $\sigma_s(\mathbf{x}_i)$, and σ_o, and computing the source integrals F_i from the sources $f(\mathbf{x})$; and then (3) solving the resulting linear system of equations (see Fig. 5).

Step 1 requires most of the work. One integration must be performed for each node-element pair. A simplifying procedure was applied to first map each element onto a standard frame of reference:

1) Let the element have vertices at $\mathbf{x_1}$, $\mathbf{x_2}$, and $\mathbf{x_3}$, where $\mathbf{x_i} = (x_i, y_i, z_i)$.

2) Translate the element so that $\mathbf{x_1}$ coincides with the origin: $\mathbf{x_1} \rightarrow (0,0,0)$.

3) Rotate the element about the Z-axis until $y_2 = 0$.

4) Rotate the element about the Y-axis until $z_2 = 0$.

5) Rotate the element about the X-axis until $z_3 = 0$.

6) Apply the same translations and rotations to $\mathbf{p}$ to maintain its position relative to the element.

After these steps, the element lies in the XY plane with one edge along the X-axis (Fig. 6b). The linear shape functions N_i for the standard triangular element are then reduced to:

$$N_1 = [\,(x_2y_3) - (y_3)x + (x_3 - x_2)y\,] / 2A,$$

$$N_2 = [\,(y_3)x - (x_3)y\,] / 2A$$

$$N_3 = [\,(x_2)y\,] / 2A$$

where $2A = 2$ (area of triangle) $= x_2y_3$.

We can now proceed to compute the integrals. Let $B_{im\upsilon}$ and $C_{im\upsilon}$ represent the integrals from the node $\mathbf{p}=\mathbf{x}_i$ over element 'm' with vertices locally labeled $\upsilon = 1$ to 3. (Each pair of indices m and υ can be mapped back to the jth node to get the contributions to B_{ij} and C_{ij}.) Then the coefficient integrals can be rewritten as:

$$B_{im\upsilon} = \int_m N_\upsilon \frac{\partial}{\partial n}\frac{1}{r}\,dS = \int_m N_\upsilon \frac{n_x (x-x_o) + n_y (y-y_o) + n_z(z-z_o)}{-r^3}\,dS$$

$$C_{im\upsilon} = \int_m N_\upsilon \frac{1}{r}\,dS$$

For the standard triangle, $dS = dx\,dy$, $n_x = n_y = 0$, $n_z = 1$, and $z = 0$:

$$B_{im\upsilon} = z_o \iint_m N_\upsilon \frac{1}{r^3}\,dx\,dy$$

$$C_{im\upsilon} = \iint_m N_\upsilon \frac{1}{r}\,dx\,dy$$

For the general case of a point $\mathbf{p}=\mathbf{x}_i$ at some distance from a given triangular element, the inner integral on X can be solved analytically (with help from the integral tables of Abramowitz and Stegun, 1965; see Appendix A). To compute the outer integral on Y, I used standard Gaussian quadrature formulas from Press et al., 1992; specifically, the ten-point Gauss-Legendre integration routine on page 133. A different approach is needed whenever the point $\mathbf{p}=\mathbf{x}_i$ is one of the vertices of the given element: r=0 at the point in question and the integrands become singular. However, in that case $B_{im\upsilon}=0$ since $z_o=0$, and $C_{im\upsilon}$ can be computed analytically. The analytic solutions have been published previously (Jin and Tullberg 1985, pg. 2-23), but I also derive them in a more appropriate form for my use in Appendix A.

Before composing the system matrix, the coefficients A_i and F_i must also be computed. F_i is strightforward: since the current source density inputs are all point sources, the right hand side integrals reduce to simple sums over all the sources. A_i, corresponding to the internal solid angle at node $\mathbf{x}_i$, requires a bit more work to compute for non-smooth surfaces. If node 'i' is translated to the origin of a unit sphere, and all of its connected elements are extended through the sphere's surface, then A_i is equal to the intersected surface area. With the faceted surfaces used here, the intersected area becomes a spherical polygon which can be decomposed into a sum of spherical (or

geodesic) triangles. The uses of these objects are thoroughly treated in textbooks on analytic geometry or spherical trigonometry: the area of a spherical triangle is proportional to the excess over 180° of the sum of its angles (Salmon 1914; Rider 1942). Therefore A_i can be computed from the sum of the angles formed in the intersection (see Appendix A for details).

The final step to solve the equations is straightforward. The models I use typically have 256 nodes to define the skin surface, and result in well-conditioned linear systems of 512 equations with 512 unknowns. Gaussian elimination works efficiently, implemented with LU decomposition and then backsubstitution from standard formulas (Press et al. 1992).

4.3.2 Use of the BEM simulator

The following steps describe the use of the BEM simulator (refer to flow chart in Fig. 7). All input and output files are in ascii format to preserve platform independence:

1. The first input is a model mesh, consisting of a closed surface which separates the two volume domains. Two text files are required, <modelname>.nodes and <modelname>.elems. The first line of each contains the integer number of nodes (N) or elements (M) that follow in the file, one per line. Each line in the nodes file defines a node with 3 floating point numbers corresponding to the (x y z) coordinates in units of cm. Each line in the element file contains 3 integers, with each integer denoting a node number by its position in the nodes file. The order of the 3 nodes must be directed so that they are arranged counterclockwise when seen from outside of the closed surface (i.e., traversing the element edges from first node to third results in a right hand screw pointing out of the surface).

2. The second input is a conductivity file, with the name <modelname>.conds. The first line contains the conductivity of the internal body and the external water, in units of S/cm (1/Ωcm). If the skin conductivity is constant, then it also goes on the first line, but in units of S/cm^2 ($1/\Omega cm^2$). If it varies with location, then N lines must follow,

containing the conductivity at each node of the mesh, one per line in the same order as the nodes. All values should be floats.

3. The final input is a sources file, <sourcename>.sources. The first line contains the interger number of sources (S) and the number of phases (P, sequential in time). The next S lines contain the (x y z) coordinates of the sources in cm. They should all lie within the model fish. The final SxP lines contain the source values at each phase in time, with P sequential blocks of S lines each in the same order as the sources. Units for the current sources are mA.

4. The simulator was written in C, and has been compiled and run on several different systems (codenamed "MacBEM" on Macs, or "fishbem" in Unix or Iris workstations). When the program is executed, it will read the model files, calculate the surface integrals, arrange the overall matrix and perform the LU decomposition[8]. The user is then repeatedly prompted for source file names. For each source file given, the results are calculated and saved in text files called <sourcename>.matsol and <sourcename>J.matsol, corresponding to the potential outside the skin and normal current density through the skin at each node. The files are both NxP lines long and have units of mV and mA/cm^2 respectively. The data is saved in P sequential blocks of N lines each.

5. After solving for the potential and current density at the fish surface, the potential in the water about the fish can be computed with a second program (codenamed "bempart3"). The input is a file with the desired locations, named <modelname>.map. This is set up exactly like the <modelname>.nodes file, except each line is now the location of a point outside the fish. The program first computes all integrals, then prompts for the matsol file tags, and finally computes the forward matrix multiplication to arrive at the result. The solution is saved to a file named <matsolname>mp.matsol, in the same format as the other matsol files.

[8]For a typical fish mesh of 256 nodes and 508 elements, solving the coefficient integrals takes about 30 seconds on a PowerMac 8500/120, with another 30 seconds needed for the LU decomposition.

Figure 4.7 BEM Flowchart

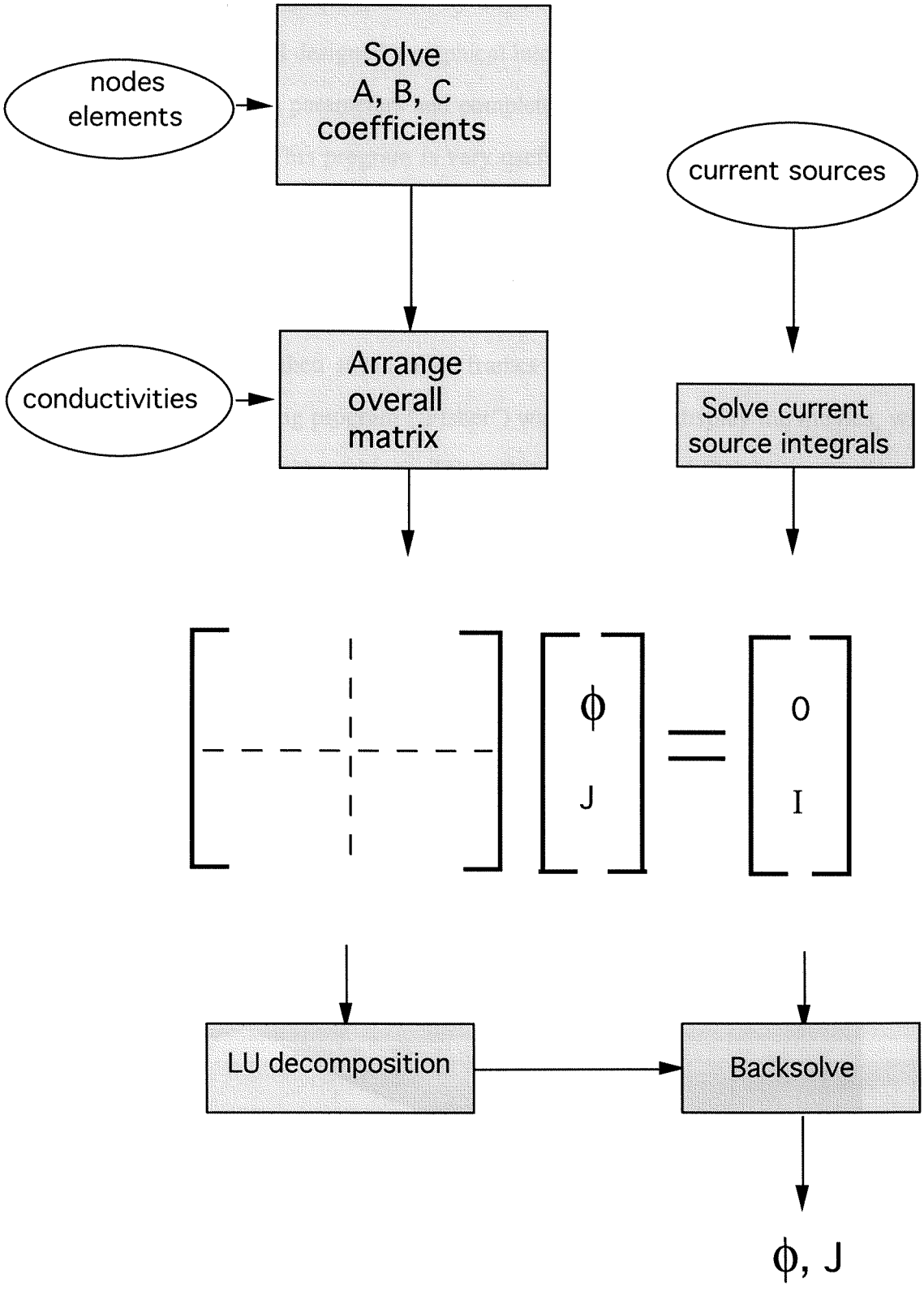

4.3.3 Visualization of simulation results

The mesh and other input files were created and the results analyzed using MATLAB (The MathWorks Inc.), aided by three custom built applications to view the results and make movies. I designed a graphical interface on an SGI workstation to allow user control of simulation parameters and complete 3-d visualization of the model and field solutions (Fig. 8). This program is very useful for verifying the model mesh and bending it to fit desired configurations. The other two applications are designed to create and view movies of fish mappings and simulations on Apple Macintoshes. The movie maker, called "Vu", uses a Delaunay triangulation to linearly interpolate between points in an irregular grid, and then saves color frames of each phase of the electric organ discharge. Another viewing program ("Fisher") was written to display the movies, with information included about the subject. The software and several Quicktime movies are available on our Web pages (www.bbb.caltech.edu/ElectricFish).

Figure 4.8 Irisvu user interface

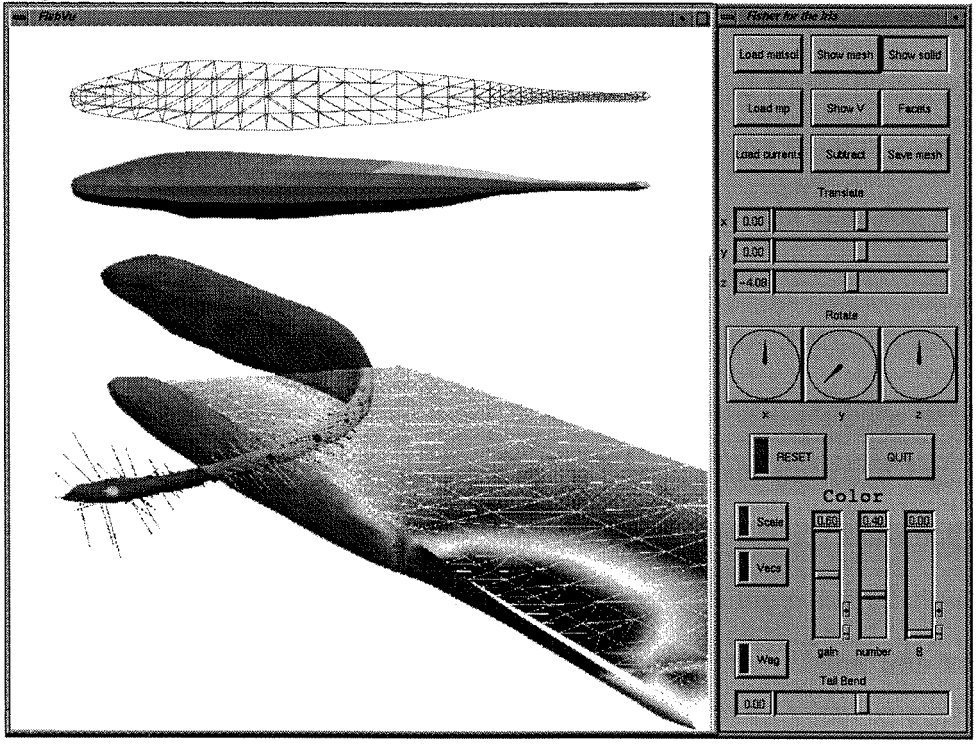

4.4 Test results

To test the simulation results I chose 5 simple cases which I could compare to analytical solutions. All model data (nodes, elements, and source files) were generated in MATLAB and exported to run on the simulator. Simulation results were then imported back into MATLAB for analysis.

4.4.1 Insulating sphere in constant field

A 1 cm radius insulating sphere (σ= 0), composed of 242 nodes and 480 triangular surface elements, was centered about the origin. To approximate a constant electric field near the origin, distant current sources were placed on either side of the object. 18 current sources of 1 mA magnitude were placed in two arrays, 9 negative sources in the plane x=-10 cm and 9 positive sources in the plane x=10 cm. Each array was arranged as a 3x3 grid on a 8x8 cm square (Fig. 9a). Two cases were then simulated, the first with the 1 cm object present, and the second with the object's size divided by 1000 (to approximate the field with no object present), so the difference between solutions represents the effect of the object. The analytic solution, an induced dipole field, was computed by first calculating the superposed potential from all sources alone, then using the result to calculate the electric field at the origin, and finally calculating the change in potential caused by an insulating sphere in a constant field (Jackson 1975, pgs. 149-152, or Ramo et al. 1984, pgs. 378-380; see also Bacher 1983):

$$\Delta\Phi = -1/2\ [a^3\ \mathbf{E}\cdot\mathbf{r} / r^3]$$

where a is the radius, **E** is the electric field vector with no object present, and **r** is the vector from the origin to the observation point. The results are shown in Fig. 9. The electric field created by the current sources alone matches the analytic field solution (Fig. 9b), which it should because it uses the same equations. From the potential along the x-axis the field at the origin was estimated to be -1.10 mV/cm. Using this value the potential perturbation due to the sphere was approximately 5% higher than found in the

simulation. The discrepancy is mainly due to the approximate mesh used to model the sphere: the analytic solution derived from a perfect sphere has magnitude proportional to volume (the a^3 constant), while the model sphere was composed of triangular facets that slightly reduced the actual volume. If we consider each element to form the base of a pyramid with the apex at the origin, and the volume of a single pyramid is 1/3 (area of base)(height), then the volume of the model "sphere" was 4.05 cm^3, while an ideal 1 cm radius sphere has volume $4\pi/3$ or 4.19 cm^3, greater by 3.4 %. The second largest source of error was that the electric field from the current sources is not exactly uniform near the origin and is highest along the x-axis. Both of these factors will systematically lower the numerical solution from the ideal case. Using E = -1.05 mV/cm in the analytic solution results in a much better match (Fig. 9c-e). Note this test only confirms the accuracy of the B integrals, because all of the $\partial\Phi/\partial n$ terms were forced to zero.

4.4.2 Conducting sphere in constant field

To test the C integrals, the sphere was next made conducting. The analytic solution is still dipolar, but now in the opposite direction and twice the magnitude:

$$\Delta\Phi = [a^3 \mathbf{E}\cdot\mathbf{r} / r^3]$$

The results are shown in Fig. 9c-e. The potential in the water outside of the sphere was about 10% greater than the analytic solution. The solution at the surface showed that the potential was very accurate but the normal currents varied from the ideal, and were too large at the peaks. This error in current solution was further explored by rerunning the simulation with different numbers of nodes and elements comprising the sphere. The error increased with the number of nodes, because the system matrix condition number increased. Meshes of 18 and 66 nodes had smaller deviations in the error distribution. The current error was also dependent on the choice of elements; however, the error in potential outside of the object was within 10% of the analytic solution for all three meshes tested. This error is on the order expected from the use of linear elements and the faceted surface approximation of an ideal sphere.

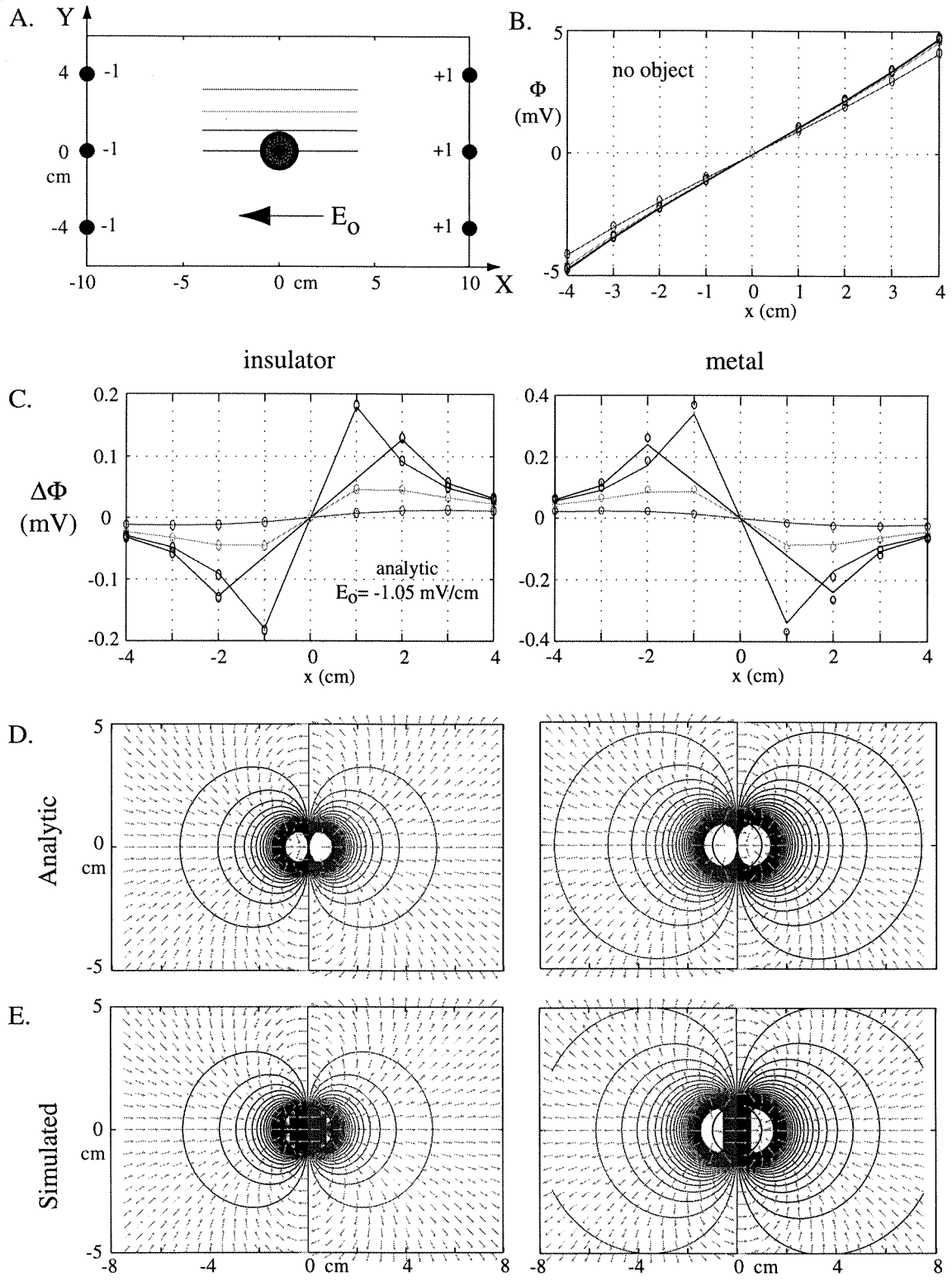

Figure 4.9 Simulations of spherical objects in constant electric field (see text). A. Model setup. B, C. 4 data sets plotted from along the lines shown in A (line= analytic, circles= simulated). D, E. Potential contours from object dipole (20 μV steps).

4.4.3 Monopole in transparent spherical skin

The next test was to add a skin boundary. I first simulated a 1 mA monopole inside a 1 cm radius spherical skin, with the conductivities of internal body, external water and bulk skin all set equal to $\sigma_w = 1/(2\ k\Omega cm)$. Since the skin is approximated as a monolayer of zero thickness, the transparent effect is accomplished by setting the equivalent skin membrane conductivity to a very large number, so that it adds no impedance between body and water. The analytic solution is that of a single point source, with radially symmetric current flowing to infinity, so there should be constant potential and current density magnitude everywhere on the surface. If the radius of the sphere is again 'a', then the potential and normal current density at the outer skin surface are:

$$\Phi = I/4\pi\sigma a \quad \text{and} \quad J = I/4\pi a^2$$

Results from the skin surface are shown in Figure 10 (left column). The potential solution is exact, but the current density is very noisy for this degenerate case. Differences between currents again correspond to differences in the set of elements. This monopole in a sphere model avoids the worst errors due to the approximate method by which the current density vectors are represented, since the average normals at vertices are approximately aligned with the radial current vector.

4.4.4 Monopole in low conductivity skin shell

Using the same spherical mesh and current source as in 4.4.3, I reset the conductivities to approximate those found in the fish: in the water $\sigma_w = 1/(2\ k\Omega cm)$, in the "body" $\sigma_b = 1/(100\ \Omega cm)$, and the skin was given a constant membrane conductance $\sigma_s = 1/(4\ k\Omega cm^2)$. In this case the approximation of the skin's normal vector should again be very accurate since all of the current is directly radially, perpendicular to the surface. The analytic solutions for J and Φ are the same as before (since the current source is ideal and the external conductivity did not change, only the potential inside the sphere and across the skin should change). The simulated results are now accurate to within 5-10% for both potential and current density (Fig. 10, right column).

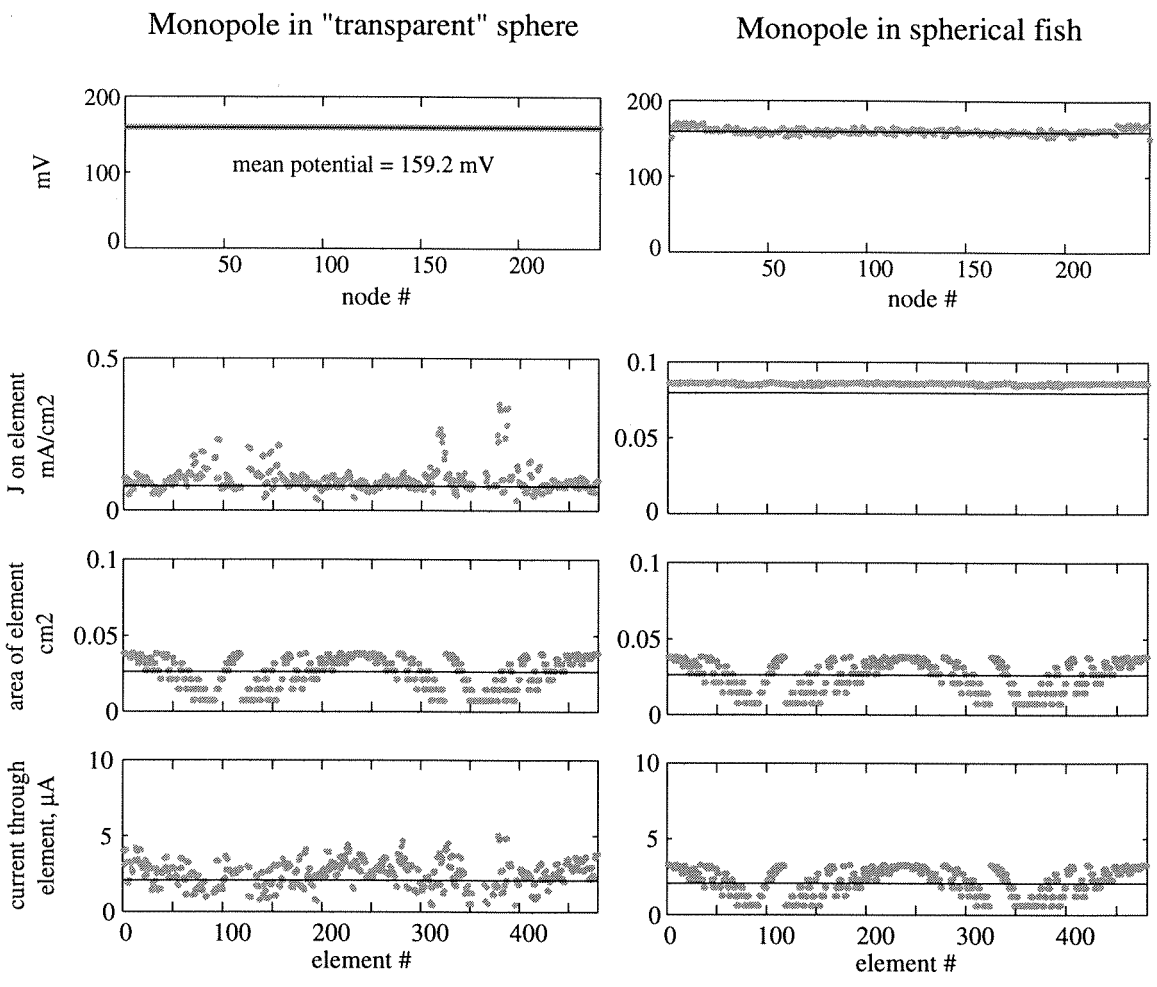

Figure 4.10 Results for test cases 4.4.3 (left column) and 4.4.4 (right column). From top to bottom: potential on surface at the node points; normal current density in the midpoint of each element; area of each element; current through each element. The black lines indicate the ideal values for a true sphere with all elements given equal area. With the realistic conductivities of test case 4.4.4 (right column), the mean simulated potential was 160.2 mV (0.66% higher than the analytic solution), the mean current density was 85.7 $\mu A/cm^2$ (7.7% higher), and the total current out of the skin was 1.059 mA (5.9% too high). The total surface area of the facted model sphere, composed of 242 nodes and 480 elements, was 12.35 cm^2 or 98.25% of a true sphere of 1 cm radius.

4.4.5 Dipole in transparent spherical skin

To try to quantify the accuracy of the skin approximation, I needed to test a more realistic fish, i.e., one in which the field is not exactly normal to the skin surface. However, the lack of analytic solutions for thin shelled, asymmetric boundaries makes this difficult. One way to test the effect of the skin is to assume a worst case scenario: use a dipole source configuration inside the electrically transparent sphere from 4.4.3 (see Figure 11). The analytic dipole field is easily calculated, and produces fields that enter and exit the spherical skin layer at many different angles to the surface. Two sources, +1 amd -1 mA, were placed on the X-axis at +1 mm and -1 mm, respectively. Since the source separation is small compared to the radius, the dipole fields can be approximated as (Ramo et al. 1984, pg 25):

$$\Phi(\mathbf{r}) = \mathbf{D}\bullet\mathbf{r} / (4\pi\sigma r^3), \qquad \mathbf{E}(\mathbf{r}) = -\nabla\Phi(\mathbf{r}) = (1/4\pi\sigma)\,[3(\mathbf{D}\bullet\mathbf{r})\mathbf{r}/r^5 - \mathbf{D}/r^3]$$

where the dipole moment $\mathbf{D}$= (source strength) x (source separation). The simulated potential in the water outside the sphere is about 5% off and varies with the number of nodes, again illustrating the systematic error due to the representation of the current density vectors (Fig. 11).

4.5 Conclusions

Test cases 1 and 2 tell me external objects can be accurately simulated, tests 3 and 4 show the simulation works well for radially symmetric problems, and case 5 shows that when the skin assumptions are deliberately violated, the simulation results may be systematically off by about 5%. The results appear good as long as we stick with (1) fish skin that is very thin and much higher resistivity than the body and water, (2) external objects that are either good insulators (normal current is zero) or good conductors (current normal to surface), and (3) only a small number of nodes on the external object when it is a good conductor (since the matrix becomes ill-conditioned with more nodes).

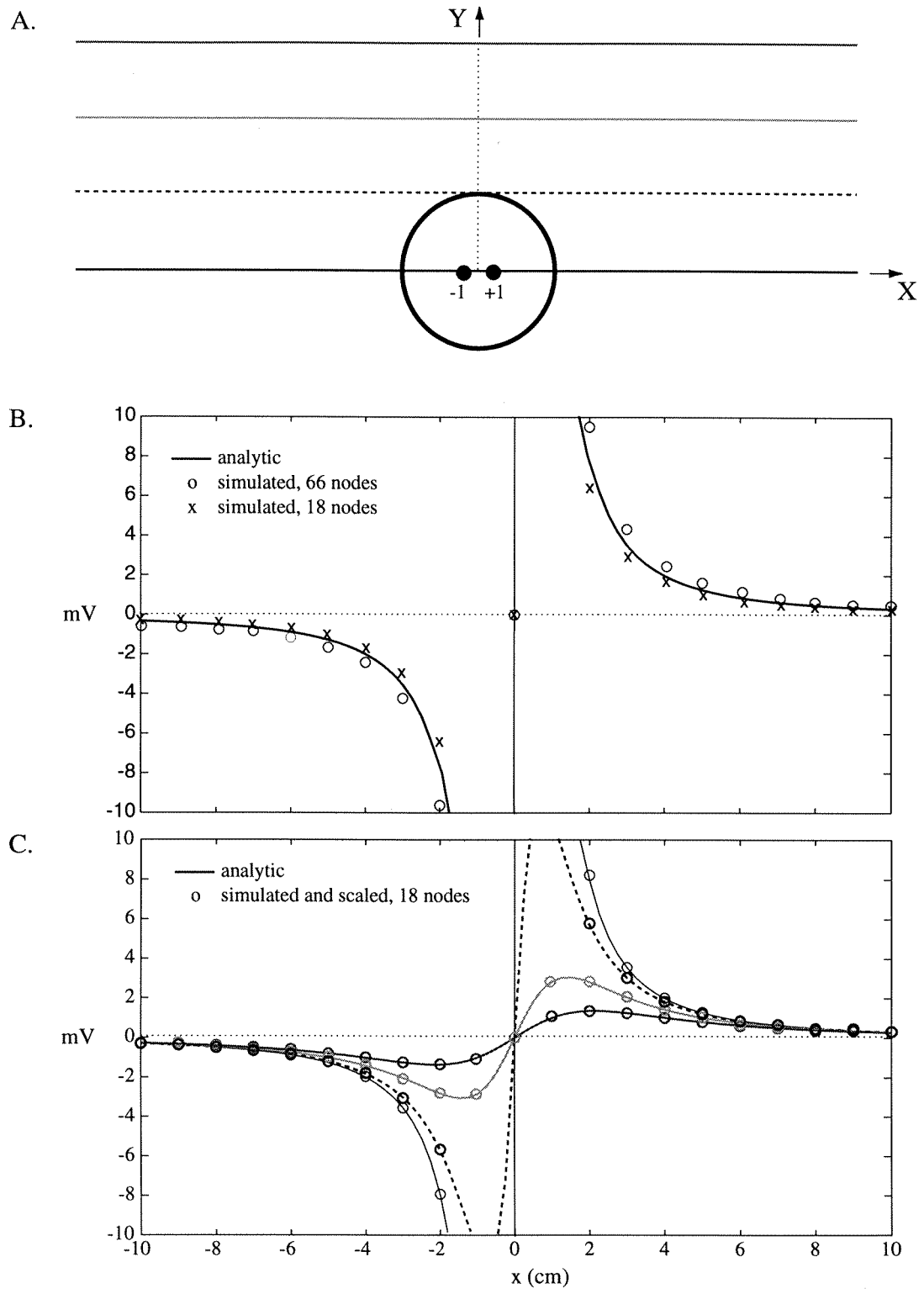

Figure 4.11 Dipole in spherical fish, from test case 4.5. A. Model setup. B. Potential plotted in the water from points along the X-axis. The errors in solutions from both 18 node and 66 node meshes were below 10%, but of opposite sign. C. Scaling the 18 node solution by a constant fits the shape of the analytic solution (on the lines in A).

Do these "good" results confirm the sufficiency of the simulator? We must examine the goals again – I am interested in how field distortions due to objects and body movements change the electric field measured across the skin. The fish model conductivities and current sources can theoretically be optimized to produce results matching the field measurements (of Chapters 2 and 3) to any arbitrary precision, given the freedom to arbitrarily arrange current sources inside the body. If (1) the sources are realistically constrained by data on the electric organ, (2) the skin conductivity is set realistically from reported measurements, and (3) the potential and normal current density near the skin surface still match the field measurements, then the current through the skin multiplied by the skin conductivity should accurately represent the stimuli to the receptors. The model can be further assessed by optimizing to measured fields in one configuration (e.g., straight tail), and then comparing simulation to measurements in a second configuration (e.g., bent tail). The final assessment of the simulator's utility awaits in Chapters 5 and 6.

"...that Torpor or Numbness which he at times induces, and from which he takes his name, was ... imitated with artificial electricity, and shewn to be producible by a quick succession of minute shocks. This in the Torpedo may perhaps be effected by the successive discharge of his numerous cylinders, in the nature of a running fire of musketry; the strong single shock may be his general volley."

John Walsh, 1773

5 Electric Fish Simulations

5.0 Summary

A high resolution boundary element method (BEM) program was developed to simulate the electric organ discharge (EOD) in realistic, three-dimensional models of weakly electric fish. Computer models of *Apteronotus leptorhynchus* and *Eigenmannia virescens* were constructed from body measurements of individual specimens, and tissue conductivities reported in the literature. The electric organ (EO) was modeled by varying current source distributions inside the fish body, with parameters constrained by data for EO structure and electrocyte activation. Comparisons between EOD maps from live fish and BEM simulations were used to optimize the simulation parameters and to iteratively refine the EO model, leading to models that accurately reproduced the EOD field patterns in these two species. The relative timing of the optimized EO current sources corresponds to and clarifies the likely command signal activation of EO segments: EO activation in *Eigenmannia* is predicted to be well synchronized, while in *Apteronotus* the EOD is predicted to result from a sequential activation of EO segments along the entire length of the body. Small variations of the model parameters can account for differences found in the EOD patterns between *Apteronotus* specimens of various frequencies and body lengths. Once the *Apteronotus* model was tuned, it was used to examine the mechanisms that could underly chirping, a well described social behavior that involves modulations in the EOD frequency and amplitude. Small rises in EOD frequency were reproduced in the model by increasing a single parameter representing the pacemaker frequency. Larger chirps also required partial reductions in electrocyte output to lower the EOD amplitude.

Full chirps, containing interruptions in the fundamental frequency, appear to result from free-running electric organ segments oscillating at their intrinsic frequencies with no entrainment from the pacemaker.

5.1 Introduction

Weakly electric fish have evolved specialized electric organs (EOs) to generate external electric fields, and an array of electroreceptors throughout the skin to monitor the resulting transdermal currents (Bullock and Heiligenberg 1986). The distribution of these currents, modulated by body orientation, external objects, and other electric fish, constitutes a peripheral electrosensory "image" used by the fish for sensory discrimination. Electroreceptor afferents encoding phase and amplitude information project directly to multiple somatotopic maps in the electrosensory lateral line lobe of the hind brain (Heiligenberg 1988), which has proved to be fruitful terrain for the study of sensory processing and integration (e.g., see Bell et al. 1993; Bastian 1994; Bell et al. in press). However, a more complete knowledge of the peripheral electrosensory input is needed for a full understanding of these systems, as well as for neuroethological studies of electrolocation strategies and social behaviors.

As shown in Chapters 2 and 3, the EOD in the water surrounding a weakly electric fish can be directly measured with high resolution in time and space. However, understanding active electrolocation requires that we determine the electrosensory inputs while the fish explores naturally, without interference from the observer. In this regard there are several limitations in the field mapping procedure: (1) the fish must be held stationary, either sedated or paralyzed, (2) the amplitude of the EOD has a wide dynamic range dependent on distance from the fish, and (3) it is difficult to measure the effects of nearby objects, which are typically a very small percentage of the intrinsic EOD

magnitude[1]. Moreover, awake behaving fish exhibit extremely fine behavioral sensitivities (e.g. in object detection, Bastian 1976; in the jamming avoidance response, Heiligenberg 1986), utilizing central convergence from their distributed array of receptors to detect signals too weak for us to measure.

In order to better study electrolocation noninvasively during natural behaviors, I have employed computer models of the fish and EOD. The intent was to use realistic simulations to predict EOD fields, modulations from body orientation and objects, and the resulting electrosensory stimuli[2]. The electric fields in the water about the fish are amenable to modern numerical techniques, and in Chapter 4 I described the development of a high resolution boundary element method program to simulate the full spatio-temporal pattern of the EOD in realistic, 3-d, electric fish models. These computer simulations permit access to the transdermal potential over the entire body surface (the electrosensory image) during natural behaviors, so that we can better visualize how a fish perceives its environment through its own generated currents and body movements.

In this chapter I report the electric fish simulator's first application: before using the simulator to quantify electrosensory images, the fish body and EO had to be accurately modeled and calibrated. Two fish models were built and tuned to replicate the EODs of two wave species of electric fish with distinct EODs, *Eigenmannia virescens* and *Apteronotus leptorhynchus*. The results of this reverse engineering clarify the significant electrical parameters affecting the external EOD waveforms, and have implications for the command signal pathway from pacemaker to EO. Fixing most parameters, the *Apteronotus* model was then also used to examine the generation of chirps, or short term rises in EOD frequency used in communication (see Discussion for background). The model results generated specific, experimentally testable predictions about changes in central control and electrocyte output.

---

[1]The charge induced on an object is proportional in magnitude to the electric field at the object's location, which falls off by about the cube of distance from the fish. The induced dipolar field from the object then falls off on the way back to the fish, again as the cube of the distance. See Appendix B, or Jackson, pg. 141.
[2]Without noise, but the question then becomes how accurate a model can we produce?

5.2 Methods

5.2.1 Modeling electric fish: Poisson's equation and the boundary value problem

As shown in the previous chapter, the electric potential $\Phi(\mathbf{x})$ generated by an electric fish can be modeled as a solution of Poisson's equation[3]. Multiplying by the conductivity $\sigma(\mathbf{x})$ results in an equation for current source densities (ρ = charge density, ε = dielectric constant):

$$-\nabla^2\Phi = \frac{\rho}{\varepsilon} \qquad \longrightarrow \qquad -\sigma\nabla^2\Phi = \sigma\frac{\rho}{\varepsilon} = I$$

Function $I(\mathbf{x})$ then corresponds to the current source density generated by the electric organ. Outside the fish this reduces to Laplace's equation since there are no current sources ($I = 0$). Inside the fish, $I(\mathbf{x})$ is the model parameter corresponding to EO activity, and is assigned for each successive phase of the EOD. Note that this formulation is for an electrostatics problem at any instant in time: in the conductive mediums in and about the fish, the dielectric relaxation time ε/σ is small enough that we can neglect charge buildup due to displacement currents (assuming small external objects compared to the fish body; equivalently, the displacement current is negligible with respect to conduction currents; see Chapter 4). Also, the skin is considered ohmic, consistent with measurements in the literature (see below); even if it had capacitive properties, the wave fish have such clean frequency spectrums that we could treat the fish skin as having constant impedance for each harmonic. The result is a boundary value problem: given the geometry of the surfaces, the conductivities corresponding to the fish, water and external objects, and the current source density generated by the electric organ, solve for the potential and electric field in and around the fish.

[3]Mais, bien sur! Chapter 4 also discusses the objectives of this approach.

5.2.2 Boundary Element Method (BEM)

In Chapter 4 I described the derivation and application of the boundary element method (BEM). BEM uses variational principals to reformulate Poisson's equation into integral relations on all boundary surfaces, thereby breaking the problem domain into three regions: the internal body of the fish, the skin layer, and the surrounding water. Computational nodes and surface elements then need only be placed on discontinuous boundaries, as in the surface mesh in Fig. 1b (for mathematical details see Brebbia et al. 1984). This greatly decreases the number of nodes required for 3-d problems compared to other numerical methods, and results in much smaller but full problem matrices. Therefore generating the model mesh becomes much more practical, at the expense of additional computational complexity (including complicated surface integrals) and some loss in generality (in BEM, each region is homogeneous in conductivity, rather than each element as in finite element methods). However, when considering the assumptions traditionally applied to electric fish, we can take full advantage of the strengths of the BEM simulator.

5.2.3 BEM application to electric fish simulation: assumptions and simplifications

Several first order approximations were applied to begin the modeling with the simplest plausible assumptions supported by experimental evidence (discussed below): the internal body conductivity is uniform and higher than that of the water; the skin layer is very thin, with conductivity a function of location on the body; and the EO is treated as a current source rather than a voltage source. Most importantly, I have assumed that the skin conductivity is very low relative to both body and water, so the current density through this thin layer can be assumed to only have a significant component normal (perpendicular) to the surface. Therefore the skin was approximated as a single surface composed of planar triangular elements, and appropriate boundary conditions then applied for compensation (equivalent to a dipole layer: Jackson 1975, pages 35-41). The

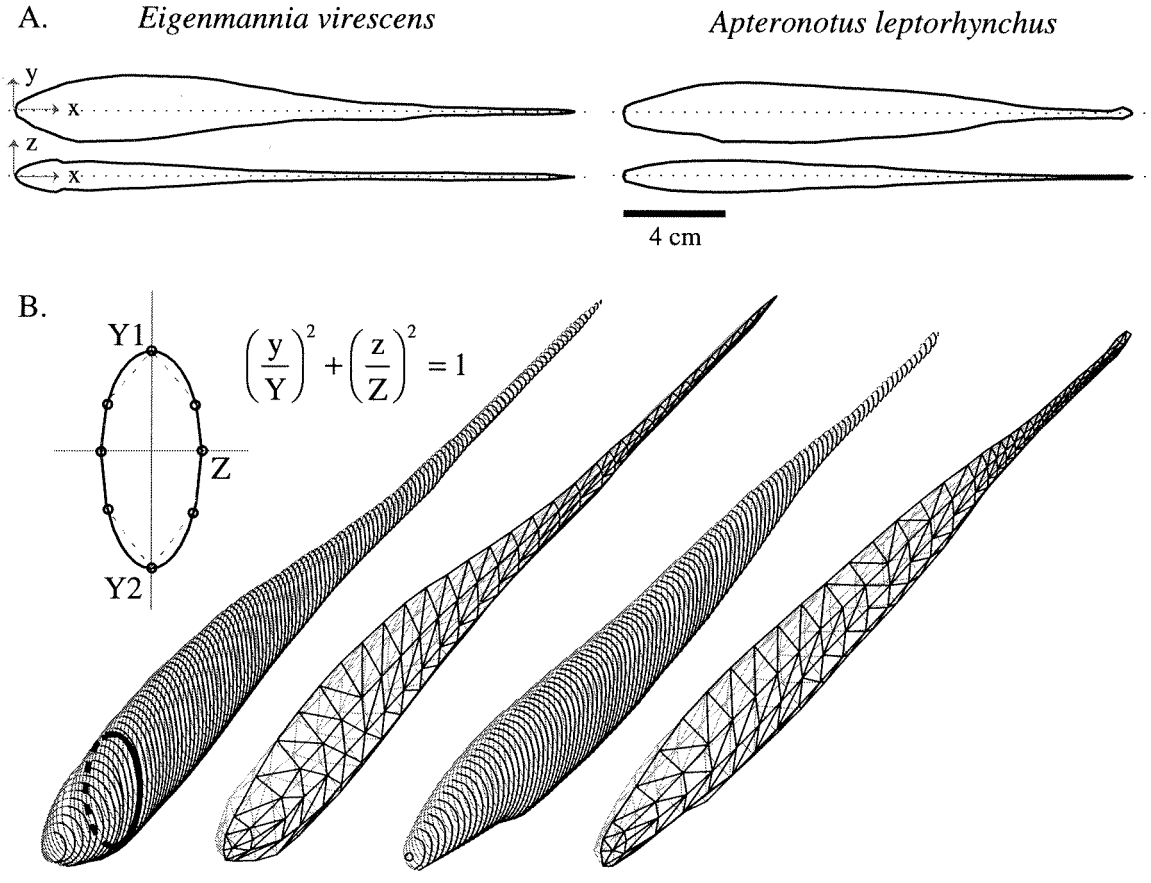

Figure 5.1 Building the fish model mesh for the BEM simulation. A. Side and top view body outlines were taken from a specimen of each species. B. Body data was used to estimate curvature at each 2 mm "slice" of the model fish. 256 node points were then chosen on the surface and connected to create a 3-d mesh of planar triangular elements. The simulation solves for both the potential and the current density at each node.

Figure 5.2 Model conductivities
Top: Bulk values for water and internal body, in μS/cm.
Bottom: Skin membrane conductivity profile along body axis, and equivalent bulk conductivity assuming 0.2 mm skin thickness (right scale).

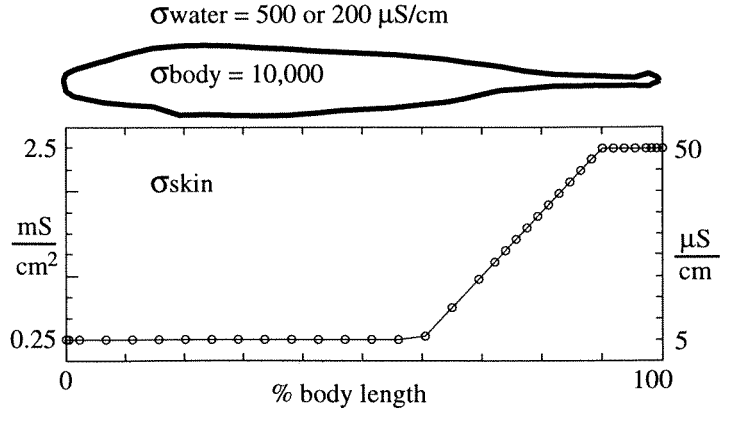

boundary conditions, shown in Chapter 4, consist of (1) continuous normal current density across the boundary, and (2) a jump in potential, equal to the transdermal voltage drop. This results in two unknown variables at each node: the external potential and the normal current density. Once these are solved on the fish surface, the fields at any point in the water about the fish can be calculated as well. If the simulations result in good approximations to the measured EOD fields, then the assumptions applied here may be adequate to describe the fish body.

5.2.4 Fish models

Skin mesh

Constructing 3-d fish models was straightforward for the BEM simulator. One individual of each species was photographed to generate overhead and sideview surface profiles. Height and width measurements were then recorded at 2 mm intervals along the body length (Fig. 1a), omitting external structures such as fins and gill openings. The surface curvature at each interval was approximated by 2 radii of curvature in each quadrant in the right half plane, centered about the origin, as in Fig. 1b. The surface was reflected about the midsagittal plane, leaving the left and right sides symmetric. Body dimensions were normalized so that the length of each model fish was 20 centimeters, but this parameter could be scaled in the simulations while maintaining the aspect ratio. Node points were then chosen along the length and height of the body, and the width was interpolated to find the third coordinate. The nodes were finally triangulated to create a mesh of planar surface elements (Fig. 1b). The models each contained 256 nodes and 508 surface elements. The results presented here are from fish oriented with straight body and tail, consistent with the mapping procedures described in previous chapters.

Fish tank

The simulator solves for the fields around a fish in an infinite body of water. In the actual measurements, however, the currents are restricted by the fish tank walls,

bottom, and water surface. To include these effects I used the method of images (Jackson 1975, page 54): suitably placed charges outside of the solution domain can replace the actual boundaries by replicating the boundary conditions. The fish mesh was therefore reflected once about each of the six tank boundaries (dimensions: 20 cm x 58 cm x 58 cm) for a first order approximation, and the final solution was thus represented by the superposition of seven separate simulations. Adding the tank boundaries in this manner compresses the currents and spreads out the isopotential contour lines.

Passive parameters (conductivities)

The surface mesh boundary separates the external water from the internal body domain, both of which were assumed constant in conductivity. Although there are likely to be variations within the body due to internal organs and tissues (including an air bladder that can extend several centimeters caudal of the pectoral girdle), constant conductivity was the simplest starting point for the model. This assumption is also prevalent in the electric fish literature (Sheich and Bullock 1974; Heiligenberg 1975; Hoshymiya et al. 1980). I used a body conductivity of 10 mS/cm (100 Ω•cm resistivity), the average reported by Sheich and Bullock (1974). The water conductivity was the same as in the mapping measurements, either 200 or 500 μS/cm (5 or 2 kΩ•cm). Sheich and Bullock (1974) also reported skin resistivities between 1-4 kΩ•cm^2 in *Eigenmannia*. However, previous simulations by Heiligenberg (1975) and Hoshimiya et al. (1980) both led to predictions that the skin conductivity at the tail should be an order of magnitude greater than on the trunk, to balance the electrical load on the organ and better fit the contour lines of field mappings. Our preliminary measurements of skin resistivity in *Apteronotus* ranged from 400 Ω•cm^2 at the tail to 7 kΩ•cm^2 on the rostral trunk (unpublished data).

In the model, the effective conductivity of the skin layer could be set for each node depending on its location on the body, and was interpolated over each element from the values at its vertices. I used 250 μS/cm^2 (4 kΩ•cm^2) for the skin over the rostral

body, and 10 times that at the tail, with a linear profile in-between (Fig. 2; similar to Hoshimiya et al. 1980). Conservatively assuming[4] a skin thickness of less than 0.2 mm, then the equivalent bulk resistivity of the rostral skin is greater than 200 kΩ•cm, or at least 40 times that of the water; the tail skin bulk resistivity of 20 kΩ•cm, while on the same order of magnitude as the water, is still 200 times higher than the internal body.

Electric organ models

In the range of water conductivities used here, these species have been shown to be closer to ideal current generators than voltage sources (Knudsen 1975). This is naturally accommodated in the BEM formulation – the EO was modeled with discrete current sources representing current exiting from points along the organ. At each instance in time, the simulations required that each source be assigned a location, magnitude, and sign, which were the principle free parameters in the model. However, there is no unique solution for the internal source configuration based on the external measured fields alone. Therefore I needed to add several constraints: (1) the sources must be located along the path the actual EO would take, (2) the sum of all source strengths must equal zero to satisfy Kerchoff's laws, (3) sequential phases of the EOD should be realized by incremental changes in the source configurations, i.e. only smooth variations are allowed in time, and (4) source waveforms had to be consistent with known electrocyte and EO properties based on the considerable information in the literature (see Discussion). For each fish, I started with the simplest EO model - a dipole. Waveforms of the sources were chosen proportional to the potential mapped near the skin surface at the tail tip *in vivo*. Sources were then added or modified as necessary to replicate the recorded waveforms (e.g., as indicated in Figs. 3 and 6). In this manner, the electric organ model was iteratively refined by varying the source distribution and strengths and comparing the results to the potential measurements.

---

[4]From my survey of the literature, weakly electric fish skin often appears to be thinner than 100 μm (see Fig. 2 in Szabo 1974; Fig. 1 in Vischer 1993; Figs. 10, 11 in Bennett 1971b; Fig. 4 in Zakon 1986).

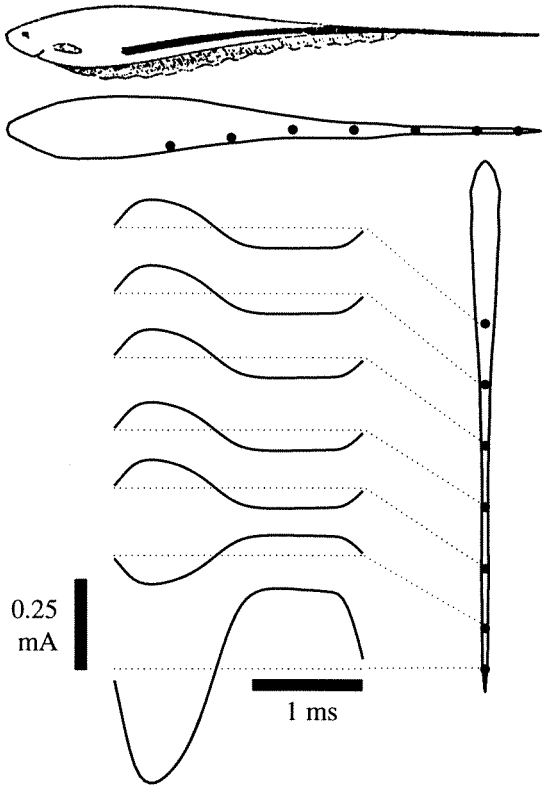

Figure 5.3 *Eigenmannia* synchronous EO model. 7 current sources were placed inside the fish at the positions indicated, along the path of the actual electric organ (top, from Heiligenberg 1975). Current wavefrom at tail tip was chosen from measured potential external to tail tip; the others are identical in time except for a scalar multiple. Relative magnitudes are [+1 +1 +1 +1 +1 -1 -4], summing to zero at any particular phase.

For the more complicated EOD of *Apteronotus*, two additional methods were necessary to explore the EO output, a bottom-up approach and a top-down approach. First, to prove the sufficiency of the BEM model with multiple sources, the fish EO was reverse engineered from its measured EOD. A number, N, of point current sources were placed along the path of the EO to represent its output. A set of N basis functions was then generated by running N simulations, each having only one of the sources set to +1 mA, and the others set to zero. A linear combination of the N solutions could then be used to approximate the potential in the water at any phase in time. Calculating the appropriate basis function coefficients then corresponds to finding the amplitude of each current source. This was accomplished by taking the entire EOD mapping in the midplane (typically over 300 waveforms), and performing a least squares fit inversion of the overconstrained linear system.

To gain better insight into the activation of the real EO, I also tried a top-down approach. The EO was modeled with 16 fixed sources spaced at one centimeter intervals along the length of the fish's body, from behind the pectorals to the tail tip (effectively dividing the EO into 15 segments; Fig. 6b). To pick a source waveform, I again looked at typical waveforms measured at the tip of the tail, where the EO is close to low impedance skin (see Figs. 9, 11). How can this type of waveform arise? The electrocytes in the EO of *Apteronotus* are composed of modified motor neuron axons, as shown in Fig. 4a (Bennett 1971a). When modeled by the equivalent circuit shown in Fig. 5 (adapted from Waxman et al. 1972), the electrocyte acts as a simple high pass filter with characteristics shown in Figs. 5a. The current generated by the active nodes at one end of the electrocyte are filtered with a time constant equal to the total series resistance times the capacitance of the inactive nodes at the other end ($\tau = RC$). The electrocyte membrane potentials recorded by Bennett (1971a; Fig. 4b) were approximated by analytic gaussian activation functions (Fig. 4c). The filtered output of an isolated electrocyte firing at 600 Hz is shown in Fig. 5b, where varying the time constant between 0.1 and 5 msec produces waveforms very similar to those seen near the fish *in vivo*.

Once a source waveform was chosen, it was swept down the organ with all parameters fixed except magnitude and delay. The delay, or onset of activation, was determined by multiplying the distance of each source from the head by the command signal conduction velocity (initially set to 10 cm/msec, estimated from the *Apteronotus* maps, and consistent with measured velocities in other gymnotiforms). The period of the activation cycle, representing the firing rate of the pacemaker command, was fixed by the fundamental frequency of the EOD cycle for each fish. Relative source magnitudes were chosen to conform to the EO volume and electromotor neuron count data from Ellis and Szabo (1980), between two and four times higher at the tail tip than in the rostral trunk.

Figure 5.4 *Apteronotus* electric organ

A. Extent of electric organ and electrocyte morphology (from Bennett 1971).

B. Activation of single electrocyte (from Bennett 1971). An action potential propagates from caudal to rostral (traces from top to bottom, indicating membrane potential), before rounding the corner and traveling back tailwards. The resulting currents add to produce the external biphasic, head-to-tail potential waveform (top-most trace).

C. In the model, the activation function for the electrocyte output waveform is approximated by summing two analytic gaussians, one postive and one negative.

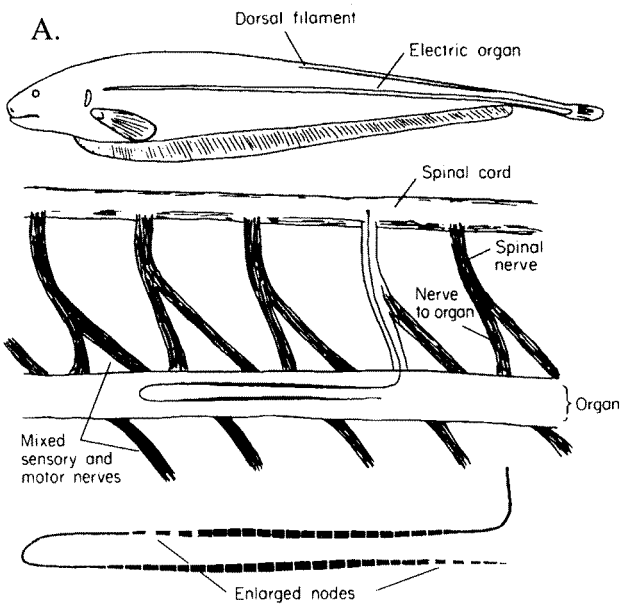

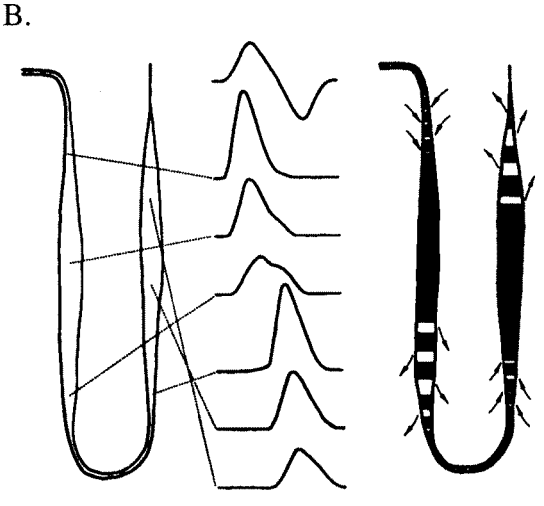

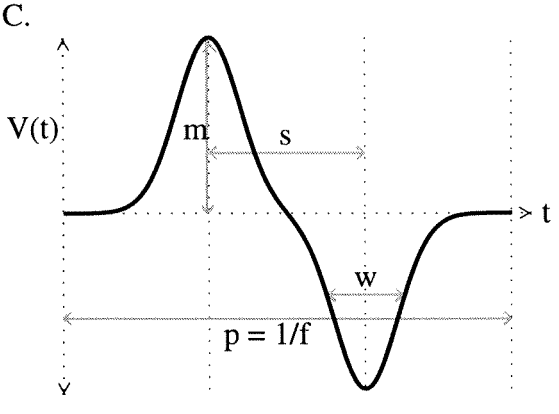

Parameters:

p = period of EOD

f = frequency of command signal (equal to EOD frequency)

m = amplitude of gaussian peaks

w = width of gaussian peaks

s = spacing between peak centers

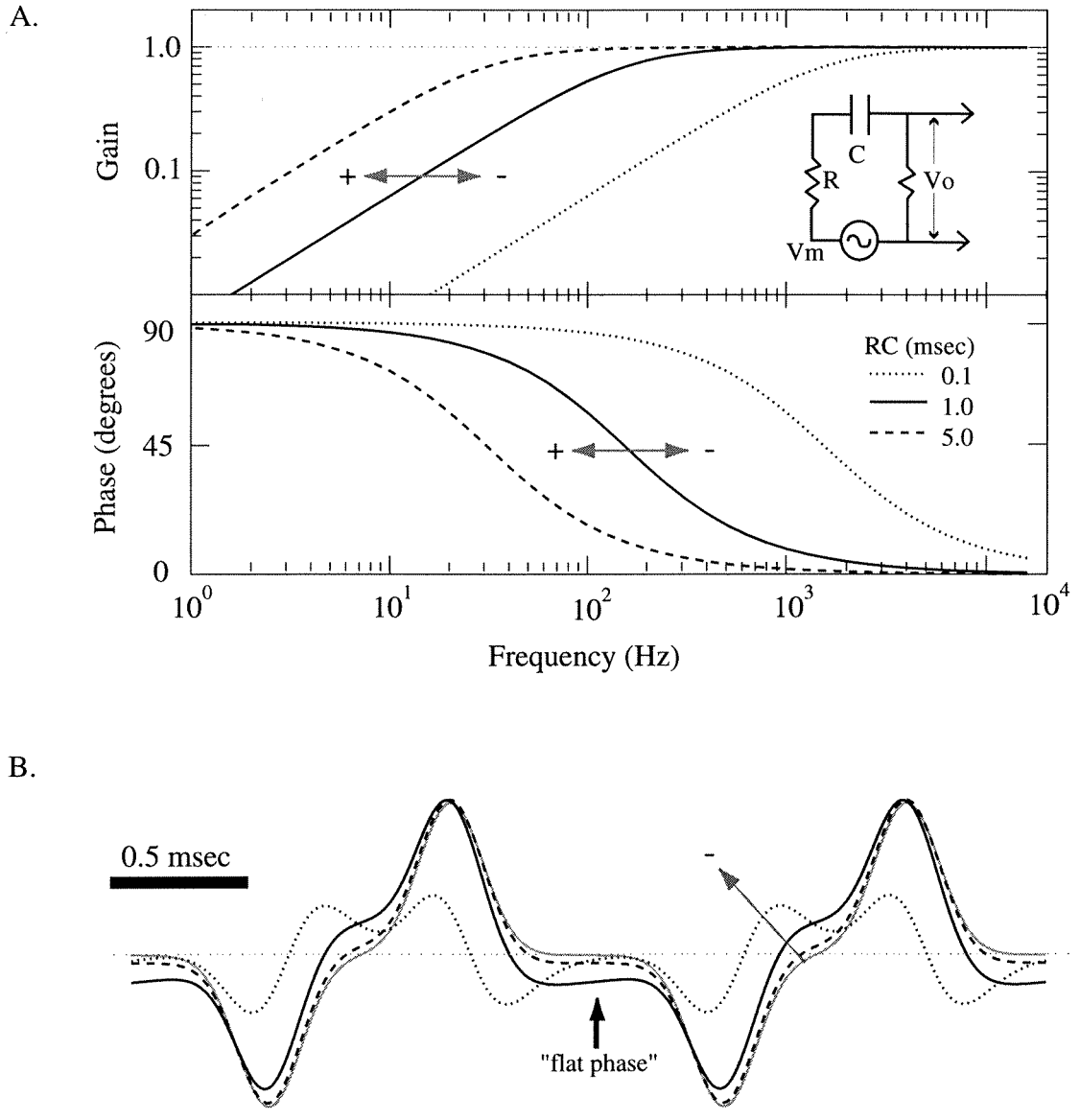

Figure 5.5 Electrocyte high pass filter. A. Gain and phase filter characteristics for the simple electrocyte circuit shown in the inset. Decreasing the time constant shifts the corner frequency higher. Amplitude and phase of the EOD fundamental will shift with respect to higher harmonics when near the corner. B. Output from continuous 600 Hz command pulse train for the same values of RC as in A. The waveform at RC= 5 msec (dashed) is very close to the input (gray), but already shows a negative bias in the flat phase between command signals (black arrow) due to capacitive discharge.

The final step was to convert the electrocyte functions into equivalent current sources for each EO segment (Fig. 6a). This could be accomplished using Thevinen equivalents if the source impedances of each segment were known. The EO typically is surrounded by connective tissue, which helps channel the currents to the EO endpoints, and so may drastically redistribute the effective sources. However, the necessary data on the connective tissue impedance is not available. Instead, the net EO current was forced to zero (obeying Kerchkoff's law) by subtracting the mean of the summed source activation functions at each point in time. To first order, this approximates the fish EO and body as a resistive grid that weights each source potential equally.

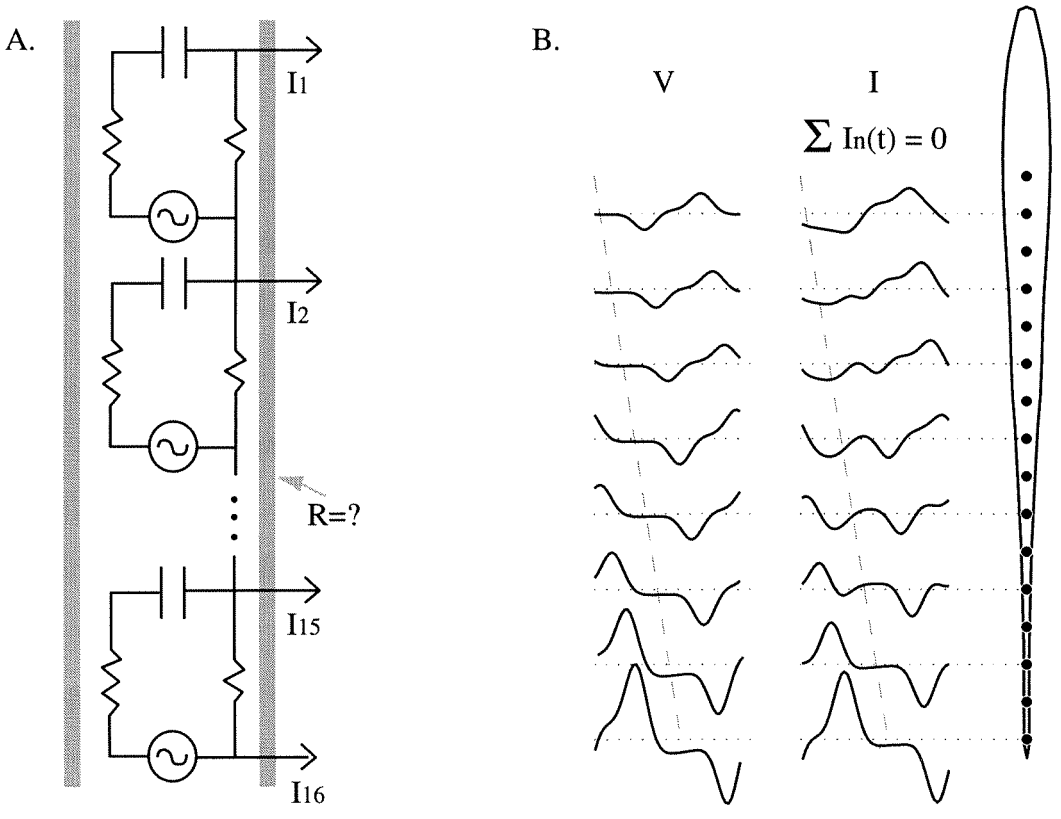

Figure 5.6 *Apteronotus* EO model. A. Combining electrocytes to create an equivalent EO multi-source model presents a problem: impedances of sources, extracellular medium, and connective tissue surrounding EO (gray) are not known. B. 16 fixed sources were spaced at 1 cm intervals, with electrocyte activation function estimated from the tail tip waveform. The waveform was swept sequentially down the body with phase delay equal to conduction velocity times distance from the head. The mean net current at each point in time is subtracted equally from each source, to force the net output current to zero.

5.2.5 Comparison to *in vivo* data

EOD potential maps

EODs were mapped from immobilized specimens of *Eigenmannia* (2 glass knives: 1 female, 1 male), and *Apteronotus* (7 brown ghosts: 4 females, 3 males; 2 black ghosts), as described in Chapters 2 and 3. Potential measurements were taken on the skin surface and in the midplane, with respect to a fixed electrode on the tank wall. Comparisons between simulation results and selected points from the experimental mappings were used to optimize the model parameters and ensure the accuracy of the simulations. Parameters were initially chosen and adjusted manually to qualitatively replicate peak spacing, peak widths and inflection points seen in the mapped EODs. For the *Apteronotus* simulations, a simple form of gradient descent was used, with a least squares fit error metric between head-to-tail waveforms, to optimize conduction velocity, peak width, and peak spacing (the parameters indicated in Fig. 4c). Model parameters were also systematically varied in multiple simulations to approximate the ranges of EODs found in the field mappings.

Frequency chirps

After the final parameters were fixed for a 600 Hz, 20 cm brown ghost model, the simulation was run at several higher frequencies to simulate waveforms that might be generated during a frequency chirp (waveforms generated at 600, 650, 700 and 750 Hz). The only parameter allowed to vary besides frequency was the peak width (parameter w in Fig. 4c), which was fixed to a constant percentage of the period (1/f). For comparison, *in vivo* EOD waveforms were continuously sampled from 6 electrodes attached to the side of a mesh tube in which the fish rested during daylight hours (data sampled from 1 brown ghost male and 1 black ghost). One second blocks of data were digitized and recorded whenever spontaneous frequency rises were detected. Some of the recorded chirps included interruptions of the fundamental EOD frequency (see below). These were investigated in the model by raising the frequency to 900 Hz and varying the phase relationships between EO sources.

5.3 Results

5.3.1 *Eigenmannia virescens*

As described in Chapter 3, the EOD of *Eigenmannia* strongly resembles an oscillating dipole, with the tail tip one pole and the body serving as an elongated opposite pole, separated by a stationary zero-potential line (Figs. 7, 8). The EOD waveforms are very uniform in shape over the body and differ from the head-to-tail waveform mainly in magnitude. The smaller amplitudes of the rostral waveforms are likely due to a decline in EO volume by 50% from the tail (Ellis and Szabo 1980), averaging by current spread in the high conductivity tissues in the rostral half of the body, and the higher resistivity skin at the head.

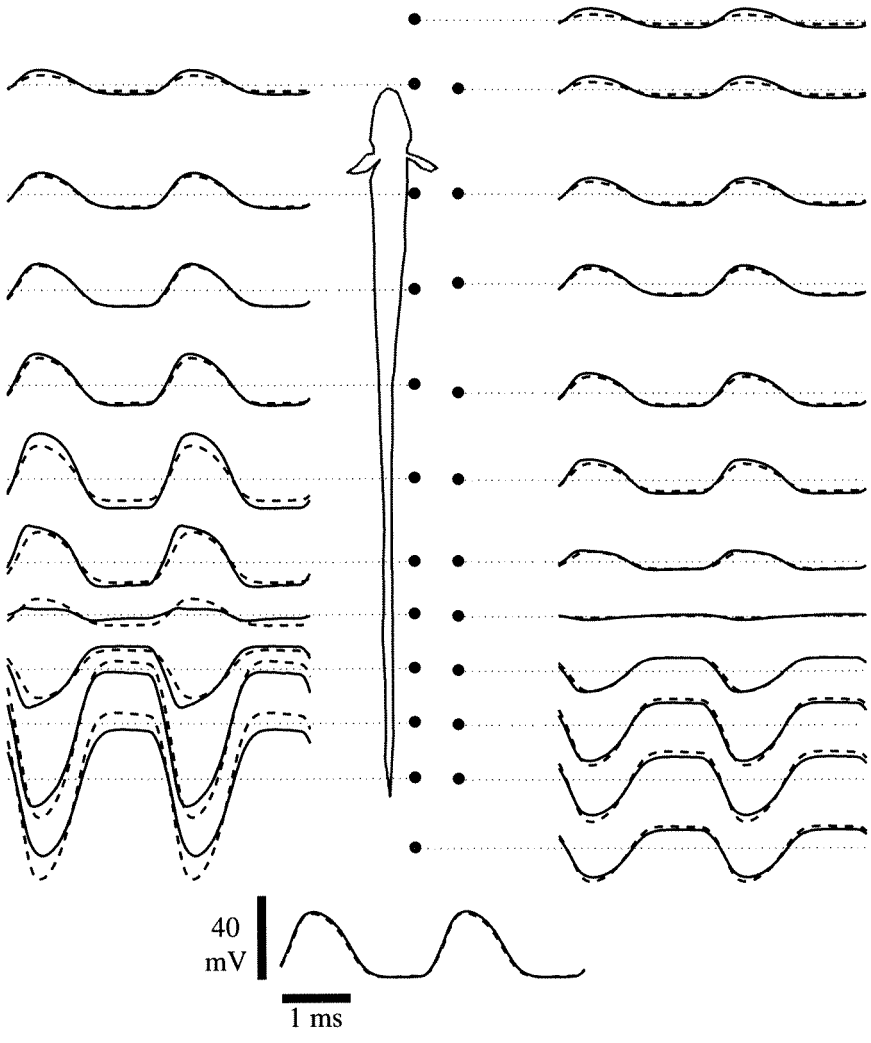

Figure 5.7

Eigenmannia EOD potential waveforms in midplane.

Solid: measured

Dashed: simulated

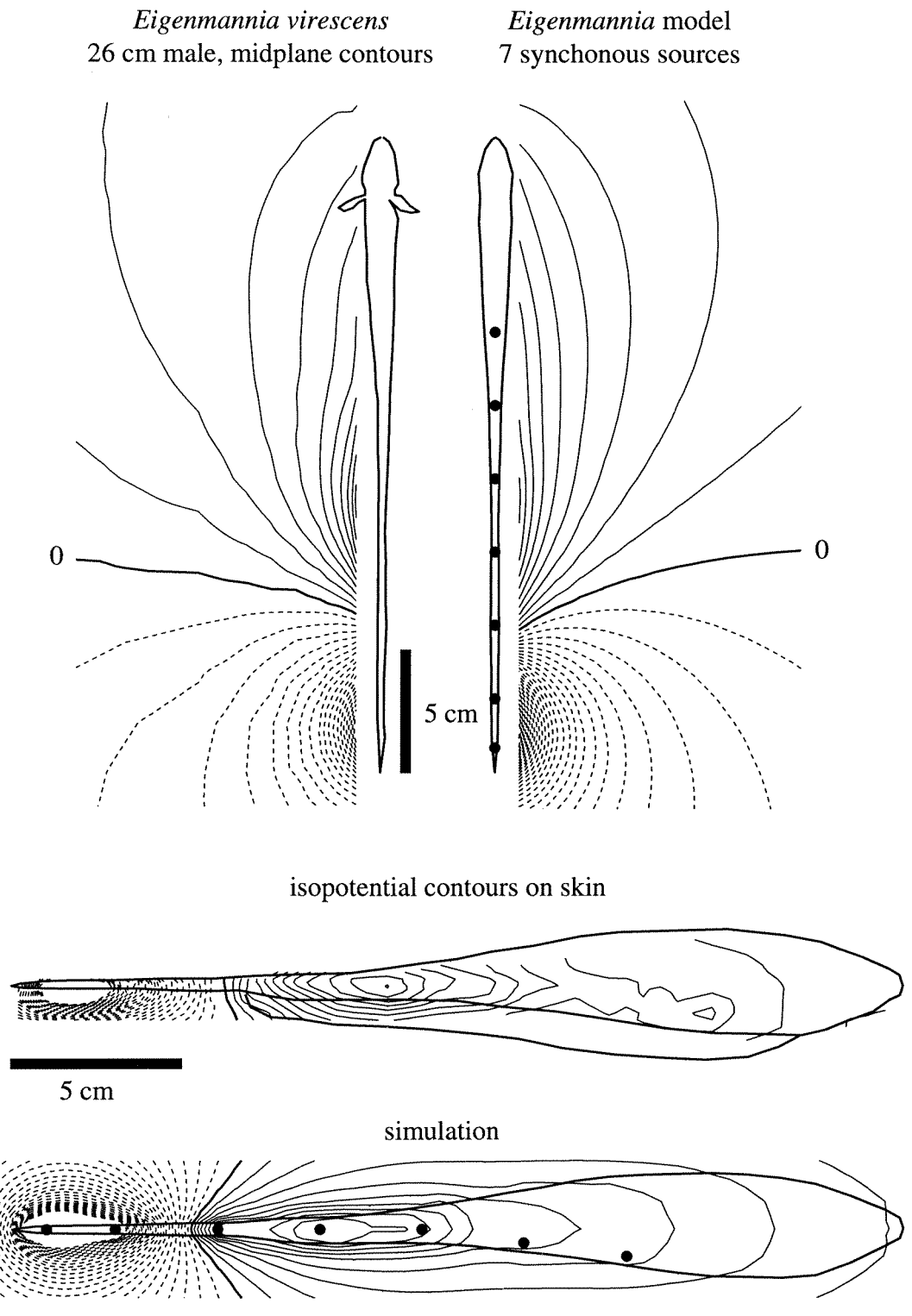

Figure 5.8 *Eigenmannia* EOD, measured vs simulated

Isopotential contour plots (2 mV steps) at phase of first peak in waveforms of Fig 7.

To replicate this in the *Eigenmannia* simulations, two models were utilized: the first a simple oscillating dipole, and the second consisted of two sources in the tail tip balanced by five sources distributed in the rostral half of the EO (Fig. 3). Simulation results from the simple oscillating dipole model matched the field mappings from *Eigenmannia* fairly well; however, the rostral fields had a much higher rate of decay with distance. Better results were obtained by generating the rostral current from multiple sources along the rostral half of the EO, which spreads the isopotential lines along the length of the body as in the field mappings. The isopotential distribution was sensitive to variations in both EO source locations and skin and internal body conductivities.

5.3.2 *Apteronotus leptorhynchus*

As described in Chapters 2 and 3, the EOD of *Apteronotus* has gross features in common with that of *Eigenmannia*. Fields are stronger at the tail, more spread and uniform along the rostral trunk and head, and mainly bipolar during the peaks of the EOD. However, local peaks and zero-crossings clearly propagate caudally along the length of the fish (Figs. 9 and 10), and many local features were found in common between individuals (Fig. 11). Variations between individual fish were apparent along the tail where the waveforms became triphasic and more complex.

For the *Apteronotus* simulations, simple dipolar models were quickly found insufficient, even when the two poles were allowed to move for different phases. The dipolar solutions were similar to certain phases during the period of the EOD; however, they were not sufficient to recreate the overall EOD pattern, which includes higher order multipole moments along the tail. For example, in several phases the potential is trimodal along the fish axis (see maps in Chapter 2). The EO required more distributed sources, with activation allowed to propagate along the fish as implied by the field maps. The multipole EO models, based on parameters taken from the literature, were more successful in reproducing features of the complex EOD patterns seen in the field measurements.

The bottom-up model closely approximated the waveforms in the actual EOD (Fig. 9b). This is not surprising since it was reverse engineered, but it does indicate that the model is sufficient to match the external fields with relatively few free parameters (the N source amplitudes). However, it is quite difficult to infer EO activation from the calculated sources (Fig. 9a). In fact, results from bottom-up models with more sources in the rostral body pointed out a major difficulty in interpretation: while currents are driven and channeled through the actual EO opposite to the external flow, the monopolar sources used in the model send current in all directions. Therefore, while the currents exiting the EO may still be accurately represented, they are just a fraction of the total current calculated at each source.

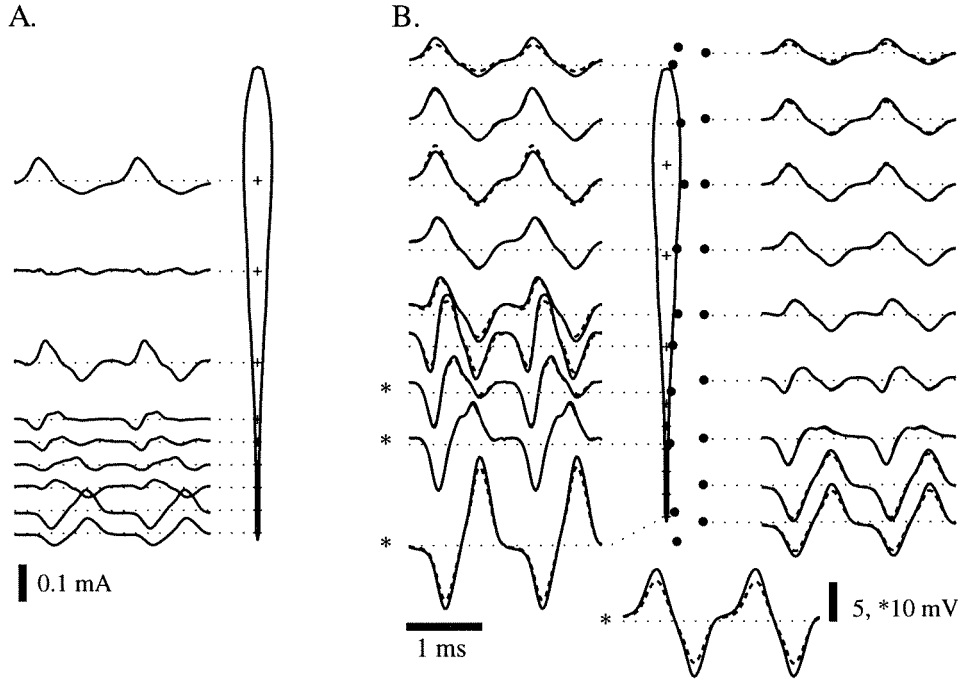

Figure 5.9 Brown ghost results from bottom-up model. A. Current source waveforms from the constrained inverse solution for nine sources at the indicated locations.
B. Potential waveforms in midplane, simulated (dashed) vs. measured (solid), from a 21 cm female with fundamental frequency of 810 Hz.

The top-down model was less successful in matching the measured fields, but is likely to be more informative of the actual EO properties. Waveforms from the midplane of a typical *Apteronotus* simulation are shown in Fig. 10a, with parameter values indicated in the caption. In this particular simulation only two parameters were allowed to vary: the activation function peak spread and the conduction velocity. Optimal values of 40% spread and 8.8 cm/msec, respectively, resulted in a head-to-tail waveform most closely resembling that of a 21 cm, 810 Hz female (Fig. 10b). Results from three other *Apteronotus* simulations are shown in Fig. 11, compared to the measured waveforms of three different fish. Variations of the model parameters replicate many of the qualitative differences between fish.

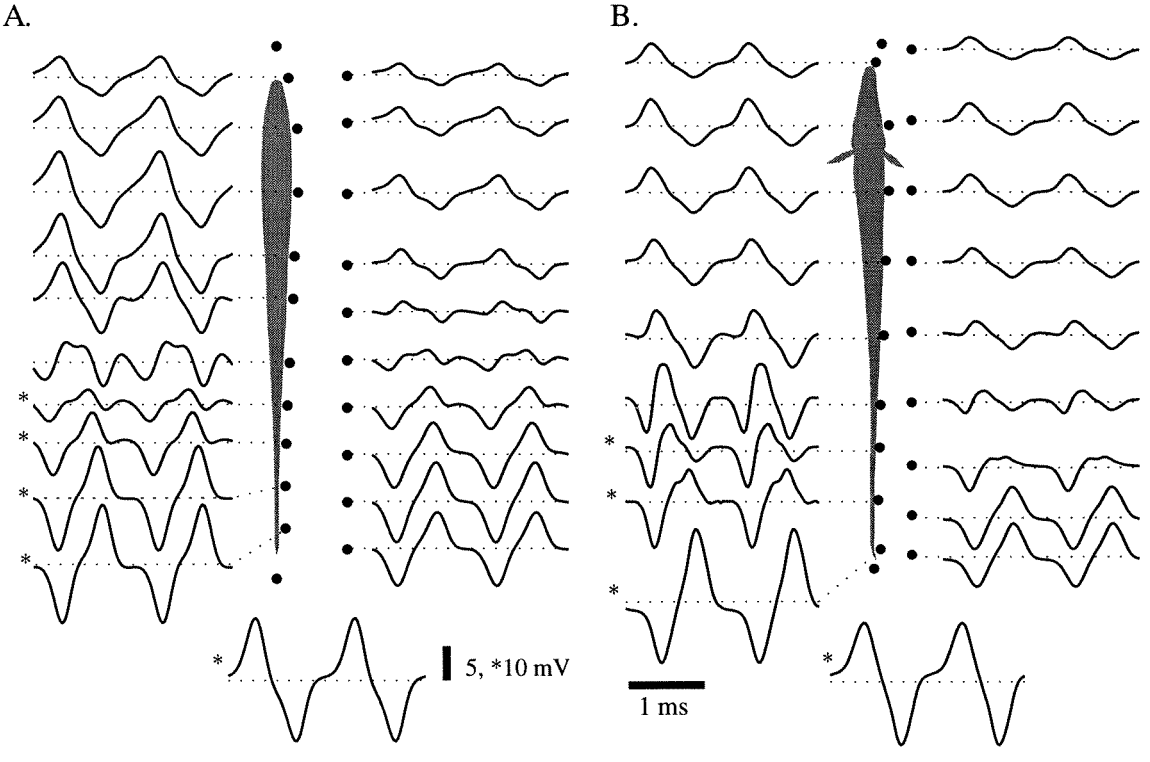

Figure 5.10 Brown ghost results from top-down model. A. Simulated waveforms in midplane with the following parameters: f= 810 Hz, s= 40%, w= 10%, RC= 2 ms, conduction velocity = 8.8 cm/ms. B. Measured waveforms from same fish as in Fig. 9. Bottom waveforms are the head-to-tail EODs from the points indicated.

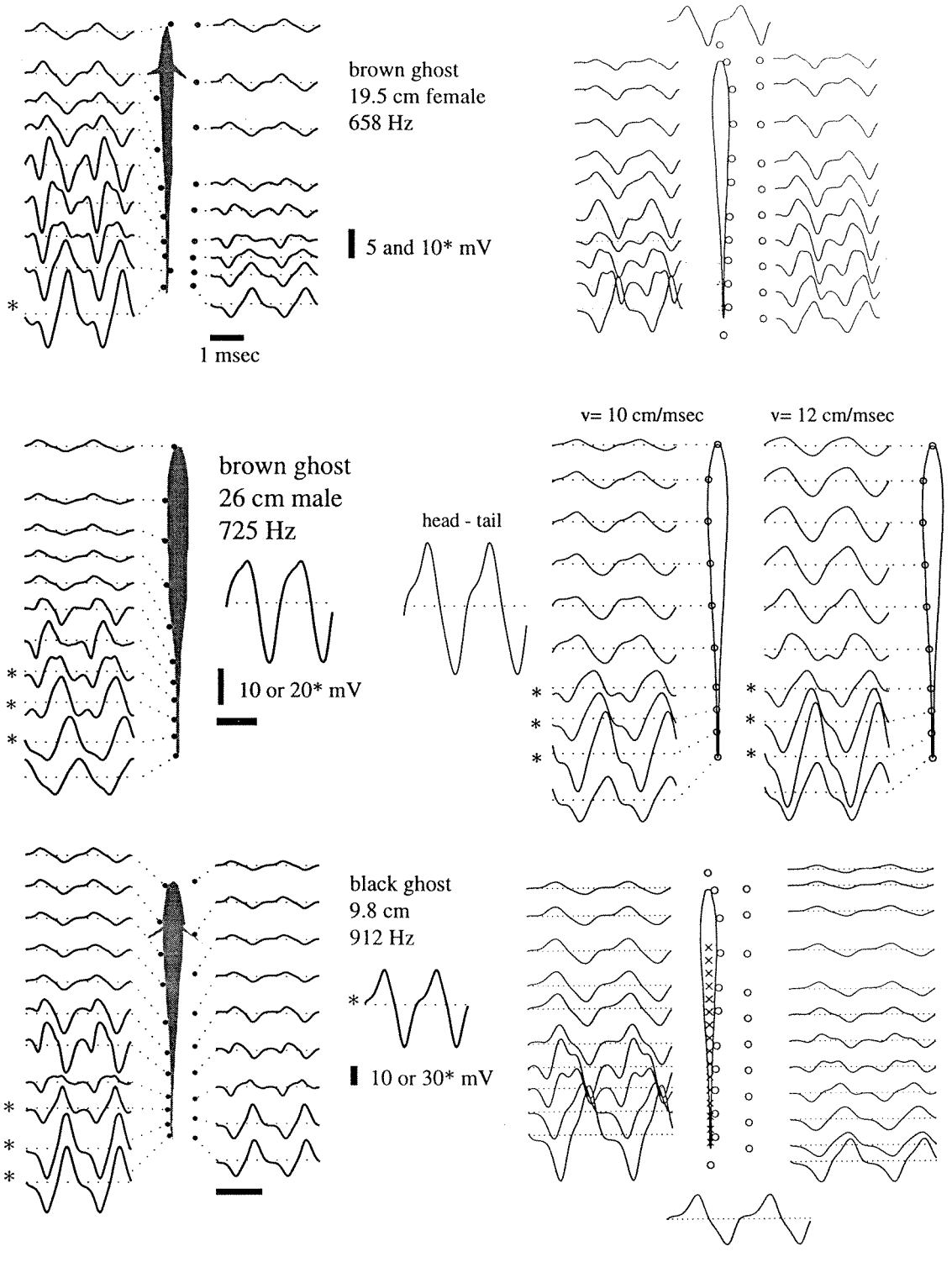

Figure 5.11 Measured EOD waveforms (left) vs. simulated waveforms from varying parameter sets (right). Model parameters are body length, conductivities, current source waveforms (peak width, spacing, and magnitude), conduction velocity, and frequency.

5.3.3 Chirp waveforms and simulations

Having optimized the *Apteronotus* model shown in Fig. 10a, the final parameters were then used to replicate the generation of chirps recorded *in vivo* (Figs. 12-15). A typical short rise in frequency spanning about 30 msec from the brown ghost recordings is shown in Fig. 13. The EOD rises from 673 to 760 Hz in frequency and loses 10% of its amplitude (measured head-to-tail) before returning to baseline (Figs. 13a). Five single period waveforms highlighted in Fig. 13b are displayed on a longer time scale in Fig. 13c, where the waveforms are each repeated twice to emphasize their divergence. Most of the speedup in frequency appears due to lessening the duration of the flat inflection phase. The black ghost chirps were similar – a typical chirp spanning about 150 msec is shown in Fig. 14. The EOD rises from 960 to 1120 Hz in frequency and loses 10% of its amplitude before returning more slowly to baseline. Again, the increase in frequency results in lessening the duration of the flat inflection phase.

In the model, the simulated chirps captured both of these effects (Fig. 12). As the frequency rose from 600 to 750 Hz, the flat phase was consistently shortened without much change to the shape of the rest of the waveform. The head-to-tail amplitude also decreased slightly; however, the percent change was dependent on the particular parameter set in use, and was sensitive to many of the parameters.

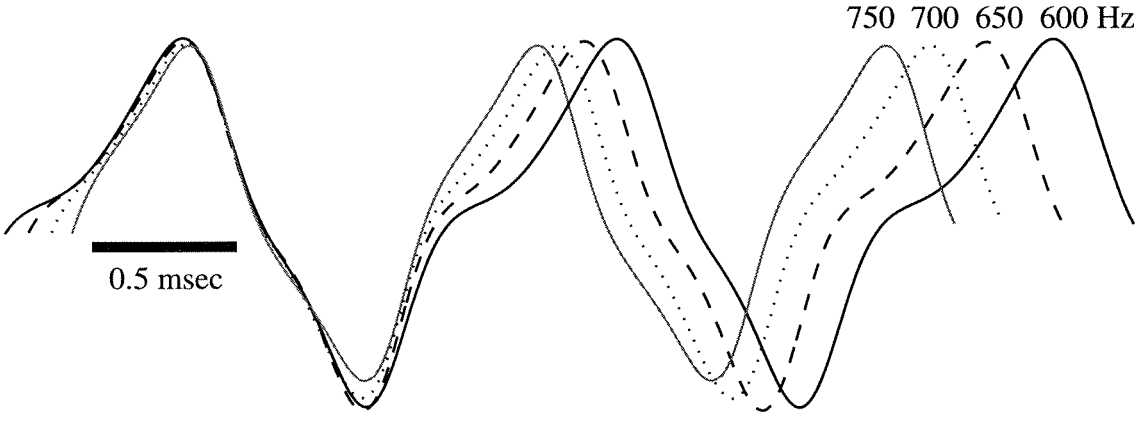

Figure 5.12 Simulated *Apteronotus* chirp waveforms

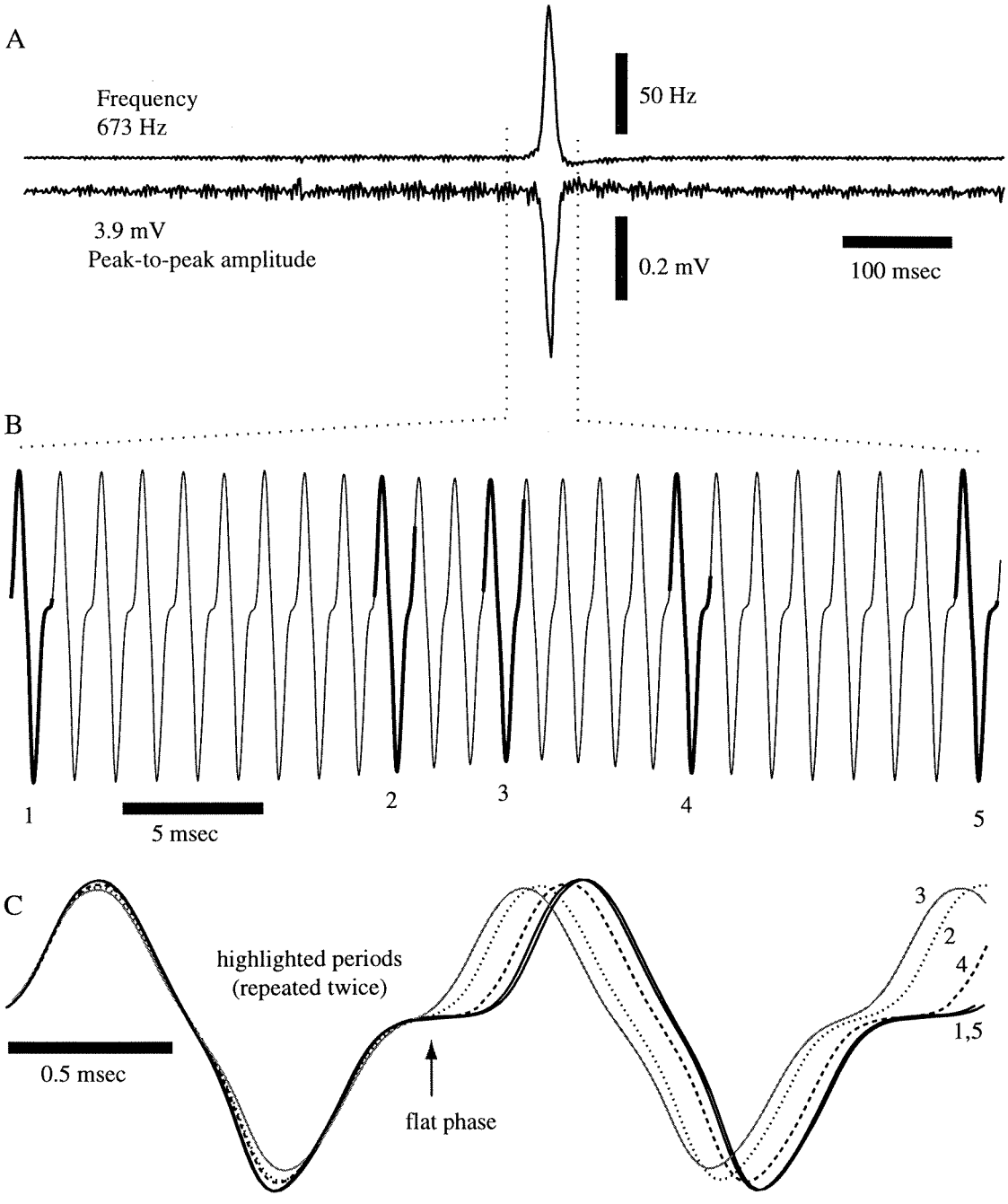

Figure 5.13 Brown ghost chirp. A. Instantaneous frequency and peak-to-peak amplitude of the head-to-tail EOD recorded near an 18 cm brown ghost (high frequency noise due to sampling artifact). B. EOD record during the chirp. Heavy lines indicate the single periods expanded and overlaid in (c). C. The major effects on the waveform: shortened duration of the flat phase (arrow), and a decrease in amplitude.

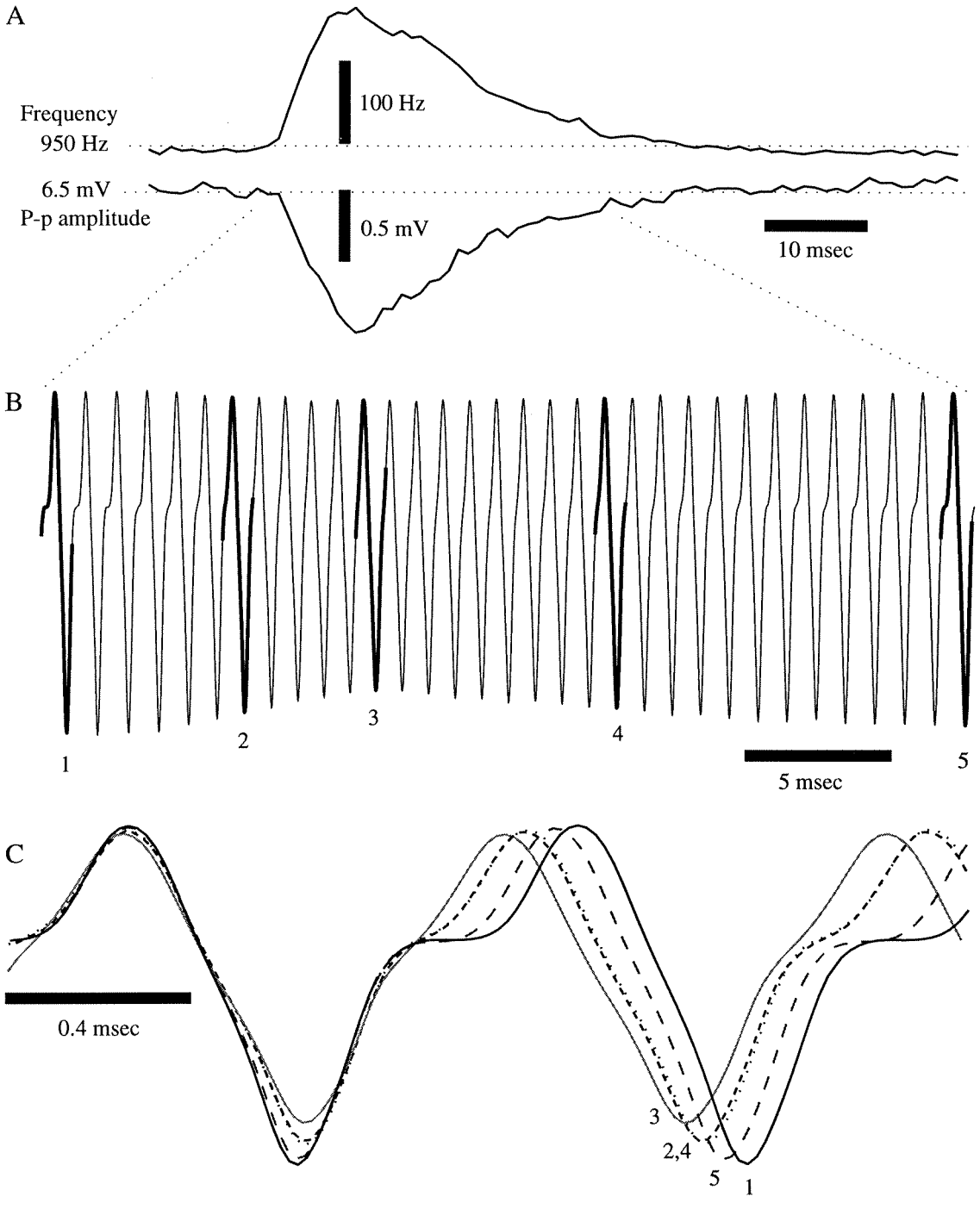

Figure 5.14 Black ghost chirp. A. Frequency and peak-to-peak amplitude of the head-to-tail EOD recorded near a 17 cm black ghost. B. EOD recorded during the chirp. C. Single periods (heavy lines in B) expanded and overlaid to show their divergence. Waveform effects are similar to those found during the brown ghost chirp.

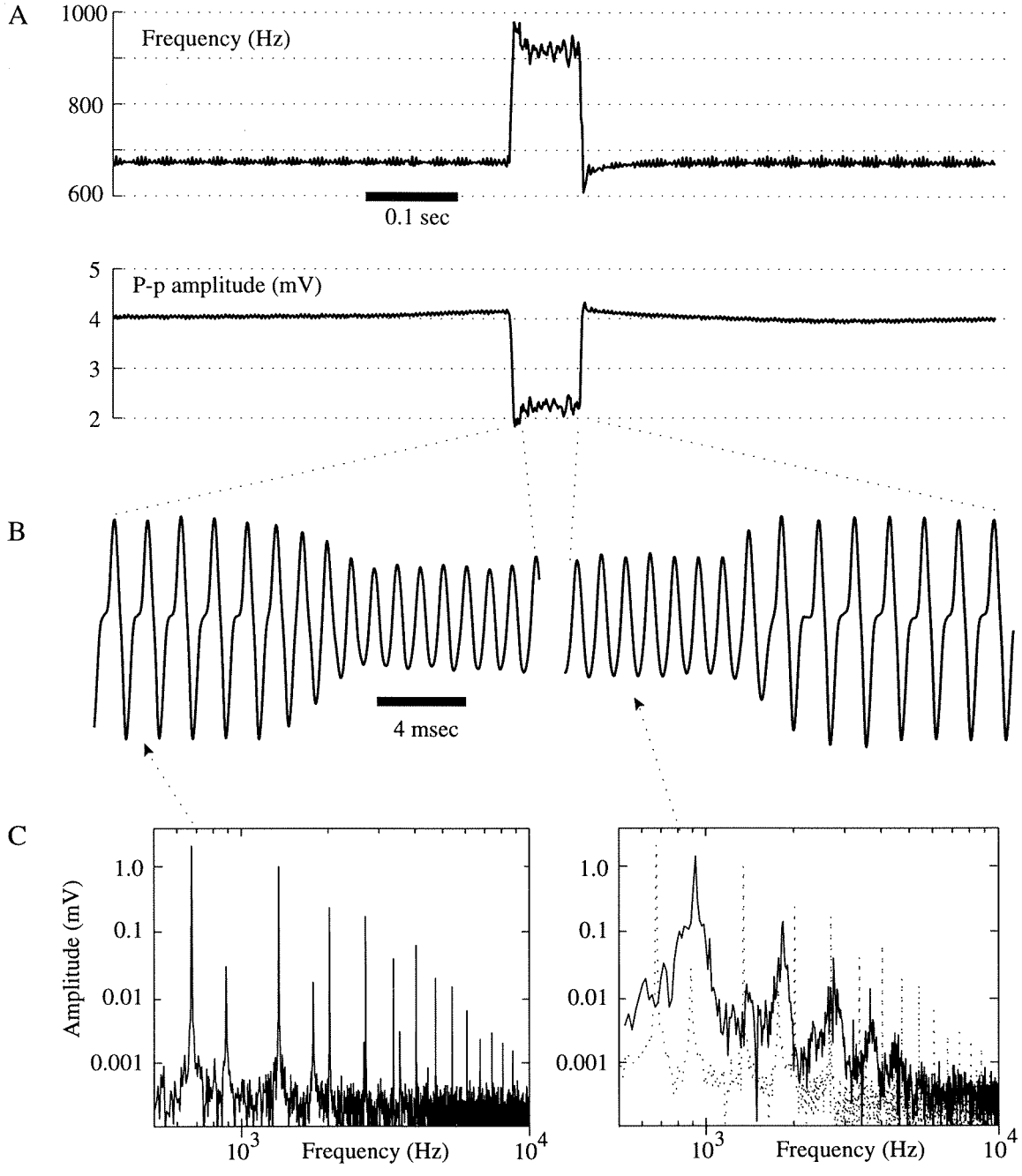

Figure 5.15 Brown ghost interruption from same fish as in Fig. 13. A. Frequency and amplitude of the head -to-tail EOD. B. Waveforms recorded at the beginning and end of the chirp. C. The fundamental frequency and harmonics disappear, to be replaced by a higher harmonically-unrelated frequency. D. Simulated interruption at 900 Hz (bottom) resembles the interruption waveform shape (top).

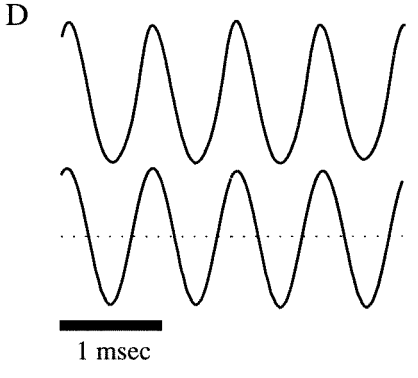

A second brown ghost chirp shown in Fig. 15 is typical of a chirp with an interruption. The fundamental frequency and its harmonics shut off for 100 msec, leaving an harmonically unrelated higher frequency with much lower amplitude. Comparing the frequency spectrums (Fig. 15c) before and during the chirp reveals that the frequency peak during the chirp is also present in the normal EOD spectrum, but at a much lower amplitude. This suggests that the free running EO has an intrinsic frequency of oscillation that is normally greatly suppressed during entrainment by the regular pacemaker command (see Discussion). Fig. 15d shows that the model can account for this type of chirp.

5.4 Discussion

Previous EOD simulations have proven very informative in exploring electrical parameters of fish models and illuminating possible sensory consequences of nearby objects. For example, Heiligenberg (1975) tested the influence of body characteristics, such as tail length on the range of electrolocation. His relatively coarse finite difference simulations also illustrated that bending the tail around objects may increase the fish's discriminatory abilities (see Fig. 10 in Heiligenberg 1975). Hoshimiya et al. (1980) used a high resolution finite element simulation with a simplified model of *Apteronotus* to qualitatively replicate many of Bastian's object effect experiments (Bastian 1976, 1986b). Bacher (1983) also simulated object effects based on an analytical model of the EO using line charges.

Although the results obtained in these previous studies were enlightening, they were all limited to simplified fish models and only one phase in time, and so allowed only a qualitative, general analysis of significant EOD characteristics. Even the high resolution finite element simulations were only computed in the fish midplane and assumed no variation in the third dimension. This inherently skews the solution from the actual fields, especially in cases such as species with thin tails (e.g., *Eigenmannia*) or

rounder bodies (e.g., *Gymnotus carapo*).[5] More sophisticated numerical techniques are now available to create quantitative, 3-d simulations with realistic model parameters specific to each species. The BEM simulations have led to a better understanding of the electromotor system driving each EOD, and allowed us to extract high resolution data relevant to electrolocation or communication.

5.4.1 Modeling the EOD

Electric fish and their electric organs have usually been treated as dipoles, with one pole the tip of the tail and the high conductivity body as the other. Bennett, in his 1971 review, showed that the currents of individual electrocytes are channeled by surrounding tissues and summed to produce the overall EOD characteristics measured externally to the fish, and that synchronization plays an important role in generating effective, stable output. He also proposed mechanisms for achieving synchronous activation along the electric organ, using conduction delays to equalize effective command path lengths. Field measurements away from the fish surface have shown that EODs can be characterized by their dipole moments (Knudsen 1975), or by their head-to-tail waveforms alone (Bass 1986). However, near the fish, where the fields are more relevant to electrolocation, the EODs can be much more complicated (e.g.: *Hypopomus*, Bennett 1971a; *Gymnotus carapo*, Watson and Bastian 1979, Caputi et al. 1989; *Apteronotus* , Bastian 1981a, Hoshimiya 1980), and so require more complex electric organ and fish body models.

Our field measurements (Chaps. 2, 3) clearly indicate that while the relative timing of electrocytes is tightly controlled, the discharge of the electric organ as a whole is not synchronous for many electric fish species. The modeling results confirm *Eigenmannia* is representative of the stereotypical dipolar electric fish, but *Apteronotus* is not.

The model parameters were used here to analyze the contributions of fish body

[5]Since the divergence of the electric field in the third dimension is forced to zero, the fundamental solutions to the field equations take different form, and lead to systematic errors: decay is slower with distance, etc.

and EO components to the overall EOD spatio-temporal pattern. EO synchronization was explored by varying the timing and magnitudes of current sources in the models to match the *in vivo* data. Parameters were constrained by data in the electric fish literature, especially physiological studies of EO and electrocyte activation as discussed below.

In general, the spatial pattern of each simulated EOD phase was greatly influenced by the strength and location of current sources representing the electric organ. Hot spots in the measured maps must often result from current leaking out along the length of the organ, despite the connective tissue surrounding the EO. This is especially apparent along the tail where the EO fills most of the volume and there is less internal shunting than in the high conductivity body tissue. The current BEM implementation does not account for EO source impedance or variations in internal conductivity.

The model results were probably also confounded by imprecise relative conductivity ratios. For example, in *Eigenmannia* the EOD potential contours on the rostral body surface outline the extent of the EO, which was not possible in the simulation without lowering the internal body conductance (compare Fig. 8b to Fig. 3a). Other discrepancies remaining between simulated and mapped fields may also indicate a need for more detailed spatial resolution in measurements of skin and body conductivity. For example, the simulations did not produce local peaks at the head of the fish as often seen in the field maps (see Chapter 2). These are likely due to "leaky" skin at the operculum and mouth, while the models have uniform high skin impedance along the rostral trunk and head. Gilling should provide a lower impedance path to the internal body, and is known to modulate the EOD outside the operculum (Montgomery and Bodznick 1994). During the field mappings we respired the curarized fish with a continuous stream of water, keeping the gill opening fixed in one position. However, measurements taken near the operculum while one fish was recovering clearly showed an amplitude modulation of almost 10%, correlated with the gilling frequency (unpublished data).

5.4.2 Timing of EO activation in *Eigenmannia*

The EOD of *Eigenmannia* was accurately reproduced with only a few synchronous current sources in the model EO. In contrast, the fish's EO is composed of hundreds of electrocytes stacked in series and parallel (discussed in more detail in Chapters 1 and 3). The head positive phase of the waveform, corresponding to activation of the posterior face of the electrocytes (Bennett 1971a), appears to be highly synchronized along the length of the EO. The similarity of potential waveforms along most of the body length with the head-to-tail waveform indicates that path length compensation works fairly well in this low frequency fish. Timing of activation has been shown to be coordinated: relay axons project to electromotor neurons in specific segments of the spinal cord (Ellis and Szabo 1980), and terminal branches from the spinal cord to the EO are thinner and longer, hence slower, in the paths leading to the anterior EO segments (Bennett 1971a). This mechanism allows the EOD to be fairly accurately modeled with a simple dipole alone, although the distributed source solution produced a closer representation of its spatial extent. Results in the model may be even more improved by utilizing continuous line sources (as in Bacher 1983) for the EO rather than discrete point sources.

5.4.3 Timing of EO activation in *Apteronotus*

In contrast to the synchronous model of *Eigenmannia*, the complex EOD pattern of *Apteronotus* could not be adequately modeled with simple synchronous sources. The propagation of potential peaks and zero-crossings seen in the maps was best replicated by sequential activation of multiple sources along the length of the model fish. This suggests a sequential activation of EO segments with an absence of command path length compensation. This hypothesis is also supported by both anatomical evidence (see below), and analog modeling - Hoshimiya et al. (1980) constructed a circuit to replicate the waveform in the triphasic EOD region of *A. albifrons*, and found it necessary to

include both a phase delay and a local current path between EO segments. Both of these conditions are built into the BEM model.

Considerable general information is known about the unique electric organ and its control in *Apteronotus* (discussed in Chapter 2). The EO in *Apteronotus* extends along the entire trunk to the tip of the tail, lying ventral to the spinal cord (Fig. 4). Relay axons from the pacemaker project down the entire spinal cord, innervating electromotor neurons all along the way (Ellis and Szabo 1980). The number of electromotor neurons counted in the spinal cord increases caudally and is correlated with the cross-sectional area of the EO, which is largest at the tail and falls off to 50% near the head (see Fig. 7 in Ellis and Szabo 1980). At regular intervals along the spinal cord, the axons of the electromotor neurons descend in nerve branches to terminate in the EO as modified endplates, which function as the electrocytes (see Fig. 4). The fine structure of these neurogenic electrocytes has been reported in detail (Waxman et al. 1972).

Representing the combined output of these electrocytes with equivalent current sources is problematic. Bennett (1971a) recorded internal potentials from an isolated electrocyte (Fig. 4b), but these cannot just simply be summed to form the head-to-tail waveform as he proposed. Action potentials propagate along the electrocyte membrane with active impedances and complex dynamics, and the external current should be more closely related to the external potentials, which are more complicated (see Fig. 46 in Bennett 1971a; Fig. 6 in Grundfest 1960). There is also little data available regarding the spatial variation of electrocytes along the length of the EO, or of the connective tissues surrounding the organ. Furthermore, there are many electrocytes in parallel and overlapping between descending nerve branches, making the resulting net external current difficult to estimate (although the synchronized electrocytes within the nerve branch to each EO segment might be adequately represented as a single functional source). Finally, the EO fills most of the volume at the tail and so most of the leakage current flows directly out the skin, while in the model current from the tail sources has an

internal path to flow back to more rostral sources. I chose to model the EO with equivalent source waveforms that produced the best matching external EOD while still fitting our known constraints. Although the actual EO activation is likely to be more complex than the simplified EO model used here, these first order approximations generated EOD waveforms very similar to those in the field maps. The model's adequacy in predicting electrosensory input will be tested in the next chapter on simulations of tail bending and object effects.

5.4.4 Relevant parameters

In each *Apteronotus* simulation the only waveform variables dependent on position along the EO were source magnitudes and time constants. The EOD amplitude is much greater near the tail than at the head, and the model used a ratio of 1:4 for the source magnitudes. Ellis and Szabo (1980) reported greater than a 4-fold increase in spinal electromotorneuron counts from head to tail, but only a 2-fold increase in cross-sectional EO surface area. This suggests electrocytes in the tail may be shorter and have smaller diameters, and therefore smaller capacitance and time constants. This is supported by the dc bias of the flat phase of the EOD waveforms in most fish, slightly negative at the tail and positive more rostral, indicated by the arrows in Fig. 10b. Matching this in the model required the asymmetry in the source waveform caused by the high pass RC filter of the simple electrocyte model. I used a ratio of 4:1 for τ from head to tail, with absolute values ranging between 0.5 and 4 msec depending on the particular frequency and EOD of each fish. These correspond to biologically plausible ranges of R (1 - 10 MΩ) and C (0.01 - 0.4 nF, conservatively estimated from the area of the passive nodes in Waxman et al. 1972). However, the flat phase bias could also correspond to differences in the length of the rostrally and caudally running segments of the electrocytes, as proposed by Bennett to explain differences between the waveforms of different Apteronotid species (1971a, pages 419 to 424). In either case, an imbalance

between EOD phases causes a capacitive return current at the end of each period, similar to the baseline offset seen in the EOD of *Eigenmannia*.

In order to maximize the output of the Apteronotus model, EO timing should be designed to coordinate discharge frequency with conduction velocity and body length. Currents in the head and tail add constructively in phase when the tail activation lags the head by slightly more than one full period. For a 20 cm fish at 600 Hz, the command signal must travel about 15 cm (the EO length) in 1.7 msec, or just under 9 cm/msec. This value is close to the 10 cm/msec estimated visually from the propagation in the field maps, and also within the maximum velocities measured in *Gymnotus carapo* (from 1 to 9 cm/msec according to path length, Lorenzo et al. 1990). Of course, the only parameter under the fish's immediate control is the pacemaker frequency. This may provide a reason for the large temperature dependence of the discharge rate (Enger and Szabo in 1968 reported a Q10 of 1.5): the pacemaker may be compensating for increases in conduction velocity with temperature in order to maintain its EOD amplitude and shape.

The peak widths and separation were found to be highly dependent on the shape of each fish's individual waveform. For example, waveforms from a large male were best fit with a 50% separation and 20% peak widths, while the female maps were usually closer to 35% separation and 10% peak widths and had longer duration flat phases (Fig. 11). This reflects the longer EOD period of the females, which typically have lower frequency than the male brown ghosts (Hagedorn and Heiligenberg 1985).

5.4.5 Chirping effects

In all wave fish species studied to date there has been reported a social behavior termed chirping (Bullock 1970, Dye and Meyer 1986, Hagedorn 1986). A chirp is a transient rise in frequency that can vary in magnitude and duration (in our recordings typically up to 20% above baseline frequency, for duration up to 100 msec; Figs. 12-14). This form of electrocommunication usually occurs during aggressive behaviors or

courtship (Hagedorn and Heiligenberg 1985), with chirp type and rate dependent on context and gender (Dulka and Maler 1993, Zupanc and Maler 1993). Experimental manipulations of the pacemaker and prepacemaker (a nucleus which modulates the frequency of the pacemaker), have recreated many of the transient changes in EOD frequency seen behaviorally (Dye 1987, Kawasaki and Heiligenberg 1990).

We can now perform simulated manipulations of the pacemaker with the more realistic *Apteronotus* model, by testing the effects of frequency changes during chirps. The simulation results correctly predicted the changes in head-to-tail EOD waveform shape (a shortening of the flat phase) due to shifts in the frequency parameter alone, for both brown and black ghost chirps. In the model, as in the field maps, the head-to-tail waveform is dominated by the large amplitude at the tail, where the flat phase corresponds to the delay between the end of activity from the current command signal to the onset of the next signal. However, the decrease in peak amplitude found during chirps was not fully matched by changing the frequency parameter alone; instead, the peak width also had to be decreased in proportion to the period. Therefore from the model results we would predict the overall loss in amplitude is due to two causes: currents more out of synchrony adding destructively out of phase, and individual sources having lower effective magnitude. In the fish, the electrocyte outputs may be lower from maintained inactivation of their active channels at higher frequencies. A similar drop in amplitude due to maintained inactivation has been previously observed in the pacemaker axon action potentials (Dye and Hieligenberg 1987).

Hagedorn and Heiligenberg (1985) showed brown ghost chirps range over a continuum from short frequency rises to long interruptions lasting up to 500 msec. During interruptions there persists a smaller amplitude oscillation at a harmonically unrelated higher frequency. This suggests that the pacemaker has been driven hard enough to totally inactivate the output of the relay axons, leaving the EO electrocytes

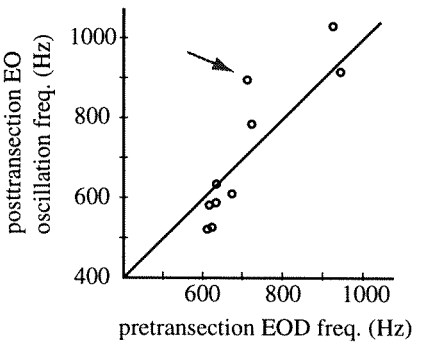

Figure 5.16 Spontaneous oscillations of the electric organ in *Apteronotus*. After transection of the spinal cord rostral to the level of the electromotor neurons, the EO oscillations differ slightly in frequency from the normal EOD. (adapted from Dye and Meyer 1986)

to oscillate on their own. It is known that the *Apteronotus* EO motorneurons will spontaneously oscillate after transection of the spinal cord near the head. Dye and Meyer (1986) measured both the pretransection and posttransection frequencies of the EO (Fig. 16), and concluded that the peak power of the intrinsic EO oscillation is close to the driven EOD frequency. However, if we look at the difference Δf between post- and pretransection, the higher frequency fish tended to have positive Δf while lower frequency fish had negative Δf. If the fish generating the chirp in Fig. 15 had a positive Δf like the one marked by the arrow in Fig. 16, then the interruption in driven command is presumably uncovering the free running EO oscillation from loosely coupled EO segments, as proposed by Hagedorn (1986, page 514). The EOD frequency spectrums in Fig. 15c provide evidence for this "natural" EO frequency: harmonics of the interruption chirp frequency are also present in the normal EOD, but greatly suppressed.

"The statements also have reference to the fish when in a straight form; if it assume a bent shape, then the lines of force around it vary in their intensity in a manner that may be anticipated theoretically."

Michael Faraday, 1839

6 Exploratory Behaviors: Description and Simulation

6.1 Introduction

Electroreception in weakly electric fish constitutes an excellent model system for the study of active control of sensory acquisition. Weakly electric fish exhibit a rich repertoire of characteristic behaviors while exploring their environment, including both body movements and modulations of the EOD interpulse interval in pulse fish (e.g., see Toerring and Belbenoit 1979). Many species are known to arch their bodies while repeatedly swimming past, or "scanning", objects (Bastian 1986b). Another typical behavior is for the fish to approach an object tail first, bending its tail towards the object (Fig. 1a, from Behrend 1984). These movements should result in significant changes in the sensory input, both in the object image and from changes in body orientation itself, a consequence termed sensory reafference (von Holst and Mittelstaedt 1950). The fish presumably utilize strategies to enhance the information available in the peripheral electrosensory image, including distinguishing between reafference and exafference.

Previous electrolocation experiments have examined the electrosensory stimuli or the physiological responses of electroreceptors independently from natural exploratory behaviors. For example, the early receptor-response studies of Hagiwara et al. (1965) and Scheich et al. (1973) reported changes in firing during the presentation of various objects and electrical stimuli to immoblized specimens of *Eigenmannia* and *Apteronotus*, but did not report the local field strength at the receptor. Bastian (1981; 1986b) did measure the change in the RMS EOD potential, together with single unit electroreceptor responses, after placing conductive and insulating spheres and cylinders at different distances and

rostro-caudal positions from *Apteronotus*. These studies were all very useful in measuring object effects on single receptor responses; however, the animals were necessarily held in fixed position, usually curarized and respirated.

In the behavioral experiments that have been reported, there were no field measurements or physiology, to avoid interference with the natural behaviors (e.g., Toerring and Belbenoit 1979; Behrend 1984; Knudsen 1974; Heiligenberg 1973; Lissmann 1963). For example, Toerring and Belbenoit (1979) cataloged six common behaviors, which they termed probing motor acts, in the pulse mormyrid *Marcusenius cyprinoides*. The probing motor acts occurred at defined distances from the test objects, and included characteristic changes in the interpulse intervals of the EOD. However, they did not measure the field spatially nor the consequences of these motor acts on the electric images or on the electroreceptor responses. We need some way to bridge these two types of experiments, to study the sensory effects of exploratory behaviors.

In this chapter I examine the sensory consequences of weakly electric fish behaviors noninvasively through simulation. I reconstructed the electric fields in the water surrounding the fish using the methods of Chapters 4 and 5. First, a model of *Eigenmannia* was used to recreate the bent tail probing behavior reported by Behrend (1984). Then I videotaped exploratory behavior from a specimen of *Apteronotus albifrons* (the black ghost). *Apteronotus* makes a good test subject because: (1) it has a neurogenic organ, so can be paralyzed and mapped effectively to verify the simulations; (2) it has a high frequency complicated EOD, in contrast to the simple EOD of *Eigenmannia*; and (3) it has a voracious appetite and is very territorial, so should be amenable to reinforcement training (as shown in Knudsen 1974). By simulating the fish's EOD with a high resolution, 3-d model, I was able to compute the temporal sequence of electrosensory image patterns over the electroreceptor array that result from the fish actively probing a foreign object. The results were used to test a simple model of electroreceptor responses and predict the entire afferent input map being projected to the electrosensory lateral line lobe (ELL) in the hindbrain.

Figure 1. *Eigenmannia* simulations

A. Tail probing behavior from Behrend (1984, Fig. 1), showing 4 overlapped, consecutive frames of video at 40 ms intervals.

B. Midplane cross section through model fish for the four frames to be simulated.

C and D. Decomposition of the movement into tail bending only (C) and body translation only (D) for separate simulations.

E. Abnormal tail probing behavior of an *Eigenmannia* after lesioning the corpus cerebelli (from Behrend 1984, Fig. 8).

F. Midplane cross section through model fish for the four lesion frames to be simulated.

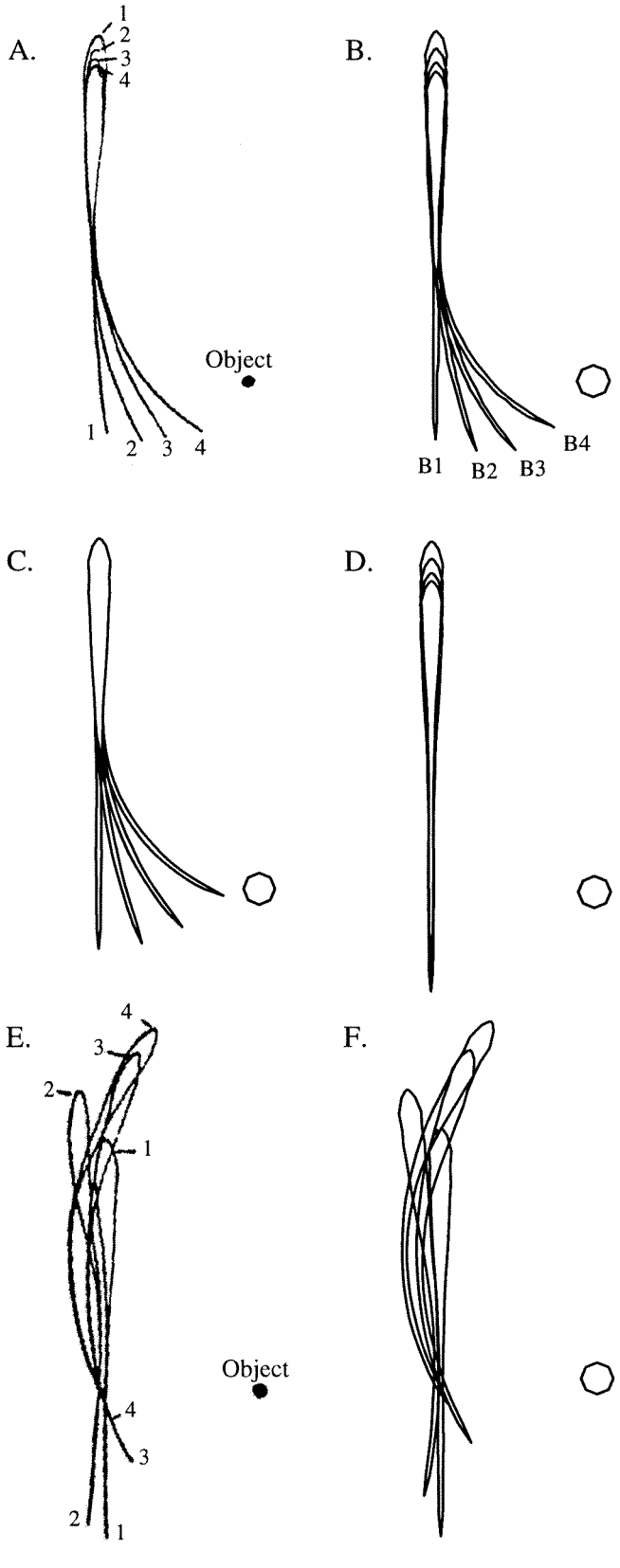

6.2 Methods

6.2.1 *Eigenmannia* behavior

I first used the simulator to analyze a previously published, tail probing behavior of *Eigenmannia*. Behrend (1984) allowed blinded specimens of *Eigenmannia* to freely roam a 50x35x15 cm tank into which was added a metal rod and a carbon rod for the fish to explore. Exploratory behaviors were recorded with a TV camera mounted under the tank. The fish displayed a stereotypical probing of objects by bending the tail and caudal half of the body towards the object. Four video frames of this behavior, spaced at 40 msec intervals, are overlaid and shown in Fig. 1a (from Fig. 1 in Behrend 1984). Each of these frames was used to orient the *Eigenmannia* model and object for simulation (Fig. 1b). Note however, that Behrend used metal and carbon rods for objects, and sometimes shorted them together outside of the tank. These unrealistic configurations were difficult to replicate in the simulation, so instead the model object used here was a faceted metal sphere ($\sigma \rightarrow \infty$) of 2.5 cm diameter, constructed of 18 nodes and 32 triangular surface elements, and centered in the midplane of the fish.

6.2.2 *Apteronotus* behavior

In addition to analyzing previously published data, I conducted my own experiments to identify and closely monitor exploratory behaviors for simulation. A black ghost (*A. albifrons*) specimen was kept in a large behavior tank (1m x 1m x 20cm) with water maintained near 2 kΩ-cm resistivity, pH 6.5, and temperature between 23 and 25 degrees C. The room was kept on a 12 hour on-off light cycle. A plastic tube near one corner supplied a resting place for the fish during the day, and a large rock (approximately 5x7x8 cm) was kept in the center of the tank. Each morning, approximately one hour before the overhead lights came on, the recording apparatus was set up under dim lighting, and black worms were placed into the center of the tank over the rock. The setup lights were then extinguished, leaving only 2 infrared spotlights for

illumination. The fish quickly learned these lighting cues and within 5 minutes would emerge from its tube to forage.

I first attempted to find characteristic behaviors during spontaneous exploration (as in Toerring and Belbenoit 1979). After the fish had been living in the tank for several weeks under the expermental regimen, it appeared well accommodated to searching for worms near the rock. I then began to substitute a sphere, either metal or ceramic, in place of the rock (see figures in Results), either during the setup time or at intervals when the fish returned to its tube. The sphere had a diameter of 2.5 cm, and was held 8 cm above the tank bottom by a 3 mm diameter plastic rod. Worms were again added near the object, and the fish's subsequent behavior was observed and videotaped. At the end of each feeding period the object was removed and the rock returned to the center of the tank.

Video was recorded during the feeding period from two angles (Fig. 2a), top and side views, using infrared video cameras (Sanyo CCD model VDC2624 – inexpensive black and white security cameras with external sync inputs). The two video signals were synchronized, combined with a custom built video mixer (Rasnow et al., in press), and recorded along with a time and date overlay on a VCR (Sony EV-S900). Stationary electrodes in the tank were also used to monitor the EOD and record it on an audio channel of the video tape. Sequences of motor behavior from the video were analyzed to identify exploratory movements, with selected frames from the relevant behaviors chosen for simulation.

6.2.3 Model setup

Both sets of behavioral data, Behrend's tail-probing in *Eigenmannia* and my own black ghost videos, were ported to the simulator with the following method. The fish's body outline from each selected video frame was used to orient the fish model appropriately for simulation (Fig. 2b). The fish model was manipulated with functions

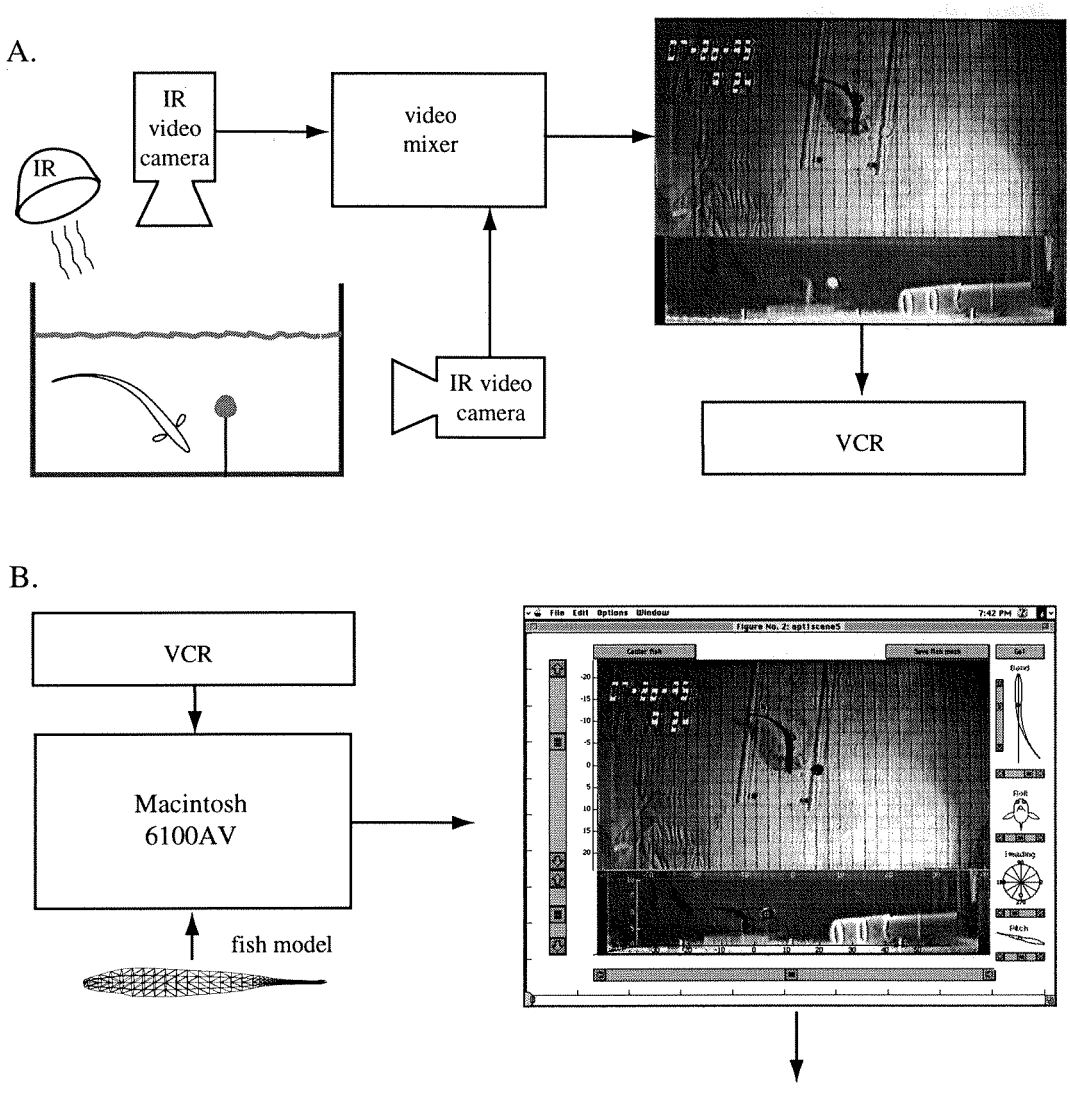

Figure 2. *Apteronotus* behaviors and simulations

A. Videotaping behaviors. Infrared video cameras imaged the fish from two orthogonal angles.

B. The videotape was later viewed in a MATLAB figure window. A 3-d wireframe model of the fish body (black) was superimposed on the video and translated, rotated, and bent (using the controls around the window) to coincide with the fish's body in the two video views.

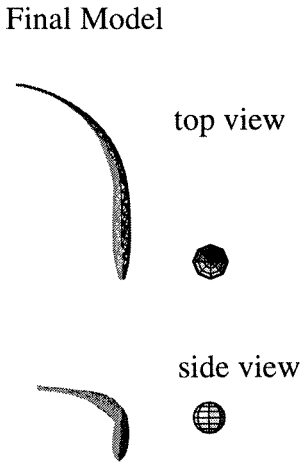

written in MATLAB 4.2 (The MathWorks) to translate and rotate the body mesh in 3-d space. The model was aligned to the real fish by overlaying the Matlab graphics window over the video, and appropriately scaling and orienting each viewpoint to match landmarks in the video. Eight parameters were required to orient the fish: 3 for translation, 3 for rotations, and 2 for tail bending. The tail was bent with a function to maintain arc length of the center line (tail length remains constant) while bending the caudal portion of the body along any desired radius of curvature (in the midplane, i.e., left or right only; see Fig. 3a). Object and fish coordinates were measured relative to the tank boundaries and saved for input to the simulator. Since the *Eigenmannia* video records were relatively simple, the model fish could be very closely aligned to the actual orientation (compare Fig. 1a and b). Replicating the black ghost video frames was more difficult, but matched well to first order (see Results).

6.2.4 Simulations

I used the boundary element method electric fish simulator described in Chapter 4, with the tuned fish models from Chapter 5. For each selected video frame, the electric potential and current density were computed on the skin, and the potential was solved for selected points in the water about the fish and object. Simulations were run both with the object present (the object condition) and without the object present (the unperturbed condition) to allow the difference due to the objects to be calculated. For the *Eigenmannia* simulations, the fish and object were both assumed to be at the same depth (Behrend's video was a top view only), so that a midplane cross-section clearly shows both fish and object outlines. I also simulated three control conditions to contrast with the reported normal behavior: tail bending with no translation (Fig. 1c), body translation with no tail bending (Fig. 1d), and finally, a sequence of positions corresponding to the abnormal behavior of a fish with a lesioned cerebellum (Fig. 1e,f; from Fig. 8 in Behrend 1984). For the simulations of the black ghost behaviors, the fish rarely oriented itself in a

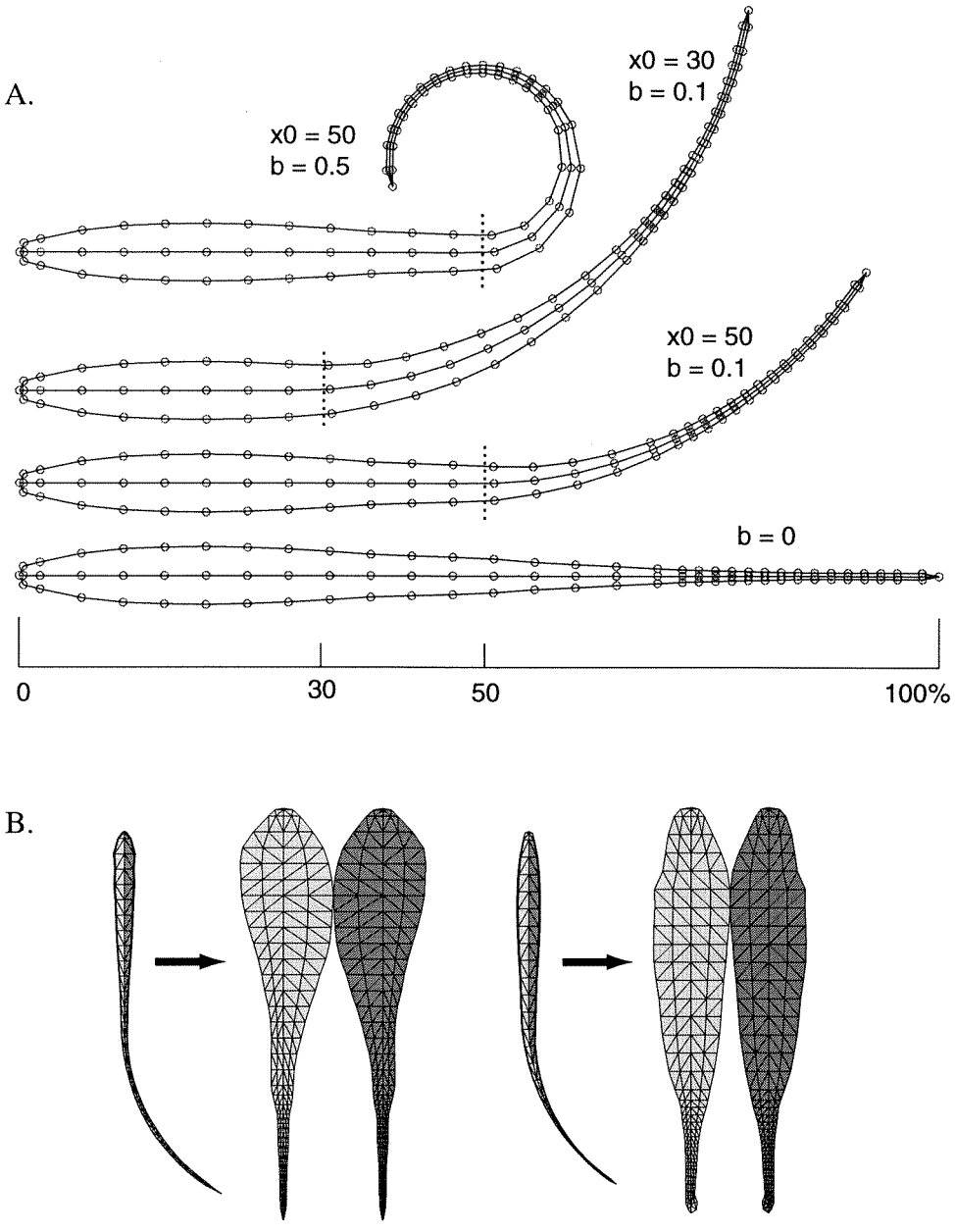

Figure 6.3 Methods A. Examples of bending the tail with 2 parameters: x0 is the position along the fish's body length at which the bend starts, and 1/b is the radius of curvature. The arc length of the center line remains constant.

B. Flattening the 3-d fish meshes to view the entire skin surface.

fashion that made planar maps convenient (see Results). Therefore only skin maps were calculated for the actual behaviors. In order to view likely effects in the midplane, three representative control conditions were slightly modified from actual frames, moving the fish and object to the same depth and midplane, with no rotations.

6.2.5 Maps of transdermal potential and receptor responses

The simulation results were used to reconstruct the electrosensory images available to the fish: the body mesh was unzipped along the belly, both halves were flattened into a flat skin map (Fig. 3b), and the transdermal potential computed at each node by dividing the current density by the skin conductivity. The resulting map represents the transdermal sensory stimuli over the entire body. Therefore, the information available to the ELL is a spatio-temporal convolution of this transdermal potential pattern with the array of electroreceptor transfer functions. As a first order example, I calculated the RMS amplitude of the transdermal potential, corresponding to a simple model of P-type electroreceptor responses (see Chapter 1 for receptor details). However, since the *Eigenmannia* model EO was perfectly synchronous, the EOD pattern was similar for all phases of the EOD period, differing only by a scalar multiple. Therefore for convenience in the *Eigenmannia* simulations, the absolute value of the transdermal potential at a single EOD phase (the head-negative peak) was used to represent the P-receptor stimuli, with results very similar to the true RMS amplitude.

6.3 Results

6.3.1 *Eigenmannia* simulations

Potential maps in the midplane

The four frames from Behrend, labeled B1 to B4, were simulated both with and without a 2.5 cm diameter conducting sphere placed at the location indicated in Figure 1b. The resulting midplane potential maps for frames B1 and B4 are shown in Figure 4, together with the difference maps between the two conditions, all taken at a phase of the

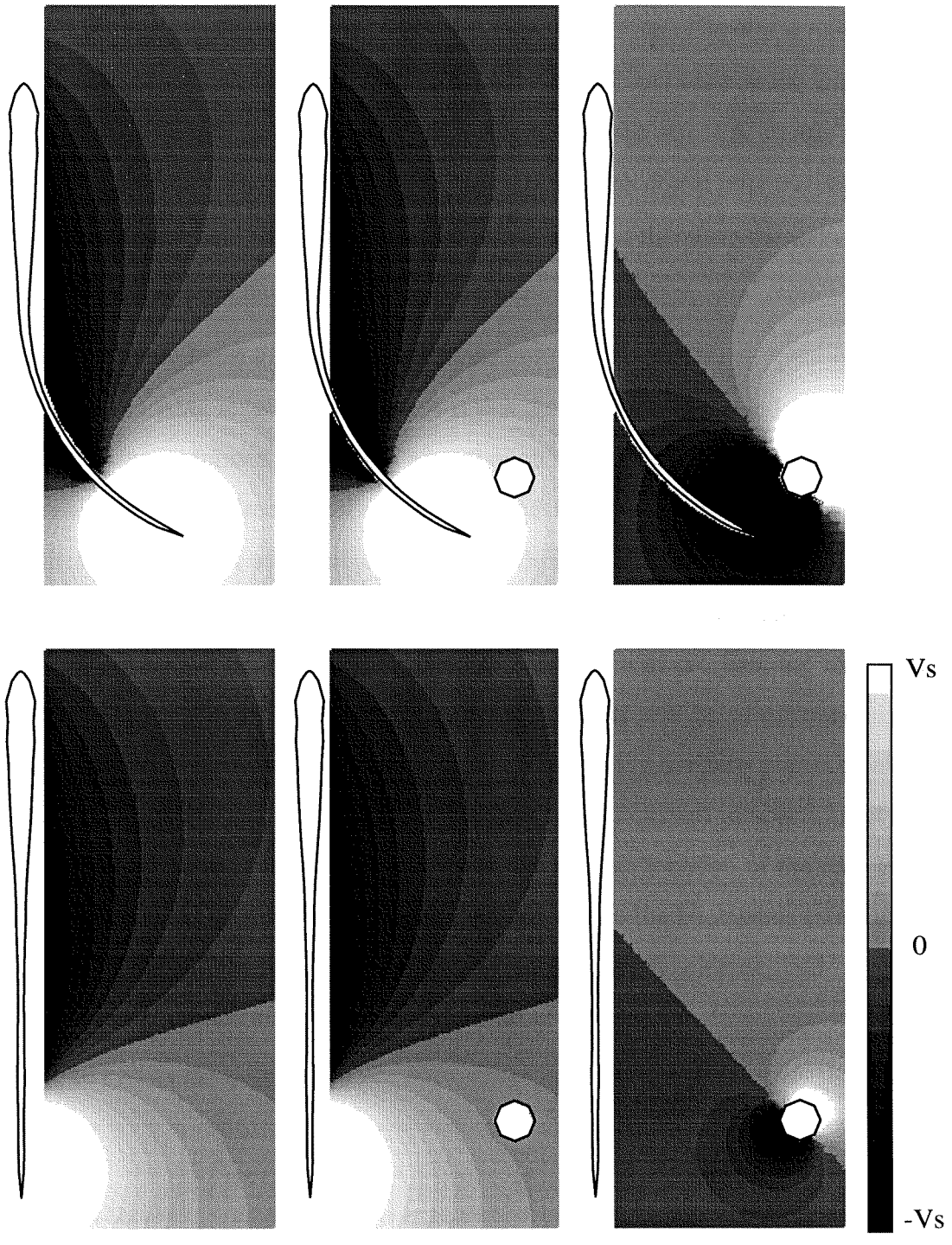

Figure 6.4 Midplane maps of potential from simulated frames B4 (top row) and B1 (bottom row). Left: no object present. Middle: object present. Right: difference maps generated by subtracting the no object map from the object map left (middle-left). Scales: Vs = 25 mV in left and middle columns, 0.25 mV in right column.

EOD near the head-negative peak of the head-to-tail waveform. The object makes a very small difference in the absolute potential (compare the middle column to the left column), but when the difference is magnified by a factor of 100 the effect is clearly that of an induced dipole (right column). Bending the tail towards the object puts the object into a much larger electric field (the gradient of the potential), and therefore the induced dipole from the object becomes much stronger.

Object effect: the induced dipole in the midplane

One surprising result from Figure 4 is that the direction of the induced dipole did not change between frames B1 and B4, even though the tail bending changed the overall field drastically. The direction of the unperturbed field vector at the object's location determines the direction of the object's induced dipole moment (Chapter 4). The two lobes of the induced dipole are separated by a zero plane, lying perpendicular to the field vector (Fig. 5). If the zero plane is mapped to the surface of the fish, the intersection forms a zero line. The difference in the external potential will be of opposite sign for surface points on opposite sides of the zero line. Overlaying the zero planes of all four frames (Fig. 5) shows that the zero plane remains fairly constant in space, implying a constant field direction at the object. However, the relative location of the zero line on the fish surface shifts slightly rostral along the body due to the backwards translation of the fish during the tail bending behavior. More significantly, the electric field vector near the skin is most perpendicular to the surface rostral of the zero line.

Figure 6.5 Object induced dipoles.

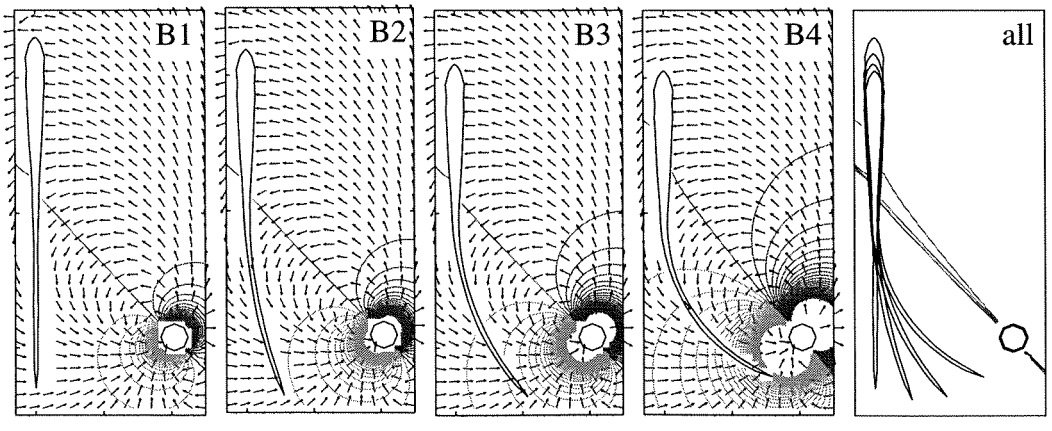

Current vectors in the midplane

Since the induced dipole from the object depends on the strength and direction of the unperturbed electric field vector, I next examined the electric field in the midplane without the object present (Fig. 6). Field vectors were calculated by taking the numerical gradient of the potential maps (as in Fig. 6a). Figure 6b is a composite of all four frames, with normalized vectors showing the direction of the electric field at regular spatial intervals. Near the tail, the only points at which the field direction remains constant throughout the tail bend (shift< 5 degrees) are in the region near the object, indicated by the dashed circle. Figure 6c shows the same data, but this time the arc swept out by each current vector is filled in, to simplify visual comparisons.

During the tail bending behavior, the fish also moves backwards, with the tip of its snout traversing almost 3 cm from frame B1 to B4. To test the importance of this translation, I simulated the tail bending without translating the body. The results (Fig. 6d) show that the field direction at the object now changes by about 30 degrees under these conditions (compare to Fig. 6c). Similarly, when the body is translated alone with no tail bending, the field at the object again changes direction (Fig. 6e). To further test the importance of the fish's movements, a second sequence of recorded movements was simulated, this time taken from Behrend's video records of a fish after cerebellar lesions had impaired its normal movement control. The field direction at the object drastically changes during the abnormal movements (Fig. 6f).

When the field magnitude is also represented by the length of each arrow, as in Figure 7, we see again that bending the tail towards the object greatly increases the field strength at the object's location. Subtracting the tail straight from tail bent conditions, without the object present, reveals the difference due to bending the tail alone (Fig. 7c,d). Comparing Fig. 7d to 7a, the current entering the rostral half of the body increases on the side towards the bend and decreases on the opposite side. This effect is further explored below.

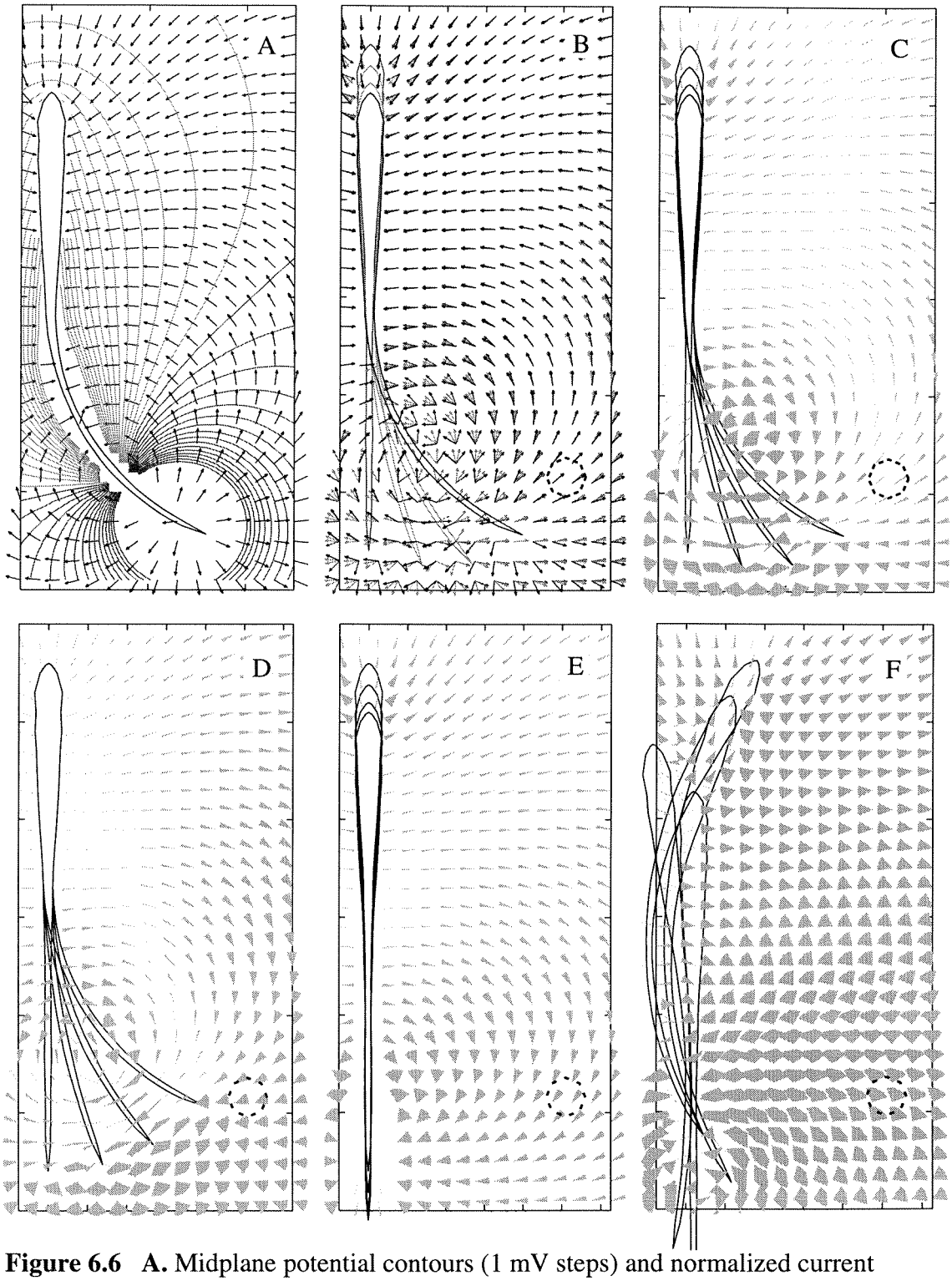

Figure 6.6 **A.** Midplane potential contours (1 mV steps) and normalized current vectors for frame B4, with no object. **B.** Current vectors overlaid for all 4 frames. **C.** Pie wedges created by filling in an arc as each vector swings from B1 to B4. **D-F.** Wedges for the three control simulations: bend only, translation only, and lesioned.

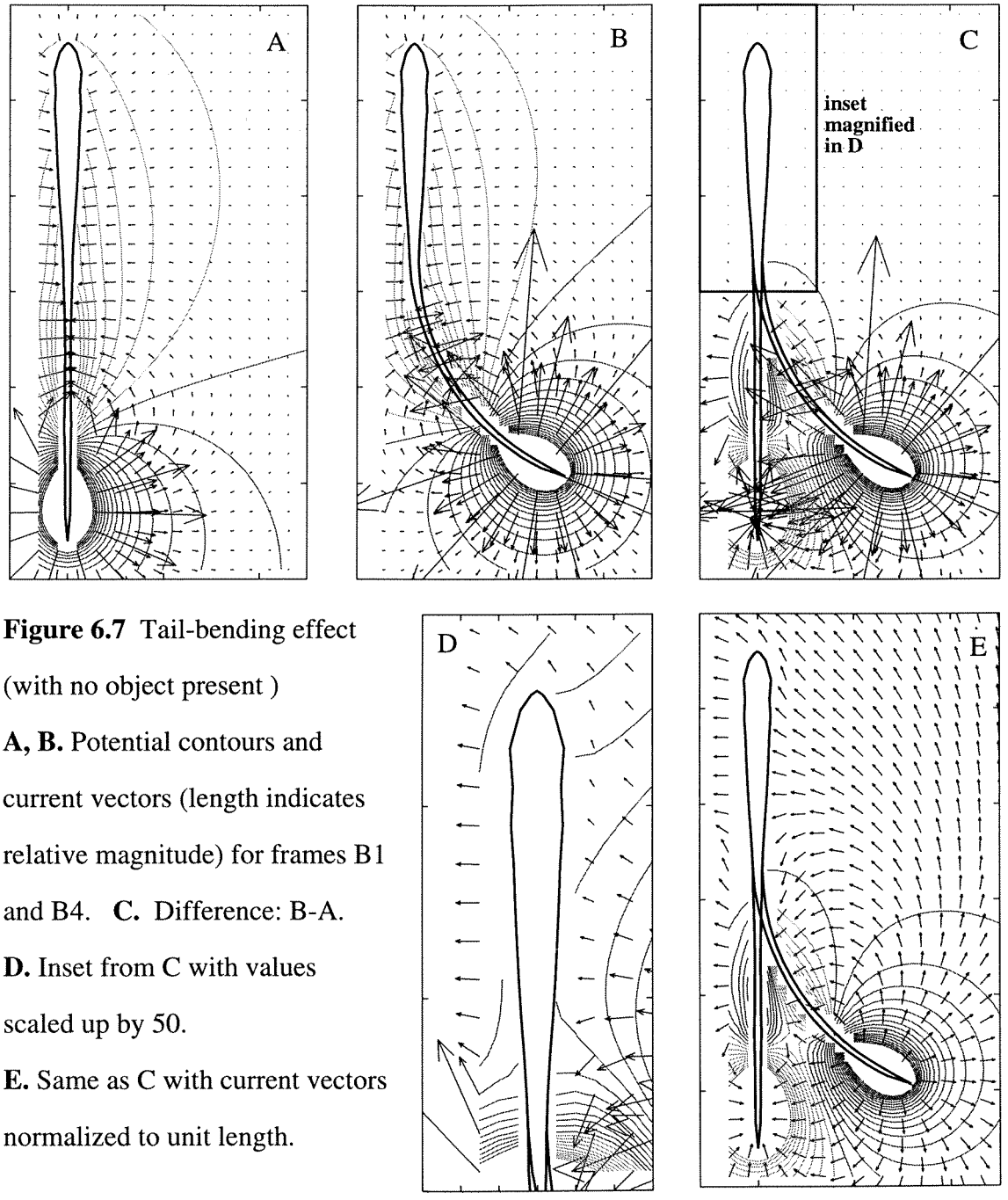

Figure 6.7 Tail-bending effect (with no object present)

A, B. Potential contours and current vectors (length indicates relative magnitude) for frames B1 and B4. **C.** Difference: B-A.

D. Inset from C with values scaled up by 50.

E. Same as C with current vectors normalized to unit length.

Transdermal potential - effect of object

While the midplane results indicate the effects of object and tail bending on the external fields, the sensory consequences must be examined at the receptor level, in the field across the skin. For purposes of comparison to Fig. 5, for each frame of the behavior I first computed the change in external potential at the skin surface due to the object. The results (Fig. 8, top row) verify that the induced dipole from the object smoothly modulates the potential external to the skin surface as expected, from around -10 μV at the tail tip to slightly positive at the nose. Next, to examine the fields across the skin, I computed the absolute value of the transdermal potential for this phase of the EOD. (Since the model EO was perfectly synchronous, the absolute value is very close to the RMS value and should approximately represent the P-receptor stimuli). Then the transdermal potential without the object was calculated and subtracted from the transdermal potential with the object present. The resulting maps (Fig. 8, middle row) represent the difference the object makes in the transdermal stimulus, i.e., the object's contribution to the overall elecrosensory image. At this level the rostral difference is less than about 1 μV in amplitude, or on the order of 1 part in 10000 of the absolute transdermal potential.

Transdermal potential - effect of tail bending alone

Since the object image is a very small percentage of the overall EOD field at the skin, it may be masked by other stimuli, such as reafferent changes in the field from the fish's tail bending. To quantify the effect of tail bending alone, the transdermal potential from the straight fish, B1, was subtracted from the transdermal potential of the three bent tail frames with no object present. The results (Fig. 8, bottom) show that tail bending does cause complicated changes in the transdermal potential that have relatively large magnitudes compared to the object image. For the midline along the rostral body, on the right side inside the bend, the RMS magnitude increased by up to 20 μV, while on the left side away from the bend, it decreased by over 100 μV (Fig. 9).

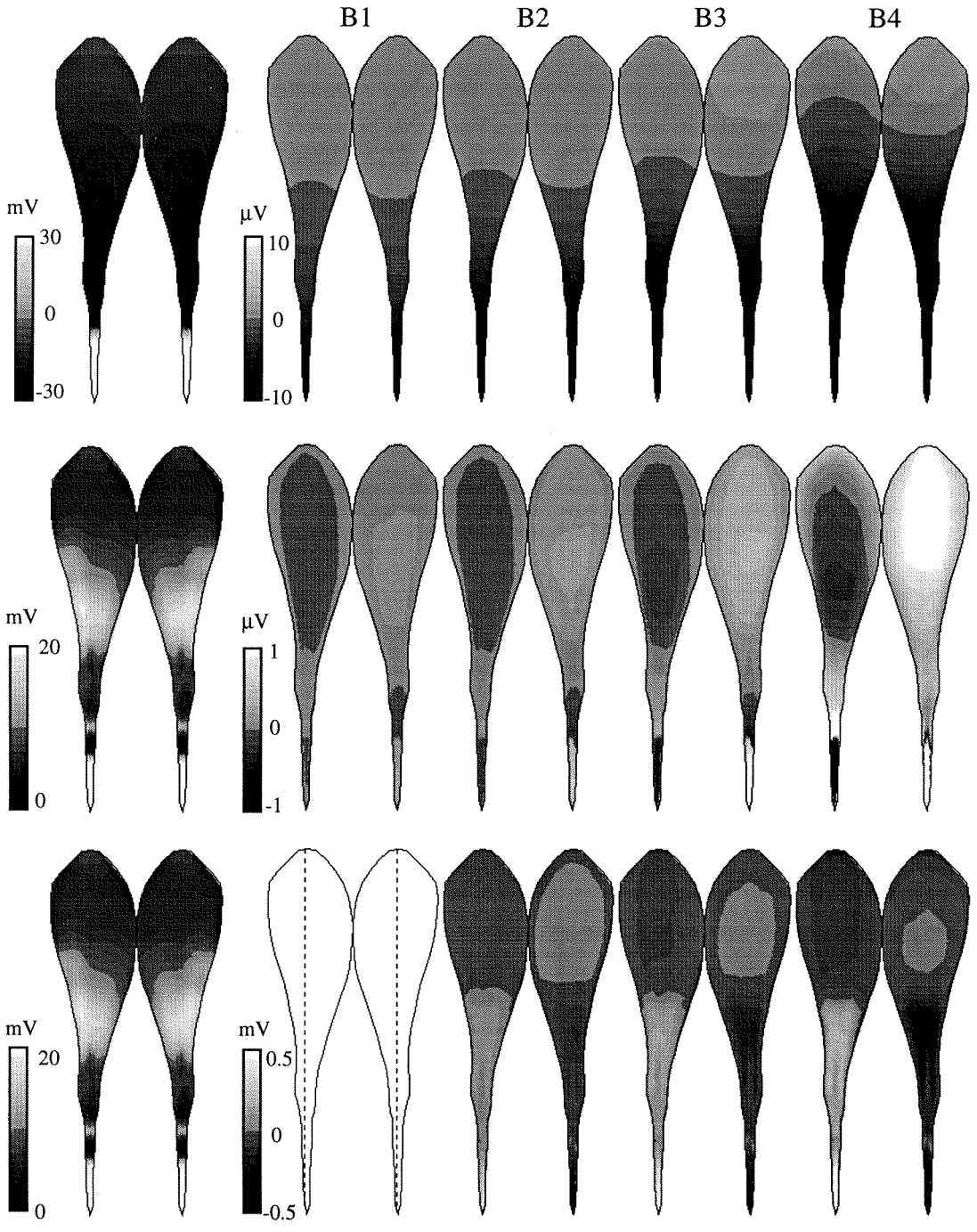

Figure 6.8 Skin maps at peak of the head-negative EOD phase. Top: external potential on skin surface (left most), and the difference due to the object at the 4 bend angles. Middle: absolute value of the transdermal potential, representing the EOD amplitude (left most), and difference maps due to object. Bottom: difference in transdermal potential due to bending the tail only (subtracting B1 from others, with no object present).

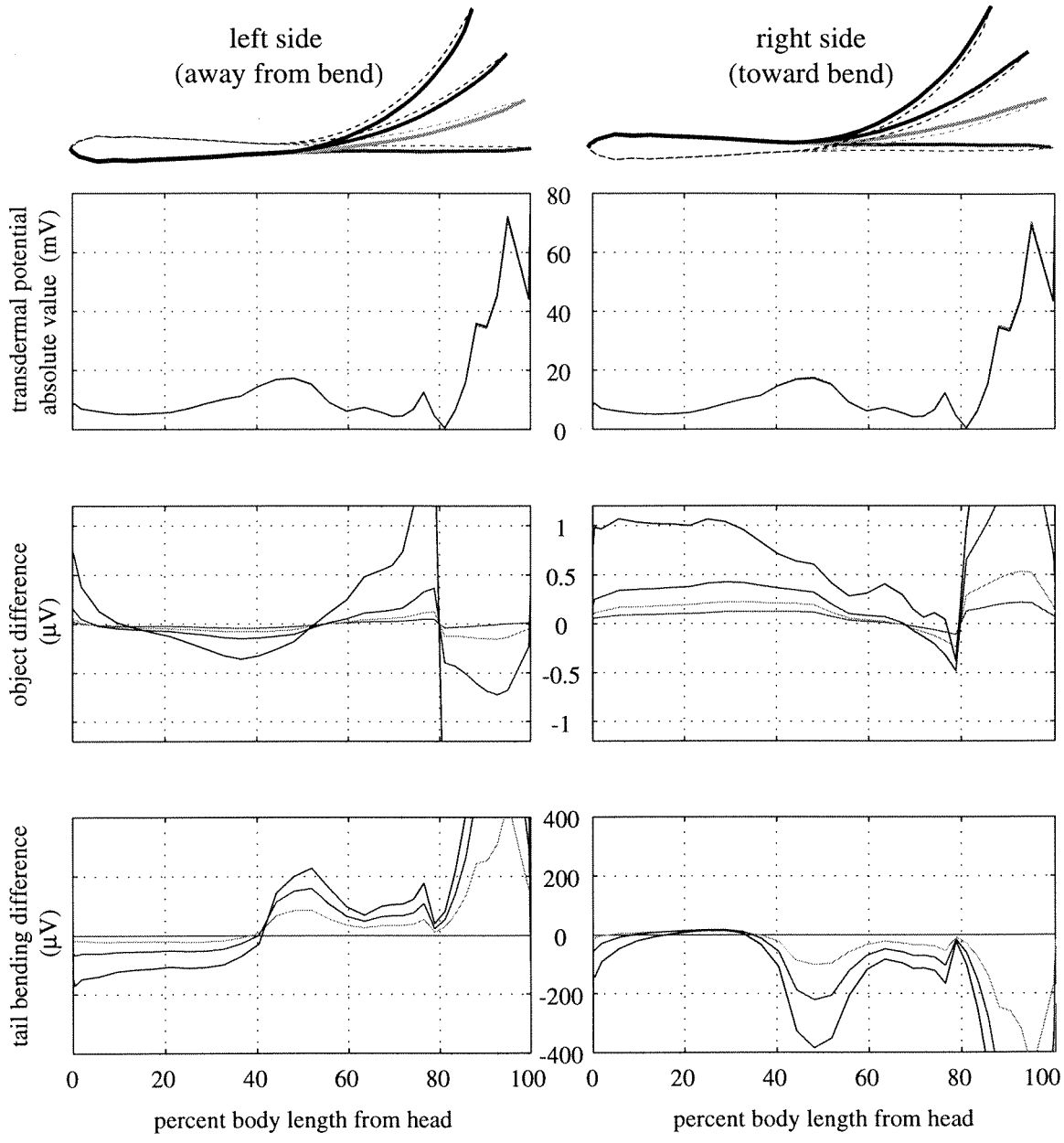

Figure 6.9 Transdermal potentials along the left and right midlines of the body (dashed lines indicated in Fig. 8). Top: the absolute value, or envelope, of the transdermal EOD; middle: the difference in amplitude due to the object; bottom: the difference in EOD amplitude due to tail bending alone. Multiple curves are for the 4 tail bending angles.

6.3.2 *Apteronotus* behavior

After a few days of acclimation following introduction to the behavior tank, the black ghost specimen learned that worms could be found near the rock in the center of the tank, and would approach that location first. When new objects were introduced later, the fish showed some novelty responses and behaviors which appeared to be scanning or orientation to the object. The specific behaviors reported below, from which I chose frames to simulate, are those which appeared significant to the fish or obviously included a novelty response to the test object.

Scenario 1: Normal feeding

In the normal tank environment before any exposure to other objects, the fish fed around the central rock in a stereotypical manner (Fig. 10a). It approached the rock head-first at a fast swim, presumably guided by memory. While oriented on its side it would circle the rock, performing a head first "cartwheel", in search of worms at the rock's base.

Scenario 2: First exposure to novel object

After two weeks of normal feeding, the rock was removed prior to the next feeding period and replaced by the metal sphere, while the fish was still in its tube. When the feeding period began, the fish swam in head-first as in the normal feeding behavior, but after approaching to approximately 5 inches from the sphere (or ~12.5 cm; distances are reported in inches to correspond to the grid spacing on the tank bottom), the fish turned aside and swam off to a corner tube (Fig. 10b).

Scenario 3: First exploration of novel object

Several minutes after first turning away from the metal sphere, the fish returned to the center of the tank, this time tail-first (Fig. 10c). It proceeded to do a tail-first cartwheel about the sphere, appearing to scan it closely. It then began to look for worms on the bottom as normal. After this first exposure, the fish *always* made its approaches to the center of the tank *tail-first*, on all subsequent days for the remainder of the experiment.

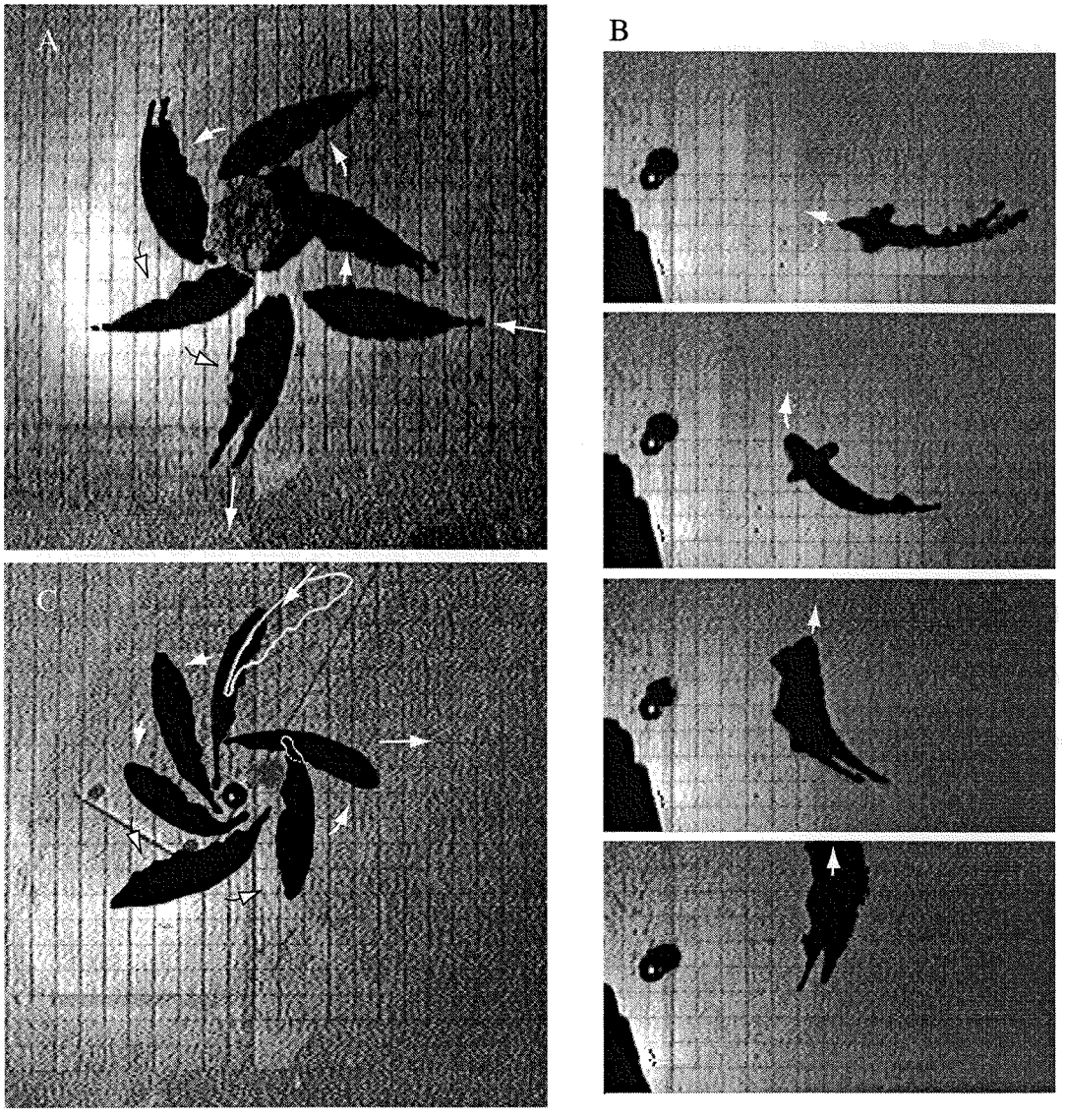

Figure 6.10 Computer enhanced infrared video records of black ghost behaviors A. Composite of 6 frames taken from initial normal feeding behavior. The fish approaches head-first and rolls onto its side (arrow on right edge) before executing a cartwheel about the rock. B. First exposure to novel object, a 2.5 cm diameter metal sphere. After approaching within 12 cm (about 4.5 inches on the bottom grid), the fish veered off and swam away. C. Minutes later the fish returned tail-first and executed a tail-first cartwheel around the sphere. (All frames were enhanced in contrast and brightness, and shadows were digitally removed in C for clarity.)

Scenario 4: Object switch during the feeding period

One week later I added a ceramic, nonconducting sphere to the tank, but this time with different timing. The fish was first allowed to forage around the rock. After it returned to its tube for a short rest during the feeding period, I replaced the rock with the ceramic sphere. Upon returning tail-first to the center of the tank at a fast swim pace (Fig. 11, frames A,B), the fish approached to within about 2.5 inches (5.2 cm) before executing a tail flip escape response (frames C-F). The fish then backed up past the object, partially rolling onto its back (frame G). After this first distant scan, it righted itself and slowly approached the sphere several times head-first (frames H,I), seeming to touch it (similar to the chin probing behavior described by Toerring and Belbenoit, 1979). The fish then swam off, quickly recovered and began to forage again normally, except for infrequent intervals during which it appeared to inspect the object. During ensuing trials, these apparent scanning instances became more and more inconspicuous, preventing further definitive conclusions as to the fish's point of attention.

6.3.2 *Apteronotus* simulations

From the recorded behaviors in Figures 10 and 11, several frames were chosen for simulation and the model appropriately oriented (see Fig. 12). In two of the frames, 10B and 11B, the fish was expecting to find the rock but instead found one of the spheres in place of the rock. For those two frames, I simulated both the actual situation with the sphere, and the expected situation with the rock (the gray outlines in Fig. 12, frames 10B and 11B). Note that in all 7 simulated frames, the fish is oriented obliquely to the object, at various rotations and angles. Therefore there was no good way to cut a plane through both the fish and object to visualize the fields in the water, so only the transdermal potentials were calculated.

Before looking at the transdermal potentials however, I wanted to examine the distortions these objects were causing in the water around the fish. Therefore three representative control conditions were modified from actual frames to orient the fish and

Figure 6.11 Black ghost novelty response to unexpected object. In the middle of a feeding period the rock was replaced by a ceramic sphere (nonconductor). The fish returned to feed tail-first (A) at a relatively fast swimming speed. After approaching to within 6.5 cm (B), the fish executed a tail flip (C to E). It proceeded to back up past the object before turning for a head-first. examination. (Notes: B-F are consecutive video frames at 30 fps. All frames computer enhanced. The rectangular outline is a plexiglass plate on tank bottom for positioning the object.)

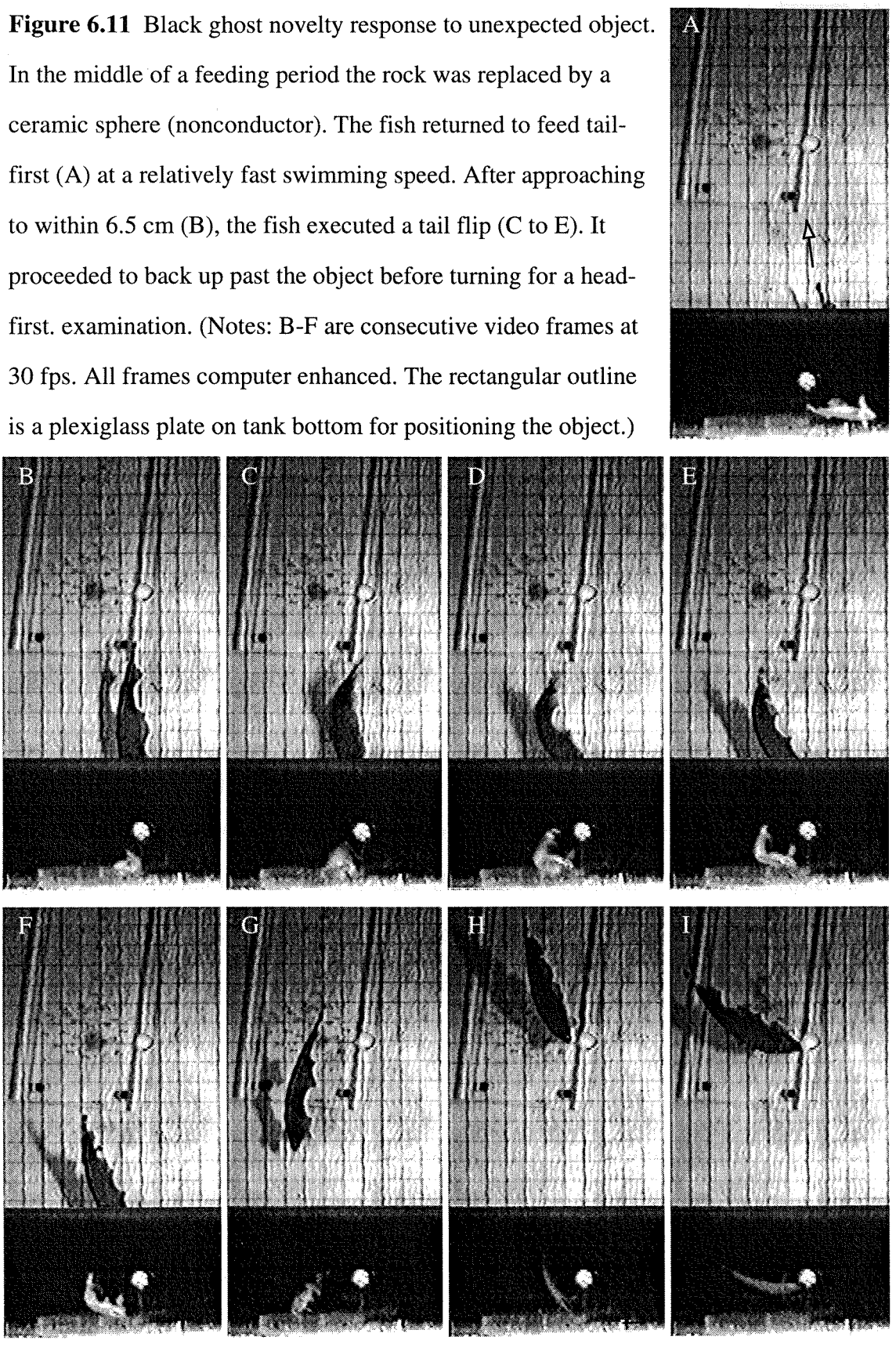

object at the same depth, resulting in the five test frames shown in Fig. 13. Frames 13A and 13B are similar to the initial head-first approach to the object as in 10A and 10B; 13C and 13D are similar to the tail-first approach to the object, as in 10C and 11B; frame 13E is similar to the tail probing behavior occurring in 10C. For convenience, frames A-D were aligned such that the fish body is perfectly straight and in line with the object.

Field maps and object effects in the control simulations

Two midplane maps from each control simulation are shown next to each model in Figure 13. One shows the overall field with the object (with potential contours at 1 mV steps, and normalized current vectors), and the other shows the difference between object and no object conditions, magnified by 100. All of the maps are taken at a phase of the EOD near the head-negative peak of the head-to-tail waveform. The results from frames A-D reflect the symmetry in their models: the currents in the difference maps are mainly parallel to the body surface, except at the head and tail tip. The potential contours indicate the induced dipole from the object is much larger for the rock than for the sphere. This was to be expected since the magnitude of the object-induced dipole should be proportional to the object's volume.

The maps for the tail probing behavior in frame E appear similar to those in the *Eigenmannia* simulations. However, the EOD is modeled after the actual *Apteronotus* EOD (see Chapter 5), which is not synchronous, but rather includes shifting and propagating patterns. Figure 14 shows 8 different phases of the EOD and the resulting revolution of the object-induced dipole over the course of the EOD period. In several phases the field at the object cannot be considered constant in space and therefore the object distortion is no longer purely dipolar. For example, in the fourth frame from the top (Fig. 14) the potential contours around the object form 4 distinct lobes (a quadrapole).

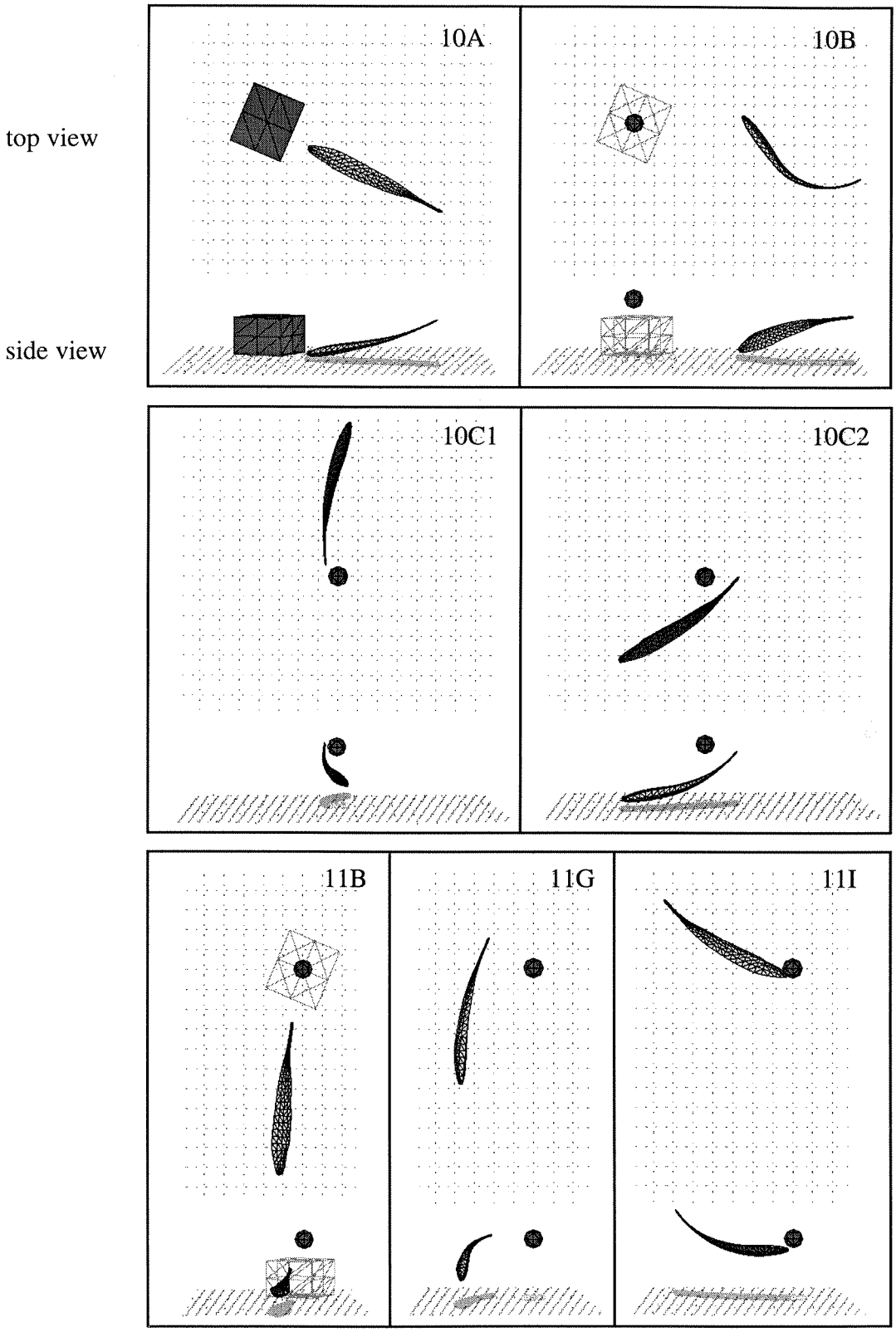

Figure 6.12 Fish models for the black ghost simulations, labeled as in Figures 10 and 11. The side views have perspective added to match the video.

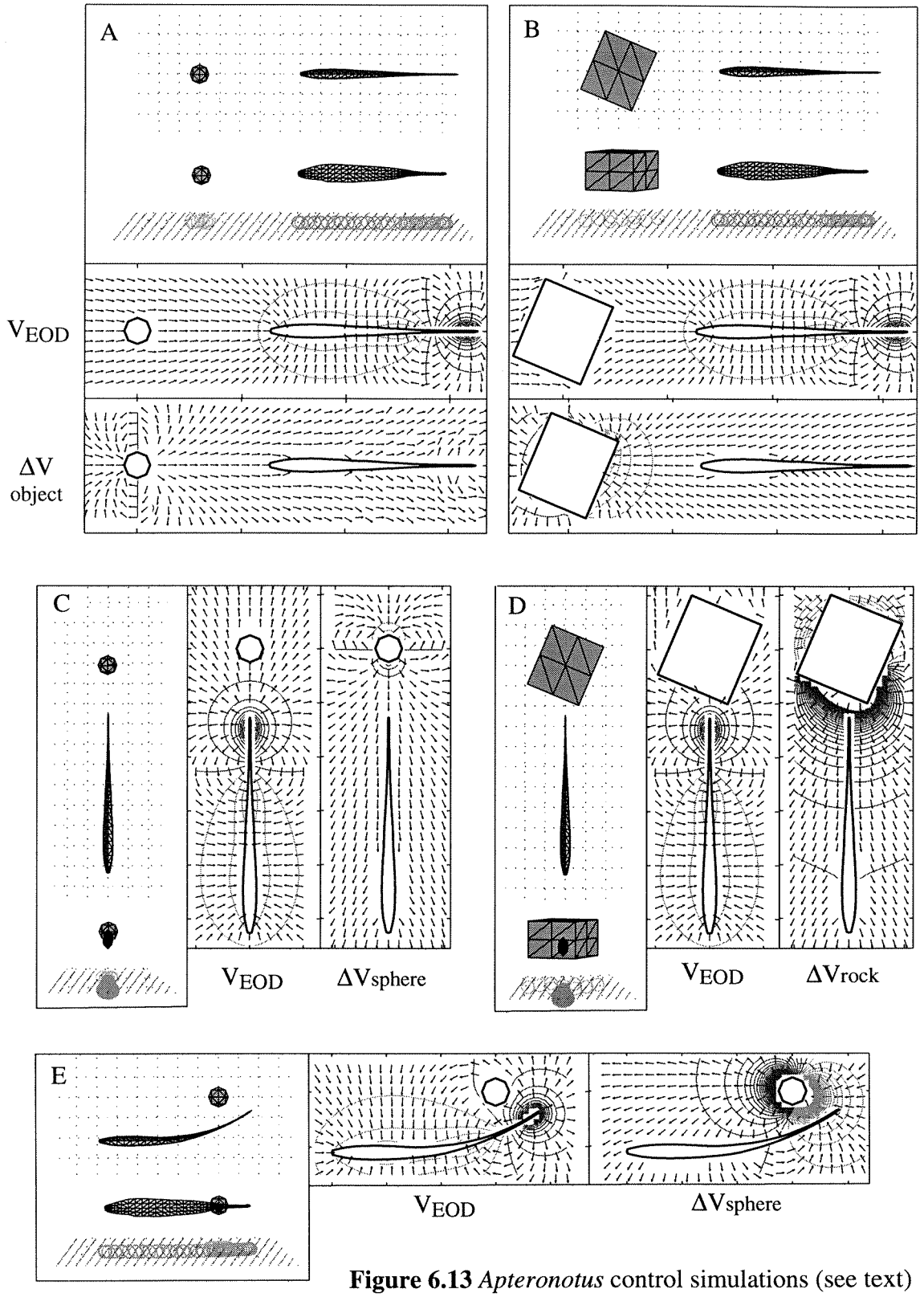

Figure 6.13 *Apteronotus* control simulations (see text)

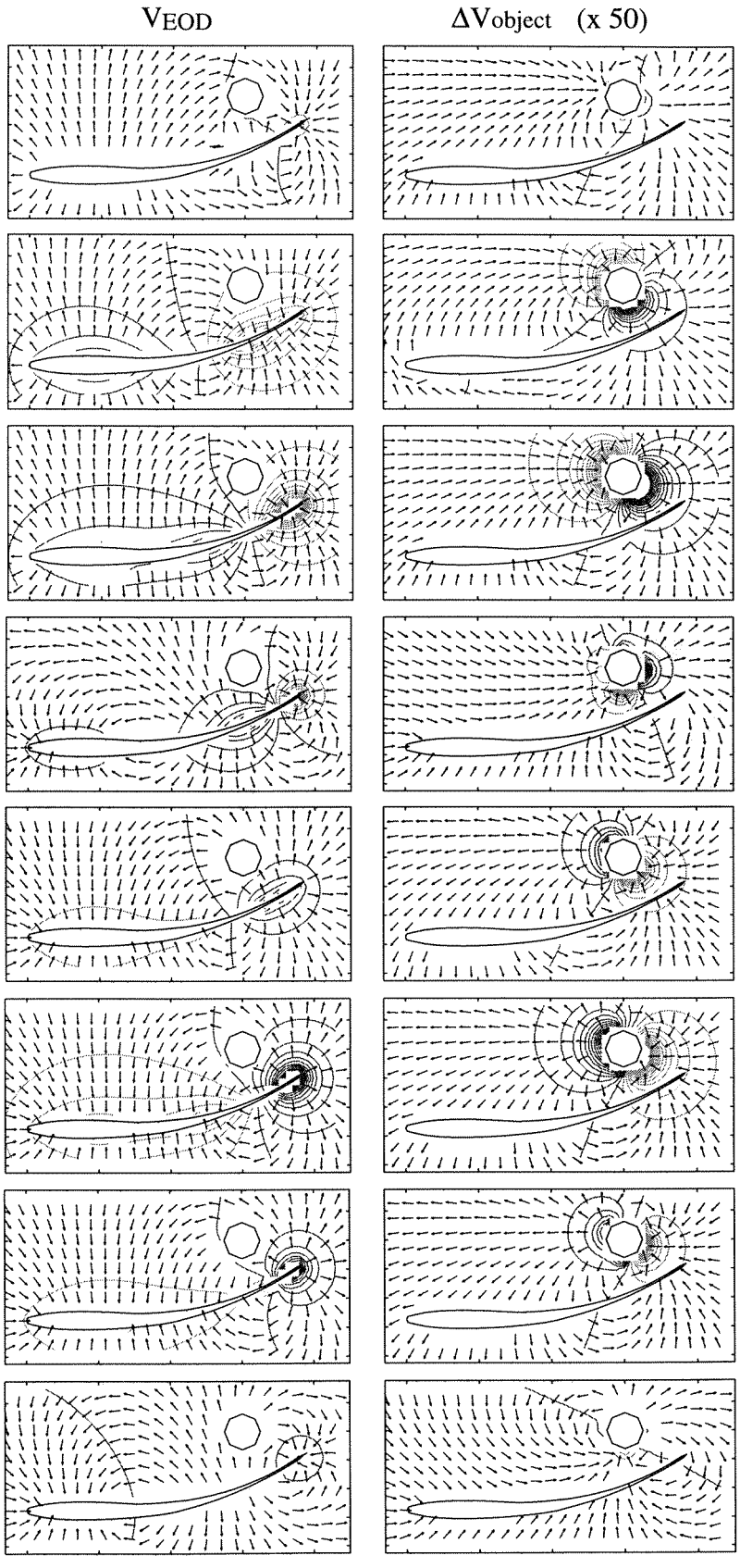

Figure 6.14

Eight midplane snapshots from one period of the *Apteronotus* EOD, at regular intervals of about 150 μS, top to bottom. Left column shows potential contours in 1 mV steps, and normalized current vectors. Right column shows difference between object and no object conditions, multiplied by 50. The propagation of EOD peaks in the first 4 frames causes the object dipole to revolve, but the dipole direction remains more constant during the second half of the EOD. RMS calculations average out these variations.

Transdermal potential in the control simulations

In order to estimate the electrosensory stimuli from the complex EOD shown in the midplane maps, the transdermal potential was calculated at 50 equally spaced phases of the EOD period, and then true RMS values were calculated. Figure 15 shows the results for the control simuations. In the two rock approaches (13A,C), the object causes changes that are on the order of 1 mV at the head and tail, about 0.1% change from the overall EOD (VEOD in the left-most skin map). The sphere approaches (13B,D) do not even register on this scale; they are below the smallest increment of 0.1 mV. These four

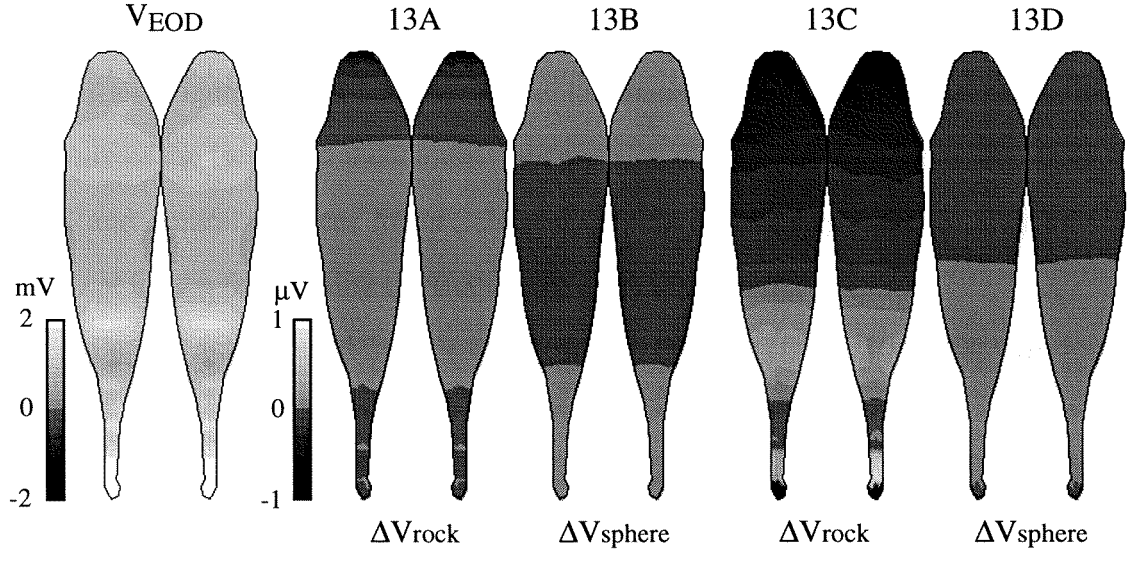

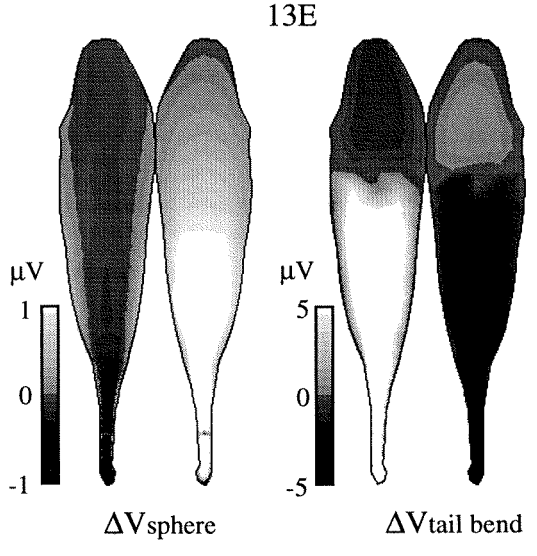

Figure 6.15 Transdermal potential (RMS) maps for the 3 black ghost simulations of Figure 13. The map labeled V_{EOD} is the overall EOD from a straight fish with no object; the others are object difference maps. Note that the models in A-D had no tail bend or rotation, i.e., they were symmetric about the long axis of the fish.

skin maps again reflect the symmetry of their respective symmetric model orientations.

The object image from the sphere is much more significant in the tail-bending control simulation (Fig. 13E). The RMS transdermal difference on the right side of the body, towards the bend, has a positive peak at the tail (well over 1 μV) that smoothly decays in amplitude rostrally. On the left side, away from the bend, the difference due to the object is negative and generally smaller but more uniform in amplitude than on the right. The map for each half of the skin is symmetric about its midline, as is expected from constraining the fish model to be upright and lie in the same plane as the object.

Transdermal potential in the behavior simulations

In the actual behaviors, the transdermal potential maps no longer maintain their symmetries (Figure 16). In particular, all of the frames have substantial differences in the curvature of the isopotential contours from one side of the fish to the other, and from the dorsal and ventral surfaces to the midlines. These spatial asymmetries may be very important for the fish's ability to electrolocate (see Discussion).

For the normal head-first close approach to the rock (frame 10A), the transdermal potential difference maxima over the rostral skin are well over 1 μV. In the first approach to a novel object (10B), if the rock had still been present the fish would have sensed a weaker version of the same pattern (ΔV_{rock}), with maximum differences from 0.2-0.3 μV. Instead, with the conducting sphere present (ΔV_{sphere}), the difference in transdermal potential is again below 0.1 μV. When the fish returned tail-first (frames 10C1, 10C2), the object was in a much stronger field close to the tail tip, and transdermal difference peaks were now found above 1 μV in amplitude. Note that the spatial pattern over the rostral body for frame 10C2 is similar to frame 13E in Fig. 15, and I expect it would remain very similar during the entire tail-first cartwheel behavior recorded in Fig. 10C, because the object is spherically symmetric. In the tail-first approach to the novel insulating sphere (frame 11B), the transdermal potential differences would have been close to 1 μV had the rock been present, but are below 0.1 μV with the sphere. Finally,

in the last simulated frame (11I) where the fish closely approaches and appears to almost touch the sphere with its snout, the transdermal pattern is very similar to the close head-first rock approach (10A). However, the negative peak at the head is stronger in amplitude and much more localized for the smaller, closer sphere than for the much larger and slightly farther rock.

6.4 Discussion

The types of "tail probing" and "scanning" behaviors recreated in these simulations have been described previously (Lissmann 1963, Heiligenberg 1975, Toerring and Belbenoit 1979, Bacher 1983, Behrend 1984, Bastian 1986b). Three common conclusions were drawn from these studies. First, many electric fish approach unknown objects tail first, swimming backwards, presumably to escape quickly in case of danger.[1] The black ghost startle reactions to novel objects in my experiments certainly supports that interpretation. Second, the fish scan and swim with rigid control of the spine and body posture, which should maintain the relative orientation of field generator to field receptors, and so reduce undesirable reafferent modulations. Both the video and simulation results presented here strongly support this conclusion. Third, the scanning or probing movements have been hypothesized to help recognize object features. For example, Heiligenberg's (1975) relatively coarse finite difference simulation showed tail bending may help increase spatial contrast, and Bacher's (1983) analytical 3-d model led him to suggest tail bending could separate object shape from position. However, the majority of previous behavioral studies did not attempt to quantify the electrosensory consequences of the fish's movements.

The electrosensory consequences of real behaviors can be quantitatively analyzed through the more realistic simulations presented here. The transdermal fields comprising

[1]Many species are able to regrow the tail if it gets bitten off or damaged, spinal cord and all (Waxman and Anderson 1986). Recently, Lundberg and Sullivan even discovered two new electric fish species that appear to feed exclusively on the tails of other weakly electric fish (New York Times 2/18/97, pg B1).

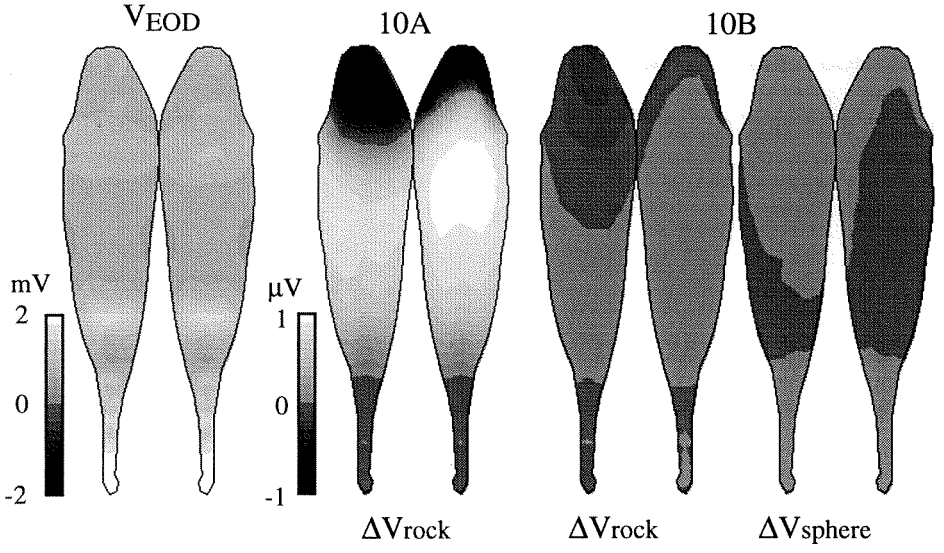

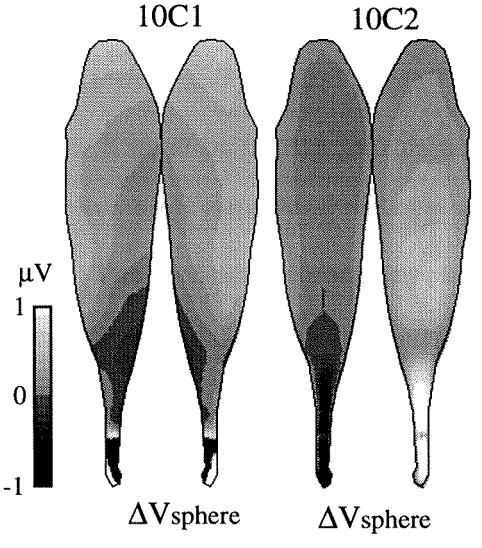

Figure 6.16 Transdermal potential (RMS) maps from the black ghost frames (labeled as in Figs. 10, 11 and 12). V_{EOD} is the overall EOD from the straight fish with no object; the others are object difference maps. The maps now show significant asymmetries due to the fish's orientations to the object (see text).

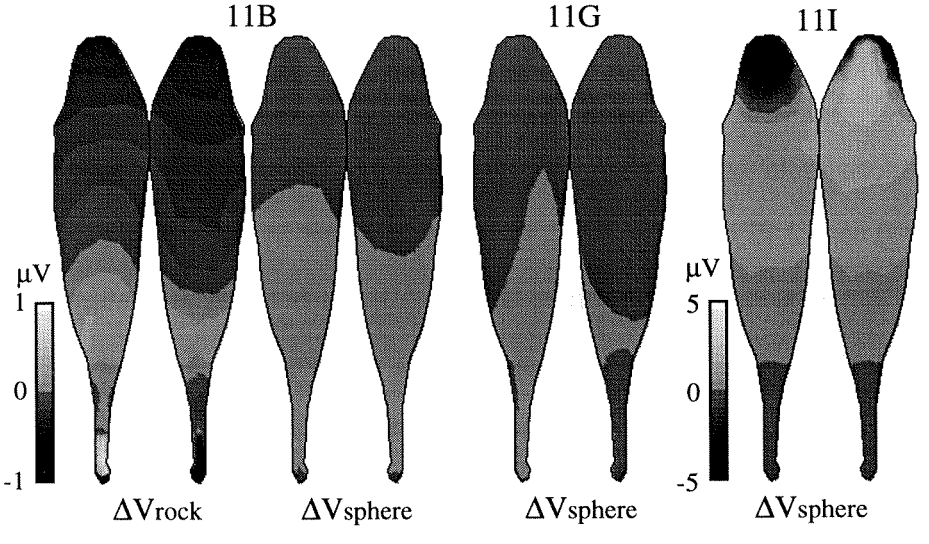

the electrosensory stimuli can be decomposed into 3 contributions: the normal EOD, modulations due to tail bending, and modulations of the EOD due to external objects, i.e., the object image. These respective contributions are discussed in separate sections below.

6.4.1 Normal EOD transdermal pattern

The normal EOD is defined here as the fields measured with straight tail orientation and no objects present. From the results shown above, the RMS magnitude of the normal transdermal stimulus ranges from 1 to 20 mV, depending on location on the body surface (V_{EOD} in Figs. 8 and 16). Since these wave-type EODs are periodic with very constant frequency and amplitude over time, as reported in Chapter 3, they serve as strong carrier signals for the much smaller amplitude external modulations. For a P-type amplitude receptor to make use of this kind of signal, it must be biased into its active output range by the local EOD magnitude, and then have high sensitivity to very small deflections around the normal bias point (see below). The first suggestions supporting this conclusion were from the measured maps of external potential on the skin surface in Chapters 2 and 3.

6.4.2 Effects of tail bending on the EOD

The EOD measurements and simulations suggest a second function for tail probing: to put the object into a much stronger electric field by moving the tail tip closer, thereby increasing the magnitude of the induced dipole from the object (see 6.4.4). However, tail bending itself causes relatively large changes in the electrosensory reafference that need to be accounted for, presumably at the level of the ELL (see 6.4.5). The tail bending simulations resulted in modulations of the normal transdermal EOD (regardless of the presence of the object) by up to 20 μV on the near side of the rostral body and over 100 μV on the far side. These changes agree well with measurements by

Bastian (1995), who found the rostral 30% of the body had transdermal amplitude modulations between 50 and 150 μV peak-to-peak for tail bending displacements ranging between ±20 to ±50 degrees (Fig. 17). Bastian reported these amplitude modulations, which are "roughly 1 to 5% of the normal EOD amplitude, are well above threshold for the receptors." Note these reafferent changes are much larger than many of the object images shown above.

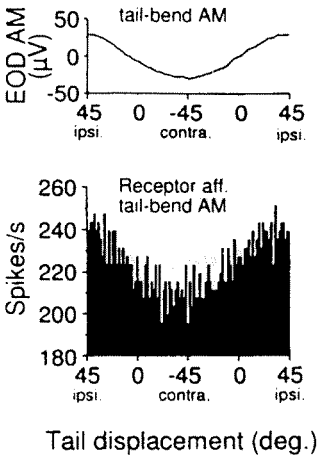

Figure 6.17 (Bastian 1995)

The tail bending simulation results were not as symmetric from side to side as Bastian's data implied, and this asymmetry may have arisen from an overlooked technical issue in the model. As can be seen in Fig. 3a, when the model tail is bent, the skin surface area compresses slightly on the side toward the bend, while it stretches on the side away. For example, when the fish model was bent at its midpoint with a radius of curvature of 10 cm (similar to frame B4), the total skin area on the right half of the caudal body decreased by 0.93%, while on the left side the area increased by 0.85%. Since the skin conductivity for each surface element is set by the values at its vertices, the conductance of an element is proportional to its area. Therefore the total skin conductance decreases slightly on the side of the bend, and increases on the other side. This should redirect a small fraction of the tail current, close to 1% of the total, from the bend side through the opposite skin. Therefore the change in skin area may account for much of the tail bending asymmetry in the transdermal results. Fortunately, the tail-bending artifact will only cause second order effects in the object image, and so the present model suffices for my purposes. But it does pose a new question to be answered: what happens to the skin conductance in the real fish when it bends its tail?

Small changes in other model parameters did not affect the results drastically, nor any of my conclusions. For example, I moved some EOD sources further rostral in the

Eigenmannia model, and only small differences resulted: the zero line from the object aligned more rostrally on the fish's body, and the tail bending effects were more symmetric, with the transdermal magnitude on the bend side increased by up to 50 μV. Finally, I must note again the model does not include gills or a mouth, possible low impedance pathways through the skin at the head. However, any discrepancy from neglecting these contributions must be small since the measured maps (Chapters 2 and 3) do not indicate large leakage currents from those areas.

6.4.3 Object effects on the EOD and contribution to the electrosensory stimulus

The overall electric field with an object present can be considered the sum of two superimposed fields: the intrinsic EOD carrier and the object induced field. To see the object effect, we subtract the intrinsic EOD field from the total field with the object present, and the results are shown to be generally dipolar fields for spherical objects (as in Figs. 4, 7, 14). This agrees with the analytic solution expected for spherical objects in a constant applied electric field (Chapter 4). Exceptions can occur when the sphere is close enough to the body in a region of varying field, so that the field can no longer be assumed constant over the object's location. For example, in the fourth phase of Fig. 14, the EOD field direction rotates in space from one side of the object to the other (V_{EOD}), and the resulting object induced field is quadrapolar (ΔV_{object}). Note that object induced dipole fields were not assumed *a priori*, as in previous simulations of Bacher (1983) and Rasnow (1996), but instead resulted directly from the simulation.

The magnitude of the object image at the skin depends linearly on the object volume, its conductivity with respect to the water, and the EOD field strength at the object's location. The object image shape, on the other hand, depends on object distance and the direction of the EOD electric field vector at the object's location. For fish with a synchronous EOD, like *Eigenmannia*, the object dipole direction and thus the object image shape remain fairly constant over the milliseconds span of a single EOD period.

Species with more complicated EODs, such as *Apteronotus*, could conceivably gain information about an object from phase differences measured by T-type timing receptors during each EOD period, e.g., information on different slices or aspects of the object from the rotating object dipole (Fig. 14). However, the P-type amplitude-encoding receptors still generate a stable image since they integrate over several periods, and their RMS input is dominated by the peak phases of the EOD that produce the largest fields.

The magnitudes of the object images simulated here, on the order of 0.1-10 μV, are extremely small compared to the normal EOD transdermal potential, but still large enough to be detected with the receptors' reported sensitivities. Bastian (1981) extrapolated from measured receptor reponses to estimate an incremental sensitivity in field strength of 0.9 μV p-p/cm in 10 kΩ-cm water, equivalent to a transdermal difference between 0.1 and 0.2 μV RMS in the model. This value represents the stimulus intensity needed to shift the receptor's firing rate by 1 spike/s. Although this incremental shift was hidden in the much higher average receptor firing rates (close to 300 spikes/s, at irregular intervals), Bastian argued higher order cells receiving inputs from multiple receptors could be much more sensitive to signals of this magnitude. This would be consistent with reported *Apteronotus* behavioral thresholds of 0.2 μV p-p/cm in 2 kΩ-cm water (Knudsen 1974), again equivalent to about 0.1 μV RMS transdermal difference in the model.

The two novelty responses reported here were performed at distances at which the object images from the sphere were likely too small to be detected, below the 0.1μV stimulus threshold. However, in both cases the fish had been expecting to find the larger rock, which would have caused detectable changes at those distances had it been present (Figs. 13, 16). This suggests that the fish may be operating with a spatial memory of its surroundings, and will react if the actual stimulus does not correspond to the expected stimulus from memory.[2]

[2]Brian Rasnow first suggested navigation from memory to me before these experiments were carried out.

6.4.4 Significance of controlled exploratory movements

The video records from our experiments support the general conclusion that these electric fish species maintain rigid body posture to reduce the number of sensory variables. *Apteronotus* appeared to keep its body relatively rigid as it arched around the object, as in the exploratory cartwheel behavior (Fig. 10c). Therefore the EOD modulation from its bent body orientation remained fairly constant (Fig. 16 frame 11C2, Fig. 15 frame 13E), which should facilitate the subsequent sensory processing. Assuming the distance could also be maintained fairly constant, any changes in the image shape would then be due to variations in object shape or conductivity. Well defined probing distances, dependent on object conductivity, were previously reported during characteristic scanning behaviors of a pulse mormyrid (Toerring and Belbenoit 1979).

In contrast to the *Apteronotus* scanning behavior, the specific movements of the *Eigenmannia* tail probing behavior appear designed to keep the field direction fairly constant at the object's location. This maintains the pattern of the object image on the rostral body surface fairly well. On the other hand, the magnitude of the object dipole is highly dependent on the tail proximity, and therefore the amplitude of the object image is highly modulated by the tail bending. Note that two time scales are involved here: stationary external objects add a DC modulation to the amplitude of the EOD as it runs at high frequency, around 300 Hz, while the change in modulation due to the tail bending happens at the frequency of the bending behavior, about 1.5 to 2 Hz (Behrend 1984).

The object image amplitude is dependent on object size as well as its distance. Therefore a third function for tail probing may be to distinguish between these variables: since the electric field strength decays by an inverse power of distance from the tail, the rate of change of the object image magnitude as the tail moves is highly dependent on the rate of change in field strength (whereas the object size remains a constant scale factor). This could be further investigated, for example, using objects of different sizes at various distances from a fish trained to discriminate size. The fish's movements could then be

restricted to test if the normal tail probing behavior is sufficient or necessary to distinguish distance from size.[3]

6.4.5 Significance of mapping to the input layer of ELL

Calculating the difference due to an object's presence is easy to do numerically on our computers. However, from the fish's point of view, only the overall field at the skin is available, with small differences in the electrosensory image over time as it moves around the object. To extract the image of the object, the fish must also somehow perform a subtraction. This could be done in two ways, either by a temporal comparison with a previous image stored in memory, or by a spatial comparison, e.g., from one side of the body to the other.[4] Furthermore, the changes in the electrosensory stimulus pattern from self-generated movements, such as tail bending, can be much larger than the object induced stimulus. So the electrosensory processing must also subtract these reafferent modulations.

There is evidence from central physiology to support all of these computations. For temporal comparisons, current research is uncovering the role of adaptive filtering in the ELL to suppress predictable inputs (Bell 1982, 1993; Bastian 1986a, 1995, 1996ab; Nelson and Paulin 1995; Bell et al. in press). ELL principal cells receive direct receptor afferent input onto their basal dendrites (or through inhibitory interneurons), while through the elaborate apical dendrites courses a massive parallel fiber tract from the EGp, a granule cell mass in the caudal lobe of the cerebellum. The parallel fibers carry electrosensory feedback, proprioceptive information (tail bend angle), and even electric organ command corollary discharge signals (in mormyrids only). The predictive function of cerebellar input to ELL appears due to anti-Hebbian synaptic plasticity at the parallel fiber-principal cell synapse. Therefore correlations between the descending signals and

---

[3] Object conductivity could be substituted for object size in this experiment, as it also contributes a constant scale factor to the object image.

[4] In engineering terms: using common mode rejection to amplify a small signal riding on a much larger carrier.

principal cell activity generate a slowly adapting negative image template to subtract from the immediate sensory input, effectively masking steady-state signals and enhancing novel features (termed expectation generation, Bell 1993). This generation and cancellation of sensory expectations can also suppress the reafferent changes from tail bending, since they are correlated with tail bend angle (Bastian 1995).

For comparisons in space, commissural pathways project between the two bilateral ELL lobes, so that each map in the ipsilateral ELL receives competitive input from its corresponding map in the contralateral ELL (Bastian et al. 1993). These connections may participate in rejecting common mode electrosensory signals, i.e., reducing responsiveness to symmetrical stimuli (side to side) compared to asymmetric stimuli (Rose 1989; Montgomery and Bodznick 1994). However, previous ELL mapping experiments make little or no mention of contralateral receptive fields, as would be expected. In the real behaviors, different rotations of the fish often centered the object image over dorsal or ventral surfaces, so comparison between top and bottom may also prove useful. While the relative contributions of these various mechanisms has yet to be determined, detailed spatial comparisons performed between stimuli from different regions of the body surface have been clearly demonstrated in investigations of the jamming avoidance response (Heiligenberg 1993).

Once the object image is unmasked, various manipulations may be employed to extract the object features: ELL principal cells have center-surround type receptive fields that can sharpen blurry edges and enhance contrast, before transmitting the image to higher levels (see Fig. 2 in Chapter 1); convergence of ELL efferents in the torus or optic tectum could then naturally integrate image shape and width, from which Bacher (1983) and Rasnow (1996) have predicted object distance and size can be calculated; and cells in cerebellum are often found with very large, complex receptive fields, including higher sensitivity to direction of object movement than to object distance or size (Bastian 1974,

1976). We can now begin to explore these network properties using the electrosensory maps produced in this thesis work.

As demonstrated here, these methods allow investigation of peripheral electrosensory images without interfering with the natural behavior of the fish, and help reveal the significance of the fish's exploratory strategies. The simulation results, when combined with the measured maps, provide the most complete, quantifiable EODs and electrosensory input to date. The simulations and field measurements also provide a testbed for further electrophysiological studies of electroreceptor transfer functions, the spatial and temporal patterns of activation of the electrosensory maps in the ELL, and the computational processing needed for electrolocation. In this manner, simulations of actual exploratory behaviors will facilitate investigations of the neural algorithms used for electroreception.

A Details of the BEM Integrals

The boundary element method requires several integrations for each node-element pair. After the appropriate transformation (see Chapter 4 Methods), each element is mapped onto a standard element in the XY plane with one edge along the X-axis, as in Figure 1.

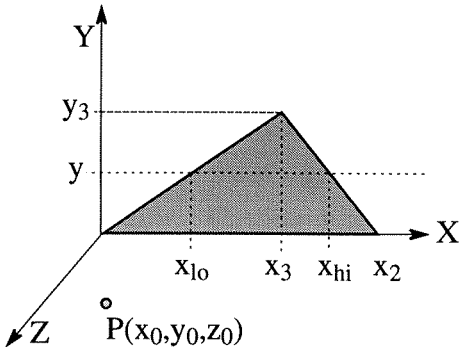

Figure 1

From Chapter 4, $B_{im\upsilon}$ and $C_{im\upsilon}$ represent the integrals from the node $\mathbf{p}=\mathbf{x}_i$ over element m with vertices locally labeled $\upsilon = 1$ to 3, as follows:

$$B_{im\upsilon} = \int_m N_\upsilon \frac{\partial}{\partial n}\frac{1}{r}\,dS = \int_m N_\upsilon \frac{n_x (x-x_0) + n_y (y-y_0) + n_z(z-z_0)}{-r^3}\,dS$$

$$C_{im\upsilon} = \int_m N_\upsilon \frac{1}{r}\,dS$$

where $r = |\mathbf{p} - \mathbf{x}|$, and the linear shape functions N_υ have the form

$$N_\upsilon = a_\upsilon + b_\upsilon x + c_\upsilon y.$$

For the standard triangle, $dS = dx\,dy$, $n_x = n_y = 0$, $n_z = 1$, and $z = 0$:

$$B_{im\upsilon} = z_0 \iint_m N_\upsilon \frac{1}{r^3}\,dx\,dy$$

$$C_{im\upsilon} = \iint_m N_\upsilon \frac{1}{r}\,dx\,dy$$

Integrals for 'B' coefficients

The general form of the B integrals (neglecting subscripts) is:

$$B = z_o \iint_{y\,x} \frac{a + bx + cy}{r^3} \, dx\, dy$$

When the point $\mathbf{p}=\mathbf{x}_i$ is one of the vertices of the given element, B=0 since $z_o=0$. (The contribution from the singularity at $\mathbf{x}=\mathbf{p}$ is accounted for in the A coefficients; see Chapter 4). For the general case of a point $\mathbf{p}=\mathbf{x}_i$ at some distance from a given triangular element, the inner integral on x can be solved analytically. Casting r in Cartesian coordinates, the inner integral (I) becomes:

$$I = \int_x \frac{a + bx + cy}{[(x-x_o)^2 + (y-y_o)^2 + z_o^2]^{\frac{3}{2}}} \, dx$$

Let $u= x-x_o$, $e= (y-y_o)^2 + z_o^2$, and $f= a + cy + bx_o$ (e and f are constant with respect to x).

$$I = \int_u \frac{f + bu}{[u^2 + e]^{\frac{3}{2}}} \, du = f \int_u \frac{du}{[u^2 + e]^{\frac{3}{2}}} + b \int_u \frac{u\, du}{[u^2 + e]^{\frac{3}{2}}}$$

Now $I = I_1 + I_2$, and we can use integral tables to compute each part. I_1 can be computed from equation 3.3.49 in Abramowitz and Stegun (1965, pg. 13).

$$I_1 = f \int_{u1}^{u2} \frac{du}{[u^2 + e]\,[u^2 + e]^{\frac{1}{2}}} = f \left. \frac{u}{e\,[u^2 + e]^{\frac{1}{2}}} \right]_{u1}^{u2}$$

I_2 is straightforward:

$$I_2 = b \int_{u1}^{u2} \frac{u\, du}{[u^2 + e]^{\frac{3}{2}}} = -b \left. \frac{1}{[u^2 + e]^{\frac{1}{2}}} \right]_{u1}^{u2}$$

At this point we can substitute back in for u, e and f. The limits on the integration are easily calculated from Figure 1:

$$x_{lo} = \frac{x_3}{y_3}\, y, \qquad x_{hi} = \frac{x_3 - x_2}{y_3}\, y + x_2$$

To compute the outer integral on y, I used standard Gaussian quadrature formulas from Press et al. (1992; the ten-point Gauss-Legendre integration routine on page 133).

Integrals for general 'C' coefficients

The general form of the C integrals (neglecting subscripts) is:

$$C = \int_{y}\int_{x} \frac{a + bx + cy}{r}\, dx\, dy$$

For the general case of a point $\mathbf{p}=\mathbf{x}_i$ at some distance from a given triangular element, the inner integral on x can again be solved analytically. The inner integral can be stated as:

$$I = \int_{x} \frac{a + bx + cy}{[(x-x_o)^2 + (y-y_o)^2 + z_o^2]^{\frac{1}{2}}}\, dx$$

Let $u= x-x_o$, $e= (y-y_o)^2 + z_o^2$, and $f= a + cy + bx_o$ (e and f are constant wrt x).

$$I = \int_{u} \frac{f + bu}{[u^2 + e]^{\frac{1}{2}}}\, du = f\int_{u} \frac{du}{[u^2 + e]^{\frac{1}{2}}} + b\int_{u} \frac{u\, du}{[u^2 + e]^{\frac{1}{2}}}$$

The first term can be computed from equation 3.3.40 in Abramowitz and Stegun (1965, pg. 13), and the second is straightforward.

$$I = f \ln\left|u + (u^2 + e)^{\frac{1}{2}}\right|\Big]_{u1}^{u2} + b\,(u^2 + e)^{\frac{1}{2}}\Big]_{u1}^{u2}$$

At this point we again substitute back in for u, e and f, and apply the same limits on the integration as for the B integrals. The outer integral on y is then computed with the same standard Gaussian quadrature formulas from Press et al. (1992; pg. 133).

When the point $\mathbf{p}=\mathbf{x}_i$ is one of the vertices of the given element, r=0 at the point in question and the integrand becomes weakly singular. In that case $C_{im\upsilon}$ can be computed analytically. The analytic solutions for integrals of this type have been published previously (Jin and Tullberg 1985, pg. 2-23), but I also derive them in the next section in appropriate form for my use.

Integrals for singular 'C' coefficients

For the singular C case, the point **p** coincides with $\mathbf{x_1}$ at the origin, and the integral can be computed using polar coordinates. For convenience, the standard element is rotated until side $\mathbf{x_2x_3}$ is perpendicular to the X-axis, intersecting at $x=\rho$ (Fig. 2). In polar coordinates, $x= r\cos\theta$, $y= r\sin\theta$, and $dxdy= r\, dr\, d\theta$.

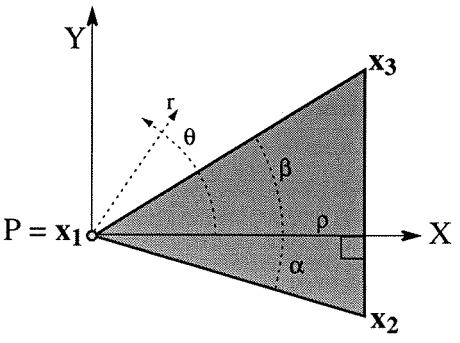

Figure A.2 On side $\mathbf{x_2x_3}$, $r = \mathrm{sqrt}(\rho^2 + \rho^2\tan^2\theta) = \rho\sec\theta$.

$$C = \int_\theta \int_r \frac{a + b\,r\cos\theta + c\,r\sin\theta}{r}\, r\, dr\, d\theta$$

$$= \int_\theta \int_r a + b\,r\cos\theta + c\,r\sin\theta \; dr\, d\theta$$

$$= \int_\theta \left[ar + \frac{b}{2}r^2\cos\theta + \frac{c}{2}r^2\sin\theta \right]_{r=0}^{r=\rho\sec\theta} d\theta$$

$$= \int_\theta a\rho\sec\theta + \frac{b}{2}\rho^2\sec\theta + \frac{c}{2}\rho^2\frac{\sin\theta}{\cos^2\theta}\, d\theta$$

The integral of $\sec\theta$ is given in Equation 4.3.117 in Abramowitz and Stegun (1965).

$$C = \left[(a\rho + \frac{b}{2}\rho^2)\ln\tan(\frac{\pi}{4} + \frac{\theta}{2}) + \frac{c}{2}\rho^2\frac{1}{\cos\theta} \right]_{\theta=-\alpha}^{\theta=\beta}$$

The necessary values of ρ, α and β can be easily calculated from the geometry of the standard triangle in Figure 2.

"To this apparatus, much more similar ...in its form to the natural electric organ *of the torpedo or electric eel, &c. than to the Leyden flask and electric batteries, I would wish to give the name of the* artificial electric organ..."

Alessandro Volta, 1800

B Historical References

Henry Cavendish (1776) An account of some attempts to imitate the effects of the Torpedo by Electricity. *Philosophical Transactions of the Royal Society of London* 66(1):196-225

Charles Darwin (1859) On the Origin of Species. Chapter 6: Difficulties on Theory - Transitions of Organs. John Murray, Albemarle Street, London

Michael Faraday (1839) Notice of the character and direction of the electric force of the *Gymnotus*. *Philosophical Transactions of the Royal Society of London* 129:1-12

James Clerk Maxwell, ed. (1879) The Electrical Researches of the Honourable Henry Cavendish, F.R.S. University Press, Cambridge

Alessandro Volta (1800) On the Electricity excited by the mere Contact of Conducting Substances of different kinds. *Philosophical Transactions of the Royal Society of London* 90:403-431 (in French). English translation in *Philosophical Magazine* 7:289-311

John Walsh (1773) Of the electric property of the torpedo. In a letter from John Walsh, Esq., F.R.S., to Benjamin Franklin, Esq., LL.D., F.R.S., Ac. R. Par. Soc. Ext., &c. *Philosophical Transactions of the Royal Society of London* 63:461-480

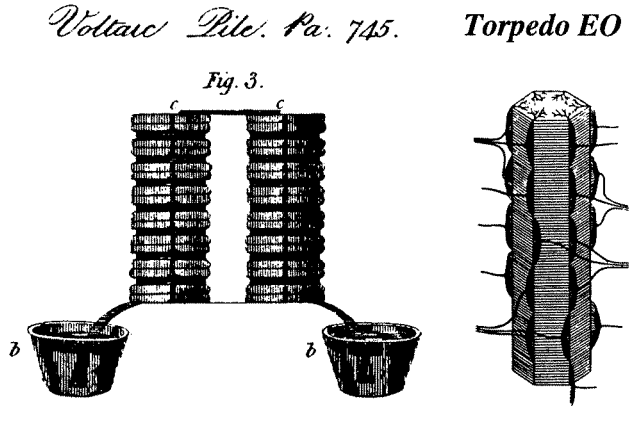

Torpedo EO

Figure B.1 (After Fig. 7 in Wu 1984.) Volta patterned his first batteries after the stacks of electrocytes found in electric organs. Left: from Plate 8 in Volta 1800. Right: from Fritsch G (1890). Die elektrischen Fische. Verlag von Veit und Comp, Liepzig.

C Bibliography

Abramowitz M, Stegun IA (1965) Handbook of Mathematical Functions. Dover Publications, New York

Alves-Gomes JA, Ortí G, Haygood M, Heiligenberg W, Meyer A (1995) Phylogenetic analysis of the South American electric fishes (Order Gymnotiformes) and the evolution of their electrogenic system: a synthesis based on morphology, electrophysiolgy, and mitochondrial sequence data. *Mol Biol Evol* 12:298-318

Assad C, Rasnow B, Bower JM (1993) Numerical simulations of the electric organ discharge of weakly electric fish. In: Proceedings of the First Annual Computation and Neural Systems Meeting, San Francisco, July 1992. Kluwer Academic Publishers.

Bacher M (1983) A new method for the simulation of electric fields, generated by electric fish, and their distorsions by objects. *Biological Cybernetics* 47:51-58

Bass AH (1986) Electric organs revisited: evolution of a vertebrate communication and orientation organ. In: Bullock TH, Heiligenberg W (eds). Electroreception. Wiley, New York, pp 13-70

Bass AH, Volman SF (1987) From behavior to membranes: testosterone-induced changes in action potential duration in electric organs. *Proc Natl Acad Sci USA* 84:9295-9298

Bastian J (1974) Electrosensory input to the corpus cerebelli of the high frequency fish *Eigenmannia virescens. J Comp Physiol* 90:1-24

Bastian J (1976) The range of electrolocation: a comparison of electroreceptor responses and the responses of cerebellar neurons in a gymnotid fish. *J Comp Physiol* 108:193-210

Bastian J (1977) Variations in the frequency response of electroreceptors dependent on receptor location in weakly electric fish (Gymnotoidei) with a pulse discharge. *J Comp Physiol* 121:53-64.

Bastian J (1981a) Electrolocation I. How the electroreceptors of *Apteronotus albifrons* code for moving objects and other electrical stimuli. *J Comp Physiol* 144:465-479

Bastian J (1981b) Electrolocation II. The effects of moving objects and other electrical stimuli on the activities of two categories of posterior lateral line lobe cells in *Apteronotus albifrons*. *J Comp Physiol* 144:481-494

Bastian J (1986a) Gain control in the electrosensory system: a role for the descending projections to the electrosensory lateral line lobe. *J Comp Physiol A* 158:505-515

Bastian J (1986b) Electrolocation: behavior, anatomy and physiology. In: Bullock TH, Heiligenberg W (eds). Electroreception. Wiley, New York, pp 577-612

Bastian J (1993) Descending control of electroreception in gymnotid fish: contrasting properties of direct and indirect pathways. *J Comp Physiol A* 173:670-673

Bastian J, Courtright J, Crawford J (1993) Commissural neurons of the electrosensory lateral line lobe of *Apteronotus leptorhynchus*: morphological and physiological characteristics. *J Comp Physiol A* 173:257-274

Bastian J (1995) Pyramidal-cell plasticity in weakly electric fish: a mechanism for attenuating responses to reafferent electrosensory inputs.*J Comp Physiol A* 176:63-78

Bastian J (1996a) Plasticity in an electrosensory system. I. General features of a dynamic sensory filter. *J Neurophysiol* 76(4):2483-2496

Bastian J (1996b) Plasticity in an electrosensory system. II. Postsynaptic events associated with a dynamic sensory filter. *J Neurophysiol* 76(4):2497-2507

Behrend K (1984) Cerebellar influence on the time structure of movement in the electric fish *Eigenmannia. Neuroscience* 13:171-178

Bell CC, Myers JP, Russell CJ (1974) Electric organ discharge patterns during dominance related behavioral displays in Gnathonemus petersii. *J Comp Physiol* 92:201-228

Bell CC, Bradbury J, Russell CJ (1976) The electric organ of a mormyrid as a current and voltage source. *J Comp Phys* 110:65-88

Bell CC (1982) Properties of a modifiable efference copy in electric fish. *J Neurophysiol* 47:1043-1056

Bell CC, Szabo T (1986) Electroreception in mormyrid fish: central anatomy. In: Bullock TH, Heiligenberg W (eds). Electroreception. Wiley, New York, pp 375-421

Bell CC (1986) Electroreception in mormyrid fish: central physiology. In: Bullock TH, Heiligenberg W (eds). Electroreception. Wiley, New York, pp 423-452

Bell CC (1993) The generation of expectations in the electrosensory lobe of mormyrid fish. *J Comp Physiol A* 173:677-680

Bell CC, Caputi A, Grant K, Serrier J (1993) Storage of a sensory pattern by anti-Hebbian synaptic plasticity in an electric fish. *Proc Nat Acad Sci* 90:4650-4654

Bell CC, Hopkins CD, Grant K, eds. (1993) Contributions of electrosensory systems to neurobiology and neuroethology. *J Comp Physiol A* 173:657-763

Bell CC, Bodznick D, Montgomery J, Bastian J (in press) The generation and subtraction of sensory expectations within cerebellum-like structures. *Brain Behav Evol*

Bennett MVL (1971a) Electric organs. In: Hoar WS, Randall DH (eds). Fish Physiology, Vol. 5. Academic Press, New York, pp 347-491

Bennett MVL (1971b) Electroreceptors. In: Hoar WS, Randall DH (eds). Fish Physiology, Vol. 5. Academic Press, New York, pp 493-574

Black-Cleworth P (1970) The role of electrical discharges in the non-reproductive social behavior of *Gymnotus carapo. Anim Behav Monographs* 3:1-77

Bower JM, Kassel J (1990) Variability in tactile projection patterns to cerebellar folium Crus IIA of the Norway rat. *J Comp Neur* 302:768-778

Bower JM (1992) Is the cerebellum a motor control device? *Behav Brain* 15:714-715

Brebbia CA, Telles JCF, Wrobel LC (1984) Boundary Element Techniques: Theory and Applications in Engineering. Springer-Verlag, Berlin

Bullock TH (1969) Species differences in effect of electroreceptor input on electric organ pacemakers and other aspects of behavior in electric fish. *Brain Behav Evol* 2:85-118

Bullock TH (1970) The reliability of neurons. *J Gen Physiol* 55:565-584

Bullock TH, Behrend K, Heiligenberg W (1975) Comparison of the jamming avoidance response in Gymnotoid and Gymnarchid electric fish: a case of convergent evolution of behavior and its sensory basis. *J Comp Phys* 103:97-121

Bullock TH (1986) Significance of findings on electroreception for general neurobiology. In: Bullock TH, Heiligenberg W (eds). Electroreception. Wiley, New York, pp 651-674

Bullock TH, Heiligenberg W, eds. (1986) Electroreception. Wiley, New York

Caputi A, Macadar O, Trujillo-Cenoz O (1989) Waveform generation of the electric organ discharge in *Gymnotus carapo. J Comp Phys A* 165:361-370

Carr CE, Maler L, Sas E (1982) Peripheral organization and central projections of the electrosensory nerves in gymnotiform fish. *J Comp Neurol* 211:139-153

Carr CE (1986) Time coding in electric fish and barn owls. *Brain Behav Evol* 28:122-133

Carr CE, Maler L (1986) Electroreception in gymnotiform fish. In: Bullock TH, Heiligenberg W (eds). Electroreception. Wiley, New York, pp 319-373

Carr CE (1990) Neuroethology of electric fish. *Bioscience* 40:259-267

Crawford JD (1992) Individual and sex specificity in the electric organ discharges of breeding mormyrid fish (*Pollimyrus isidori*). *J Exp Biol* 164:79-102

Dulka JG, Maler L (1994) Testosterone modulates female chirping behavior in the weakly electric fish, *Apteronotus leptorhynchus*. *J Comp Physiol A* 174:331-343

Dye JC, Meyer JH (1986) Central control of the electric organ discharge in weakly electric fish. In: Bullock TH, Heiligenberg W (eds). Electroreception. Wiley, New York, pp 71-102

Dye JC (1987) Dynamics and stimulus-dependence of pacemaker control during behavioral modulations in the weakly electric fish, *Apteronotus* . *J Comp Physiol A* 161:175-185

Dye JC, Heiligenberg W (1987) Intracellular recording in the medullary pacemaker nucleus of the weakly electric fish, *Apteronotus*, during modulatory behaviors. *J Comp Physiol A* 161:187-200

Ellis DB, Szabo T (1980) Identification of different cell types in the command (pacemaker) nucleus of several gymnotiform species by retrograde transport of horseradish peroxidase. *Neuroscience* 5:1917-1929

Enger PS, Szabo T (1968) Effect of temperature on the discharge rates of the electric organ of some gymnotids. *Comp Biochem Physiol* 27:625-627

Franchina CR, Hopkins CD, Schneiderman A (1990) The dorsal filament of the weakly electric Apteronotids is specialized for electroreception. Soc Neurosci Abstr 16:1327

Franchina CR, Hopkins CD (1996) The dorsal filament of the weakly electric Apteronotidae (Gymnotiformes; Teleostei) is specialized for electroreception. *Brain Behav Evol* 47:165-178

Fritzsch B (1993) Evolutionary gain of non-teleostean electroreceptive systems. *J Comp Physiol* 173:710-712

Grundfest H (1960) Electric fishes. *Scientific American* 205(Oct):115-124

Hagedorn M, Heiligenberg W (1985) Court and spark: electric signals in the courtship and mating of gymnotoid fish. *Anim Behav* 33:254-265

Hagedorn M (1986) The ecology, courtship, and mating of gymnotiform electric fish. In: Bullock TH, Heiligenberg W (eds). Electroreception. Wiley, New York, pp 497-525

Hagiwara S, Szabo T, Enger PS (1965) Electroreceptor mechanisms in a high frequency weakly electric fish, *Sternarchus albifrons*. *J Neurophysiology* 28:784-799

Hayami K (1992) A projection transformation method for nearly singular surface boundary element integrals. In: Brebbia CA, Orszag SA (eds). Lecture Notes in Engineering. Springer-Verlag, Berlin

Heiligenberg W (1973) Electrolocation of objects in the electric fish *Eigenmannia*. *J Comp Physiol* 87:137-164

Heiligenberg W (1975) Theoretical and experimental approaches to spatial aspects of electrolocation. *J Comp Physiol* 103:247-272

Heiligenberg W (1977) Principles of electrolocation and jamming avoidance in electric fish. In: Barlow HB (ed). Studies of brain function. Springer, Berlin, pp 1-85

Heiligenberg W, Bastian J (1984) The electric sense of weakly electric fish. *Annual Rev Physiol* 46:561-583

Heiligenberg W (1986) Jamming avoidance responses: model systems for neuroethology. In: Bullock TH, Heiligenberg W (eds). Electroreception. Wiley, New York, pp 613-649

Heiligenberg W (1988) Electrosensory maps form a substrate for the distributed and parallel control of behavioral responses in weakly electric fish. *Brain Behav Evol* 31:6-16

Heiligenberg W (1989) Coding and processing of electrosensory information in gymnotiform fish. *J Exp Biol* 146:255-275

Heiligenberg W (1991) Neural Nets in Electric Fish. MIT Press, Cambridge

Hille B (1984) Ionic channels of excitable membranes. Sinauer Assoc., Sunderland MA

Hopkins CD (1976) Stimulus filtering and electroreception: Tuberous electroreceptors in three species of Gymnotoid fish. *J Comp Physiol* 111:171-207

Hopkins CD (1986a) Behavior of Mormyridae. In: Bullock TH, Heiligenberg W (eds). Electroreception. Wiley, New York, pp 527-576

Hopkins CD (1986b) Temporal structure of non-propagated electric communication signals. *Brain Behav Evol* 28:43-59

Hopkins CD (1988) Neuroethology of electric communication. *Ann Rev Neurosci* 11:497-535

Hopkins CD, Westby GWM (1986) Time domain processing of electric organ dischare waveforms by pulse-type electric fish. *Brain Behav Evol* 29:77-104

Horowitz P, Hill W (1989) *The Art of Electronics*. 2nd Ed, Cambridge University Press, 1989

Hoshimiya N, Shogen K, Matsuo T, Chichibu S (1980) The *Apteronotus* EOD field: waveform and EOD simulation. *J Comp Physiol* 135:283-290

Jackson JD (1975) Classical Electrodynamics (2nd ed). Wiley & Sons, New York

Jin H, Tullberg O (1985) More on boundary elements for three-dimensional problems. In: Brebbia CA, Maier G, eds. Boundary Elements VII: Proceedings of the 7th International Conference, Villa Olmo, Lake Como, Italy. Springer-Verlag, Berlin

Kawasaki M, Rose G, Heiligenberg W (1988) Temporal hyperacuity in single neurons of electric fish. *Nature* 336:173-176

Kawasaki M, Heiligenberg W (1990) Different classes of glutamate receptors and GABA mediate distinct modulations of a neuronal oscillator, the medullary pacemaker if a gymnotiform electgric fish. *J Neuroscience* 10:3896-3904

Kawasaki M (1993) Independently evolved jamming avoidance responses employ identical computational algorithms: a behavioral study of the African electric fish, *Gymnarchus niloticus*. *J Comp Physiol* 173:9-22

Kawasaki M (1996) Comparative analysis of the jamming avoidance-response in African and South American wave-type electric fishes. *Biol B* 191:103-108

Kirschbaum F (1983) Myogenic electric organ precedes the neurogenic organ in apteronotid fish. *Naturwissenschaften* 70:205-207

Knudsen E (1974) Behavioral thresholds to electric signals in high frequency electric fish. *J Comp Physiol* 91:333-353

Knudsen E (1975) Spatial aspects of the electric fields generated by weakly electric fish. *J Comp Physiol* 99:103-118

Kramer B, Otto B (1991) Waveform discrimination in the electric fish *Eigenmannia*: sensitivity for the phase differences between the spectral components of a stimulus wave. *J Exp Biol* 159:1-22

Langner G, Scheich H (1978) Active phase coupling in electric fish: behavioral control with microsecond precision. *J Comp Physiol* 128:235-240

Lissmann HW, Machin KE (1958) The mechanism of object location in *Gymnotus niloticus* and similar fish. *J Exp Biol* 35:451-486

Lissmann HW (1963) Electric location by fishes. *Scientific American* 208(3):50-59

Lorenzo D, Sierra F, Silva A, Macadar O (1990) Spinal mechanisms of electric organ synchronization in Gymnotus carapo. *J Comp Physiol A* 167:447-452

Macadar O, Lorenzo D, Velluti JC (1989) Waveform generation of the electric organ discharge in *Gymnotus carapo* . II. Electrophysiological properties of single electrocytes. *J Comp Physiol A* 165:353-360

Maler L, Sas E, Rogers J (1981) The cytology of the posterior lateral line lobe of high frequency weakly electric fish (Gymnotidei): dendritic differentiation and synaptic specificity in a simple cortex. *J Comp Neural* 195:87-140

Maler L, Mugnaini E (1993) Organization and function of feedback to the electrosensory lateral line lobe of gymnotiform fish, with emphasis on a searchlight mechanism. *J Comp Physiol A* 173:667-670

McGregor PK, Westby GWM (1992) Discrimination of individually characteristic electric organ discharges by a weakly electric fish. *Anim Behav* 43:977-986

McKibben JR, Hopkins CD, Yager DD (1993) Directional sensitivity of tuberous electroreceptors: polarity preferences and frequency tuning. *J Comp Physiol A* 173:415-424

Meek J (1993) Structural organization of the mormyrid electrosensory lateral line lobe. *J Comp Physiol A* 173:675-677

Miall RC, Weir DJ, Wolpert DM, Stein JF (1993) Is the cerebellum a Smith predictor?. *J Motor Behav* 25:203-216

Miall RC, Wolpert DM (1996) Forward models for physiological motor control. *Neural Networks* 9(8):1265-1279

Moller P, Fritzsch B (1993) History of electroreception. *J Comp Physiol A* 173:734-737

Montgomery JC (1984) Noise Cancellation in the Electrosensory System of the Thornback Ray: Common Mode Rejection of Input Produced by the Animal's own Ventilatory Movement. *J Comp Physiol* 155:103-111

Montgomery JC, Bodznick D (1994) An adaptive filter that cancels self-induced noise in the electrosensory and lateral line mechanosensory systems of fish. *Neurosci Lett* 174:145-148

Nelson ME, Paulin MG (1995) Neural simulations of adaptive reafference suppression in the elasmobranch electrosensory system. *J Comp Physiol A* 177:723-736

Paulin MG (1993a) The role of the cerebellum in motor control and perception. *Brain Behav Evol* 41:39-50

Paulin MG (1993b) A model of the role of the cerebellum in tracking and controlling movements. *Human Movement Sci* 12:5-16

Plonsey DG (1969) Bioelectric Phenomena. McGraw-Hill, New York

Press WH, Teukolsky SA, Vetterling WT, Flannery BP (1992) Numerical Recipes in C, 2nd edition. Cambridge University Press, Cambridge

Ramo S, Whinnery JR, Van Duzer T (1984) Fields and waves in communication electronics, 2nd ed. Wiley, New York

Rasnow B, Assad C, Nelson ME, Bower JM (1989) Simulation and measurement of the electric fields generated by weakly electric fish. In: Touretzky D (ed) Advances in Neural Network Information Processing Systems. Kaufmann Publishers, San Mateo CA, pp 436-443

Rasnow B, Assad C, and Bower JM (1993) Phase and amplitude maps of the electric organ discharge of the weakly electric fish, *Apteronotus leptorhynchus*. *J Comp Physiol A* 172:481-491

Rasnow B (1996) The effects of simple objects on the electric field of*Apteronotus leptorhynchus*. *J Comp Physiol A* 178:397-411

Rasnow B, Assad C, Hartmann MJ, Bower JM (in press) Applications of multimedia computers and video mixing to neuroethology. *J Neurosci Methods*

Reddy JN (1984) An Introduction to the Finite Element Method. McGraw-Hill, New York

Rider PR (1942) Plane and spherical trigonometry. The MacMillan Company, New York

Robinson DA (1968) The Electrical Properties of Metal Microelectrodes. *Proc. IEEE* 56:1065-1071

Rose GJ (1989) Suppression of 'common mode' signals in the central electrosensory system. Soc Neurosci Abstr 15:348

Salmon G (1914) A Treatise on the Analytic Geometry of Three Dimensions. Longmans, Green and Co., London

Scheich H, Bullock TH, Hamstra RH (1973) Coding properties of two classes of afferent nerve fibers: high-frequency electroreceptors in the electric fish, *Eigenmannia*. *J Neurophysiol* 36:39-60

Scheich H, Bullock TH (1974) The detection of electric fields from electric organs. In: Fessard A (ed) Handbook of Sensory Physiology, Vol III/3. Springer-Verlag, Berlin Heidelberg New York, pp 201-256

Shumway CA (1989a) Multiple electrosensory maps in the medulla of weakly electric gymnotiform fish. I: physiological differences. *J Neuroscience* 9:4388-4399

Shumway CA (1989b) Multiple electrosensory maps in the medulla of weakly electric gymnotiform fish. I: anatomical differences. *J Neuroscience* 9:4400-4415

Sperry RW (1950) Neural basis of the spontaneous optokinetic response produced by visual neural inversion. *J Comp Physiol Psychol* 43:482-489

Strang G, Fix GJ (1973) An analysis of the finite element method. Prentice-Hall, NJ

Szabo T (1974) The anatomy of the specialized lateral line organs of electroreception. In: Fessard A (ed) Handbook of Sensory Physiology, Vol 3: Electroreceptors and Other Specialized Receptors in Lower Vertebrates. Springer-Verlag, Berlin, pp 13-58

Tang W (1988) Transforming domain into boundary integrals in BEM. In: Brebbia CA, Orszag SA (eds). Lecture Notes in Engineering. Springer-Verlag, Berlin

Toerring MJ, and Belbenoit P (1979) Motor programmes and electroreception in mormyrid fish. *Behav Ecol Sociobiology* 4:369-379

Trujillo-Cenoz O, Echague JA, Macadar O (1984) Innervation pattern and electric organ discharge waveform in *Gymnotus carapo* (Teleostei; Gymnotifromes). *J Neurobiol* 15:273-281

Trujillo-Cenoz O, Echague JA (1989) Waveform generation of the electric organ discharge in *Gymnotus carapo* . I. Morphology and innervation of the electric organ. *J Comp Physiol A* 165:343-351

Viancour TA (1979) Electroreceptors of a weakly electric fish I. Characterization of tuberous receptor organ tuning. *J Comp Physiol* 133:317-325

Vischer HA (1993) Morphological and pharmacological aspects of electroreceptor development. *J Comp Physiol A* 173:715-717

von der Emde G, Bleckmann H (1992) Extreme phase sensitivity of afferents which innervate mormyromast electroreceptors. *Naturwissenschaften* 79:131-133

von Holst E, Mittelstaedt H (1950) Das Reafferenzprinzip. *Naturwissenschaften* 37:464-476

Watanabe A, Takeda K (1963) The change of discharge frequency by AC stimulus in a weakly electric fish. *J Exp Biol* 40:57-66

Watson D, Bastian J (1979) Frequency response characteristics of electroreceptors in the weakly electric fish, *Gymnotus carapo*. *J Comp Physiol* 134:191-202

Watson DF (1981) Computing the N-Dimensional Delaunay Tesselation with Application to Voroni Polytopes. *Computer J* 24:167-172

Waxman SG, Pappas GD, Bennett MVL (1972) Morphological correlates of functional differentiation of nodes of Ranvier along single fibers in the neurogenic electric organ of the knife fish Sternarchus. *J Cell Biology* 53:210-224

Waxman SG, Anderson MJ (1986) Regeneration of central nervous system structures: *Apteronotus* spinal cord as a model system. In: Bullock TH, Heiligenberg W (eds). Electroreception. Wiley, New York, pp 183-208

Westby GWM (1984) Electroreception and communication in electric fish. *Sci Prog Oxf* 69:291-313

Weinstock R (1974) Calculus of Variations. Dover Publications, New York

Westby GWM (1988) The ecology, discharge diversity and predatory behavior of gymnotifrome electric fish in the coastal streams of French Guiana. *Behav Ecol Sociobiol* 22:341-354

Williams R, Rasnow B, Assad C (1990) Hypercube simulation of electric fish potentials. Concurrent computation technical report, Caltech Concurrent Computation Program

Wu CH (1984) Electric fish and the discovery of animal electricity. *American Scientist* 72:598-607

Xu Z, Payne JR, Nelson ME (1996) Logarithmic time-course of sensory adaptation in electrosensory afferent nerve-fibers in a weakly electric fish. *J Neurophysiol* 76:2020-2032

Hopkins CD (1993) Directional characteristics of tuberous electroreceptors in the weakly electric fish, *Hypopomus* (Gymnotiformes). *J Comp Physiol* 173:401-414

Zakon HH (1986) The electroreceptive periphery. In: Bullock TH, Heiligenberg W (eds). Electroreception. Wiley, New York, pp 103-156

Zakon HH(1987) Hormone-mediated plasticity in the electrosensory system of weakly electric fish. *Trends Neurosci* 10:412-421

Zakon HH (1987b) Variation in the mode of receptor cell addition in the electrosensory system of gymnotiform fish. *J Comp Neurol* 262:195-214

Zupanc G, Maler L (1993) Evoked chirping in the weakly electric fish, *Apteronotus leptorhynchus*: a quantitative biophysical analysis. *Can J Zool* 71:2301-2310